GaAs-Based Distributed Feedback Lasers Based on GaAs-InGaP Regrowth Technology

By

Hongchi Lei

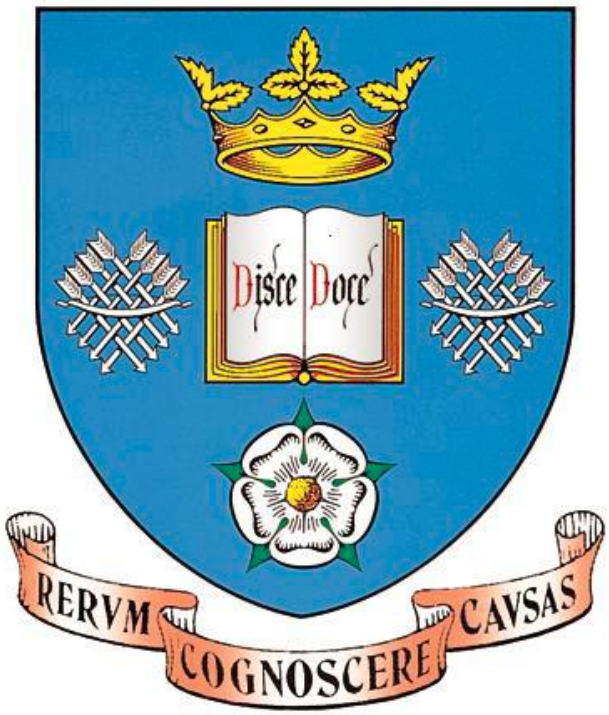

Department of Electronic and Electrical Engineering

Thesis submitted to the University of Sheffield for the degree of Doctor of Philosophy

September 2017

This Page
Intentionally
Left Blank

Abstract

This thesis describes the conceptualisation and realisation of GaAs-based self-aligned stripe (SAS) distributed feedback lasers (DFB) based on GaAs-InGaP regrowth technology, and its incorporation into the development of master oscillator power amplifier (MOPA) photonic integrated circuit (PIC).

GaAs-based SAS DFB lasers operate via a single longitudinal mode and provide a robust, portable and low cost solution to enable a broad range of potential applications. Compared to other waveguides, e.g. ridge waveguide, SAS structures enable narrower active regions and demonstrate better characteristics with a lower sensitivity to temperature.

In my designs, InGaP/GaAs buried gratings are formed utilising an Al-free grating sequence GaAs-InGaP-GaAs, whilst the SAS waveguides are realised via a stripe-etched n-doped InGaP optoelectronic confinement layer, where no AlGaAs is exposed during the fabrication process.

Chapter 1 goes through the development of DFB lasers over almost 5 decades since its birth in 1970s, followed by discussion of the gap between present GaAs-based PIC technologies and their commercialisation. After, Chapter 2 introduces the experimental methodology involved in the research activities conducted: fundamental principles of DFB lasers and the 4-stage research process.

The following 3 chapters describe the 3 main projects in this research. Chapter 3 begins with the design of 2×, 4× and 6× InGaAs QWs narrow ridge DFB lasers in, and then moved onto the conceptualisation and realisation of 2× and 4× InGaAs QWs SAS DFB lasers in Chapter 4. This SAS-DFB technology was then applied to the development of monolithically integrated 4× InGaAs QWs MOPA PIC in Chapter 5.

In Chapter 6, I outline some future work to be conducted for further achievement. An optimised design of SAS-DFB-MOPA is first discussed. I then present some preparatory works for two other potential future directions: widely tunable GaAs-based sampled grating distributed Bragg reflector laser (SG-DBR) and high power ~1180nm In(Ga)As/GaAs DWELL (dot-in-a-well) SAS-DFB-MOPA.

Dedicated to my parents,

Chun Lei and Hui Yuan

And all of my friends

Without whom none of my achievement would be possible

Acknowledgement

First of all, I would like to gratefully acknowledge my supervisor, Dr. Kristian Groom. He has provided me patient and tolerant guidance during these years. Without his support and help, I would not have completed what I have achieved.

Then, I would like to express my sincere appreciation to the University of Sheffield and EPSRC National Centre for III-V Technologies for offering me this precious opportunity to conduct my research here whilst facilitating the entire process.

Next, I would also like to thank all the senior members in the III-V centre, Nasser, Ben, Dave, Ken, Saurabh, Richard, Ed, Rob, Jon, Paul, etc. and those who have offer assistance and guidance to my research.

Also, many thanks to all my dear colleagues in these years, especially Xiao, Wei, Siming, Kejia, Omar, Tim, Brett, Avan, etc and all those who have accompanied me during my stay and offered me help and support.

Last but not least, I would like to sincerely thank my parents who have been supporting and encouraging me unconditionally since the beginning till now.

List of Publications

- **Related Paper**

Hongchi Lei, Benjamin J. Stevens, Paul W. Fry, Nasser Babazadeh, Gary Ternent, David T. Childs and Kristian M. Groom, "A GaAs-based self-aligned stripe distributed feedback laser." *Semiconductor Science and Technology*, vol. 31, no. 8, 2016.

In preparation:

DFB lasers operate via dual lateral modes for THz radiation generation

GaAs-based self-aligned stripe DFB master oscillator power amplifier (MOPA)

- **Related Oral Talk**

Hongchi Lei, Kristian M. Groom, Andrey B. Krysa, Benjamin J. Stevens, Nasser Babazadeh, Paul W. Fry, Gary Ternent, Stephen Thoms, David T. Childs and Richard A. Hogg, "Optimisation of GaAs-Based Distributed Feedbakc Lasers Operating ~1000nm" *UK Semiconductors 2014 & UK Nitrides Consortium Summer Meeting*, July 2014

List of Acronyms

AFM	atomic-force microscopy
AR / HR	anti-reflection / high reflection
ASE	amplified spontaneous emission
BH	buried heterostructure
CW (current source)	continuous wave (current source)
DBR (laser)	distributed Bragg reflector (laser)
DFB (laser)	distributed feedback (laser)
DHS	double heterostructure
DI (water)	deionised (water)
DWELL	dot-in-a-well
EL / PL (spectrum)	electroluminescence / photoluminescence (spectrum)
FMM	film mode matching
FP	Fabry-Pérot
FWHM	full width at half maximum
GS / ES	ground state / excited state
ICP (etch)	inductively coupled plasma (etch)
IFVD	impurity-free vacancy diffusion
LPE	liquid phase epitaxy
MBE	molecular beam epitaxy
MOPA	master oscillator power amplifier
MOVPE	metalorganic vapour phase epitaxy
OSA	optical spectrum analyser
PECVD	plasma-enhanced chemical vapour deposition
PIC	photonic integrated circuit
QW / QD	quantum well / quantum dot
RIE	reactive ion etching
RTA	rapid thermal annealing
RWG	ridge waveguide
SAS	self-aligned stripe
SG-DBR (laser)	sample grating distributed Bragg reflector (laser)
SHB	spatial hole burning
SLM	single longitudinal mode
SMSR	side mode suppression ratio
SOA	semiconductor optical amplifier
TEC	thermo-electric cooling
VECSEL	vertical external-cavity surface-emitting laser

This Page
Intentionally
Left Blank

Contents

Abstract ..... **i**

Acknowledgement ..... **iii**

List of Publications ..... **iv**

List of Acronyms ..... **v**

Chapter 1. Introduction **1**

1.1 Background 2

1.1.1 InP-based and GaAs-Based Lasers 3

1.1.2 Single Longitudinal Mode Laser 6

1.2 Fundamental Principle of Semiconductor Lasers 8

1.2.1 Energy Bands and Band Gap 8

1.2.2 Optical Properties of Semiconductor 10

1.2.3 Laser Structures 11

1.3 Distributed Feedback Lasers 17

1.3.1 First Realisation in the 1970s 17

1.3.2 Development of InP/InGaAsP DFBs 19

1.3.3 Towards Higher Single Longitudinal Mode Yield 23

1.3.4 On-Chip Thin Film Heater 26

1.3.5 Maturity of GaAs-Based System: Shift back to Shorter Wavelength 29

1.3.6 Commercially Available DFBs (650-1450nm) 31

1.3.7 Recent Development 33

1.4 Grating Fabrication Methods 36

1.4.1 Surface Grating 36

1.4.2 Buried Grating (Overgrown Grating) 44
1.5 Photonic Integration of DFB Lasers 49
1.5.1 Monolithic Photonic Integration 50
1.5.2 Maturity in InP-Based PICs (>1200nm) 51
1.5.3 Lack of Development of GaAs-Based PICs (<1200nm) 52
1.5.4 Overcoming the Technological Barrier 53
1.6 Project Motivation 55
1.7 Thesis Outline 56
1.8 Reference 59

Chapter 2. Fundamental Principles of DFB and Experimental Methodology ... 69

2.1 Fundamental Principles of DFB Laser 69
2.1.1 Light as Electromagnetic Waves 69
2.1.2 Fundamental Principles of DFB Lasers 71
2.1.3 DFB Design in This Research 79
2.2 Experimental Methodology 81
2.2.1 Device Design – Fimmwave Waveguide Simulation 81
2.2.2 Wafer Growth – Metal Organic Vapour Phase Epitaxy 84
2.2.3 Device Fabrication 85
2.2.4 Device Characterisation 97
2.3 Reference 107

Chapter 3. GaAs-Based Narrow Ridge Distributed Feedback Lasers 109

3.1 DFB Simulation 110
3.1.1 Fimmwave – Waveguide Modelling Software 112
3.1.2 Strain-Balanced QW Design 113

3.1.3 Design and Simulation 115
3.1.4 Summary 119
3.2 Preparation Works 120
3.2.1 MBE and MOVPE Comparison: Broad Area Lasers 123
3.2.2 Comparison of 2×, 4× and 6× QWs Mesa Diodes 124
3.2.3 Comparison of 2×, 4× and 6× QWs Broad Area Lasers 127
3.2.4 Summary 135
3.3 DFB Fabrication 136
3.3.1 Planar Growth 137
3.3.2 Grating Patterning and Etching 137
3.3.3 Over-Growth 141
3.3.4 Laser Fabrication 142
3.4 DFB Characterisation 148
3.4.1 Characterisation of Two 1mm Long Representative Devices 150
3.4.2 Re-Simulation of Over-Etched Ridge Waveguide 158
3.4.3 Characterisation of Longer Devices 159
3.4.4 Thermal and Current Tuning Measurement 163
3.4.5 Overall Summary of DFB Tuning Measurement 166
3.4.6 Comparison of Experimental and Simulated Coupling Coefficients 167
3.5 Conclusion 171
3.6 Reference 173

Chapter 4. GaAs-Based Self-Aligned Stripe Distributed Feedback Lasers 175

4.1 Structural Design of SAS-DFB 177
4.1.1 Advantage and Novelty 178
4.1.2 Original Design and Simulation 180
4.1.3 Design Modification 182
4.1.4 Final Structure Design 186
4.2 Growth and Fabrication 188

4.2.1 Sample Growth 189
4.2.2 Device Fabrication 192
4.3 Characterisation and Discussion 196
4.3.1 4×QWs SAS-DFB 196
4.3.2 2×QWs SAS-DFB 207
4.3.3 Validation of Simulation 209
4.3.4 Further Simulation for Future Work 213
4.4 Conclusion 215
4.5 Reference 217

Chapter 5. GaAs-Based Monolithically Integrated Self-Aligned Stripe Master Oscillator Power Amplifier 219

5.1 Master Oscillator Power Amplifier 220
5.1.1 Discrete MOPA Designs 220
5.1.2 Monolithically Integrated MOPA Designs 222
5.2 Development of Monolithically Integrated MOPA 224
5.2.1 Realisations for Wide Tunability 224
5.2.2 Realisation for High Power 226
5.2.3 Realisations for Different Wavelength Generation 228
5.2.4 Disadvantages of Monolithic MOPA 229
5.3 SAS-MOPA Design 230
5.3.1 Waveguide: Self-Aligned Stripe (SAS) 230
5.3.2 Section Geometry: DFB and Flared SOAs 232
5.4 Device Manufacture 235
5.4.1 Epitaxial Growth 236
5.4.2 Device Fabrication 239
5.5 Device Characterisation 242
5.5.1 DFB Laser Sections Characterisation 242

5.5.2 SOA Sections Characterisation 245
5.5.3 Characterisation of MOPAs with Straight SOAs 252
5.5.4 Characterisation of MOPAs with Tilted SOAs 259
5.5.5 Comparison and Discussion 268
5.5.6 An Observed Issue of the Device Pumping Scheme 274
5.6 Conclusion 277
5.7 Reference 280

Chapter 6. Future Work 283

6.1 Optimisation of SAS-DFB-MOPA 283
6.2 SAS-SGDBR 286
6.3 1180nm In(Ga)As/GaAs DWELL SAS-DFB-MOPA 290
6.4 Reference 298

Chapter 7. Conclusion 301

Appendix I: Fimmwave Simulation Example 305

This Page
Intentionally
Left Blank

Chapter 1. Introduction

After Einstein showed the existence of stimulated emission, the first laser action was developed in 1960 by Maiman [1] in ruby. The word “laser” is the acronym for “light amplification by stimulated emission of radiation”. A laser is also regarded as a laser oscillator, which generates laser light output without light input. This means that a laser performs initially as a light emitter, as well as a light amplifier. In the past half century, the blooming of semiconductor lasers has vigorously boosted the development of optical systems. Today, semiconductor lasers are undoubtedly playing increasingly significant roles in numerous applications, such as optical data storage, spectroscopy, metrology, material processing and medical treatments. Especially, the use of semiconductor lasers in optical data transmission makes them the backbone supporting today's Information Age. Semiconductor lasers demonstrate better lasing performance over other alternatives like dye lasers or gas lasers. In general, they operate more robustly and reliably while generating highly coherent optical waves at sufficiently high output powers, whilst maintaining a high efficiency of electrical-to-optical power-conversion. In addition, semiconductor lasers are smaller and cheaper than alternatives.

This chapter starts with the background and fundamental principles of semiconductor lasers (Sections 1.1 and 1.2), then moves onto the core research topic of this thesis, i.e. distributed feedback (DFB) lasers. Section 1.3 establishes an overview of the historical development of DFB lasers since the 1970s. In Sections 1.4 and 1.5, two core technologies involved in my research are discussed, i.e. grating fabrication and photonic integration, followed by an overall description of the project motivation (Section 1.6).

1.1 Background

The concept of semiconductor lasers was first demonstrated and reported in 1962 by several groups [2]-[5]. Since then, semiconductor lasers have undergone an all-aspect development during the next 55 years to this day, including the design concepts of epitaxial structures and waveguides, and their related fabrication methods and techniques. The fundamental concept of semiconductor lasers is shown in Fig. 1-1: a laser utilises stimulated emission, (a), in a gain material within a layered epitaxially-grown structure, e.g. (b) a double heterostructure "p-i-n" junction, which is fabricated into an optical waveguide geometry that provides lateral optoelectronic confinement (e.g. ridge waveguide) with certain mechanisms providing optical feedback for the generated optical wave (e.g. front-end facets or grating), as shown in (c). This will be described in detail in in the Section 1.2.

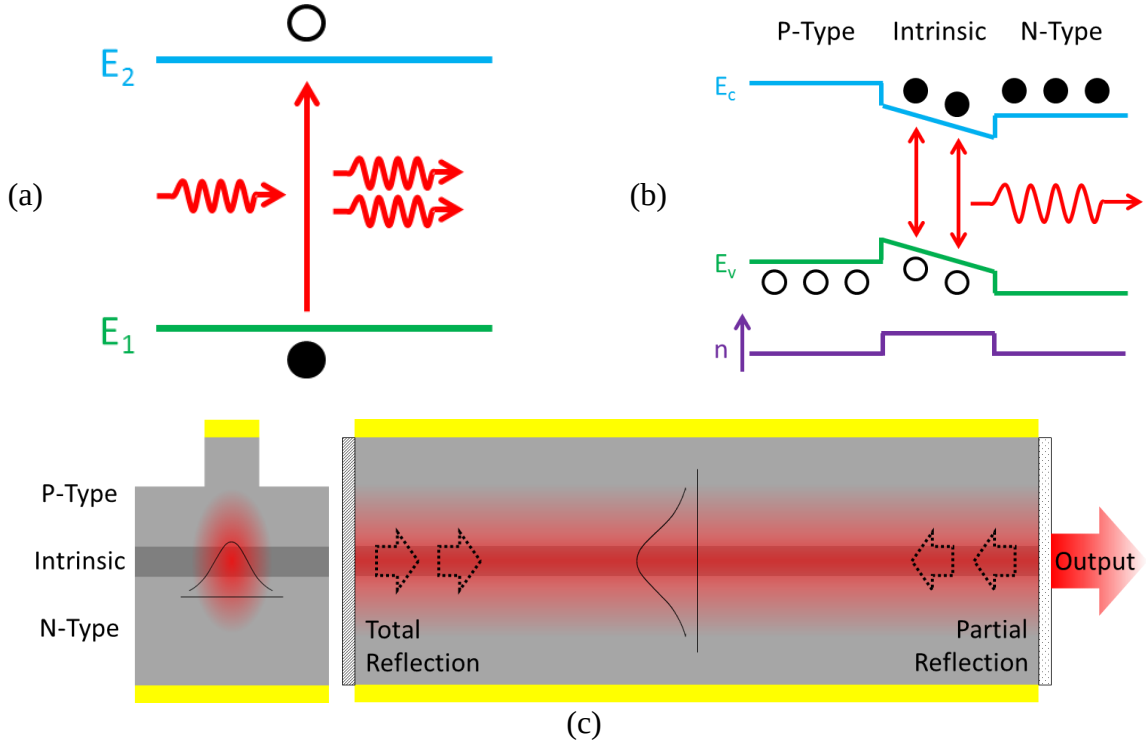

Figure 1-1: Fundamental concept of semiconductor lasers: (a) stimulated emission, (b) double heterostructure "p-i-n" junction and (c) ridge waveguide Fabry-Pérot (FP) laser with asymmetric facet reflectivity

In the design and development of a laser with an anticipated functionality, it is significant that the lasing performance matches the set of required characteristics, including spectral profile, beam profile and L-I (light output to current injection) profile. The spectral profile concerns aspects like the lasing wavelength, linewidth and whether emission is via multi-mode or single mode. The requirement in the beam profile of a laser is either based on the condition of its direct usage or in accord with the situation where its output light needs to be coupled into a next section (a fibre or device).

For a commercially available laser, a packaging method is chosen in accord with its characteristics (output beam profile, output power and operating temperature) and its expected application situations, which concerns the limitation of package size/shape, whether a fibre is needed and so on.

Nowadays, most commercial semiconductor lasers in the wavelength range from 650nm to 2μm are based on two major types: GaAs-based lasers (grown on gallium arsenide substrates) and InP-based lasers (grown on indium phosphide substrates).

1.1.1 InP-based and GaAs-Based Lasers

The wavelength of a laser is primarily determined by the bandgap energy of the intrinsic material (active region). Although any direct-bandgap semiconductor can theoretically be used to produce lasers, the requirements for different alloys, i.e. epitaxial layers, to be lattice-matched and capable of being precisely doped limit the options of available material systems.

Fig. 1-2 maps several commonly used alloys into coordinates of band gap energy (left-hand y-axis) and lattice constant (x-axis) at room temperature. The corresponding wavelength associated with the band gap energy is shown on the right-hand y-axis.

Both InP-based and GaAs-based laser systems use the alloys of the same constituents: gallium (Ga), aluminium (Al), indium (In), arsenic (As) and phosphorus (P), but grown in the compositions lattice-matched to InP and GaAs respectively. Additionally, for the applications requiring longer wavelengths (~10μm), quantum cascade lasers (QCL) were developed operating via inter-sub-band transitions, whilst gallium nitride (GaN) system is developed for applications requiring a shorter wavelength of ~400nm.

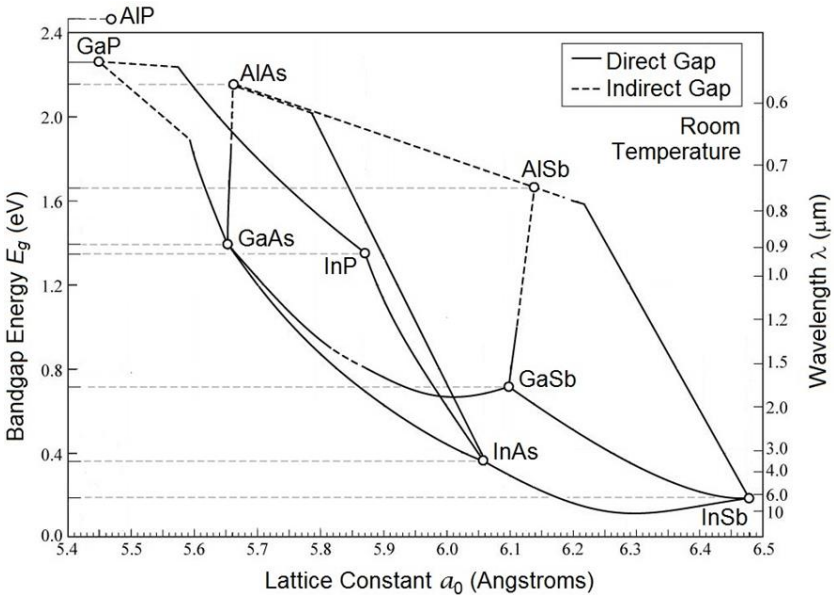

Figure 1-2: Lattice constant and bandgap energy of various III-V semiconductors at room temperature (adapted from Tien, 1988) [6]

For applications requiring wavelengths in the range of 1.3μm-2μm, lasers are fabricated with InP-based material systems. Especially, in long-haul optical communications, InP-based lasers lasing at wavelengths of 1300nm, 1480nm and 1550nm have been intensively studied, and their development has underpinned the improvement in fibre optic communications and the internet revolution. But for

applications like optical information recording/processing, optical measurement, biomedical applications and sensing requiring wavelengths shorter than ~1200nm, InP-based materials are no longer suitable due to the material's bandgap energy (E_g), where InP is used as the cladding and the band-gap offset becomes undesirable ($\Delta E_c \sim \Delta E_g$) for <1200nm, which severely limits their potential to satisfy a rapidly growing demand for innovation in this wavelength regime.

The GaAs-based material systems are for the wavelength range of 650nm-1200nm, and overlap with InP-based systems up to 1310nm has been realised. Compared to their counterparts, GaAs-based components with better performance are beginning to enter the market in large volume (e.g. those based on quantum dots sold by the QD Laser Inc., Japan). To date, devices operating up to ~1600nm are also available on GaAs, e.g. diluted nitrides (GaInNAsSb) [7], bismides (GaAsBi) [8] and bilayer QDs [9].

Fig. 1-3 shows the range of active material systems available to be grown on GaAs and the range of wavelengths they can access, together with some typical applications that can be addressed at these wavelengths.

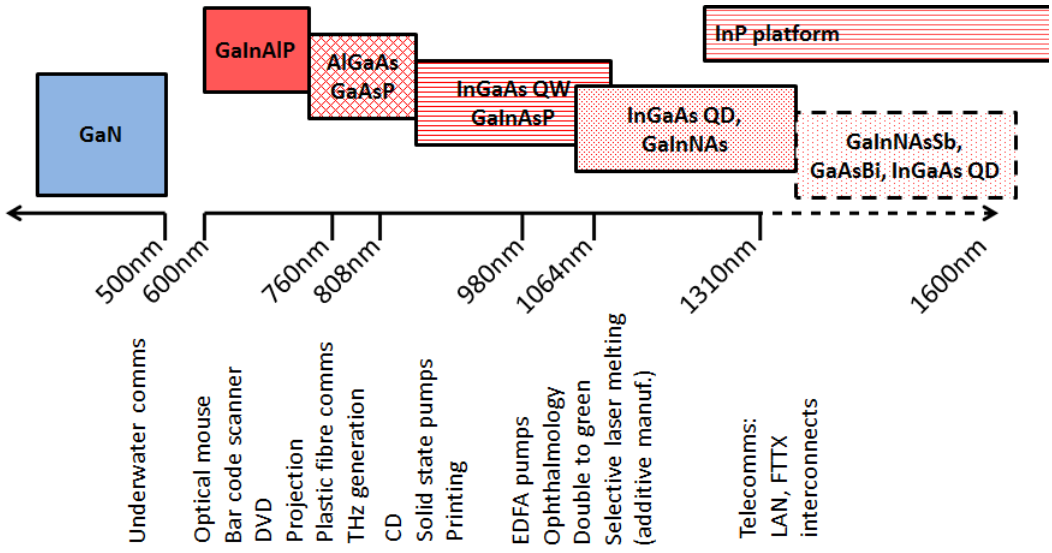

Figure 1-3: Potential spectral range addressed on GaAs, available active materials and associated applications with impacts envisioned, where the solide line represents commercially available materials and wavelength eregion, whilst the dotted line represents research grade materials and wavelength region

Wavelengths of 650nm-780nm are commonly used in optical storage and displays; 785nm, 808nm, 830nm, 920nm and 940nm are commonly used for solid state pumping and printing; 980nm is used for erbium doped fibre amplifier (EDFA) pumping in telecommunications; ~1060nm can be used for green light (520~560nm) generation through second harmonic generation (SHG), i.e. frequency doubling; and ~1300nm can be used for optical communications substituting InP-based lasers. In terms of manufacture, GaAs-based lasers benefit from the use of larger substrates (6 inch) for reduced fabrication costs. Furthermore, GaAs-based lasers enjoy a more favourable band off-set, which improves carrier confinement thus enabling higher temperature operation. Additionally, GaAs is also a cheaper and more robust material.

1.1.2 Single Longitudinal Mode Laser

For many applications, stable lasing operation via a single longitudinal mode (SLM) with a sufficiently narrow linewidth and a sufficiently high side mode suppression ratio (SMSR). Traditional Fabry-Pérot (FP) lasers, as illustrated in Fig. 1-1, are no longer feasible for such a spectral profile. Based on the concept of FP lasers, SLM can be achieved by introducing periodically structured mechanisms in the laser designs to provide wavelength selectivity in a similar way to diffraction gratings.

Fig. 1-4 illustrates the schematic diagrams of three well-studied SLM laser structures: (a) distributed Bragg reflector laser (DBR), (b) distributed feedback laser (DFB) and (c) vertical-cavity surface-emitting laser (VCSEL). A DFB laser employs a periodic structure (grating) along the gain medium, whilst a DBR laser has one or two DBR (grating) sections located on one or both sides of a gain section, and a VCSEL

utilises the epitaxially grown layers as the diffraction grating. Despite some advantages provided by VCSEL lasers (e.g. high beam quality with low divergence), DFB and DBR lasers are more favourable not only because the limitation of the maximum output power for a single VCSEL laser, but also due to their capability of being monolithically integrated into photonic integrated circuits (PICs), where a majority of optical systems are designed and realised with transverse propagation of light, i.e. edge emitting.

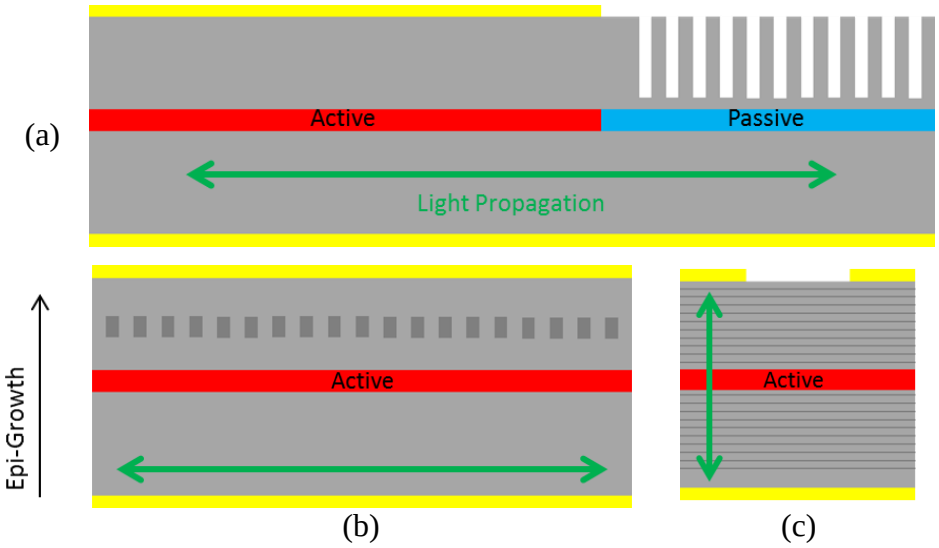

Figure 1-4: Schametic diagram of (a) DBR laser, (b) DFB laser and (c) VCSEL

Between DBR and DFB lasers, the latter has prevailed as the more cost-effective option. In addition, instead of having passive gratings located outside the active region, DFB lasers have gratings fabricated along the length of the waveguide. Although the grating functions under the same electrical and thermal operating conditions as the laser, which may result in less independency compared to the gratings in DBR lasers, the DBR lasers suffer from severe mode-hopping at high power [4], and hence the DFB has become the natural choice in single mode laser design. Furthermore, although both DFB and DBR lasers have potential for incorporation as the light source in PIC designs due to their independence upon cleaved facets for optical feedback, an additional active/passive integration technique is usually required even in the simplest DBR-PIC designs for a better device performance.

1.2 Fundamental Principle of Semiconductor Lasers

This section outlines the most related principles of semiconductor lasers, which support the laser design and development in the following chapters. This part starts with the energy bands and band gap, which are the ultimate determiners of the optoelectronic properties a material; then moves onto the optical properties of semiconductors, in which the stimulated emission process is the basis of laser operation; followed by several significant aspects of the structural design of semiconductor lasers, including the double hetero-structure (DHS), quantum well, laser cavity and waveguide design.

1.2.1 Energy Bands and Band Gap

In solids, isolated atoms are brought together at a balance between attractive and repulsive forces. Such a process significantly changes the electron energy levels. To avoid violating the Pauli Exclusion Principle, with the decreasing distance between atoms, electron wave functions start to overlap and split into discrete energy levels in the form of bands, as illustrated in Fig. 1-5. For a solid, the two highest energy bands, i.e. valance band and conduction band, are important in determining its optical-electrical properties. The forbidden energy gap between valance and conduction bands (E_g) is called the energy gap.

Kronig-Penney model considers an ideal one-dimensional single crystal array. The potential satisfies the same spatial period corresponding to lattice spacing. By applying Schrödinger equation, the result, as shown in Fig. 1-6 (a), which can be simplified to a

reduced zone version as highlighted by the yellow area, shows that there are a series of allowed energy bands with forbidden bands in-between.

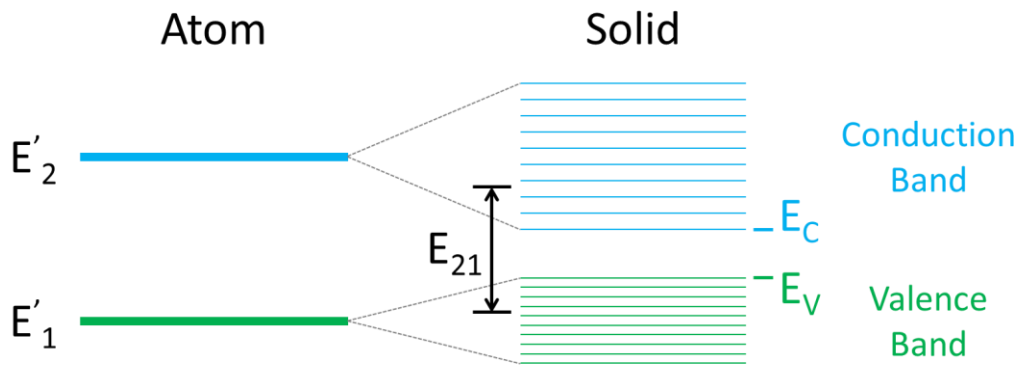

Figure 1-5: Development of discrete energy levels into energy bands [10]

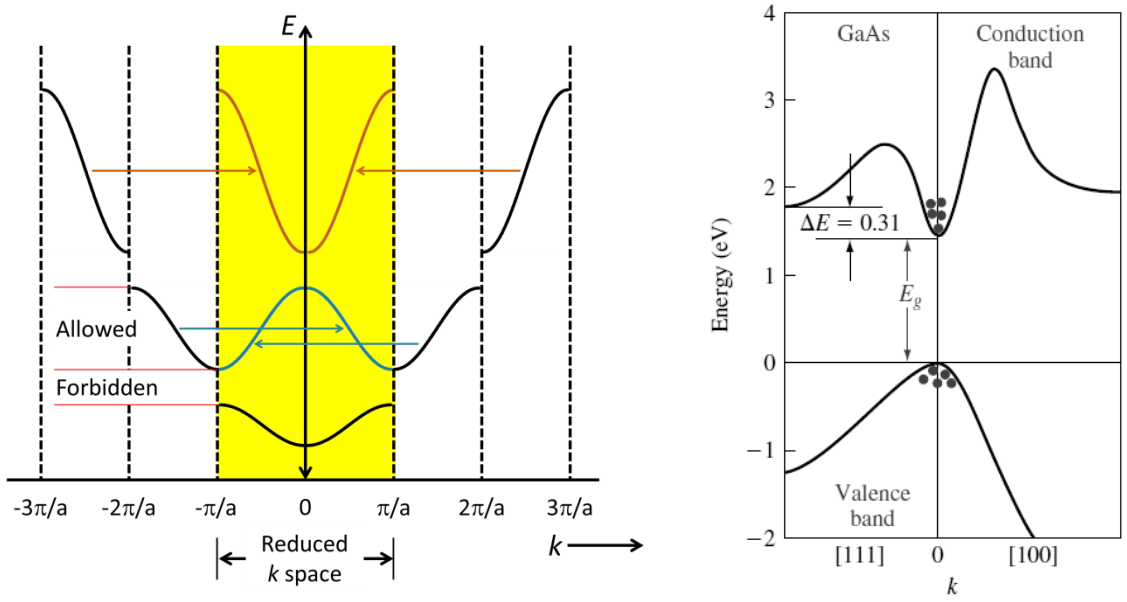

(a) (b)

Figure 1-6: (a) E-k relationships of Kronig-Penney mode and its reduced zone representation (yellow area) and (b) energy band structure of gallium arsenide (GaAs) [11]

In real 3-dimensional crystals, the E-k relationship is much more complicated than the Kronig-Penney model. Fig. 1-6 (b) shows the E-k relationship of gallium arsenide (GaAs), which illustrates significant difference between the calculated ones as shown in Fig. 1-6 (a). The nature of being a direct bandgap semiconductor (minimum energy of conduct band and maximum valance band energy are at the same k) makes GaAs an ideal material for developing semiconductor lasers.

1.2.2 Optical Properties of Semiconductor

The principle of semiconductor lasers lies in the interaction between light and semiconductor materials. As shown in Fig. 1-7, there are three ways that light (photons) interacts with electrons in semiconductor material, i.e. absorption, spontaneous emission and stimulated emission. In the figure the dots represent electrons, the circles represent holes and the waved arrows represent optical waves.

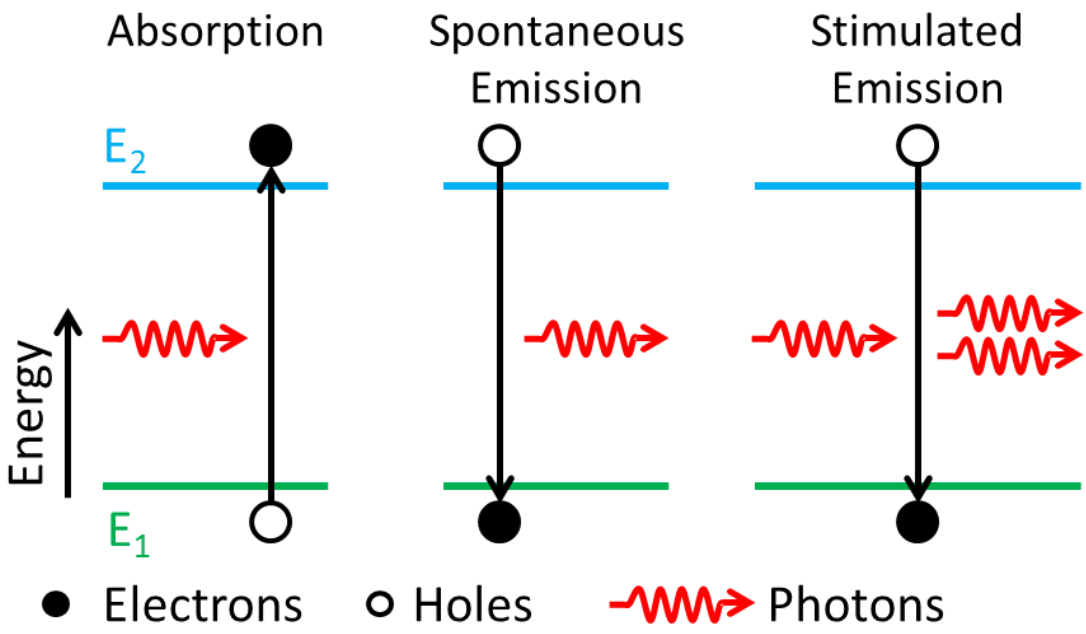

Figure 1-7: Three ways that a electron interacts with a photon: absorption, spontaneous emission and stimulated emission [12]

Absorption refers to the process that an electron initially in a lower energy level absorbs the energy from a photon and gets excited to a higher energy level.

Spontaneous emission refers to the process when an electron initially in a higher energy level jumps back to a lower energy level and releases the energy in the form of a photon. This process and the propagation direction of the generated photon are both random.

Stimulated emission refers to the process when an electron initially in a higher energy level is stimulated by a photon to jump back to a lower energy level to generate a photon with identical properties to the initial photon.

In addition to the above 3 processes, there is also non-radiative recombination, including Auger recombination and recombination at defects. In such processes, a conduction band electron recombines with a valence band hole while generating no useful photons, but phonons or lattice vibration. In the context of the semiconductor laser, these processes should be avoided, because they represent the loss of electrons which do not contribute to the gain.

1.2.3 Laser Structures

The process of stimulated emission provides optical gain to an incident wave by generating a coherent wave, i.e. same direction and phase. Therefore, the optical radiation propagating through the medium will be amplified as long as the stimulated emission process overwhelms the absorption in the cavity which requires a high density of electrons in the conduction band. However, under thermal equilibrium, more electrons naturally exist in the valance band resulting in the absorption process surpassing the stimulated emission.

Therefore, the material has to be driven into a non-equilibrium state to invert the carrier population by energy injection. For semiconductor lasers, population inversion is realised by injecting current into a p-n junction-based structure.

➢ Double Heterostructure (DHS)

The first generation semiconductor lasers [2]-[5] were designed as homo-junction structures working at forward biased condition. As illustrated in Fig. 1-8, a homo-junction structure can be regarded as a normal p-n junction with an additional intrinsic (un-doped) layer in-between. Electrons are injected from the n-type region and holes from the p-type region, thereby achieving population inversion in the intrinsic layer. These structures suffered from a weak confinement of injected electrons and holes

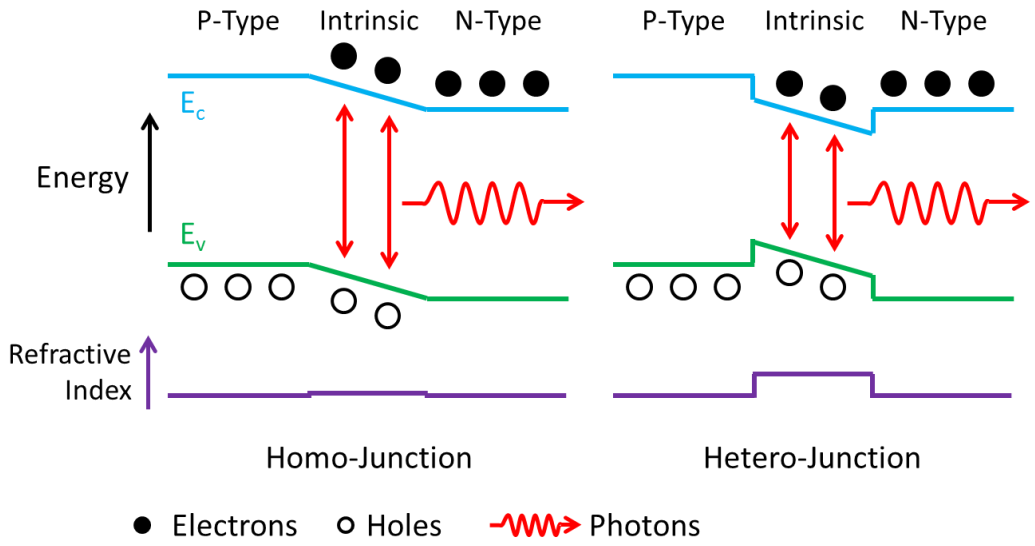

Figure 1-8: Band structure and refractive index step profiles of homo-junction and hetero-junction structures [12]

The concept of the double heterostructure (DHS) was first formulated in 1963 independently by Russian researchers Alferov and Kazarinov [13] and U.S. researcher Kroemer [14], and was realised for room temperature operation in 1969 [15]. From the 1960s to the 1970s, international competition in studying heterostructure (hetero-junction) lasers [16]-[18] was fierce, and the realisation of the DHS led to a huge development of semiconductor lasers.

A shown in Fig. 1-8, a DHS is formed by sandwiching an un-doped layer of one material with a smaller bandgap by two cladding layers, p-doped and n-doped respectively, of another material with a larger bandgap. A “p-i-n” junction is formed and the carrier confinement in the intrinsic layer is provided by the bandgap offset, which provides a potential well for carriers entering this region. The intrinsic materials also have higher refractive indices than that of the cladding materials, resulting in a favourable photon confinement through total internal reflection.

➢ Quantum Well

As described above, the DHS provides both optical and electrical confinements. When the thickness of the middle layer is reduced to be comparable to the de Broglie wavelength of the electron and holes (approximately 40 atomic layers thick), the allowed energy levels in the layer is no longer continuous, but quantised. This is when the DHS becomes a quantum well (QW) structure, in which quantum physics effects can be exploited in laser design at room temperature.

Fig. 1-9 illustrates the quantisation of the allowed energy levels in an ideal “infinite well” model, where the barriers on both sides of the quantum well are infinitely high, such that the wave-function is zero. Viewing this as a simple “particle-in-a-box” model, by applying Schrödinger's equation, the calculated allowed discrete sinusoidal wave-functions are with quadratically spaced energy levels.

Fig. 1-10 compares the optical absorption spectrum in a bulk structure and in a quantum well structure, where the existence of excitons is neglected. In a bulk structure, the profile of the curve follows that of the density of states.

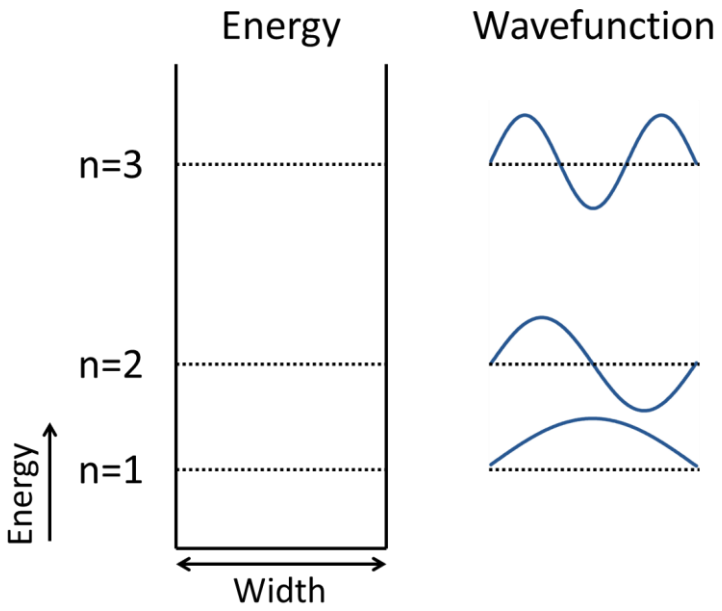

Figure 1-9: Illustration of quantisation in an "infinite well" through the "particle-in-a-box" model [19]

In a quantum well structure, the transitions in the valence and conduction bands are only allowed to occur between the states with the same quantum number, resulting in a "sub-bands" profile.

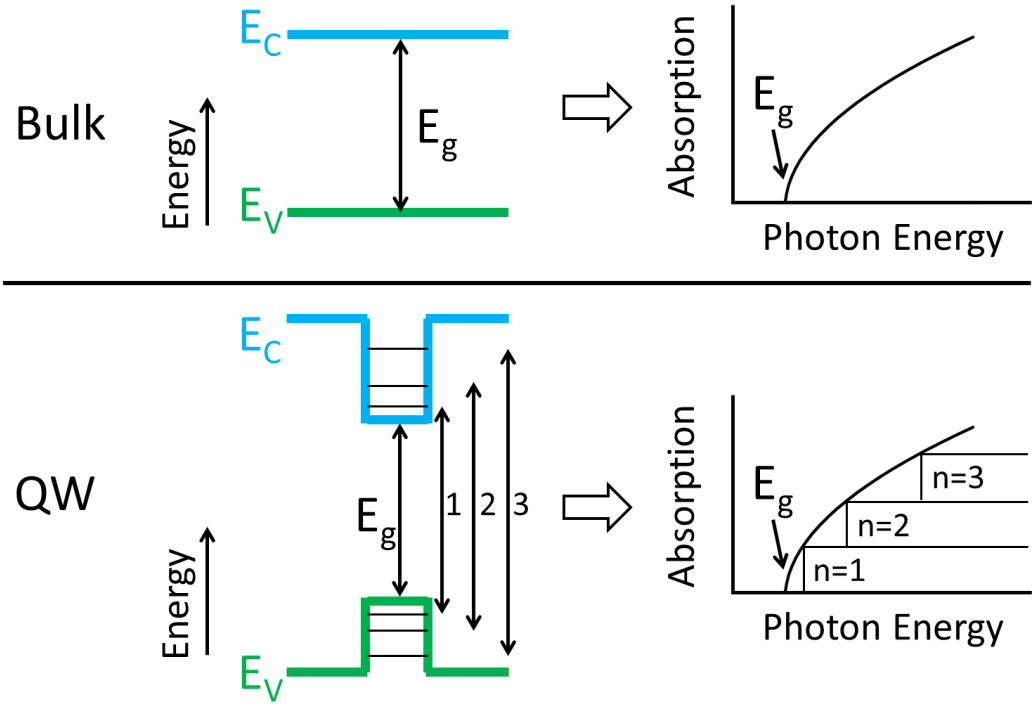

Figure 1-10: Optical absorption in a bulk structure and in a quantum well structure (excitonic effects are neglected) [19]

➢ Fabry-Pérot (FP) Laser Cavity

The manufacture of semiconductor lasers is based on epitaxial growth techniques. Therefore, the semiconductor lasers are either surface-emitting lasers, e.g. VCSELs, or edge-emitting lasers. FP lasers are a traditional edge-emitting laser type. They achieve optical feedback for amplification by letting the optical radiation resonate inside the cavity between facet mirrors, where the cavity is formed of (or partially formed of) gain medium. Other alternatives include DFB lasers and DBR lasers in which the optical feedback is distributed along the periodically structured diffraction grating.

Fig. 1-11 shows a FP cavity consisting of a highly-reflective coated rear mirror, a partially defined gain medium and an uncoated or anti-reflective coated front mirror, where the gain medium is pumped.

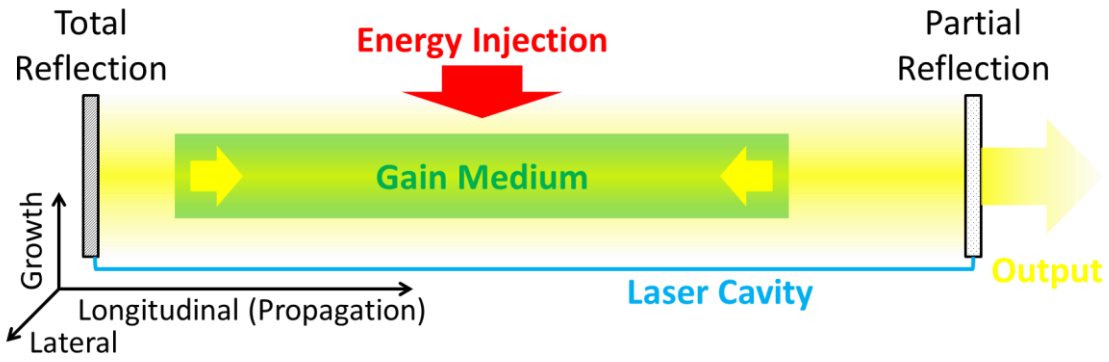

Figure 1-11: Schematic diagram of a FP laser with partially defined gain medium [12]

When the light is propagating in the cavity, a certain portion of it is repeatedly reflected back between the facets. Its intensity increases (obtains gain) if the injected current is high enough to achieve population inversion for stimulated emission to dominate the process. With increasing current, the gain increases until a threshold current is reached for the gain of a round trip to compensate the sum of internal loss and mirror loss. This is when the device starts to lase. With higher current injection, both gain and carrier density clamp in an operating laser.

➢ Waveguide Structures

The lateral confinement of the photon and carriers is realised through waveguide geometries. Lateral confinement is especially significant for the development of single longitudinal mode (SLM) lasers that also require a single lateral mode operation [20].

For gain-guided laser structures, this is achieved by laterally confining the gain stripe. As illustrated in Fig. 1-12 (a), the pumping current is limited to a predefined stripe contact. Although the injected current spreads laterally underneath, the current density will reduce to a level that the active region is dominated by absorption, so that the optical field is confined to the stripe area.

Index guiding can be achieved in the structures with lateral variation of refractive index. Fig. 1-12 (b) shows a ridge laser with weak index guiding which is further contributed with gain guiding. Fig. 1-12 (c) shows a buried DH laser with strong index guiding which dominates the lateral optical field confinement.

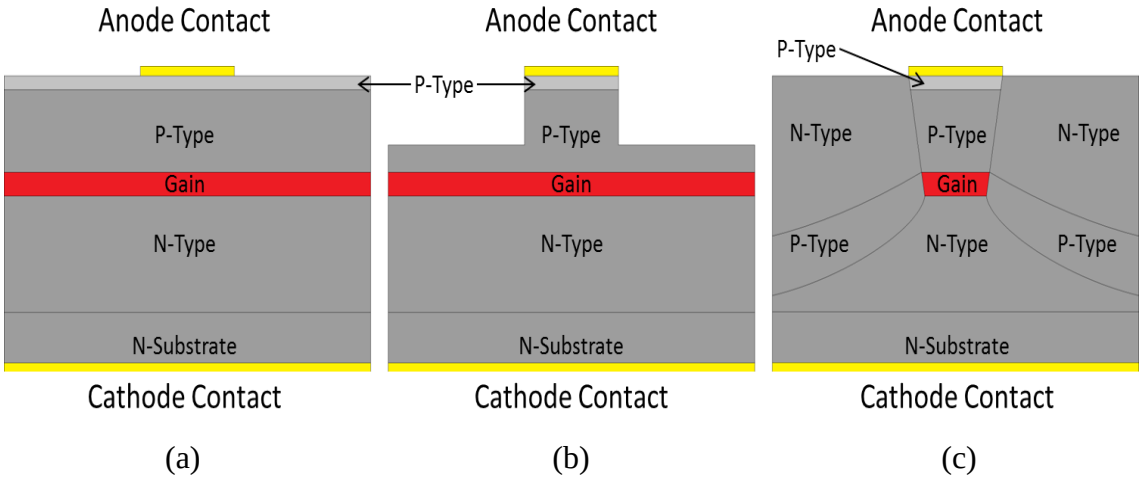

Figure 1-12: Schematics of edge-emitting laser diode structures [20]: (a) gain guided, (b) ridge waveguide: week index guiding and (c) buried heterostructure (BH): strong index guiding

Comparably, in buried DH lasers, strong index-guiding and a strong carrier confinement in the lateral direction can both be achieved. Also, such structures usually have lower threshold current density with a more stable mode pattern.

1.3 Distributed Feedback Lasers

This section takes a historical view and briefly introduces the development of DFB lasers during the recent 4 decades since their conceptualisation and realisation in the 1970s to the present days.

1.3.1 First Realisation in the 1970s

The fundamental concept of the DFB laser was developed by Herwig Kogelnik, Charles Shank and other co-workers in Bell Laboratories during 1969-1972: the coupled wave theory for thick hologram gratings [21] and its effect upon stimulated emission [22], and led to publication of the 'Coupled-Wave Theory of Distributed Feedback Lasers' [23], where the DFB lasers is defined as the laser structures "provide feedback via backward Bragg scattering from periodic perturbations of the refractive index and/or the gain of the laser medium itself".

The first generation DFB lasers were developed by several groups in 1974-1975: the research group in Xerox Palo Alto Research Centre [24] and the group of Hitachi Ltd. and California Institute of Technology [25] were 2 pioneers. In their reports, both research groups employed the same method to form the corrugation: p-AlGaAs grown on etched GaAs. Fig. 1-13 shows the schematic diagram of the GaAs/AlGaAs DHS DFB reported in [25]. The laser was fabricated in a 2-step LPE (liquid -phase epitaxy) process. In the first step, 4μm n-$Al_{0.3}Ga_{0.7}As$ and 1.5μm p-GaAs were grown on n-GaAs substrate. After etching the corrugations (period: 340nm, 3rd order, depth: 90nm) into the p-GaAs layer, in the second step 3μm p-$Al_{0.3}Ga_{0.7}As$ and 1μm p-GaAs were grown

on the corrugated surface. This design demonstrated 811nm single mode lasing at 80-l00K with a threshold current density of 2500A/cm^2 in pulsed operation.

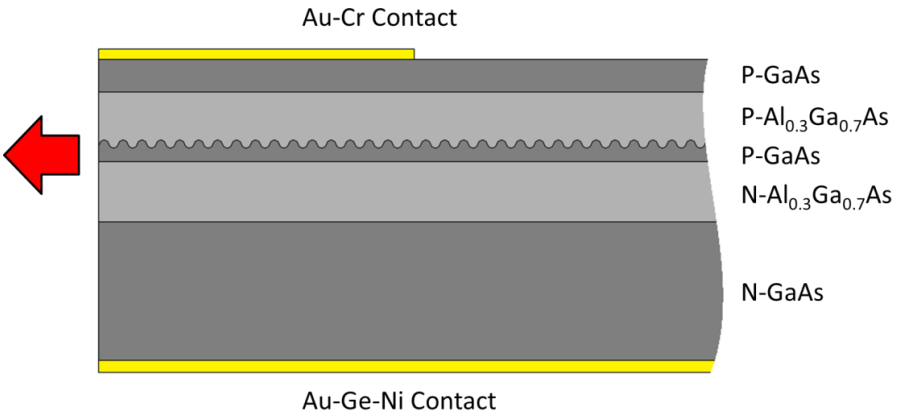

Figure 1-13: Schematic diagram of the GaAs/AlGaAs DHS DFB reported in [25]

In comparison, a single heterojunction GaAs/AlGaAs laser was reported in [24], where the corrugations were directly etched into the GaAs substrate with 30μm AlGaAs grown above, which consisted of a GaAs n-type substrate, a GaAs p-type diffused layer and a AlGaAs p-type grown layer. The devices demonstrated a threshold current density of 1200A/cm^2 in pulsed operation at ~77K. By applying different corrugation periods, they successfully designed a range of DFBs lasing at wavelengths from 843nm to 856nm. But their design concept was not continued further due to many advantages of DHS structures, such as better electrical and optical confinement.

Since very beginning, researchers already started to realise the potential for DFB lasers to be monolithically integrated, enabled through their independence upon end mirrors. Hitachi furthered their DHS DFB study and in 1977 they reported a frequency-multiplexing light source model consisting of a monolithically integrated GaAs/AlGaAs DFB laser array [26], as shown in Fig. 1-14. By exploiting the ~20nm gain spectrum width of GaAs, they demonstrated a 6 channel design with the shortest lasing wavelength of ~891.2nm and the longest of ~903.1nm, with a ~2nm difference between channels. In terms of the active/passive integration, they employed an off-set method by

first etching the waveguide sections down to the substrate immediately after the definition of grating areas, followed by overgrowth of AlGaAs to complete both the grating and the passive waveguide sections.

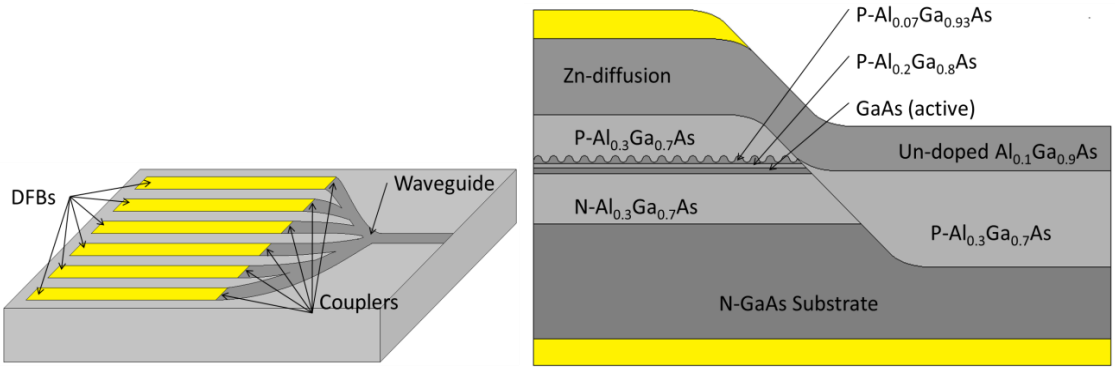

Figure 1-14: Schematic diagram of first generation DFB monolithic integration: frequency-multiplexing DFB array reported in [26]

Despite the weak performance of the prototype above, it demonstrated the potential for DFB lasers to be used in monolithically integrated photonic systems.

1.3.2 Development of InP/InGaAsP DFBs

In the 1980s, research concentrated on InP/InGaAsP DFB lasers operating in the wavelength range of 1.3μm to 1.5μm. Because this range matches the application for long haul high bit rate communications system due to their stability in SLM operation under high-speed direct modulation with low dispersion and low loss in silica optical fibres. During that time, one extensively studied waveguide design was the BH DFBs. As for the cavity design, the lasers usually had one cleaved facet for fibre coupling and a specially designed rear structure like a tilted facet, unexcited regions or window regions to assist in suppression of the FP mode.

In 1982, Matsuoka at el. from Atsugi Electrical Communications Laboratories of Nippon Telegraph and Telephone (NTT) corporation developed a 3-step LPE growth

process for the fabrication of a 1.5μm BH GaInAsP/InP DFB laser [27] [28]. Fig. 15 (a) shows their improved device designs [28], where the corrugation was etched in the P-doped InGaAsP guide layer immediately above active region. In the earlier version [27], as shown in Fig. 1-15 (b), the corrugation was etched into the N-InP substrate prior to an N-doped InGaAsP guide layer and the active region, where the active region was overgrown above the corrugated surface. In both designs, a P-N-P-N junction was performed as current blocking mechanism to achieve lateral carrier and photon confinement.

Matsuoka also studied the effect of the grating phase at the cleaved facet to achieve a high SLM yield [29], in which they verified that both the threshold current and the lasing wavelength are periodically correspondent to the relative position of the facet to the grating. Later, they applied an anti-reflection/high-reflection (AR/HR) facet configuration to their designs and achieved 45mW output power with SMSR over 30dB [30] in 1986.

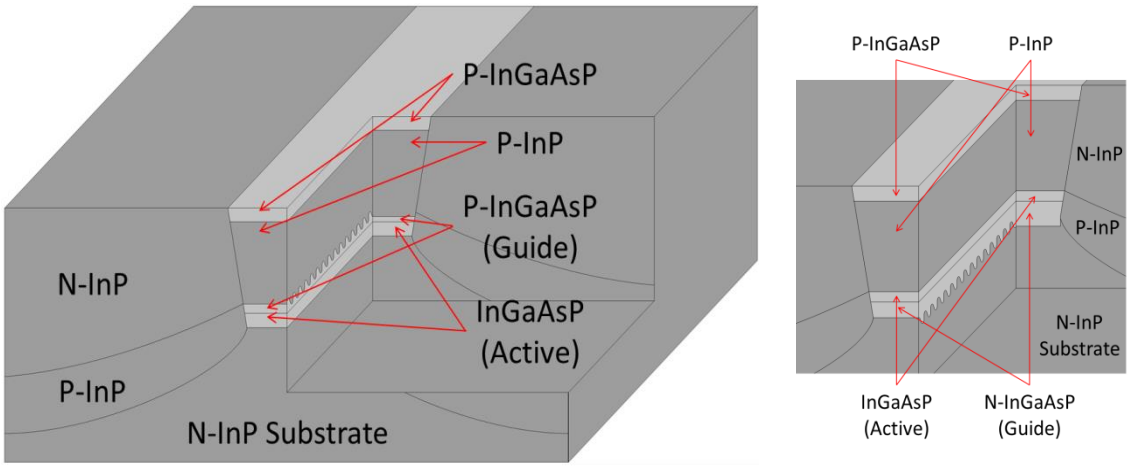

(a) (b)

Figure 1-15: Matsuoka's BH InGaAsP/InP DFBs with buried grating with (a) corrugation formed above the active region in P-doped InGaAsP guide layer as reported in [28] and (b) corrugation formed below the active region in N-doped InGaAsP guide laye [27]

In 1984, Kitamura, Yamaguchi, Mito, Murata and Kobayashi, researchers in Opto-Electronics Research Laboratories (NEC Corporation), reported their 1.3μm [31] and

1.55μm [32] InGaAsP/InP DFB designs in a double-channel planar BH, where they achieved stable CW SLM operation over 100^{o}C. Their DFBs were fabricated with a buried InGaAsP/InP corrugation (period: 395nm, 2nd order, thickness: 70nm), as illustrated in Fig. 1-16. The fabrication of this structure was a 3-stage process. Firstly, a layer of n-InP buffer layer, an un-doped active layer and a p-InGaAsP guiding layer were grown on an n-InP substrate. Then, the corrugation was etched into the guiding layer prior to a 2nd growth of a layer of p-InP to infill the corrugation. Before the 3rd growth to complete the buried structure (p-n-p-n current blocking layers), a mesa area was etched between a double-channel structure to form the stripe geometry.

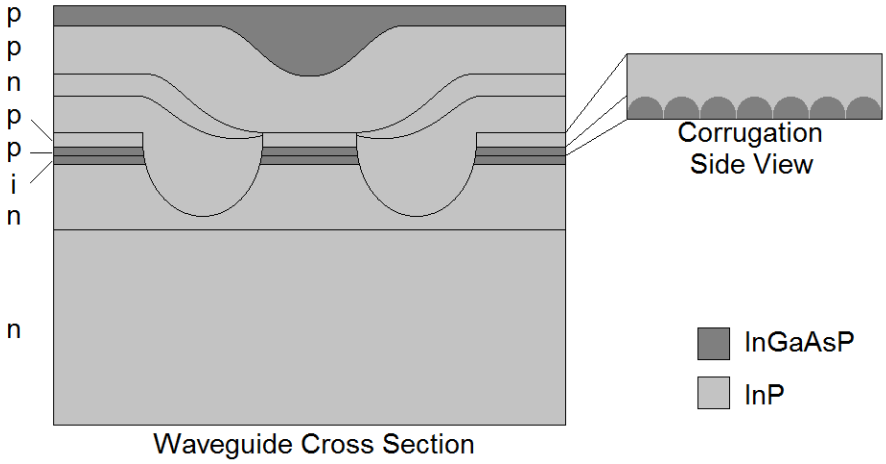

Figure 1-16: DFB double-channel planar BH laser diode (DFB-DC-PBH LD) developed by Kitamura et al. [32]

In 1988, Kakimoto and other researchers in Mitsubishi Electric Corporation, developed a 1.5μm-wavelength high-efficiency (0.39 mW/mA) low-threshold narrow-beam-profile (FWHM: 25^{o}) GaInAsP/InP DFB p-substrate partially inverted BH (PPIBH) using a MOCVD technique for a thinner active region [33] [34]. In their 3-stage design, a p-InP buffer layer, a GaInAsP active layer and a n-GaInAsP guiding layer were first grown on p-InP substrate by MOCVD; after formation of corrugation on the guiding layer, a n-InP cladding layer was grown by MOCVD again; after the etch of mesa structure, the LPE was then employed to grow both current blocking layers on

both sides of the mesa (where the diffusion of Zn from the surrounding p-type InP blocking layers results in p-type inversion of the tips of the n-InP blocking layers) and a n-GaInAsP contact layer.

In addition to the development in transverse waveguide (i.e. edge-emitting) designs described above, an alternative concept was surface-emitting DFB. During 1987 to 1990, Macomber and co-workers, in the Hughes Danbury Optical Systems, Inc. (Perkin-Elmer Corporation), conceptualised and realised the surface-emitting DFB, where the facet reflection were first time eliminated [35]. After, they developed a 2-D array of surface-emitting DFBs and achieved Watts of output power [36], followed by further improvement made in the beam quality [37]. Fig. 1-17 illustrates the device concept of their designs: a finite gain area was defined by current pumping on an essentially infinite 2nd order gold grating on the p-contact surface.

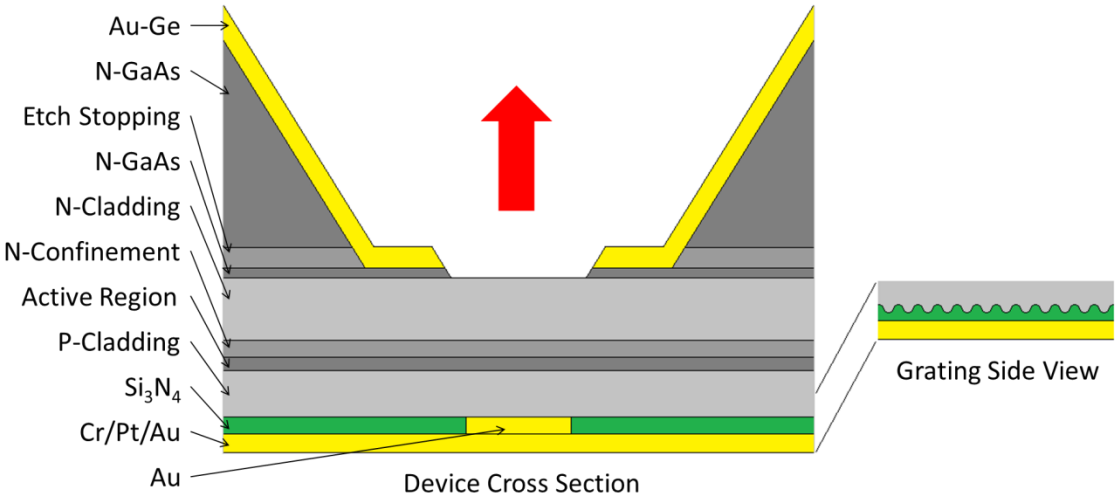

Figure 1-17: Illustration of the concept of surface-emitting DFB reported in [37] [38]

They also studied the variation of slope efficiency, threshold current and beam profile (both far-field and near field) with varying grating periodicity, stripe length and thickness of p-cladding [38], and demonstrated that optimisation of the grating-waveguide and geometry can significantly improve the properties. However, these devices suffered from poor lateral beam quality due to multi-mode operation.

1.3.3 Towards Higher Single Longitudinal Mode Yield

From the mid-1980s, it was found that the SLM yield of the fabrication of DFB lasers with uniform (non-wavelength-shifted) gratings was undesirably low. This was due to their nature of having 2 degenerate modes on both sides of the Bragg wavelength and the uncertainty of facet phase. Since then, researchers were led into the improvement of the SLM yield.

➢ Quarter-Wavelength-Shift (QWS) and Spatial Hole Burning (SHB)

One solution was the introduction of a λ/4 phase shift into the grating (earlier versions existed, e.g. π/2 phase shift), resulting in a single mode with the lowest threshold gain. However, it was found both theoretically and experimentally that in phase-shifted DFBs the distribution of the optical intensity along the laser cavity can be significantly altered, which leads to severe spatial-hole-burning (SHB). This influences the stability of SLM when applying more current injection for higher power operation.

Soda et al., researcher from Fujitsu Laboratories Limited, investigated high-power phase-adjusted SLM operation taking SHB into consideration. In 1984, they reported a GaInAsP/InP phase-adjusted DFB design with a step-like non-uniform stripe width which demonstrated stable SLM operation [39], as illustrated in Fig, 1-18. After, they achieved high power operation on their phase-adjusted DFB lasers. By introducing an asymmetric quarter-wavelength-shifted, where the shift was positioned a distance away from the centre of the laser, the devices demonstrated a high efficiency and a large threshold gain difference under high-power operation [40]. Further study demonstrated

an 80% SLM operation yield in moderately-coupled (*KL* = 1.25) devices due to a large threshold gain difference [41].

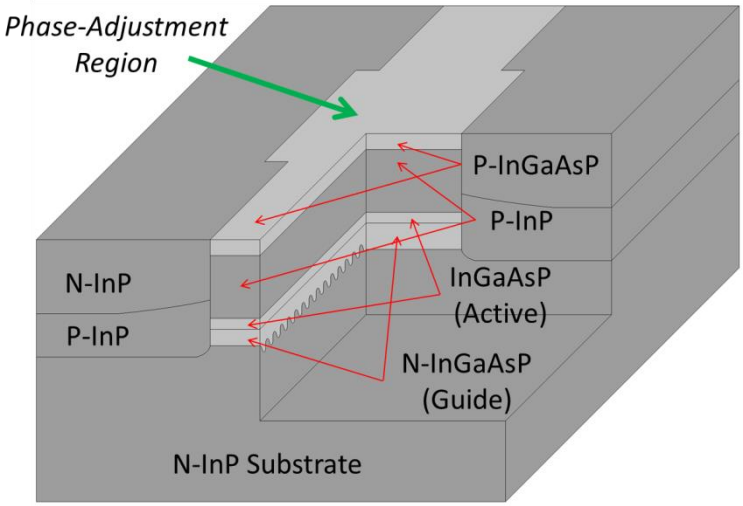

Figure 1-18: Schematic diagram of the phase-adjusted DFB with phase-shifter step-like stripe geometry developed by researchers in Fujitsu Laboratories Limited [39]

Later, they achieved SLM operation over a wide temperature range by designing a weak coupling (*KL* = 0.7) grating with an asymmetric facet reflectivity configuration (R_{front} = 0.05 and R_{rear} = 0.31) with a designed-in detuning between the peak gain and the lasing wavelength [42], where the introduction of detuning was based on the studies by Ogita at el. [43] focusing on the linewidth reduction. In 1987, Ogita verified that the linewidth can be reduced through fine control of the detuning effect [43], where a reduction of 50% was experimentally observed for DFBs purposely designed for their lasing wavelength to be 10nm shorter than the gain peak wavelength [44], where it was shown that a narrower linewidth can be achieved by increasing the front facet reflectivity. For their devices, a minimum value of linewidth was experimentally measured at a reflectivity of 0.05, while a low front facet reflectivity was necessary for a higher yield for stable SLM operation, as reported in [45]. During that time, in addition to above proposed methods for SHB suppression in λ/4-shifted DFBs by Fujitsu, other methods included: gratings with non-uniform amplitude [46], corrugation-pitch modulation [47] and stripe-width modulation [48].

➢ Gain-/Loss-Coupled DFB

Another solution for higher SLM yield was the introduction of gain-coupling into the grating mechanism. The study of gain-coupled DFBs started from the late 1980s. In 1988, researchers working in the Optical Measurement Technology Development Co., Ltd. (Japan) contributed to the development of the first generation of gain-coupled GaAlAs/GaAs DFB laser.

As reported by Luo et al., gain coupling can be achieved either by direct corrugation of the active region [49] [50] or by fabricating buried absorptive gratings [51]. In the early 1990s, several groups over the world conducted research comparing gain-coupled and index-coupled DFB lasers, including David, Morthier, Vankwikelberge and co-workers from Ghent University [52]-[54]; Lowery and Novak from the University of Melbourne [55]; and Suhara, Islam and Yamada from Kanazawa University [56]. They found that, in addition to a higher single-mode yield, gain-coupled DFBs perform better in most situations, benefitting from higher resistance to external feedback, more stable single-mode operation, less severe SHB effect and potentially longer modulation bandwidths. In the mid-1990s, some groups achieved gain-coupled DFBs through the introduction of current blocking gratings, e.g. periodically distributed n-InP segments in p-InP cladding [57] [58].

Towards the end of the 1990s, laterally-coupled metal gratings (absorptive) were developed [59]-[61], which were desirable since the fabrication process is material independent. This method will be described in more detail in Section 1.4.1.

1.3.4 On-Chip Thin Film Heater

One important feature of DFB lasers is their thermal tunability, which is mainly due to the thermal effect upon the grating mechanism in DFB lasers. There are 2 mechanisms through which an increase in temperature can affect the wavelength selection of the gratings.

For index-coupled DFBs, the refractive indices in the grating materials are temperature dependent, which influence the Bragg wavelength of the periodic structure. Furthermore, thermal expansion of the grating materials due to increasing temperature can also influence the determination of Bragg wavelength, especially for laterally-coupled semiconductor-air or metal gratings.

Since the 1990s, many groups have attempted to utilise the thermal tuning phenomenon to develop tunable DFB lasers. One typical method was to fabricate on-chip thermal elements, e.g. a thin film heater. Fig. 1-19 shows a typical design of on-chip thin-film heater on a narrow ridge waveguide defined by etched trenches.

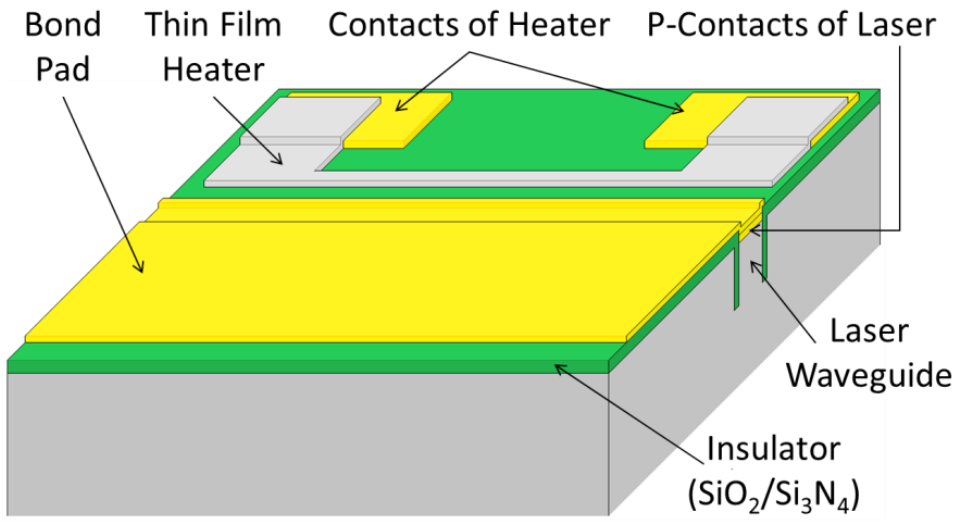

Figure 1-19: Schematic diagram of a typical thin film heater design

As can be seen, the heater was deposited to a distance along the ridge upon the dielectric isolation layer, which is able to controllably generate heat upon increasing the applied current. In fact, the concept of this thermal element is highly device-independent.

As shown in Fig. 1-20, it can also be easily applied on other types of waveguides, including conventional side-wall etched ridge waveguides and self-aligned-stripe waveguides.

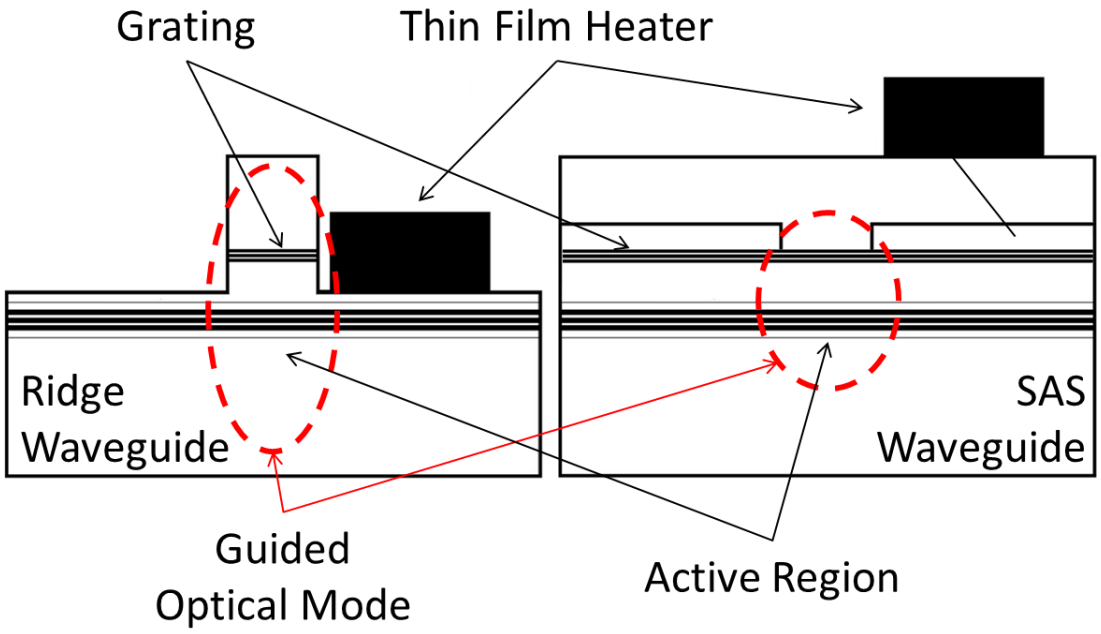

Figure 1-20: Schematic diagram of thin film heater designed for difference waveguides

Sakano and colleagues from Hitachi Ltd. developed a platinum thin film heater and reported in 1992 [62]. A tuning wavelength of 4nm (1548nm at I_{heater}=0mA, 1552 nm at I_{heater}=230mA) was achieved through a 0.7μm thick 15μm wide 0.8μm long Pt stripe heater, with a tested resistance of 17Ω, deposited along the laser ridge on a 0.2μm thick SiO_2 insulation layer.

Following-up research led by Aoki (also from Hitachi Ltd.) improved the functionality of their thin-film heater designs [63] [64] in the late 1990s, where they achieved a 5nm stable SLM tuning range with a low electric power of 400mW.

More recently, groups from China applied this concept. In 2013, Zhang reported a widely tunable dual-mode distributed feedback laser design [65], where a spacing of the duo-mode spacing can be tuned between 0.34nm to 8.06nm. In 2014, Meng demonstrated a thermally tuned DFB design [66], where a tunability of 15 channels with 100GHz spacing was achieved.

One should keep in mind that the extent to which the thermal effect induces a wavelength shift in the gain peak and in the DFB wavelength is different. With an increasing operating temperature, the former shifts significantly faster than the latter and affects the detuning between the gain peak and the DFB peak. Therefore, the design of the grating period is necessary to match the tuning range of the gain peak, which is usually with a Bragg wavelength positioned on the long wavelength side of the gain peak. Furthermore, this different tuning rate could result in mode hopping from lasing via a shorter DFB mode to a longer one. The mode-hopping phenomenon should be differentiated from the above continuous wavelength tuning.

It was suggested that QD lasers might be more suitable for tunable DFB laser designs. Compared to quantum well lasers, quantum dot lasers theoretically have a lower threshold current and higher temperature stability, resulting in the gain peak exhibiting reduced sensitivity to temperature, which means that the change of detuning while thermal tuning is less severe in QD DFBs than in QW DFBs.

Gerschutz et al. at Nanoplus reported a 1305nm 2μm wide 600μm long ridge DFB (metal grating) laser incorporating InGaAs/GaAs QD layers [67], which operates with a temperature-independent threshold at ~17mW from 20^{o}C to 85^{o}C, where the decrease in slope efficiency is reported to be lower than 10% in this range, whilst demonstrating a typical tunability of 0.1nm/^{o}C.

1.3.5 Maturity of GaAs-Based System: Shift back to Shorter Wavelength

The need for development of DFB lasers at shorter wavelengths had long existed in the 1980s. As addressed in Section 1.1.1, GaAs-based material system is the choice for the wavelength range 650nm-1200nm, where the InP-based material system is no longer suitable. It was not until the maturity of GaAs-based material systems, including InGaAs, GaAs, AlGaAs and InGaP, in the 1990s that made their realisation possible.

Since the beginning of the 2000s, the Ferdinand-Braun-Institut has been one of the leading forces in the development of GaAs-based DFB lasers. Fig. 1-21 illustrates their GaAs-based DFB concept developed and matured by Wenzel, Klehr and colleagues. As seen, their index-coupled ridge waveguide DFB incorporates a grating layer fabricated in the AlGaAs p-cladding above the active region.

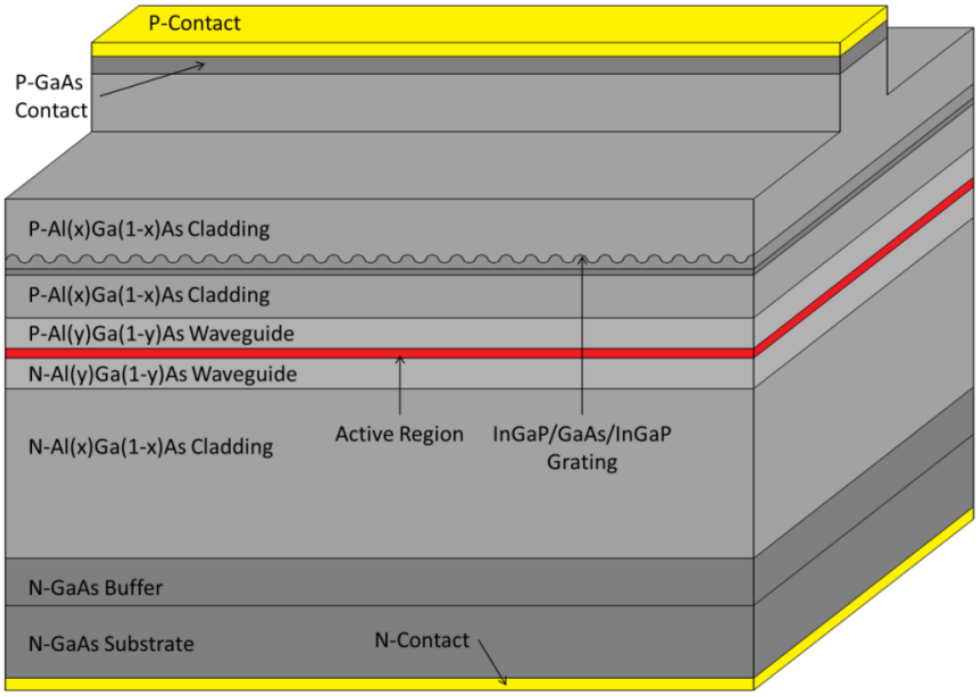

Figure 1-21: Schematic diagram of Ferdinand-Braun-Institut's GaAs-based buried grating ridge DFB lasers with a cladding-waveguide-core-waveguide-cladding layer structure, where the Al composition, x, in cladding is higher than that, y, in waveguide, and an InGaP-GaAs-InGaP Al-free grating layer sequence

In the early 2000s, they developed a buried grating fabrication technique utilising an InGaP-GaAsP-InGaP Al-free grating layer sequence. Since 2006, they improved the grating fabrication sequence to be InGaP-GaAs-InGaP, where the InGaP is lattice-matched to GaAs. As to their epitaxial layer design, instead of directly sandwiching the active region by upper- and lower- claddings, they applied a graded-cladding scheme, where the active region is firstly surrounded by lower Al-concentration AlGaAs waveguide layers, then sandwiched by higher Al concentration AlGaAs cladding layers, which provides a higher transverse optical confinement.

In 2004, they reported a 1.5mm long 2μm wide ridge waveguide AR/HR coated DFB laser with a 14nm GaAsP QW and AlGaAs/GaAsP gratings, operating at ~783nm with an output power of 200mW [68]. Then, in 2006, they demonstrated a 1.5mm long 2.2μm wide ridge waveguide (RW) AR/HR coated DFB laser using the same grating technique, operating at ~976nm with an output power of 500mW [69]. Another 1.5mm long 2.2μm wide RW AR/HR coated DFB laser, this time with a 7nm InGaAs QW embedded in GaAsP barrier layers operating at ~894nm with an output power of 250mW, was reported in 2007 [70].

In 2009, Stevens et al. reported an alternative grating fabrication technology based on a GaAs-InGaP-GaAs sequence to form GaAs/InGaP gratings. This particular design will be described in detail in Section 1.4.2 and the fabrication process will be described in Chapter 3.

1.3.6 Commercially Available DFBs (650-1450nm)

It is useful to establish a general understanding of today's commercially available DFB lasers operating in the range of 650nm to ~1450nm that one can purchase or make quotation request. Six well-known DFB suppliers are NTT (Japan), Eblana Photonics (Ireland), Nanoplus (Germany), Thorlabs (United States), Eagleyard (Germany) and Ferdinand-Braun-Institut (Germany). By summarising the specifications provided on their product webpages, Table 1-1 presents an up-to-date list of today's commercially available DFB lasers.

As illustrated, Eblana Photonics, Eagleyard and Thorlabs provide devices operating at specific wavelengths, i.e. 689nm, 760nm, 764nm, 767nm, 780nm, 795nm, 852nm, 855nm, 935nm, 1030nm, 1064nm, 1083nm, 1278nm, 1310nm and 1392nm.

As to NTT, Nanoplus and Ferdinand-Braun-Institut, they provide solutions for customised devices. NTT and Nanoplus provide DFB lasers mainly for gas sensing applications with an available wavelength range of 760nm to 14000nm and 1260nm to 2330nm respectively.

In comparison, Ferdinand-Braun-Institut offers solutions for high power DFB lasers specifically in the wavelength range of 760nm to 1080nm. According to their online description, they can achieve up to 500mW output power whilst keeping an SMSR higher than 50dB.

This research is aimed at developing high power high performance DFB lasers utilising self-aligned stripe waveguides, which can then be packaged into standalone devices or integrated in photonic integrated circuits for the realisation of new functions. The motivation behind will be described in Section 1.6 in more detail.

Wavelength (nm)	Applications	P_{out} (mW)	I_{th} (mA)	SMSR (dB)	Linewidth (MHz)	Suppliers
689	Sr sensing	10	50	~40	<3-4	Eblana Photonics
760 to 830	760nm: O_2 sensing 780/795nm: Rb sensing 780nm: Rb atomic clocks	~500		>50	<10	Ferdinand-Braun-Institut
		5	15	>35	-	Nanoplus
760	O_2 sensing	10	60	~40	<3-4	Eblana Photonics
		40	70	50	~2	Eagleyard
764		40	70	50	~2	
767	K spectroscopy	50	70	50	~2	
780	Rb sensing (D2) Rb atomic clocks	80	70	45	0.6	
		12	60	~40	<3-4	Eblana Photonics
		15	40	40	2	Thorlabs
795	Rb sensing (D1)	80	70	45	0.6	Eagleyard
830 to 920	852/894nm: Cs sensing 894nm: Cs atomic clocks	~500	-	>50	<10	Ferdinand-Braun-Institut
		10	20	>35	-	Nanoplus
852	Cs sensing (D2)	150	70	45	0.6	Eagleyard
855	THz generation	150	70	45	2	
920 to 1080	935nm: H_2O sensing 980nm: EDFA pumping 1064nm: THz generation	~500	-	>50	<10	Ferdinand-Braun-Institut
to 1100		20	20	>35	-	Nanoplus
935	H_2O sensing	80	70	45	2	Eagleyard
1030 1064	Seed laser for fibre laser	600 pulsed	70	25	2	
1064	Nd: YAG replacement	80	70	45	2	
1083	Magnetometer He polarisation	80	70	50	2	
1100 to 1300	1278nm: HF sensing	20	15	>35	-	Nanoplus
1278	HF sensing	8	12	~40	<2	Eblana Photonics
1300 to 1450	1341nm: HBr sensing 1392nm: H_2O sensing	20	20	>35	~2	NTT
		5	30	>35	-	Nanoplus
1310	Communication	2	7	40	-	Thorlabs
1392	H_2O sensing	10	12	~40	<2	Eblana Photonics

Information Source	
NTT	https://www.ntt-electronics.com/en/products/photonics/gas_sensing.html
Eblana Photonics	http://www.eblanaphotonics.com/optical-sensing.php
Nanoplus	http://nanoplus.com/en/products/distributed-feedback-lasers/
Ferdinand-Braun-Institut	https://www.fbh-berlin.de/forschung/photonik/department-optoelektronik/lasertypen/dfb-laser
Thorlabs	https://www.thorlabs.com/newgrouppage9.cfm?objectgroup_id=7928
Eagleyard	http://www.eagleyard.com/products/single-frequency-laser-diodes/

Table 1-1: Up-to-date commercially available DFB lasers

1.3.7 Recent Development

There are many developing directions for future advancement of DFB lasers. This section briefly reviews a number of DFB-related developments reported in recent years.

- **GaAs-Based Photonic Integration**

GaAs-based DFB laser and photonic integrated circuit (PIC) technology is one important developing direction. This will be introduced in detail in Section 1.5.

- **Improvement of Fabrication Methods / Design Concepts**

The persistent pursuit for improvement and optimisation based on present development is as important as exploring new fields. In recent years, some reports have described new design concepts and new methods for optimisation. In 2012, researchers from the Ferdinand-Braun-Institut reported a novel grating fabrication method to achieve "floating" buried gratings as an improvement to their well-developed InGaP-GaAs-InGaP method [77]. As described, after the 1st growth, the top grating GaAs/InGaP sequence was patterned and etched through the GaAs cap-layer. The wafer was then transferred back into the reactor, where the un-capped InGaP was etched *in-situ*. After the regrowth of the reminder of the AlGaAs cladding layer, the remaining GaAs/InGaP segments form the "floating" buried grating. In 2013, Zhao et al. reported a 16-channel DFB laser array using nano-imprint technology [78]. This mechanical imprint process was first introduced in 1995, but rarely used for DFB fabrication until the recent decade. Nano-imprint technology is a promising solution to reduce the cost of grating fabrication, because the stamps, once fabricated, can be used hundreds of times.

- **DFB on Si**

The integration of electronic and optical systems has been a hot topic in the recent decade, where the ability to integrate III-V materials with Si is the key. Tian et al. at Ghent University recently demonstrated InGaP/InP O-band DFB lasers grown directly on (001) silicon [74]. Meanwhile, researchers from the Tokyo Institute of Technology conceptualised a laterally pumped GaInAsP/InP membrane DFB grown on Si by using a 2μm thick BCB adhesive bonding [75]. Alternatively, direct growth of III-V epi-layers on Si is also reported [76], where a low density of threading dislocations was achieved by applying thermal annealing to the combination of a nucleation layer and dislocation filter layers.

- **THz Generation**

THz radiation (from several tenths THz to several THz) is useful sources for applications in sensing and spectroscopy, THz imaging for quality control, THz data communication and security purposes as well. Among numerous methods, continuous wave THz generation using dual mode semiconductor lasers (optical heterodyning schemes) is highly favourable, where two optical waves with different wavelengths are selected to generate electromagnetic waves with terahertz frequencies. Fig. 1-22 shows an example of this optical heterodyne conversion (photo-mixing) process, where the mixing of $sin(\omega_a t)$ and $sin(\omega_b t)$ results in a beating $[sin(\omega_a t) + sin(\omega_b t)]^2$. In this example, $\omega_a : \omega_b = 11:10$.

In recent years, reported design concepts (demonstrated or under development) include dual-mode lasing of DFB laser [71], in-series integration of DFB and DBR [72] and DFB laser arrays [73].

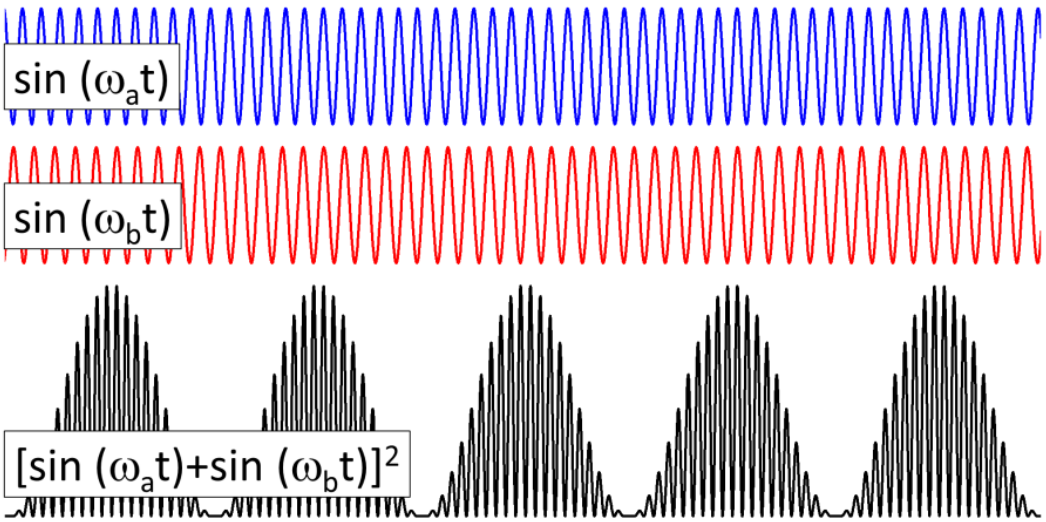

Figure 1-22: Example: interference of two optical waves sin($\omega_a t$) and sin($\omega_b t$), where $\omega_a : \omega_b$ = 11 : 10

- **Blue DFBs**

Blue lasers are a suitable light source for many applications, including underwater communications where the conventional acoustic methods suffer from slow data rates and short reach. Single longitudinal mode blue lasers are desirable and their development can also broaden the scope of the DFB family. Thomas et al. reported a 1mm long 1.5μm wide laterally-coupled InGaN/GaN DFB ridge laser with 0.5μm wide 520nm deep lateral gratings on both sides, operating at 430nm with 40mW (with 390mA current injection) output and an SMSR of 22dB [79]. Compared to InP-based and GaAs-based DFB lasers, there remains a significant opportunity for further improvement.

1.4 Grating Fabrication Methods

A key aspect of the manufacture of DFB lasers is the fabrication of the grating structures. In general, the distributed feedback is established by a periodical variation of refractive index (index-coupled) and/or a periodically modulated gain medium (complex- or gain-coupled laser).

This section discusses various grating fabrication methods developed during the past 4 decades and their suitability for inclusion in my GaAs-based DFB design. Categorising by the positions of the gratings, two main approaches are surface gratings and buried gratings.

1.4.1 Surface Grating

For the surface gratings, the grating patterns are defined on the surface of the device by etched surface corrugation, deposited surface metal grating and laterally etched groove-type grating [80]. More recently, the development of lateral metal gratings combined the concepts of the latter two, by forming metal gratings at either side of the etched laser ridge.

➢ Surface Corrugation

Etched surface corrugations were used early on in development of DFBs. Applying this technique, the top layers of the sample (i.e. contact layer and p-cladding layer) are etched to form the corrugation, prior to deposition of the p-contact. Fig. 1-23 shows a

schematic diagram of this technique developed by Zory et al. in 1970s. In 1974, Zory and colleagues reported their approach to fabricate V-groove diffraction gratings in GaAs by selective etching when he was working in IBM Thomas J. Watson Research Centre [81]. In 1975, they attempted to realise a DFB mechanism through surface-emitting double-heterostructure AlGaAs diode lasers with surface corrugation surrounding the output aperture [82]. Zory continued his work at the University of Florida, and in 1990, he led the theoretical study of the coupling coefficient of metallised corrugations on GaAs-AlGaAs heterostructure diode lasers [83].

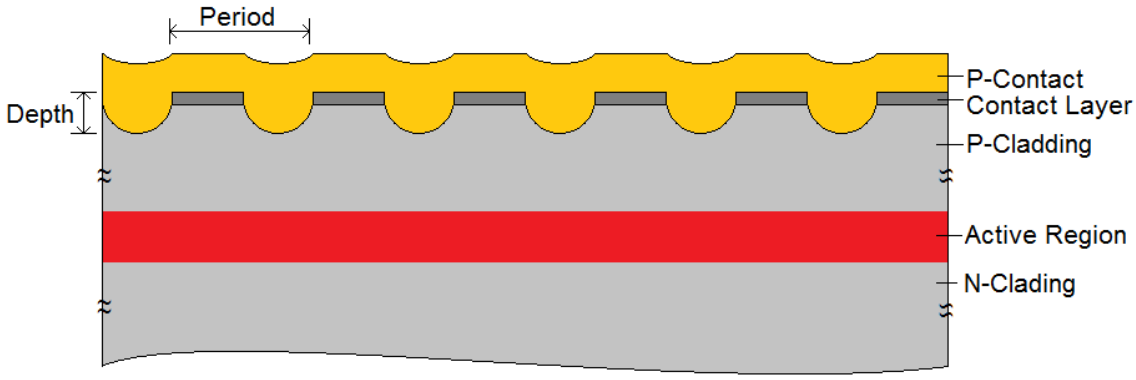

Figure 1-23: Schematic diagram of a surface corrugation as reported in [83]

Many research groups adopted this technique, including the development of surface emitting DFBs conducted by Macomber in the late 1980s, as mentioned in Section 1.3.2, which was based on this p-contact corrugation etch technique [35] [36]. When it came to the 1990s, this method became more sophisticated and was widely applied on InGaAsP/InP systems. In 1994, two researchers from the University of Munich, Rast and Muhlhoff, reported their 1.55μm InGaAsP/InP ITG-DFB-BCRW (integrated-twin-guide DFB bridge-contacted ridge-waveguide) with surface corrugation formed by directly etching 200nm into the top of the p-InGaAsP guiding/contact layer, followed by Ti/Au metallisation [84].

- **Disadvantages**

It is significant for the operation of a DFB laser that a sufficient portion of the guided optical mode interacts with the grating mechanism. Therefore, this technique requires either very thin upper cladding and contact layers or a very deep uniform transfer of the grating into the upper cladding, or both. However, a thinner upper cladding layer results in a higher optical loss to the surface metal and lower device efficiency. As for deeply etching the top layers, if applying this method in GaAs-based DFB designs, the upper cladding is then required to be an Al-free compound, i.e. InGaP, which means the loss of the flexibility in waveguide design offered by all-composition lattice-matched AlGaAs cladding. Otherwise, a deeply etched corrugation into the upper cladding results in the exposure of AlGaAs to the air in the fabrication process, affecting the long-term reliability of the laser.

➢ Surface Metal Grating

Another widely studied method is that of surface metal gratings. Unlike the surface corrugation method, this method does not require the top layers of the samples to be corrugated (etched). Instead, the grating pattern is formed entirely through the periodical definition of metal adjacent to the laser ridge.

In 1997, Osowski and colleagues (University of Illinois Urbana-Champaign) developed their asymmetric cladding gain-coupled DFB designs incorporating an InGaAs/GaAs single quantum well with AlGaAs cladding [59] [60]. Fig. 1-24 (a) shows the first version of their study [59], where 30nm thick Ti gratings (Λ=326 nm, 2nd order, duty cycle = 30%) were firstly deposited prior to a shallow ridge etch, which was followed by SiO_2 deposition. Lastly a 2μm wide stripe was opened for p-metal

deposition (1.5/130nm Ti/Au). However, the dimensions of the duty cycle were difficult to control with this lift-off procedure, which also limited the minimum achievable grating period.

In [60], an improved procedure was reported where the lift-off process was replaced by direct metal deposition into an oxide grating pattern. As illustrated in Fig. 1-24 (b), the grating pattern (Λ=160.5nm, 1st order, duty cycle = 40%) was defined in an 80nm thick SiO_2. The following metal deposition (30/3/150nm Ti/Pt/Au) formed both the metal grating and the p-contact.

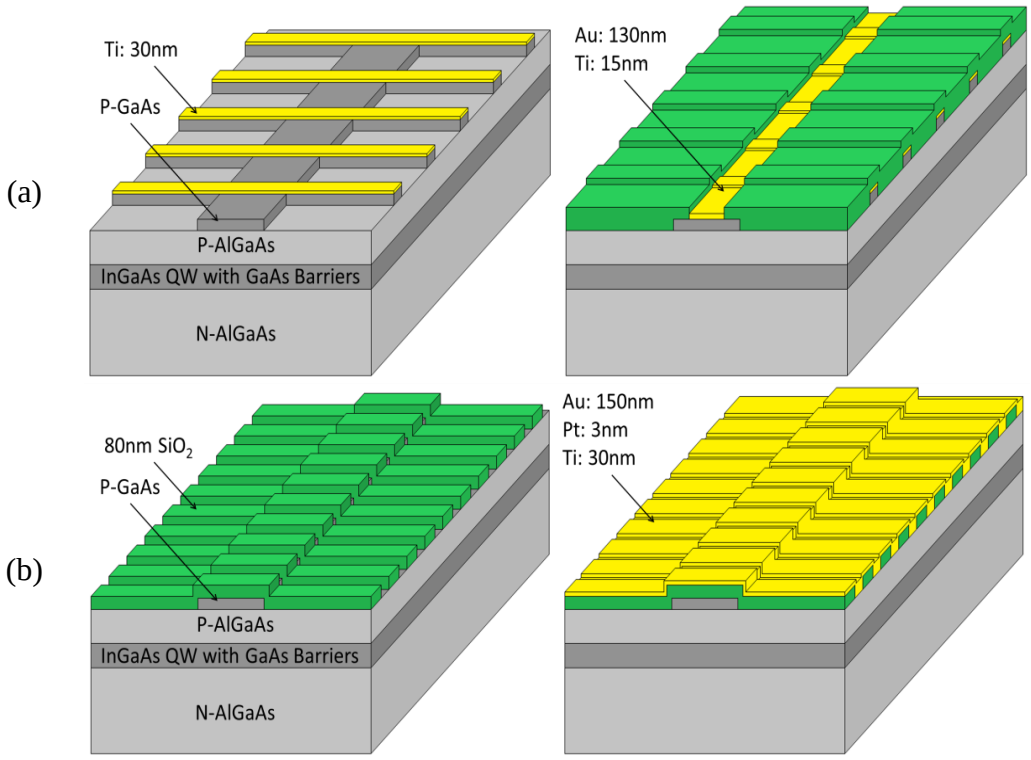

Figure 1-24: Schematic diagrams of Ti surface grating fabrication procedures reported by Mark Osowski and colleagues realised through (a) lift-off procedure reported in [59] and (b) metal deposition on oxide grating procedure reported in [60]

Higher single mode yield with higher resistance to back-reflected optical wave are exhibited in such loss-coupled DFB designs, compared to index-coupled DFB designs due to the mode degeneracy problems with cleaved facets.

- **Disadvantages**

These designs require a very thin upper cladding layer (reducing the separation between the pattern and the centre of the guided mode) to obtain sufficient coupling between the optical mode and the grating pattern. This results in absorption loss caused by deposition of the metal electrode on the thin cladding layer. This also limits the capability to tailor the waveguide design for potential device optimisation. Furthermore, the required thin upper cladding layers significantly limits the feasibility for such DFB laser designs to be further developed into a monolithically integrated module for other potential applications or improved functionalities.

➢ Groove-Type Grating

Groove-type gratings utilise the index difference between the semiconductors and the air (or other deposited protective material, e.g. polyimide), where periodic grooves are uniformly and deeply etched into the semiconductor. In the late 1990s, this technique was extensively used in the study of DBR lasers both in the well-developed InGaAsP/InP material system and in developing InGaAs-InGaP-GaAs systems [85]-[89]. Fig. 1-25 illustrates the concept behind typical groove-type grating DBR designs. As shown, the grating sections are deeply etched (a) entirely through or (b) to closely above the core.

When applying to DFBs, the grooves are etched on both sides along the ridge, as illustrated in Fig. 1-26. Because the position of the formed gratings is on either side of the propagating optical mode, it is also known as the lateral-coupled DFBs (index-coupled in this case). In order to achieve sufficient overlap between the optical mode and the grating, the grooves are usually deeply etched [80].

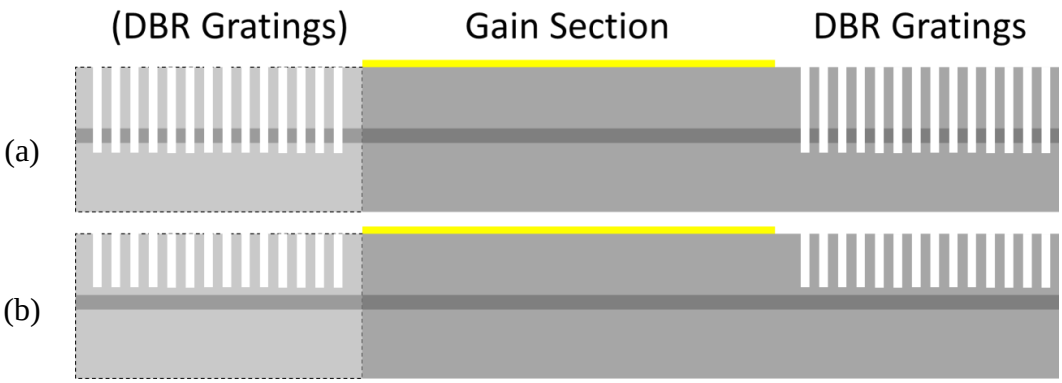

Figure 1-25: Schematic diagrams of typical DBR designs with groove-type gratings deeply etched in DBR grating section(s): (a) entirely through and (b) above the core

Since the mid-1990s, lateral-index-coupled gratings became a popular method to manufacture DFB lasers due to the elimination of overgrowth processes [90]. In such structures, the evanescent part of the optical waves propagating along the waveguide interacts with the grating to establish distributed feedback.

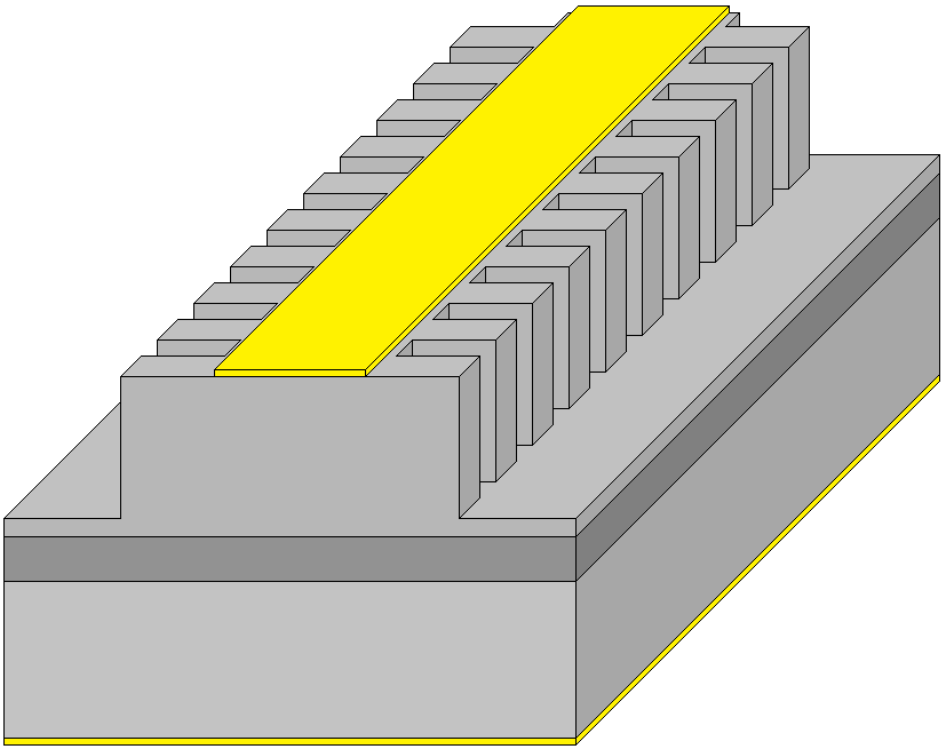

Figure 1-26: Schematic diagrams of typical DFB designs with groove-type gratings deeply etched along the laser ridge [80]

Since only the evanescent part interacts with the grating, the optical confinement factor in the grating is usually two orders lower (~10^{-4}) than that in overgrown gratings [61] and the distance between the core of waveguide and the bottom of the etched

grating is critical for the determination of the coupling coefficient [90]. Because of the strict requirement for fine, smooth, and deeply etched grooves, electron-beam lithography (EBL) has been the optimal patterning method, in spite of its high cost and slow speed making it unsuitable for mass-manufacturing.

More recently, in 2011, Millett and colleagues, researchers from the University of Ottawa, successfully patterned and fabricated a 1310 nm InGaAsP/InP lateral-coupled DFB laser with a 3rd order grating using stepper lithography, which is comparably high-yield and low-cost [91]. In 2013, Li and Cheng (University of Texas) demonstrated the feasibility of optical interference lithography for patterning 2μm-deep 1st order gratings for InGaAsP/InP lateral-coupled DFBs [92], where the gratings were first etched into a dielectric layer and then transferred to both sidewalls.

- **Disadvantages**

This method suffers from two main disadvantages, which both result because of its nature of using the evanescent part of the optical wave. Firstly, there is a maximum ridge width that a laser can be fabricated with. Secondly, it requires a fine control of the distance from the bottom of the deeply etched gratings to the waveguide core. Both these significantly limit the tailor-ability of waveguide design, and the latter also increases the complexity of the fabrication process. Furthermore, despite the improvement made for InGaAsP/InP DFB lasers using this approach, an unavoidable drawback when applying to the GaAs-based material system is the exposure of the AlGaAs upper-cladding layers to air, which requires complicated passivation or protection techniques or a trade-off in the device performance and lifetime.

➢ Lateral Metal Grating

This method can be recognised as the combination of surface metal gratings and groove-type gratings, where metal gratings are deposited along the laser ridge adjacent to the side-walls of the ridge. Kamp and Forchel, researchers from the University of Würzburg, contributed to development of this material independent method.

In 2001, they demonstrated DFB operation on several material systems using chromium as the grating material [61], which has an absorption coefficient of $2.8\times10^{5}cm^{-1}$ at a wavelength of 1000nm resulting in a gain coupling coefficient of approximately $5\text{-}20cm^{-1}$ for their devices. Fig. 1-27 illustrates the concept of their design: a 2-3μm wide ridge was etched to ~150nm above the waveguide layer, and then a 15nm thick Al_2O_3 isolation layer separating semiconductor and the gratings was deposited prior to the use of electron beam lithography for grating patterning. During the grating fabrication the top of the ridge was protected using a Ti/Ni mask, which was then removed together with deposited Al_2O_3 and Cr in a HF dip in the last step.

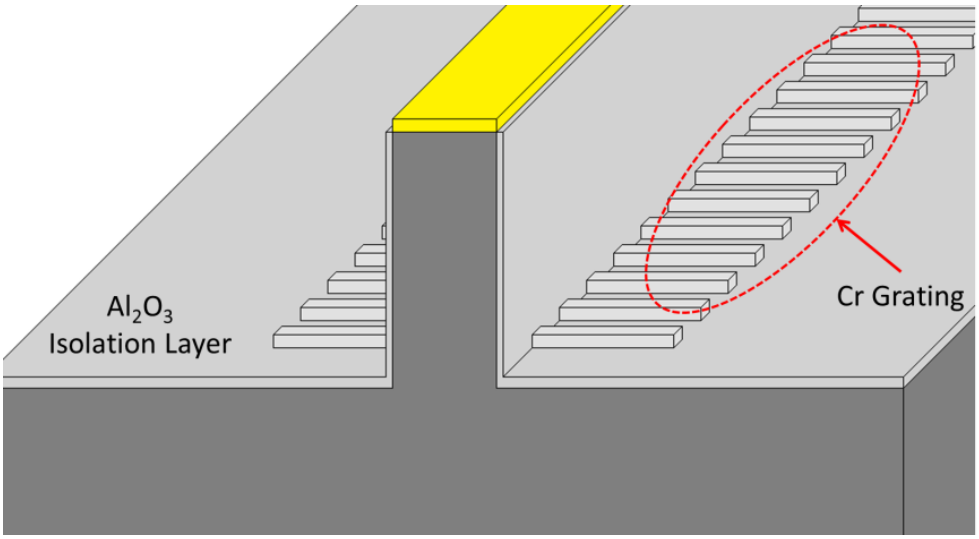

Figure 1-27: Schematci diagram of complex-coupled DFB with Cr grating developed in [61]

Their research was soon adopted for fabricating commercial DFB lasers by a German laser supplier, Nanoplus Nanosystems and Technologies GmbH. Due to the nature of

being material independent, the adoption of this lateral Cr grating technology allows Nanoplus to design and fabricate DFBs on different compound semiconductors systems, e.g. InP, GaAs and GaSb. Today, Nanoplus provides customised DFB lasers over a wide range of wavelengths from 0.76 to 14μm (in-lab research reported up to 16μm [93]). Their product portfolio mainly focuses on tunable laser diode spectroscopy (TDLS) applications, e.g. gas sensing applications, where a high output power is usually not necessary. According to their product specifications, for the wavelength range of our interest, i.e. GaAs-based DFB: 650nm-1200nm, the typical output power specified for DFBs with lasing wavelength range of 760-830nm is 5mW; and 10mW for wavelength range of 830-920nm; and 20mW for wavelength range of 920-1300nm.

- **Disadvantages**

However, these laterally loss-coupled gratings suffer from a low-yield in the manufacture process, due to the need for gratings to be independently written for each laser ridge, making it a very expensive method. Another drawback is the high level of optical loss in the waveguide design of these designs [94], and because of the weak overlap of the fundamental lateral mode with the grating, only narrow ridge lasers are possible [95].

1.4.2 Buried Grating (Overgrown Grating)

To fabricate buried gratings, an overgrowth step is involved for the in-fill and planarisation of the etched grating patterns (by chemical etching and/or dry etching) in the top layer(s) of a previously grown structure, such that a grating is formed in the laser waveguide and/or active region. Based on how the buried gratings are formed, they can

provide distributed feedback via index-, complex- and gain- coupled mechanisms [54] [96]-[98].

In a buried grating DFB laser, the coupling coefficient of the laser optical mode to the grating can be tailored reproducibly and accurately by changing the thickness of the grating and the distance between grating and active region. This method involves patterning, etching and overgrowth, which means that the fabrication processes have to be designed accordingly for each unique material system. Although this technique had been well-developed in InP-based DFBs, e.g. InGaAsP/InP gratings, past methods to transfer to GaAs-based material systems proved difficult to fabricate high-quality gratings.

Attempts to overgrow AlGaAs on GaAs have proven unsuccessful due to mass transport effects destroying the grating profile and the inability to adequately planarise without degrading the grating [99]. Also, overgrowth on patterned AlGaAs is not feasible due to oxidisation of the Al-containing regrowth surface.

➢ Al-Free Structures

In some reports, Al-free structures were developed in order to entirely avoid the risk of oxidisation, such as the InGaP-GaAs-InGaP buried heterostructure DFB reported in 1993 by researchers from Oki Electric Industry Co., Ltd. [100], where the device design employed a mesa-etch-overgrowth (matured in InGaAsP/InP DFBs) process to form the p-n-p-n InGaP current blocking mechanism. A 30nm thick overgrown grating pattern was etched on the top of the n-doped InGaP lower cladding layer, followed by growth of the InGaAs/GaAs QW (grating planarised by the 100nm GaAs lower barrier layer), p-doped InGaP upper cladding layer and p-doped GaAs contact layer.

During 1998 to 2000, researchers from University of Wisconsin-Madison reported their achievements in high power operation (>1W) with their broad-stripe DFB designs for several lasing wavelengths: 730nm [101], 893nm [102] and 980nm [103].

However, Al-free structures have no flexibility for the optical mode control afforded by AlGaAs cladding. This is because the InGaP cladding is only lattice matched to GaAs at one stoichiometry, whereas AlGaAs is lattice-matched over its full range of possible Al compositions.

➢ Low Al Structures

In some reported designs, low Al concentration claddings were used to reduce the effect caused by oxidisation, such as the structure reported in [104] by the Ferdinand-Braun-Institut where $Al_{0.15}Ga_{0.85}As$ waveguides were used. Although this reduces the risk to some extent, it will still limit the extent to which the waveguide can be tailored.

➢ *In-Situ* Etching Method

In order to avoid the exposure of AlGaAs to air during the etch-overgrowth process, some research groups developed *in-situ* etching methods, where the sample is grown-etched-overgrown in the reactor chamber. Ferdinand-Braun-Institut reported their method involving *in-situ* CBr_4-etching within the MOVPE reactor prior to overgrowth, to allow regrowth upon etched AlGaAs surfaces [105]. However, such *in-situ* etching methods require precise control of the etching process and can be susceptible to non-uniformity, un-monitored etching and contamination from the chamber walls, making it an unrealistic manufacturing methodology.

➢ Al-Free Grating Sequence Methods

As mentioned in Section 1.3.5, since the early 2000s, the Ferdinand-Braun-Institut led a rapid development of GaAs-based ridge DFBs based on their Al-free grating layer sequence fabrication technique [68]-[70]: GaAs/AlGaAs buried gratings formed by InGaP-GaAs-InGaP (developed from their earlier GaAsP/AlGaAs gratings formed by InGaP-GaAsP-InGaP).

In 2009, Stevens et al. from the University of Sheffield demonstrated a novel method of grating fabrication. By altering the sequence to be GaAs-InGaP-GaAs, an additional GaAs in-fill layer was grown prior to growth of the upper-cladding to planarise the etched InGaP matrix, which results in formation of a GaAs/InGaP buried grating. Compared to the Ferdinand-Braun-Institut's GaAs/AlGaAs grating, the main advantage of Stevens' GaAs/InGaP grating lies in a higher index contrast in most of the cases. Fig. 1-28 illustrates the buried gratings formed by these two methods. Take 1μm wavelength as an example, the refractive indices of GaAs, $Ga_{0.49}In_{0.51}P$ and $Al_xGa_{1-x}As$ are ~3.50, ~3.15 and ~3.30 (x = 0.42) respectively.

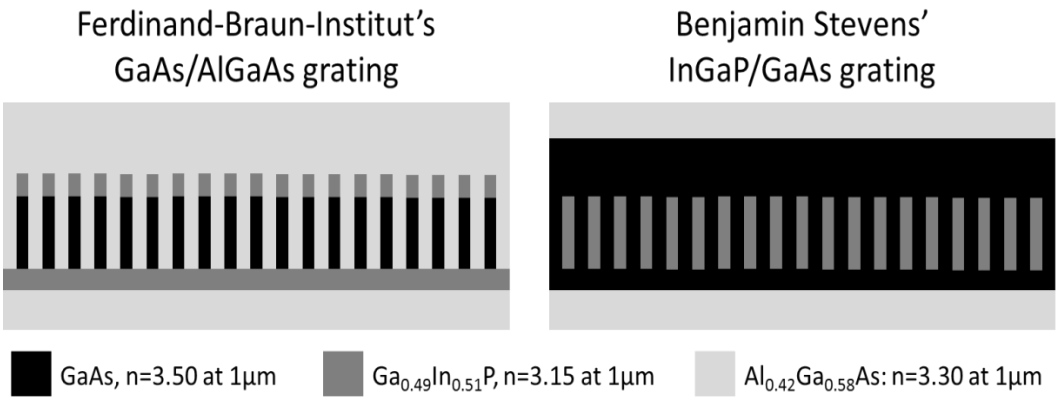

Figure 1-28: Comparison of GaAs/AlGaAs and GaAs/InGaP buried gratings

The difference obtained from GaAs/AlGaAs is approximately 0.20 (x=0.3), whilst that of GaAs/InGaP is 0.35. Although this can be improved by using a higher Al

concentrations, e.g. n_{AlGaAs} (x=0.6) ~ 3.19 thus the difference becomes 0.31, but sacrificing the flexibility provided by full Al% range in waveguide design.

Furthermore, in most buried grating DFBs, tailoring of the coupling coefficient is achieved by adjusting the thickness of the grating and its distance from the active region, and of course the waveguide geometry. It can be estimated that the GaAs/InGaP grating by Stevens et al. benefits from a higher effective refractive index near the grating region due to the stacking of GaAs layers, which leads to a stronger photon confinement. Therefore, the Stevens et al.'s method allows the grating layer to be formed further away from the active region. Also, the flexibility in adjusting the thickness of the lower GaAs layer and in-fill GaAs layer offers additional waveguide design flexibility.

Both these features are desirable for more complicated waveguide designs, e.g. self-aligned stripe DFBs. The detailed fabrication process will be described in Chapter 3.

1.5 Photonic Integration of DFB Lasers

Today, more and more applications require high power DFB lasers operating via a single frequency at an output power of hundreds of milliWatts. High power stand-alone DFB lasers could be realised using two methods.

One straightforward method is to design devices operating with a high volume of current injection. However, even with a high-performance heat-sinking mechanism incorporated in the package, the level of self-heating generated under high current density is still difficult to dissipate. Furthermore, the grating is corrugated along with the gain region, such that they share the same electrical and thermal conditions. With high current injection, the influence of current density and self-heating upon the grating will result in a red-shift of the DFB lasing peak.

Another method is to incorporate a longer gain region to achieve the same level of output power at a lower current density. However, compared to short cavity DFB lasers, long cavity structures suffer from less stable single longitudinal mode operation and less robust modulation performance with respect to SHB and mode hoping, and of course larger device sizes.

With above limitations of developing stand-alone high power DFB lasers, a monolithically integrated DFB master oscillator power amplifier (DFB-MOPA) could present a promising method to fill this gap. In a DFB-MOPA, the DFB section, i.e. the master oscillator (MO), only needs to be pumped moderately to provide stable SLM lasing with sufficient power to be coupled into a semiconductor optical amplifier (SOA), i.e. the power amplifier (PA).

1.5.1 Monolithic Photonic Integration

Real-life applications are usually based on functioning modules incorporating more than one optical component, and optical systems, including the MOPA, are composed discretely, where each integrated component is individually developed, manufactured and packaged, which makes it very difficult to further optimise the system in terms of smaller sizes, lower costs and higher efficiency.

In the research and development of lasers and optical systems, one constant theme is the pursuit of better performance, lower cost and higher efficiency, as well as the realisation and conceptualisation of new functionalities. Therefore, among the many research and development directions being pursued today, photonic integrated circuits (PICs) are regarded as a highly promising trend for next-generation optical system design.

In the electronics industry, the world has witnessed the success achieved through monolithically integrating an increasing number of electronic components into a single device. By achieving greater processing power, higher reliability, lower cost, smaller device size and reduced power requirements, new devices have been developed for a wide range of applications.

PICs are conceptually very similar to electronic integrated circuits (ICs) since they simplify optical system design by integrating many optical components such as lasers, modulators, amplifiers in analogy to the transistors, capacitors, resistors of the electronic integrated circuit. The result is a simplification of an optical system with increased functionality and the reductions in cost, space, power consumption as well as the improvement in reliability provided by the IC concept.

Integration of a number of components into a PIC can greatly reduce the requirement on the number of optical packages and the multiple costs incurred through burn-in of individual components. The reduction in the number of fibre couplings reduces the complex assembly and alignment as well as the cumulative coupling losses associated with each fibre coupling (meaning that lower powers can be used for the same system performance compared to discretely packaged devices). Diagnostic devices can also be integrated allowing functional on-wafer testing at the wafer level (without the need for discrete device separation and testing), reducing manufacturing time and cost. In addition to performance and cost benefits PICs also enable increased functionality, enabling functions that would otherwise not be technically or economically viable.

1.5.2 Maturity in InP-Based PICs (>1200nm)

Today, optical networks are mainly based on transmission around 1310nm and 1550nm due to the dispersion and loss characteristics of standard single mode optical fibres. As such, discrete components have been developed over the years on InP which adequately serve the wavelength range 1300nm to 1650nm [106]-[109]. More recently, the development of InP-based PICs has been driven by the need for optimisation of optical networks applications [110] [111]. With 1550nm the preferred wavelength for long haul telecoms, PIC development has furthermore been limited to this wavelength.

Over the last 2 decades, the development of InP-based PIC has enabled the realisation of complex widely tuneable lasers and wavelength division multiplexing (WDM) PICs with increasing number of components and increasing bandwidth for data communications [112]-[115]. In recent years, further development of InP PIC

technologies has conceptualised the integration realised on silicon-on-insulator (SOI) to achieve large-scale integration of electronic and photonic integrated circuits [116] [117].

However, if photonic integration of a range of active and passive components is required at wavelengths shorter than ~1200nm, such as for a number of biomedical applications, there is presently no available PIC technology, and a hybrid method is the only present option. This severely limits the potential to satisfy a rapidly growing demand for innovation in this wavelength regime, as described in Section 1.1.1.

1.5.3 Lack of Development of GaAs-Based PICs (<1200nm)

It is not envisaged that GaAs would replace InP as the platform of choice for 1300 or 1550nm data communications in the short term as a result of the large gap in sophistication between InP PICs, developed over more than 20 years, and the conceptual GaAs PICs which have yet to be developed. Whilst long term cost savings for the telecoms industry should be kept in mind, it is the new functionality in the wavelength range 650nm to 1310nm that is the ultimate driving force behind GaAs PIC technology. For example there are a large number of applications within the burgeoning biomedical imaging field that are presently served by a wide range of disparate discrete components, many of which do not meet the ultimate specification requirements of the application, or are based on research laboratory grade components or components which do not lend themselves to widespread proliferation due to their size, cost, or long term reliability. Widely tuneable lasers based on PIC technologies can replace current micro-electro-mechanical systems (MEMS) as better light sources for spectroscopic applications [118]-[120].

At this stage it is difficult to predict the full extent to which medium and large scale photonic integration will impact this field, but one can imagine lab-on-a-chip functions that would be possible through up-scaling to medium to large scale integration, and the development of a small scale capability within the timeframe of this project is expected to prompt further interest and scope for application in both associated and disparate fields of investigation.

1.5.4 Overcoming the Technological Barrier

Although ICs in GaAs have been used for the development of monolithic microwave integrated circuits (MMICs), the GaAs-based PIC applications have not yet been commercialised. In general, PICs require multiple growths (1) to realise the integration of active and passive components, e.g. butt-joints, (2) to form certain structures for particular components, e.g. buried gratings, (3) to form certain waveguide structures, e.g. buried waveguides.

Buried waveguides benefit from many advantages over alternatives, including greater flexibility, better functionality, improved heat dissipation, smaller active sizes and controllable optical profiles. For these reasons, they are commonly adopted in the design of PICs.

In GaAs material systems (based on GaAs substrates), AlGaAs is the ideal waveguide cladding material. Being lattice matched to GaAs at all Al compositions, the refractive index of AlGaAs can be tailored by changing its stoichiometry for waveguide design. However, the requirement for multiple growth results in the major technological barrier when transferring sophisticated InP-based PIC approaches to GaAs. As is known,

aluminium containing layers oxidise immediately when exposed to air, which means that manufacture processes involving overgrowth upon etched AlGaAs layers are not reliable. As a result, simply transferring methods developed on InP for telecoms applications to GaAs/AlGaAs materials is not an option.

Alternative methods such as Al-free epitaxial structures [121] or *in situ* etching and regrowth within MOVPE chamber [122] suffer from the difficulties in process control, reliability and design flexibility.

Overcoming this technological barrier is significant for exploiting the potential of GaAs PICs. The group at Sheffield has developed a serious of in-lab proof-of-concept GaAs-based devices, including self-aligned stripe (SAS) lasers [123], distributed feedback (DFB) lasers [99] and super-luminescent diodes [124], using a novel GaAs regrowth technology allowing Al cladding layers for full optical flexibility. My project benefits from this breakthrough and aims at furthering the scope of this method in the development of SAS GaAs-based DFB lasers and their incorporation into photonic integration.

1.6 Project Motivation

This project aims to develop high power GaAs-based DFB lasers targeting the increasing number of applications requiring SLM operation in the wavelength range from 650nm to 1300nm. Furthermore, it is hoped that the possibility of developing a generic platform technology for development and manufacture of GaAs-based PICs can be realised, such that a variety of applications can be realised using the same family of manufacture processes. This technology could provide a route to significant reductions in device cost and increases in functionality with respect to reliability and efficiency.

Within the project, stand-alone DFBs with ridge and SAS waveguide geometries are studied, and the monolithic integration of the DFB-MOPA is investigated. The development of ridge DFBs represents preparatory work conducted to enable the realisation of a novel SAS-DFB, which effectively integrates a buried optical waveguide, gain block and wavelength filter into one device. Subsequently, MOPA devices realise the monolithic integration of a small subset of photonic components based on the generic SAS buried device methodology, where two SAS-DFB-MOPA prototype designs are fabricated and characterised. Their successful demonstration represents the initial stages in the development of a standard generic platform for more complex GaAs photonic integration, allowing extension to a range of disparate fields. In the future, a wide range of additional advanced building block photonic components could be developed for inclusion in the GaAs PIC toolkit. Components such as optical amplifiers, splitters, spot size converters, and active-passive couplings should be studied. PICs could be designed and developed for a wide range of possible applications such as in generation of THz radiation for process control and security spectroscopy systems, and tuneable lasers for use in biomedical imaging and spectroscopy.

1.7 Thesis Outline

This thesis consists of 7 chapters, including this introductory chapter, an experimental methodology chapter, 3 research and experiment chapters, a future work chapter and a conclusion chapter.

- **Chapter 2: Fundamental Principles of DFB and Experimental Methodology**

In this chapter, I first present the fundamental principles of developing DFB lasers, i.e. the coupled wave theory. I then introduce the experimental methodology involved in this project. The device development process in each following experiment chapter has undergone a typical 4-stage research process: waveguide design, wafer growth, device fabrication and device characterisation. Fimmwave, supplied by Photon Design, has been used for waveguide design and these designed epitaxial layer structures were grown in the EPSRC National Centre for III-V Technologies built in Sheffield. Devices were mostly fabricated in the device fabrication clean rooms and characterised using characterisation setups.

- **Chapter 3: GaAs-Based Narrow Ridge Distributed Feedback Lasers**

In this chapter, I present the development process for a set of narrow ridge 2×, 4× and 6× QWs DFB lasers operating at ~1000nm. This study was primarily carried out as preparatory work to support the development of the SAS DFB lasers in Chapter 4. The research started with ridge waveguide modelling to simulate the confinement factors in QWs (Γ_{QWs}) and grating layer ($\Gamma_{grating}$), so as to design three 2×QWs structures with different $\Gamma_{grating}$, and structures for 4× and 6× QWs with a constant $\Gamma_{grating}$. Broad area

lasers were first made prior to the make of DFBs to compare the properties of samples: (1) grown by MOVPE and MBE and (2) incorporating 2×/4×/6× QWs. In the fabrication of DFBs, A two-stage growth process was used, associated with a grating patterning-etching process between the planar growth and the overgrowth. 3μm wide ridge waveguide DFBs were fabricated and characterised. Simulations were validated through the comparison of experimentally estimated and simulated confinement factors in the grating layer for each structure.

- **Chapter 4: GaAs-Based Self-Aligned Stripe Distributed Feedback Lasers**

In this chapter, I describe the conceptualisation and realisation of SAS DFB lasers. Based on previous research of SAS lasers utilising an InGaP optoelectronic confinement layer [123] and DFB lasers employing buried GaAs/InGaP index-coupled grating [99], this study incorporated the grating layer immediately below the stripe geometry with a distance above the active region. A 3-stage growth process was used, associated with 2 patterning-etching processes between the planar growth and 1st overgrowth to form the grating and between the 1st overgrowth and 2nd overgrowth to form the stripe geometry respectively. 3μm SAS DFBs were fabricated and characterised. The experimental measurement was fed back into the simulation through comparison of experimentally estimated and simulated confinement factor in the grating layer and the comparison of experimentally measured and simulated far-field beam profile.

- **Chapter 5: GaAs-Based Monolithically Integrated Self-Aligned Stripe Master Oscillator Power Amplifier**

In this chapter, the research conducted in Chapter 4 [125] has been furthered into the photonic integrated circuit theme. I introduce the conceptualisation of monolithically integrated GaAs-based SAS MOPA devices incorporating an SAS DFB and tapered

SAS SOA. MOPA structures with two different SOA geometries were designed, fabricated and tested. Due to the poor quality of the 2nd overgrowth, the SOA sections are highly defective which makes it impossible to drive the SOAs with a CW current source. The devices were characterised with DFB sections CW pumped and the SOA sections pulsed pumped. The experimental findings are compared and discussed, together with suggestions for future device optimisation.

- **Chapter 6: Future Work**

In this chapter, I first present an optimised version of SAS-DFB-MOPA based on study conducted in Chapter 6. After, I describe some preparatory works for future research, including (1) the study of active-passive integration on 1060nm InGaAs QD material using impurity free vacancy disordering and (2) the comparison of ground state lasing and excited state lasing properties of a set of ~1180nm In(Ga)As/GaAs DWELL materials. These preparatory works are aimed at the conceptualisation of (1) GaAs-based sampled-grating DBR (SG-DBR) tunable lasers and (2) ~1180nm QD SAS-DFB-MOPA based on the GaAs-InGaP regrowth technology.

- **Chapter 7: Conclusion**

In this final chapter, all the studies conducted are summarised.

1.8 Reference

[1] T. H. Maiman, "Stimulated Optical Radiation in Ruby," *Nature*, vol. 187, no. 4736, pp. 493-494, June 1960.

[2] R. N. Hall, G. E. Fenner, J. D. Kingsley, T. J. Soltys and R. O. Carlson, "Coherent light emission from GaAs junctions," *Physical Review Letters*, vol. 9, no. 9, pp. 366-368, November 1962.

[3] M. I. Nathan, W. P. Dumke, G. Burns, F. H. Dill Jr. and G. Lasher, "Stimulated emission of radiation from GaAs p-n junctions," *Applied Physics Letters*, vol. 1, no. 3, pp. 62-64, November 1962.

[4] N. Holonyak Jr. and S. F. Bevacqua, "Coherent (visible) light emission from Ga ($As_{1-x}P_x$) junctions," *Applied Physics Letters*, vol. 1, no. 4, pp. 82-83, 1962.

[5] T. M. Quist, R. H. Rediker, R. J. Keyes, W. E. Krag, B. Lax, A. L. Mcwhorter and H. J. Zeigler, "SEMICONDUCTOR MASER OF GaAs," *Applied Physics Letters*, vol. 1, no. 4, pp. 91-92, 1962.

[6] E. F. Schubert, *Light-emitting diodes*. Cambridge: Cambridge University Press, 2006.

[7] S. R. Bank, H. Bae, L. L. Goddard, H. B. Yuen, M. A. Wistey, R. Kudrawiec and J. S. Harris, "Recent Progress on 1.55-μm Dilute-Nitride Lasers," *IEEE Journal of Quantum Electronics*, vol. 43, no. 9, pp. 773-785, September 2007.

[8] S. J. Sweeney, "Bismide-alloys for higher efficiency infrared semiconductor lasers," *22nd IEEE International Semiconductor Laser Conference*, Kyoto, Japan, pp. 111-112, 2010.

[9] M. A. Majid, D. T. D. Childs, H. Shahid, S. Chen, K. Kennedy, R. J. Airey, R. A. Hogg, E. Clarke, P. Howe, P. D. Spencer and R. Murray, "Toward 1550-nm GaAs-Based Lasers Using InAs/GaAs Quantum Dot Bilayers," *IEEE Journal of Selected Topics in Quantum Electronics*, vol. 17, no. 5, pp. 1334-1342, September-October 2011.

[10] L. A. Coldren, S. W. Corzine and R. K. Sink, *Solutions manual for diode lasers and photonic integrated circuits*. New York: John Wiley & Sons, 1997.

[11] R. Ishihara, "Lecture 3: Introduction to Quantum Theory of Solids," class notes for Solid State Physics, TU Delft OpenCourseWare, 2016. [Online]. Available: https://ocw.tudelft.nl/course-lectures/ssp-l3-qantum-theory-solids/, Accessed on: 20 January 2017.

[12] D. J. Mowbray, "Lecture 14 – Nanostructure based devices – Interband lasers," class notes for PHY6002 Inorganic Semiconductor Nanostructures, University of Sheffield, 2013.

[13] Z. I. Alferov and R. F. Kazarinov, "Semiconductor laser with electric pumping," Inventor's Certificate 181737 [in Russian], Appli. 950840, priority as of March 30, 1963.

[14] H. Kroemer, “Semiconductor laser with electric pumping,” U.S. Patent 3 309 553, (Filed Aug. 16, 1963) 1967.

[15] Z. I. Alferov, V. M. Andreev, E. L. Portnoy and M. K. Trukan, “AlAs-GaAs heterojunction injection lasers with a low room-temperature threshold,” *Fiz. Tekh. Poluprovodn.*, vol. 3, pp. 1328-1332, 1969. [Sov. Phys. Semicond., vol. 3, pp. 1107-1110, 1970].

[16] I. Hayashi, M. B. Panish, P. W. Foy and S. Sumski, “JUNCTION LASERS WHICH OPERATE CONTINUOUSLY AT ROOM TEMPERATURE,” *Applied Physics Letters*, vol. 17, no. 3, pp. 109-111, August 1970.

[17] R. D. Burnham, N. Holonyak Jr., H. W. Korb, H. M. Macksey, D. R. Scifres, J. B. Woodhouse and Zh. I. Alfërov, “Double Heterojunction AlGaAsP Quaternary Lasers,” *Applied Physics Letters*, vol. 19, no. 2, pp. 25-28, July 1971.

[18] M. Adams and M. Cross, “Wave-guiding properties of GaAs / AlxGa1−xAs heterostructure lasers,” *Physics Letters A*, vol. 32, no. 3, pp. 207-208, 1970.

[19] D. A. B. Miller, “Optical Physics of Quantum Wells,” in *Quantum Dynamics of Simple Systems*, 1st ed., G.-L. Oppo, S. M. Barnett, E. Riis and M. Wilkinson, Ed. Edinburgh, Scotland: SUSSP Publications, 1997, pp. 239-266.

[20] G. Morthier and P. Vankwikelberge, *Handbook of distributed feedback laser diodes*. Boston: Artech House, 2013.

[21] H. Kogelnik, “Coupled wave theory for thick hologram gratings,” *The Bell System Technical Journal*, vol. 48, no. 9, pp. 2909-2947, Nov. 1969.

[22] H. Kogelnik and C. V. Shank, “STIMULATED EMISSION IN A PERIODIC STRUCTURE,” *Applied Physics Letters*, vol. 18, p. 152, 1971.

[23] H. Kogelnik and C. V. Shank, “Coupled-Wave Theory of Distributed Feedback Lasers,” *Journal of Applied Physics*, vol. 43, no. 5, pp. 2327-2335, 1972.

[24] D. R. Scifres, R. D. Burnham and W. Streifer, “Distributed-feedback single heterojunction GaAs diode laser,” *Applied Physics Letters*, vol. 25, no. 4, pp. 203-206, 1974.

[26] K. Aiki, M. Nakamura and J. Umeda, “A frequency-multiplexing light source with monolithically integrated distributed-feedback diode lasers,” *IEEE Journal of Quantum Electronics*, vol. 13, no. 4, pp. 220-223, April 1977.

[27] T. Matsuoka, H. Nagai, Y. Itaya, Y. Noguchi, Y. Suzuki and T. Ikegami, “CW operation of DFB-BH GaInAsP/InP lasers in 1.5 μm wavelength region,” *Electronics Letters*, vol. 18, no. 1, pp. 27-28, January 1982.

[28] Y. Itaya, T. Matsuoka, Y. Nakano, Y. Suzuki, K. Kuroiwa and T. Ikegami, “New 1.5 μm wavelength GaInAsp/InP distributed feedback laser,” *Electronics Letters*, vol. 18, no. 23, pp. 1006-1008, November 1982.

[29] T. Matsuoka, H. Nagai, Y. Noguchi, Y. Suzuki and Y. Kawaguchi, “Effect of the Grating Phase at the Cleaved Facet on DFB Laser Properties,” *Japanese Journal of Applied Physics*, vol. 23, part 2, no. 3, 1984.

[30] J. Yoshida, Y. Itaya, Y. Noguchi, T. Matsuoka and Y. Nakano, “Sufficiently side-mode-suppressed high-output-power 1.5μm DFB lasers,” *Electronics Letters*, vol. 22, no. 6, pp. 327-328, March 13 1986.

[31] M. Yamaguchi, M. Kitamura, I. Mito, S. Murata and K. Kobayashi, "Highly efficient single-longitudinal-mode operation of antireflection-coated 1.3 μm DFB-DC-PBH LD," *Electronics Letters*, vol. 20, no. 6, pp. 233-235, March 15 1984.

[32] M. Kitamura, M. Yamaguchi, S. Murata, I. Mito and K. Kobayashi, "Low-threshold and high temperature single-longitudinal-mode operation of 1.55 μm-band DFB-DC-PBH LDs," *Electronics Letters*, vol. 20, no. 14, pp. 595-596, July 1984.

[33] S. Kakimoto, N. Yoshida, A. Takemoto, Y. Kawama, Y. Nakajima and Y. Sakakibara, "Highly efficient 1.5 mu m DFB-PPIBH laser diode with very narrow beam," *Electronics Letters*, vol. 24, no. 24, pp. 1500-1502, November 1988.

[34] Y. Ohkura and S. Kamimoto, "1 Gbit/s RZ zero-bias modulation of extremely low-threshold GaInAsP/InP DFB PPIBH laser," *Electronics Letters*, vol. 24, no. 23, pp. 1461-1462, November 1988.

[35] S. H. Macomber, J. S. Mott, R. J. Noll, G. M. Gallatin, E. J. Gratrix, S. L. O'Dwyer and S. A. Lambert, "Surface-emitting distributed feedback semiconductor laser," *Applied Physics Letters*, vol. 51, p. 472, 1987.

[36] J. S. Mott and S. H. Macomber, "Two-dimensional surface emitting distributed feedback laser arrays," *IEEE Photonics Technology Letters*, vol. 1, no. 8, pp. 202-204, August 1989.

[37] S. H. Macomber, J. S. Mott, B. D. Schwartz and R. S. Setzko, "Beam Quality Improvements In Surface Emitting Distributed Feedback Lasers," *Lasers and Electro-Optics Society Annual Meeting, 1990. LEOS '90. Conference Proceedings., IEEE*, pp. 401-402, 1990.

[38] S. H. Macomber, "Nonlinear analysis of surface-emitting distributed feedback lasers," *IEEE Journal of Quantum Electronics*, vol. 26, no. 12, pp. 2065-2074, December 1990.

[39] H. Soda, K. Wakao, H. Sudo, T. Tanahashi and H. Imai, "GaInAsP/InP phase-adjusted distributed feedback lasers with a step-like nonuniform stripe width structure," *Electronics Letters*, vol. 20, no. 24, pp. 1016-1018, November 1984.

[40] H. Soda, H. Ishikawa and H. Imai, "Design for single-mode asymmetric quarter-wavelength-shifted DFB laser with high differential efficiency," *Electronics Letters*, vol. 23, no. 11, pp. 598-599, May 1987.

[41] H. Soda, Y. Kotaki, H. Sudo, H. Ishikawa, S. Yamakoshi and H. Imai, "Stability in single longitudinal mode operation in GaInAsP/InP phase-adjusted DFB lasers," *IEEE Journal of Quantum Electronics*, vol. 23, no. 6, pp. 804-814, June 1987.

[42] H. Soda, K. Kihara, M. Furutsu, M. Matsuda, H. Seki, S. Ogita, H. Ishikawa and H. Imai, "Wide temperature range of stable single-mode operation in weakly coupled asymmetric mirror reflectivity DFB lasers," *Electronics Letters*, vol. 23, no. 14, pp. 724-725, July 1987.

[43] S. Ogita, M. Yano, H. Ishikawa and H. Imai, "Linewidth reduction in DFB laser by detuning effect," *Electronics Letters*, vol. 23, no. 8, pp. 393-394, April 1987.

[43] Y. Kotai, H. Soda, K. Wakao, H. Ishikawa, S. Yamakoshi and H. Imai, "High-efficiency operation of phase-adjusted DFB laser by asymmetric structure," *Electronics Letters*, vol. 22, no. 9, pp. 462-463, April 1986.

[44] S. Ogita, M. Hirano, H. Soda, M. Yano, H. Ishikawa and H. Imai, "Dependence of spectral linewidth of DFB lasers on facet reflectivity," *Electronics Letters*, vol. 23, no. 7, pp. 347-349, March 1987.

[45] K. Kamite, H. Soda, K. Kihara, H. Nishimoto and H. Ishikawa, "Effect of front facet reflectivity on transmission characteristics of asymmetric reflectivity DFB lasers," *Electronics Letters*, vol. 24, no. 19, pp. 1228-1229, September 1988.

[46] G. Morthier, K. David, P. Vankwikelberge and R. Baets, "A new DFB-laser diode with reduced spatial hole burning," *IEEE Photonics Technology Letters*, vol. 2, no. 6, pp. 388-390, June 1990.

[47] M. Okai, N. Chinone, H. Taira and T. Harada, "Corrugation-pitch-modulated phase-shifted DFB laser," *IEEE Photonics Technology Letters*, vol. 1, no. 8, pp. 200-201, August 1989.

[48] Y. Nakano and K. Tada, "Analysis, design, and fabrication of GaAlAs/GaAs DFB lasers with modulated stripe width structure for complete single longitudinal mode oscillation," *IEEE Journal of Quantum Electronics*, vol. 24, no. 10, pp. 2017-2033, October 1988.

[49] Y. Luo, H. L. Cao, M. Dobashi, H. Hosomatsu, K. Tada and Y. Nakano, "GaAlAs/GaAs single quantum well gain-coupled distributed feedback laser," *IEEE Photonics Technology Letters*, vol. 3, no. 12, pp. 1052-1054, December 1991.

[50] Y. Luo, Y. Nakano, K. Tada, T. Inoue, H. Hosomatsu and H. Iwaoka, "Fabrication and characteristics of gain-coupled distributed feedback semiconductor lasers with a corrugated active layer," *IEEE Journal of Quantum Electronics*, vol. 27, no. 6, pp. 1724-1731, June 1991.

[51] Yi Luo, Weimin Si, Shengzhong Zhang, Di Chen and Jianhua Wang, "Fabrication of GaAlAs/GaAs gain-coupled distributed feedback lasers using the nature of MBE," *IEEE Photonics Technology Letters*, vol. 6, no. 1, pp. 17-20, January 1994.

[52] K. David, G. Morthier, P. Vankwikelberge and R. Baets, "Yield analysis of non-AR-coated DFB lasers with combined index and gain coupling," *Electronics Letters*, vol. 26, no. 4, pp. 238-239, February 1990.

[53] G. Morthier, P. Vankwikelberge, K. David and R. Baets, "Improved performance of AR-coated DFB lasers for the introduction of gain coupling," *IEEE Photonics Technology Letters*, vol. 2, no. 3, pp. 170-172, March 1990.

[54] K. David, G. Morthier, P. Vankwikelberge, R. G. Baets, T. Wolf and B. Borchert, "Gain-coupled DFB lasers versus index-coupled and phase shifted DFB lasers: a comparison based on spatial hole burning corrected yield," *IEEE Journal of Quantum Electronics*, vol. 27, no. 6, pp. 1714-1723, June 1991.

[55] A. J. Lowery and D. Novak, "Performance comparison of gain-coupled and index-coupled DFB semiconductor lasers," *IEEE Journal of Quantum Electronics*, vol. 30, no. 9, pp. 2051-2063, September 1994.

[56] M. Suhara, S. Islam and M. Yamada, "Criterion of external feedback sensitivity in index-coupled and gain-coupled DFB semiconductor lasers to be free from excess intensity noise," *IEEE Journal of Quantum Electronics*, vol. 30, no. 1, pp. 3-9, January 1994.

[57] C. Kazmierski, D. Robein, D. Mathoorasing, A. Ougazzaden and M. Filoche, "1.5-μm DFB lasers with new current-induced gain gratings," *IEEE Journal of Selected Topics in Quantum Electronics*, vol. 1, no. 2, pp. 371-374, June 1995.

[58] Z. M. Chuang, C. Y. Wang, W. Lin, H. H. Liao, J. Y. Su and Y. K. Tu, "Very-low-threshold, highly efficient, and low-chirp 1.55-μm complex-coupled DFB lasers with a current-blocking grating," *IEEE Photonics Technology Letters*, vol. 8, no. 11, pp. 1438-1440, November 1996.

[59] M. L. Osowski, R. Panepucci, I. Adesida and J. J. Coleman, "A strained-layer InGaAs-GaAs asymmetric cladding gain-coupled DFB laser with titanium surface gratings by metalorganic chemical vapor deposition," *IEEE Photonics Technology Letters*, vol. 9, no. 4, pp. 422-424, April 1997.

[60] M. L. Osowski, J. S. Hughes, R. M. Lammert and J. J. Coleman, "An asymmetric cladding gain-coupled DFB laser with oxide defined metal surface grating by MOCVD," *IEEE Photonics Technology Letters*, vol. 9, no. 11, pp. 1460-1462, November 1997.

[61] M. Kamp, J. Hofmann, F. Schäfer, M. Reinhard, M. Fischer, T. Bleuel, J. P. Reithmaier and A. Forchel, "Lateral coupling - a material independent way to complex coupled DFB lasers," *Optical Materials*, vol. 17, no. 1-2, pp. 19-25, June-July 2001

[62] S. Sakano, T. Tsuchiya, M. Suzuki, S. Kitajima and N. Chinone, "Tunable DFB laser with a striped thin-film heater," *IEEE Photonics Technology Letters*, vol. 4, no. 4, pp. 321-323, April 1992.

[63] M. Aoki, M. Komori, A. Taike, R. Yamabi and K. Uomi, "Low-power-consumption thin-film heater-loaded wavelength-tunable DFB laser," *Fifth Asia-Pacific Conference on ... and Fourth Optoelectronics and Communications Conference on Communications*,, Beijing, China, vol. 2, pp. 1548-1549, 1999.

[64] M. Aoki, A. Ohishi, M. Shirai, R. Kaneko, H. Kuwano and S. Tsuji, "Thin-film heater-loaded wavelength-tunable integrated laser/modulator," *Conference Digest. 2000 IEEE 17th International Semiconductor Laser Conference. (Cat. No.00CH37092)*, Monterey, CA, USA, pp. 47-48, 2000.

[65] C. Zhang, S. Liang, H. Zhu and W. Wang, "Widely tunable dual-mode distributed feedback laser fabricated by selective area growth technology integrated with Ti heaters," *Optics Letters*, vol. 38, no. 16, August 2013.

[66] J. Meng, H. Deng and J. He, "Thermally Tuned V-Cavity Tunable Laser with On-Chip Thin-Film Heater," *Asia Communications and Photonics Conference 2014*, OSA Technical Digest (online) (Optical Society of America, 2014), paper AW3A.4., 2014

[67] F. Gerschutz, M. Fischer, J. Koeth, I. Krestnikov, A. Kovsh and A. Forchel, "Temperature insensitive 1305 nm InGaAs/GaAs quantum dot distributed feedback lasers," *2008 Conference on Lasers and Electro-Optics and 2008 Conference on Quantum Electronics and Laser Science*, San Jose, CA, pp. 1-2, 2008.

[68] H. Wenzel, A. Klehr, M. Braun, F. Bugge, G. Erbert, J. Fricke, A. Knauer, M. Weyers and G. Tränkle, "High-power 783 nm distributed-feedback laser," *Electronics Letters*, vol. 40, no. 2, pp. 123-124, January 2004.

[69] H. Wenzel, J. Fricke, A. Klehr, A. Knauer and G. Erbert, “High-power 980-nm DFB RW lasers with a narrow vertical far field,” *IEEE Photonics Technology Letters*, vol. 18, no. 6, pp. 737-739, March 2006.

[70] A. Klehr, H. Wenzel, O. Brox, F. Bugge, G. Erbert, T-P. Nguyen and G. Tränkle, “High-power 894 nm monolithic distributed feedback laser,” *Optics Express*, vol. 15, no. 18, pp. 11364-11369, 2007.

[71] H.-C. Ryu, N. Kim, S.-P. Han, H. Ko, J.-W. Park, K. Moon and K. H. Park, “Simple and cost-effective thickness measurement terahertz system based on a compact 155 μm λ/4 phase-shifted dual-mode laser,” *Optics Express*, vol. 20, no. 23, p. 25990, Febuary 2012.

[72] N. Kim, S.-P. Han, H.-C. Ryu, H. Ko, J.-W. Park, D. Lee, M. Y. Jeon and K. H. Park, “Distributed feedback laser diode integrated with distributed Bragg reflector for continuous-wave terahertz generation,” *Optics Express*, vol. 20, no. 16, p. 17496, 2012.

[73] M. Sun, S. Tan, F. Guo, S. Liu, Q. Kan, D. Lu, R. Zhang, W. Zhao, S. Liang, W. Wang, R. Broeke, F. M. Soares and C. Ji, “Integrated Four-Wavelength DFB Diode Laser Array for Continuous-Wave THz Generation,” *IEEE Photonics Journal*, vol. 8, no. 4, pp. 1-8, August 2016.

[74] B. Tian, Z. Wang, M. Pantouvaki, P. Absil, J. V. Campenhout, C. Merckling and D. V. Thourhout, “Room Temperature O-band DFB Laser Array Directly Grown on (001) Silicon,” *Nano Letters*, vol. 17, no. 1, pp. 559-564, November 2017.

[75] K. Fukuda, D. Inoue, T. Hiratani, T. Amemiya, N. Nishiyama and S. Arai, “Preliminary reliability test of lateral-current-injection GaInAsP/InP membrane distributed feedback laser on Si substrate fabricated by adhesive wafer bonding,” *Japanese Journal of Applied Physics*, vol. 56, no. 2, p. 028002, October 2017.

[76] S. Chen, W. Li, J. Wu, Q. Jiang, M. Tang, S. Shutts, S. N. Elliott, A. Sobiesierski, A. J. Seeds, I. Ross, P. M. Smowton and H. Liu, “Electrically pumped continuous-wave III-V quantum dot lasers on silicon,” *Nature Photonics*, vol. 10, no. 5, pp. 307-311, July 2016.

[77] C. Schultz, P. Crump, A. Maassdorf, O. Brox, F. Bugge, A. Mogilatenko, H. Wenzel, S. Knigge, B. Sumpf, M. Weyers and G. Erbert, "Buried DFB gratings floating in AlGaAs with low oxygen contamination enable high power and efficiency DFB lasers," *2012 IEEE Photonics Society Summer Topical Meeting Series*, Seattle, WA, pp. 59-60, 2012.

[78] J. Zhao, X. Chen, N. Zhou, K. Qian, L. Wang, X. Huang and W. Liu, “Experimental demonstration of a 16-channel DFB laser array based on nanoimprint technology,” *Semiconductor Science and Technology*, vol. 28, no. 5, April 2013

[79] T. J. Slight, O. Odedina, W. Meredith, K. E. Docherty and A. E. Kelly, “InGaN/GaN Distributed Feedback Laser Diodes With Deeply Etched Sidewall Gratings*,” IEEE Photonics Technology Letters*, vol. 28, no. 24, pp. 2886-2888, December 2016.

[80] S. Oku, T. Ishii, R. Iga and T. Hirono, “Fabrication and performance of AlGaAs-GaAs distributed Bragg reflector lasers and distributed feedback lasers utilizing first-

order diffraction gratings formed by a periodic groove structure," *IEEE Journal of Selected Topics in Quantum Electronics*, vol. 5, no. 3, pp. 682-687, May-June 1999.

[81] L. Comerford and P. Zory, "Selectively etched diffraction gratings in GaAs," *Applied Physics Letters*, vol. 25, pp. 208-210, 1974.

[82] P. Zory and L. Comerford, "Grating-coupled double-heterostructure AlGaAs diode lasers," *IEEE Journal of Quantum Electronics*, vol. 11, no. 7, pp. 451-457, July 1975.

[83] H. J. Luo and P. S. Zory, "Distributed feedback coupling coefficient in diode lasers with metallized gratings," *IEEE Photonics Technology Letters*, vol. 2, no. 9, pp. 614-616, September 1990.

[84] A. Rast and A. Muhlhoff, "Characterisation of InGaAsP/InP ITG-DFB-BCRW lasers with contacted surface grating for λ=1.55μm," *IEE Proceedings - Optoelectronics*, vol. 141, no. 5, pp. 323-326, October 1994.

[85] T. Baba, M. Hamasaki, N. Watanabe, P. Kaewplung, A. Matutani, T. Mukaihara, F. Koyama and K. Iga, "A novel short-cavity laser with deep-grating distributed Bragg reflectors," *Japanese Journal of Applied Physics*, vol. 35, pp. 1390-1394, pt. 1, 1996.

[86] R. M. Lammert, J. S. Hughes, S. D. Roh, M. L. Osowski, A. M. Jones and J. J. Coleman, "Low-threshold narrow-linewidth InGaAs-GaAs ridge-waveguide DBR lasers with first-order surface grating," *IEEE Photonics Technology Letters,* vol. 9, pp. 149-151, 1997.

[87] T. Mukaihara, N. Yamanaka, N. Iwai, K. Nishikata, T. Ishikawa, and A. Kasukawa, "1.3 μm GaInAsP lasers with Bragg reflector consisting of semiconductor and air," *Conference Proceedings. LEOS 97. 10th Annual Meeting IEEE Lasers and Electro-Optics Society 1997 Annual Meeting*, pp. 272-273, paper TuQ2, 1997.

[88] R. M. Lammert, A. M. Jones, C. T. Youtsey, J. S. Hughes, S. D. Roh, I. Adesida and J. J. Coleman, "InGaAsP-InP ridge-waveguide DBR lasers with first-order surface gratings fabricated using CAIBE," *IEEE Photonics Technology Letters*, vol. 9, pp. 1445-1447, 1997.

[89] Y. Yuan, T. Brock, P. Bhattacharya, C. Caneau and R. Bhat, "Edge-emitting lasers with short-period semiconductor/air distributed Bragg reflector mirrors," *IEEE Photonics Technology Letters*, vol. 9, pp. 881-883, 1997.

[90] R. Martin, S. Forouhar, S. Keo, R. Lang, R. Hunsperger, R. Tiberio and P. Chapman,, "CW performance of an InGaAs-GaAs-AlGaAs laterally-coupled distributed feedback (LC-DFB) ridge laser diode," *IEEE Photonics Technology Letters*, vol. 7, no. 3, pp. 244-246, March 1995.

[91] R. Millett, K. Dridi, A. Benhsaien, H. Schriemer, K. Hinzer and T. Hall, "Fabrication-tolerant 1310nm laterally coupled distributed feedback lasers with high side mode suppression ratios," *Photonics and Nanostructures - Fundamentals and Applications*, vol. 9, no. 2, pp. 111-118, 2011.

[92] J. Li and J. Cheng, "Laterally-coupled distributed feedback laser with first-order gratings by interference lithography," *Electronics Letters*, vol. 49, no. 12, pp. 764-766, June 2013.

[93] W. Zeller, L. Naehle, P. Fuchs, F. Gerschuetz, L. Hildebrandt and J. Koeth, “DFB Lasers Between 760 nm and 16 μm for Sensing Applications,” *Sensors*, vol. 10, no. 4, pp. 2492-2510, 2010.

[94] Q. Gaimard, L. Cerutti, R. Teissier and A. Vicet, “Distributed feedback GaSb based laser diodes with buried grating,” *Applied Physics Letters*, vol. 104, no. 16, p. 161111, April 2014.

[95] H. Wenzel, J. Fricke, J. Decker, P. Crump and G. Erbert, “High-Power Distributed Feedback Lasers With Surface Gratings: Theory and Experiment,” *IEEE Journal of Selected Topics in Quantum Electronics*, vol. 21, no. 6, pp. 352-358, November-December 2015.

[96] J. Buus, “Mode selectivity in DFB lasers with cleaved facets,” *Electronics Letters*, vol. 21, no. 5, p. 179, 1985.

[97] Z. Chuang, C. Wang, W. Lin, H. Liao, J. Su and Y. Tu, “Very-low-threshold, highly efficient, and low-chirp 1.55-μm complex-coupled DFB lasers with a current-blocking grating,” *IEEE Photonics Technology Letters*, vol. 8, no. 11, pp. 1438-1440, 1996.

[98] C. Park *et al*., "Low-threshold loss-coupled laser diode by new grating fabrication technique," *IEEE Photonics Technology Letters*, vol. 9, no. 1, pp. 22-24, January 1997.

[99] B. J. Stevens, K. M. Groom, J. S. Roberts, P. W. Fry, D. T. D. Childs and R. A. Hogg, “Distributed feedback laser employing buried GaAs/InGaP index-coupled grating,” *Electronics Letters*, vol. 46, no. 15, pp. 1076-1077, July 2010.

[100] Y. K. Sin, H. Horikawa and T. Kamijoh, “InGaAs-GaAs-InGaP distributed feedback buried heterostructure strained quantum-well lasers for high-power operation at 0.98 mu m,” *IEEE Photonics Technology Letters*, vol. 5, no. 9, pp. 966-968, September 1993.

[101] A. Al-Muhanna, J. K. Wade, T. Earles, J. Lopez and L. J. Mawst, “High-performance, reliable, 730-nm-emitting Al-free active region diode lasers,” *Applied Physics Letters*, vol. 73, no. 20, pp. 2869-2871, 1998.

[102] T. Earles, L. J. Mawst and D. Botez, “1.1 W continuous-wave, narrow spectral width (<1 Å) emission from broad-stripe, distributed-feedback diode lasers (λ=0.893 μm),” *Applied Physics Letters*, vol. 73, no. 15, pp. 2072-2074, December 1998.

[103] C. Chang, T. Earles and D. Botez, “High CW power narrow-spectral width (< 1.5 Å) 980 nm broad-stripe distributed-feedback diode lasers,” *Electronics Letters*, vol. 36, no. 11, p. 954-955, 2000.

[104] C. M. Schultz, P. Crump, H. Wenzel, O. Brox, A. Maabdorf, G. Erbert and G. Trankle, "11W broad area 976 nm DFB lasers with 58% power conversion efficiency," *Electronics Letters*, vol. 46, no. 8, pp. 580-581, April 2010.

[105] A. Maaßdorf, C. Schultz, O. Brox, H. Wenzel, P. Crump, F. Bugge, A. Mogilatenko, G. Erbert, M. Weyers and G. Tränkle, “In-situ etching of patterned GaAs/InGaP surfaces for highly efficient 975nm DFB-BA diode lasers,” *Journal of Crystal Growth*, vol. 370, pp. 226-229, 2013.

[106] J. P. Reithmaier et al 2005, 'InP based lasers and optical amplifiers with wire-/dot-like active regions', *Journal of Physics D: Applied Physics*, vol. 38, no. 13, p. 2088, June 2005.

[107] F. Lelarge et al., "Recent Advances on InAs/InP Quantum Dash Based Semiconductor Lasers and Optical Amplifiers Operating at 1.55 μm," *IEEE Journal of Selected Topics in Quantum Electronics*, vol. 13, no. 1, pp. 111-124, January-Februarys 2007.

[108] R. Schwertberger, D. Gold, J.P. Reithmaier, A. Forchel, "Epitaxial growth of 1.55 μm emitting InAs quantum dashes on InP-based heterostructures by GS-MBE for long-wavelength laser applications," *Journal of Crystal Growth*, vol. 251, no. 1-4, pp. 248-252, April 2003.

[109] F. Lelarge, B. Rousseau, B. Dagens, F. Poingt, F. Pommereau and A. Accard, "Room temperature continuous-wave operation of buried ridge stripe lasers using InAs-InP (100) quantum dots as active core," *IEEE Photonics Technology Letters*, vol. 17, no. 7, pp. 1369-1371, July 2005.

[110] R. Nagarajan *et al.*, "InP Photonic Integrated Circuits," *IEEE Journal of Selected Topics in Quantum Electronics*, vol. 16, no. 5, pp. 1113-1125, September-October 2010.

[111] F. A. Kish *et al.*, "Current Status of Large-Scale InP Photonic Integrated Circuits," *IEEE Journal of Selected Topics in Quantum Electronics*, vol. 17, no. 6, pp. 1470-1489, November-December 2011.

[112] M. L. Masanovic, V. Lal, J. S. Barton, E. J. Skogen, L. A. Coldren and D. J. Blumenthal, "Monolithically integrated Mach-Zehnder interferometer wavelength converter and widely tunable laser in InP," *IEEE Photonics Technology Letters*, vol. 15, no. 8, pp. 1117-1119, August 2003.

[113] M. Masanovic, V. Lal, J. Summers, J. Barton, E. Skogen, L. Rau, L. Coldren and D. Blumenthal, "Widely tunable monolithically integrated all-optical wavelength converters in InP," *Journal of Lightwave Technology*, vol. 23, no. 3, pp. 1350-1362, 2005.

[114] A. Ward, D. Robbins, G. Busico, E. Barton, L. Ponnampalam, J. Duck, N. Whitbread, P. Williams, D. Reid, A. Carter and M. Wale, "Widely tunable DS-DBR laser with monolithically integrated SOA: design and performance," *IEEE Journal of Selected Topics in Quantum Electronics*, vol. 11, no. 1, pp. 149-156, January-February 2005.

[115] B. Mason, G. A. Fish, S. P. DenBaars and L. A. Coldren, "Widely tunable sampled grating DBR laser with integrated electroabsorption modulator," *IEEE Photonics Technology Letters*, vol. 11, no. 6, pp. 638-640, June 1999.

[116] J. V. Campenhout, P. R. Romeo, P. Regreny, C. Seassal, D. V. Thourhout, S. Verstuyft, L. D. Cioccio, J.-M. Fedeli, C. Lagahe and R. Baets, "Electrically pumped InP-based microdisk lasers integrated with a nanophotonic silicon-on-insulator waveguide circuit," *Optics Express*, vol. 15, no. 11, p. 6744, 2007.

[117] J. V. Campenhout, L. Liu, P. R. Romeo, D. V. Thourhout, C. Seassal, P. Regreny, L. D. Cioccio, J.-M. Fedeli and R. Baets, "A Compact SOI-Integrated Multiwavelength Laser Source Based on Cascaded InP Microdisks," *IEEE Photonics Technology Letters*, vol. 20, no. 16, pp. 1345-1347, 2008.

[118] M. Spreemann, M. Lichtner, M. Radziunas, U. Bandelow and H. Wenzel, "Measurement and Simulation of Distributed-Feedback Tapered Master-Oscillator Power Amplifiers," *IEEE Journal of Quantum Electronics*, vol. 45, no. 6, pp. 609-616, June 2009

[119] S. O'Brien, R. Lang, R. Parke, J. Major, D. F. Welch and D. Mehuys, "2.2-W continuous-wave diffraction-limited monolithically integrated master oscillator power amplifier at 854 nm," *IEEE Photonics Technology Letters*, vol. 9, no. 4, pp. 440-442, April 1997.

[121] N.-T. Yeh, W.-S. Liu, S.-H. Chen, P.-C. Chiu and J.-I. Chyi, "InAs/GaAs quantum dot lasers with InGaP cladding layer grown by solid-source molecular-beam epitaxy," *Applied Physics Letters*, vol. 80, no. 4, pp. 535-537, 2002.

[120] D. Welch, R. Parke, D. Mehuys, A. Hardy, R. Lang, S. O'brien and S. Scifres, "1.1 W CW, diffraction-limited operation of a monolithically integrated flared-amplifier master oscillator power amplifier," *Electronics Letters*, vol. 28, no. 21, p. 2011, 1992.

[122] M. Nido, I. Komazaki, K. Kobayashi, K. Endo, M. Ueno, T. Kamejima and T. Suzuki, "AlGaAs/GaAs self-aligned LD's fabricated by the process containing vapour phase etching and subsequent MOVPE regrowth," *IEEE Journal of Quantum Electronics*, vol. 23, no. 6, pp. 720-724, January 1987.

[123] K. M. Groom, B. J. Stevens, P. J. Assamoi, J. S. Roberts, M. Hugues, D. T. D. Childs, R. R. Alexander, M. Hopkinson, A. S. Helmy and R. A. Hogg, "Quantum Well and Dot Self-Aligned Stripe Lasers Utilizing an InGaP Optoelectronic Confinement Layer," *IEEE Journal of Selected Topics in Quantum Electronics*, vol. 15, no. 3, pp. 819-827, May-June 2009.

[124] P. D. L. Greenwood et al., "Quantum Dot Superluminescent Diodes for Optical Coherence Tomography: Device Engineering," *IEEE Journal of Selected Topics in Quantum Electronics*, vol. 16, no. 4, pp. 1015-1022, July-August 2010.

[125] H. Lei, B. J. Stevens, P. W. Fry, N. Babazadeh, G. Ternent, D. T. Childs and K. M. Groom, "A GaAs-based self-aligned stripe distributed feedback laser," *Semiconductor Science and Technology*, vol. 31, no. 8, p. 085001, 2016.

Chapter 2. Fundamental Principles of DFB and Experimental Methodology

This chapter consists of two main sections. In the first section, the most important fundamental principles of distributed feedback lasers are introduced, upon which some discussions in Chapter 1 are theoretically supported. The second section describes the experimental techniques involved in my research.

2.1 Fundamental Principles of DFB Laser

This section first discusses the nature of light in terms of electromagnetic wave and related wave equation. Then I introduce the coupled-wave theory developed by Kogelnik and Shank in 1972 [1] together with more recent interpretation by Morthier in his book "Handbook of distributed feedback laser diodes" [2]. After, the main design concept of DFB lasers in my research is described.

2.1.1 Light as Electromagnetic Waves

In 1864, Maxwell combined the electromagnetism equations and suggested the existence of transvers electromagnetic waves and proposed that light is an electromagnetic wave with a free space propagation speed of:

$$c = \sqrt{\frac{1}{\mu_0 \varepsilon_0}}$$

where μ_0: *permeability of free space and* ε_0: *permittivity of free space*

As an electromagnetic wave, light is a combination of propagation of time varying electric field and magnetic field. According to Maxwell, the wave equation is:

$$\nabla^2(\vec{\mathrm{E}}, \vec{\mathrm{H}}) = \frac{1}{\mathrm{c}^2}\frac{\partial^2}{\partial \mathrm{t}^2}(\vec{\mathrm{E}}, \vec{\mathrm{H}})$$

where $\vec{E}$: *electric field and* $\vec{H}$: *magnetic field*

The equation implies that the fields propagate with a speed of *c*, which equals to:

$$\mathrm{c} = \nu\lambda_0$$

where ν: *frequency of oscillation and* λ_0: *wavelength in vacuum*

The speed of propagation in a medium with refractive index of *n* is:

$$\upsilon = \frac{\mathrm{c}}{\mathrm{n}} = \nu\lambda \quad \text{and} \quad \mathrm{n} = \sqrt{\mu_\mathrm{r}\varepsilon_\mathrm{r}}$$

where μ_r: *relative permeability and* ε_r: *relative permittivity*

The magnetic field can be omitted for a simple mathematical generalisation of the wave equation:

$$\mathrm{E}(\mathrm{x}, \mathrm{y}, \mathrm{z}, \mathrm{t}) = \mathrm{E}_0 \cos(\omega \mathrm{t} - \vec{\mathrm{k}} \cdot \vec{\mathrm{r}} + \varphi)$$

where $\vec{k}$: *wave vector,* $|\vec{k}| = \frac{2\pi}{\lambda}$ *and* $\vec{r}$: *vector from origin to* (x, y, z)

2.1.2 Fundamental Principles of DFB Lasers

An easy way to quickly understand the operation of distributed feedback lasers (DFB) is that the optical feedback of intra-cavity radiation is no longer provided by two reflective end-facets, but is "distributed" as many refractive sources along the cavity. This "distribution" is realised by periodically structuring the waveguide as a diffraction grating, as shown in Fig. 2-1 (a) and (b).

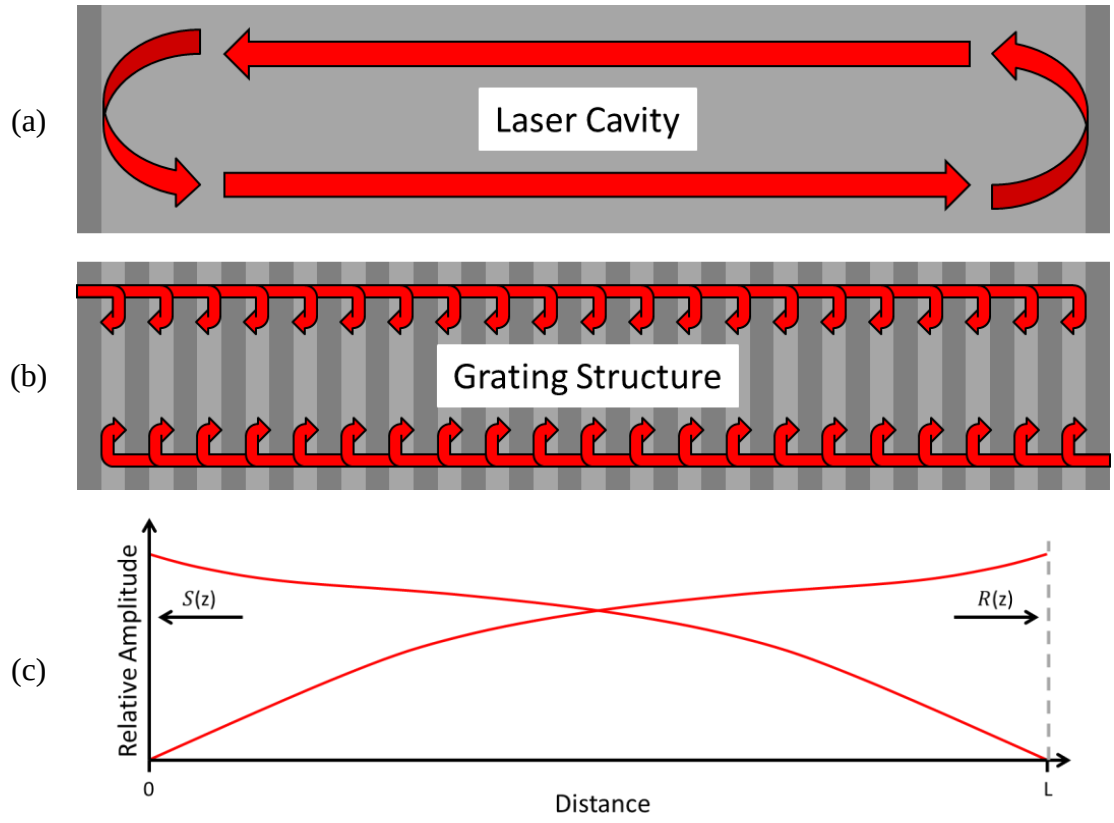

Figure 2-1: Propagation of light in laser cavity of (a) a F-P laser, (b) a DFB laser and the relative amplitude of the 2 conter-running waves, i.e. R(z) and S(z)

In DFB lasers, the grating structure provides an optical feedback with wavelength selection, which has the maximum reflectivity at around the Bragg wavelength (λ_B):

$$\lambda_B = 2\Lambda n_{eff}$$

where Λ: *grating period and* n_{eff}: *effective refractive index*

➢ Coupled Wave Theory

Kogelnik and Shank's coupled wave theory is based on the scalar wave equation [1], here E is the complex amplitude of a field of angular frequency (ω) which is independent of x and y:

$$\frac{\partial^2}{\partial z^2}E + k^2E = 0$$

Defining the spatial modulation of the refractive index, n, and gain constant, α:

$$n(z) = n + n_1\cos(2\beta_0 z) \quad \text{and} \quad \alpha(z) = \alpha + \alpha_1\cos(2\beta_0 z)$$

$where\ \frac{\pi}{\beta_0}: spatial\ periodicity$

At Bragg condition:

$$\frac{\pi}{\beta_0} = \frac{\lambda_{medium}}{2} = \frac{\lambda_{air}}{2n} \rightarrow \beta_0 \equiv \frac{n\omega_0}{c}$$

For the theory developed in [1], it was assumed that:

$\omega \approx \omega_0$, laser oscillates at about the Bragg frequency ω_0

$\alpha \ll \beta_0, \quad n_1 \ll n, \quad \alpha_1 \ll \beta_0$

Therefore:

$$k^2 = \beta^2 + [2j\alpha + 4(\frac{\pi n_1}{\lambda_0} + \frac{1}{2}j\alpha_1)]\beta\cos(2\beta_0 z)$$

Defining coupling constant:

$$\kappa = \frac{\pi n_1}{\lambda_0} + \frac{1}{2}j\alpha_1, \quad \text{(per unit length)}$$

In such a structure, the electric field *E* can be described using the two significant counter-running waves, as sketched in Fig. 2-1 (c), *R* and *S*:

$$E(z) = R(z)\exp(-j\beta_0 z) + S(z)\exp(j\beta_0 z)$$

When substituting *E* into the wave function, if neglecting second derivatives $\frac{\partial^2 R}{\partial z^2}$ and $\frac{\partial^2 S}{\partial z^2}$ and inserting all the assumptions, then:

$$-R' + (\alpha - j\delta)R = j\kappa S \quad \text{and} \quad S' + (\alpha - j\delta)S = j\kappa R$$

where δ *is the resonant frequency, equals to* $(\beta^2 + \beta_0^2)/2\beta \approx \beta - \beta_0$

In [1], *R* and *S* were assumed in the form:

$$R = r_1 e^{\gamma z} + r_2 e^{-\gamma z} \quad \text{and} \quad S = s_1 e^{\gamma z} + s_2 e^{-\gamma z}$$

where $\gamma^2 = \kappa^2 + (\alpha - j\delta)^2$

After applying all the boundary conditions:

$$\gamma + (\alpha - j\delta) = \pm j\kappa e^{\gamma L} \quad \text{and} \quad \gamma - (\alpha - j\delta) = \mp \kappa e^{-\gamma L}$$

$$\kappa = \pm \frac{j\gamma}{\sinh(\gamma L)}$$

where L is the cavity length

With given *L* and κ, a set of modes can be calculated corresponding to eigenvalues (generally complex) of γ, which further corresponds to a pair of α and δ:

$$\alpha - j\delta = \gamma \coth(\gamma L)$$

Consider a gain-free structure, where $\alpha=0$ and κ is real. Fig. 2-2 shows the sketch of dispersion curves where the propagation constant is plotted as a function of ω/c. As shown, a stopband of width $2\pi n_1/\lambda$ is centred at the Bragg frequency.

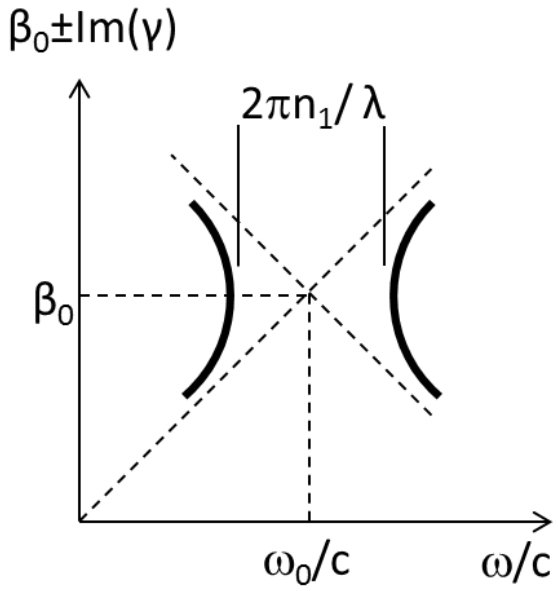

Figure 2-2: Sketch of dispersion curves of a gain-free structure [1]

- **Mode Spectrum**

For the waveguide cavity in my research, photon lifetime (τ_p) is related to the threshold gain (g_{th}) by the equation:

$$\Gamma_a \nu_g g_{th} = \frac{1}{\tau_p} = \nu_g(\tilde{\alpha}_m + \tilde{\alpha}_c)$$

where $\tilde{\alpha}_m$: *mirror losses*, $\tilde{\alpha}_c$: *cavity losses*

Through solving the wave equation with boundary ($z=0$ and $z=L$) values equal to zero, the solution of the lasing mode is a set of propagation vectors β' and their corresponding threshold gain g_{th}, which results in two with lowest and identical g_{th} corresponding to the two degenerate modes [1]-[3].

Fig. 2-3 (a) presents the characteristic spectrum showing the resonance of the modes in an index-coupled non-phase-shifted structure. As can be seen, the spectrum is symmetric centring at Bragg frequency (v_{Bragg}). There is no resonance at v_{Bragg} corresponding to the stopband discussed earlier. It is also found that the two modes locating closest on both sides of v_{Bragg} sharing the same lowest threshold gain, corresponding to 2 degenerate modes in a non-phase-shifted DFB laser.

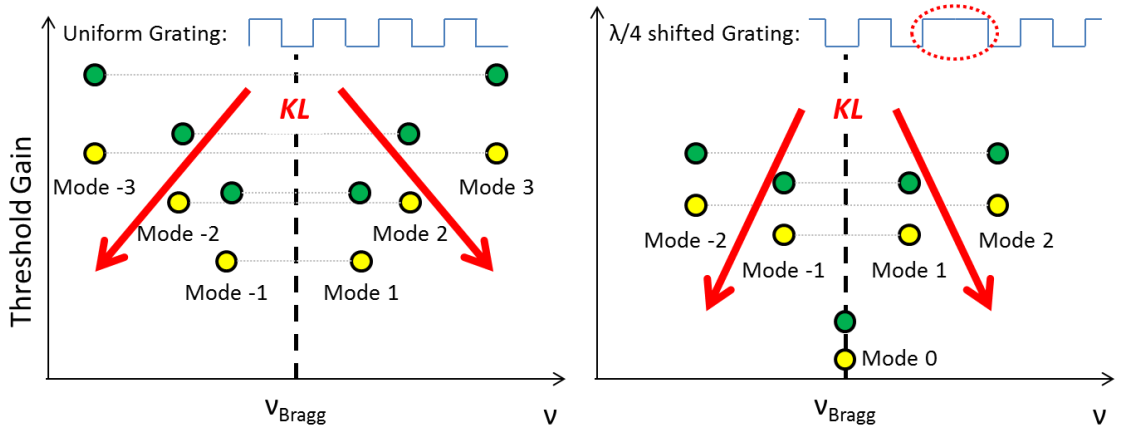

Figure 2-3: Sketch of characteristic spectrum of the resonance modes of structures with (a) a uniform grating and (b) a λ/4 shifted grating [2]

Fig. 2-3 (b) presents the characteristic spectrum showing the resonance of the modes in an index-coupled quarter-wavelength-shifted structure. As can be seen, the spectrum is also symmetric centring at v_{Bragg}. Compared to the former, there is a resonant mode with lowest threshold gain right at v_{Bragg}, corresponding to the single mode selected in a quarter-wavelength-shifted DFB laser.

In real laser operation, the mode with the lowest threshold gain lases. Due to the difficulty in precisely aligning cleaved facets to the grating, a facet phase shift contributes to the grating phase condition, adding a degree of variability in laser-to-laser uniformity. In my design, I exploited the random phase shift associated with cleaved facets in order to break the degeneracy and ensure single-mode operation. Its simplicity of manufacture makes it a suitable method for research purposes.

In the solution described above, the lowest two modes for different κL values are the two symmetrically located dots closest to the $(\beta' - \beta o)\, L = 0$ grid line. In practice, not only because of the structural imperfection, but also because of effects such as spatial hole burning (SHB) and random facet phase, the threshold gain of one of the two modes decreases compared to the other one.

- **Light Intensity Distribution**

Although λ/4-shifted DFB lasers do not have the issue of having 2 degenerate modes, the distribution of the light intensity has a pointing curve profile at the phase-shift location as sketched in Fig. 2-4 (a), which can easily cause SHB and further affecting the mode stability of the laser.

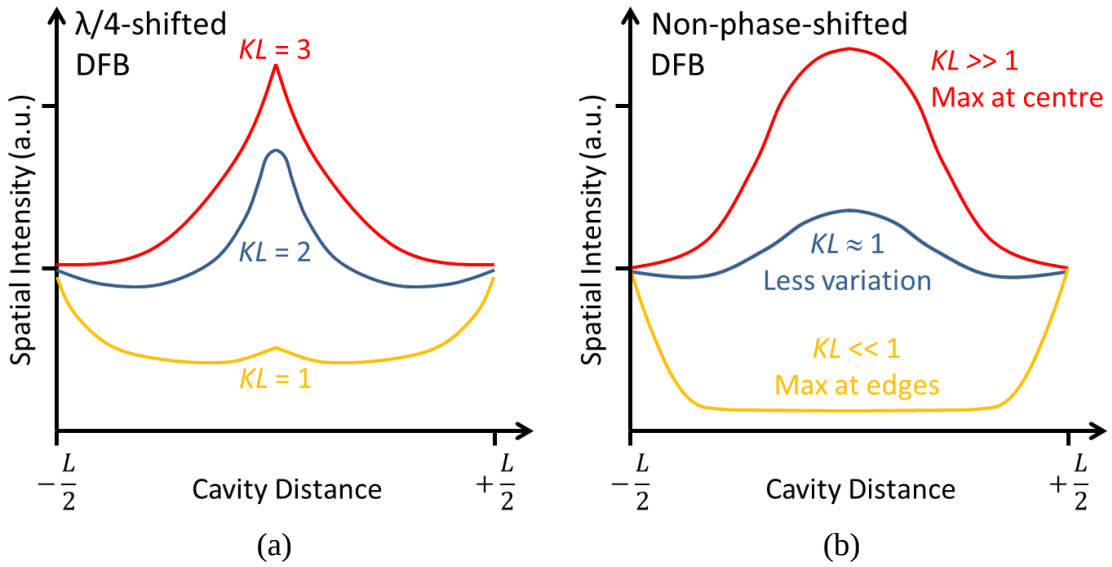

Figure 2-4: Schematic diagrams of longitudinal variation of spatial intensity distribution of (a) an AR-coated λ/4 shifted DFB for 3 coupling values [2] and a non-phase-shifted DFB with different coupling levels [1]

Fig. 2-4 (b) sketches the spatial light intensity along the laser cavity of a non-phase shifted grating [1]. As illustrated, for devices with $\kappa L<1$, the highest optical intensity is

at the edges of the grating. For devices with κL>1, the highest optical intensity is in the centre of the grating. For high power operation, the former can significantly damage the output facet, while the latter can cause SHB and affect the mode stability.

In my non-phase-shifted DFB structures, κL were designed to be equal to 1, which has a less significant impact on intensity variation, to reduce the effect of SHB for better laser performance [4] [5].

➢ Simulation of Coupling Coefficient

The performance of such a structure is based on its coupling coefficient (K), which can be linked to the optical confinement factor in the grating (Γ_g). In my research, 1st order rectangular 50/50 GaAs/InGaP gratings were designed and fabricated. Γ_g is given by the following equation:

$$\Gamma_g = \frac{\kappa \lambda_B}{2(n_1 - n_2)}$$

where λ_B: Bragg wavelength; n_1, n_2: refractive indices of grating materials

For laser waveguide design, I used Fimmwave by Photon Design, which is a software-based refractive index mode solver, to obtain important simulation data, such as the confinement factors in the active region and in the grating. In the design stage, n_1, n_2 and λ_{DFB} are known and Γ_g is simulated in order to calculate κ. The value of κL affects the location of SHB.

Typically, it is called critically-coupled for a DFB laser to have a κL of 1 (over-coupled for κL >1 and under-coupled for κL <1).

➢ Experiment Approximation of Coupling Coefficient

In practice, the coupling coefficient can be approximated experimentally [6] by measuring the wavelength spacing ($\Delta\nu$) between two adjacent sub-threshold DFB modes either side of the Bragg wavelength and the longitudinal mode spacing ($\Delta\nu_{long}$):

$$\kappa_{meas} = \frac{\pi \times \Delta\nu}{2 \times L \times \Delta\nu_{long}}$$

where L: the cavity length of device; $\Delta\nu$, $\Delta\nu_{long}$ are measured in the unit of cm^{-1}

This gives me a method to validate the simulation of layer structure design by comparing the calculated coupling coefficient from simulated confinement factors and experimentally measured coupling coefficients.

More importantly, we wish to realise a high-power DFB laser and to do so, we need a good grasp of the design rules and their relation to practical realisation through verifying the accuracy of the design tool. This comparison of waveguide properties between simulation result and experimental measurement allows us to do so.

Also, it is important for my future waveguide design, especially in more complicated photonic integrated circuit (PIC) designs, starting with the simplest 2 component integrated MOPA design.

In MOPA design, we need to be able to design the DFB portion for κL~1 to achieve best practice, as explained above. Therefore, it is necessary to get a handle of κ control here using this exercise, and then determine the required L through examination of laser performance as a function of cavity length.

2.1.3 DFB Design in This Research

The comparison among different grating fabrication techniques have been made above. Fig. 2-5 illustrates two DFB structures with (a) laterally-coupled grating and (b) overgrown grating respectively. The majority of nowadays DFB lasers are manufactured using one of these schemes.

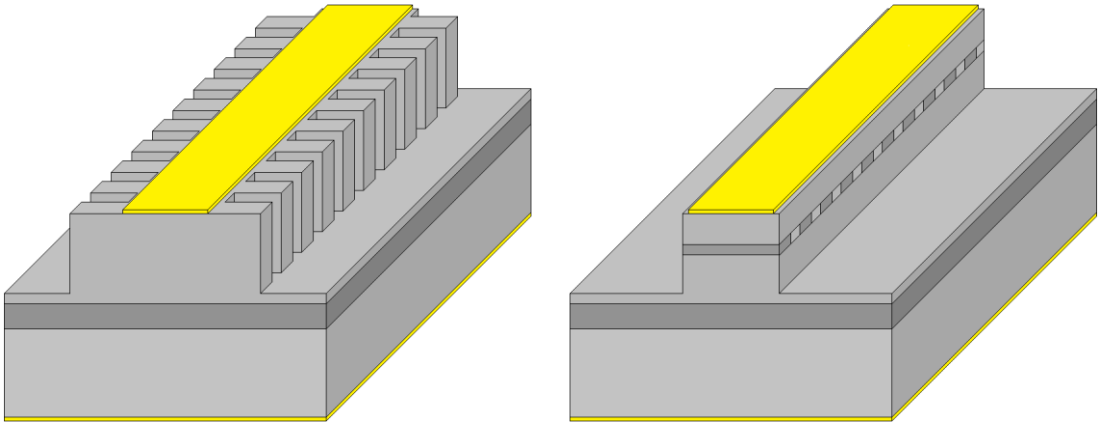

(a) (b)

Figure 2-5: Schematic of DFB structures with (a) lateral grating and (b) overgrown grating

In this research, the index-coupled overgrown grating, as first reported in [7], was adopted. This was achieved by choosing two lattice-matched materials with different refractive index at the designed lasing wavelength. GaAs and InGaP were used to form the grating through the periodical variation of the effective refractive index. These materials are lattice-matched and offer a large refractive index difference allowing them to be positioned far away from the active region.

Furthermore another important reason for choosing GaAs/InGaP is that they allow selective etching by etchant 1:1 HCl/H_3PO_4. In fabrication, the first growth stops after the GaAs-InGaP-GaAs grating layer. The lower layer acts as etch stop to the wet chemical for InGaP etching and to protect the underlying Al-containing layer, and the

upper layer not only acts as a cap for selective etching, but also minimises the possibility of As-P exchange at the re-growth surface.

As reported in previous work by my research group [7], the main design concept includes:

- **Overgrown grating: $In_{0.49}Ga_{0.51}P$/GaAs matrix**

The lattice-matched $In_{0.49}Ga_{0.51}P$/GaAs pair has a high refractive index contrast. Therefore the grating layer can be formed a relatively long distance away from the active region. Therefore any deleterious effects in the active region resulting from the grating etch and re-growth processes are minimised.

- **Cladding layers: $Al_{0.42}Ga_{0.58}As$**

Using $Al_{0.42}Ga_{0.58}As$ as the cladding layer provides greater design flexibility than using Al-free structures, because $Al_xGa_{1-x}As$ is lattice-matched to GaAs for all composition of x (Al %), unlike InGaP cladding, which is only lattice-matched for one stoichiometry. Since $Al_{0.42}Ga_{0.58}As$ is not exposed to atmosphere during manufacture of the buried grating structure, the oxidation process of Al can be ignored [8].

- **Active region: $In_{0.17}Ga_{0.83}As$ multiple quantum wells**

InGaAs QW lasers normally emit within the range 900-1100nm with relatively high reliability in terms of sudden failure and typical lifetime. Therefore, whilst access to a platform for advanced components on GaAs enables us to exploit the novel properties of exotic active media such as quantum dots, diluted nitrides or even bismides, we started this program using a well-developed and well-known QW scheme for emission at ~980nm, where robust, high gain material allows study of the device without the ambiguity associated with using “developing” materials.

2.2 Experimental Methodology

In general, each project in the following chapters has undergone a typical 4-stage research process: waveguide design, wafer growth, device fabrication and device characterisation.

In the initial stage, Fimmwave, by Photon Design, is employed to simulate the designed waveguides and optimise confinement factors. Simulation of the waveguide provides significant parameters for study, e.g. guided mode profile and optical confinement factor in selected layers. In the second stage, these layer designs are grown at the EPSRC National Centre for III-V Technologies based in Sheffield. In the third stage, these wafers are fabricated into devices in our clean room according to the parameters in the simulated waveguide design. Further, for the manufacture of the grating structures and self-aligned stripes, regrowth processes are involved, which will be described in detail in Chapter 3, 4 and 5. In the last stage, the performance properties of devices are characterised using purpose-built experimental setups, including those used to measure the light-output and voltage as a function of injected current, i.e. L-I-V properties, emission spectrum and far-field beam profile.

2.2.1 Device Design – Fimmwave Waveguide Simulation

For a semiconductor light emitting device, especially a laser, the waveguide structure directly influences its optical properties. Therefore, waveguide design is typically performed at the initial stage of device-focused research. This was a critical starting point for my research, and particularly important for the devices to be described in the

following chapters. To accurately simulate the designed waveguide, I used Fimmwave, computer software supplied by Photon Design, to model 2-D waveguide structures, as illustrated in Fig. 2-6. Fimmwave has a variety of mode solvers and a variety of waveguide definition user interfaces [9]. Among the many available solvers, I adopted the Film Mode Matching (FMM) solver for my research. This semi-analytical and fully-vectorial solver is based on the FMM method [10] [11], which is optimised for epitaxially grown structures in my projects. An exemplary waveguide simulation process is described in Appendix I.

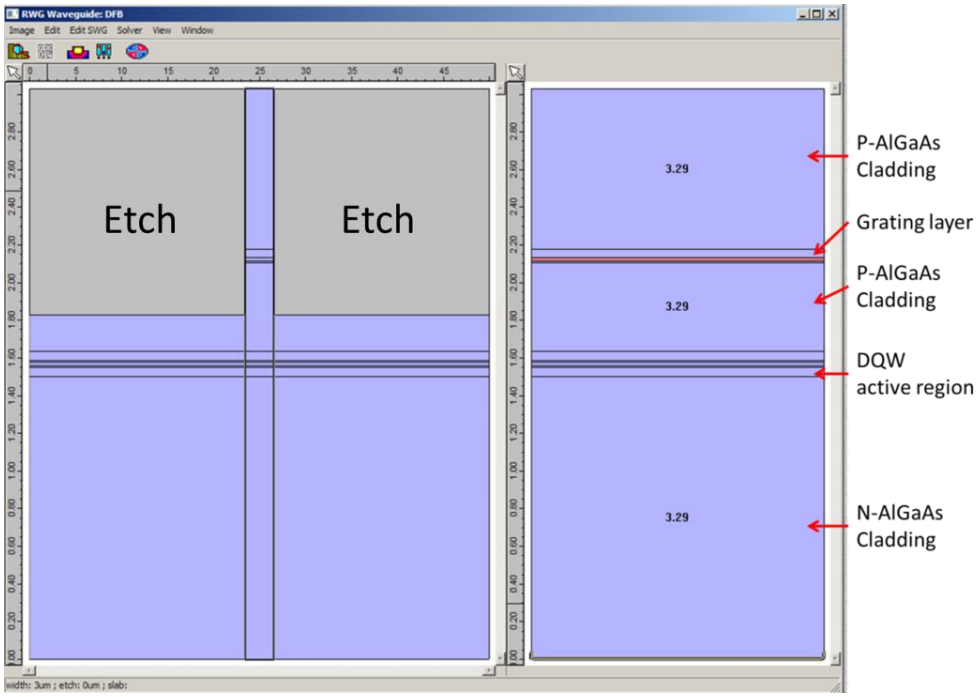

Figure 2-6: Simulation of a ridge waveguide DFB laser using Fimmwave

FMM method is one of many numerical methods for calculating vector mode fields, which is especially efficient for layered waveguides with a rectangular geometry. The core concept of this method is under the assumption of the materials to be isotropic, non-magnetic and non-absorbing.

As illustrated in Fig. 2-7, the solver simulates a given waveguide in the form of a matrix of rectangles, which are laterally defined by a number of slices (M) and vertically defined by a sequence of layers (N). For each rectangle (m, n), the refractive index is $n_{(m,n)}$, such that the

relative permittivity (dielectric constant) is $\varepsilon_{(m,n)} = n_{(m,n)}^2$. For each slice, the software then builds a 2D mode from its TE and TM 1D modes.

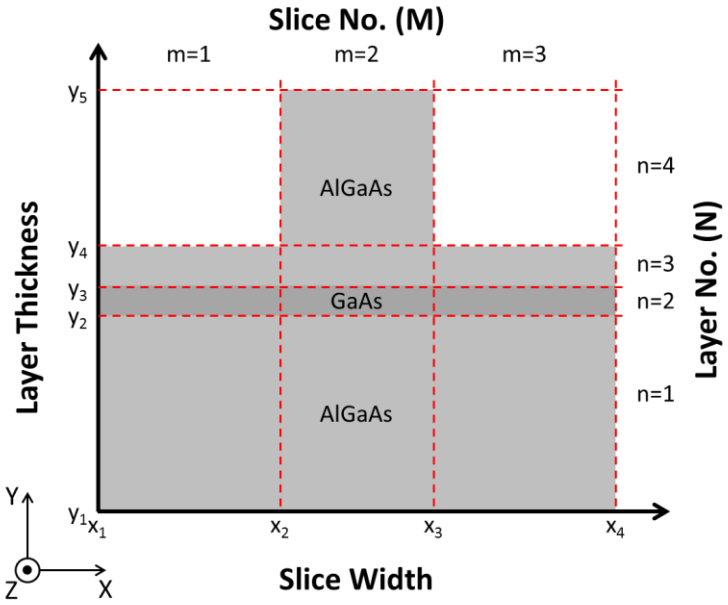

Figure 2-7: Simulation of a typical ridge waveguide cross section

Electromagnetic filled components are in the form of:

$$F(x,y,z,t) = \Phi(x,y)e^{j(\omega t-\beta z)}, where\ \omega = kc = 2\pi c/\lambda_{vacuum}$$

By inserting into Maxwell's equations, for all points inside rectangle (m, n), i.e. $x_m < x < x_{m+1}$ and $y_n < y < x_{n+1}$,

$$\partial_x^2\Phi + \partial_y^2\Phi = [\beta^2 - k^2\epsilon_{(m,n)}]\Phi$$

By gathering the modes with the same z-component (k_z) of the modal wave-vector and adjusting the modal amplitudes to match the distribution at interfaces, a waveguide mode can be found in terms of a set of slice mode amplitudes.

Considering TE polarization for the interest of my research, i.e. electric field component E_x, the boundary continuity conditions require: (a) E_x and $\partial_y E_x$ are continuous between layers (lateral boundaries) and (b) εE_x and $\partial_x E_x$ are continuous between slices (vertical boundaries). This is only possible for a certain number of discrete β (certain values of k_z).

2.2.2 Wafer Growth – Metal Organic Vapour Phase Epitaxy

Both molecular beam epitaxy (MBE) and metal organic vapour phase epitaxy (MOVPE) methods for arsenides growth are available at the EPSRC National Centre for III-V Technologies in Sheffield. In my research, most of the wafers and all the overgrowths were grown by MOVPE, using the Thomas Swan Flip-top Shower-head reactor, as pictured in Fig. 2-8.

Figure 2-8: Thomas Swan Flip-top Shower-head reactor [13]

The operating principle of MOVPE can be described in the following way: In the chamber, the required elements are carried as a component of gaseous precursors and mix when brought together in close proximity to a heated-substrate surface [12]. In this reaction, the precursors are decomposed and the semiconductor compound is formed on the surface. A certain switching sequence of valves in the gas lines allows the growth of layered structures. The preference of MOVPE over MBE was manifold: The higher growth temperature of MOVPE results in a comparatively smaller occurrence of O_2 incorporation into upon the Al-containing wafer layers, hence lower resistivity and higher quality cladding layers. Furthermore, in the formation of the GaAs/InGaP/GaAs overgrown gratings, the diffusive nature of the MOVPE growth process enables grating in-fill and planarisation of the overgrown GaAs, which fills in the etched InGaP matrix prior to the growth of upper layers.

2.2.3 Device Fabrication

The devices studied in this thesis have been fabricated mostly in the device fabrication clean rooms in Sheffield, with the only exception being DFB grating definition, for which we relied upon the EPSRC National Centre for III-V Technologies in Glasgow to pattern to our designs.

The three common device fabrication processes involved in preparation of my devices were lithography, etching and metallisation. Other fabrication techniques included dielectric deposition, device facet coating and nanoscale structural measurement.

➢ Common Fabrication Techniques

- **Lithography – Photolithography / E-Beam Lithography**

By exposing photosensitive polymer (e.g. Shipley positive photoresist, SPR350) with UV light through a chrome-patterned quartz photomask on a Karl-Suss MJB3 Mask Aligner, pictured in Fig. 2-9 (a), the pre-designed patterns on the mask are transferred onto the surface upon developing in MF-26A developer. During development, the exposed resist is removed and the non-exposed regions remain.

By using the vacuum contact mode, the achievable feature resolution is down to 600nm. However, the grating periods of the DFB lasers in my designs are only ~150nm. Therefore, for grating patterning, electron beam lithography (EBL) has been employed instead of photolithography. The EBL was performed using Vistec equipment in the EPSRC National Centre for III-V Technologies nanofabrication partner in Glasgow.

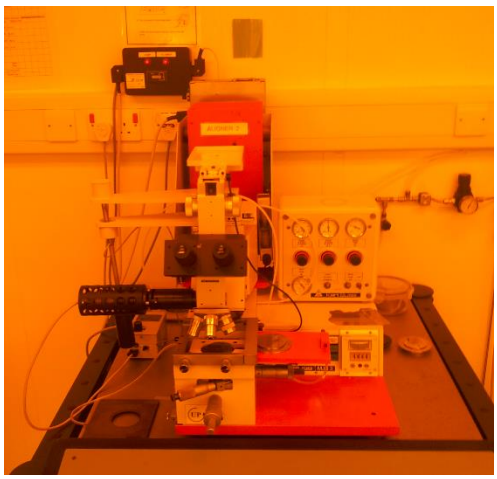

(a)

(b)

Figure 2-9: (a) Karl-Suss MJB3 Mask Aligner and (b) Oxford Plasma-Lab ICP (Inductively Coupled Plasma) Etch System

- **Etching – Wet Etch / Dry Etch (RIE / ICP)**

Etching is an important process in device fabrication. This includes semiconductor etching, e.g. electrical-isolation trench etching or ridge etching, and dielectric etching, e.g. contact window etching. Different etching methods are adopted for different fabrication requirements. For example, both ICP, pictured in Fig. 2-9 (b), Argon dry etch and wet chemical etch using 1:1 HCl/H_3PO_4 etchant (selectively etching InGaP over GaAs) were applied for grating fabrication; only wet etch was adopted for ridge etching in broad area laser fabrication using 1:1:1 $HBr/CH_3COOH/K_2Cr_2O_7$ etchant; RIE dry etch using CHF_3/O_2 (35sccm/5sccm) was performed to open windows in Si_3N_4 coated surfaces, to allow application of remote bond-pads to narrow ridge devices.

- **Metallisation**

A thermal evaporator (Edwards 306 Coating System), pictured in Fig. 2-10 (a), has been used as the main tool for contact metallisation, including Au/Zn/Au p-ohmic-contact, In-Ge/Au n-ohmic-contact and Ti/Au bond pad, where titanium is chosen due

to its strong adhesion to both Si_3N_4 and gold. The deposition process is real-time monitored by a crystal thickness monitor, pictured in Fig. 2-10 (b), positioned adjacent to the sample being coated. In order to form ohmic contacts, annealing is performed to the sample by a Mattson Rapid Thermal Annealing System (RTA) for 3 seconds at 360^{o}C to diffuse Zn into the GaAs layer. The RTA is pictured in Fig. 2-10 (c).

(a)

(b)

(c)

Figure 2-10: Metallisation equipments: (a) Edwards 306 Coating System, (b) deposition crystal thickness monitor and (c) Mattson Rapid Thermal Annealing System (RTA)

The following two sections (2.2.2 and 2.2.3) describe two standard device fabrication processes. Broad area laser structure (50μm ridge width) is a simple laser waveguide used to compare or study the lasing characteristics of grown structures. In such broad devices, the effect of process-induced variability, such as side-wall roughness and waviness, is minimised compared to narrow-ridge lasers (where sidewalls have greater influence), aiding comparison of material properties. They also have the advantage of a faster time to be processed. Mesa diodes are fabricated to study the spontaneous emission characteristics of a grown structure.

➢ Standard Fabrication Process I: Broad Area Laser

The wafer is cleaved to a suitable size for processing, followed by a 3-stage wash (n-Butyl, Acetone and IPA) to remove any contamination from handling. Then, the sample is heated up on the 100°C hot plate for 1 minute to remove any residual IPA. The fabrication process then consists of 3 stages.

- **Stage I: Front Contact**

As shown in Fig. 2-11, to define the pattern for contact deposition, SPR 350 positive photoresist is spun onto the sample at 4000rpm for 30 seconds, followed by 1 minute hard bake at 100°C on a hot plate. The sample is then exposed under the 'CONTACTS' mask using an MJB3 Mask Aligner, with the cleaved edges perfectly aligned to the mask. After 1 minute development in MF26A, the patterns from the mask transfer into the photoresist with 43μm-wide defined stripes being opened in the photoresist.

After rinsing in DI water, 1 minute oxygen plasma ash is performed to ensure full removal of photoresist in the exposed areas.

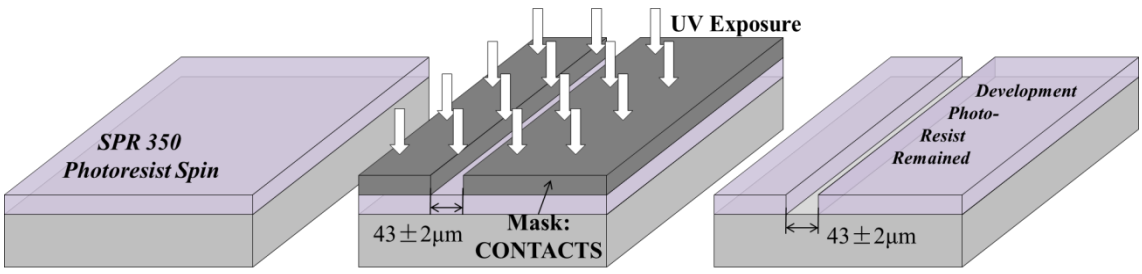

Figure 2-11: Photoresist spin and exposure under 'CONTACTS' mask and development

Before metal deposition, the sample is firstly washed in 19:1 DIW/Ammonia solution to remove any existing oxide on the opened areas, then rinsed in DI water and blown dry. This step is significant because the presence of any oxides between the

semiconductor surface and the contact to be deposited will increase the contact resistance.

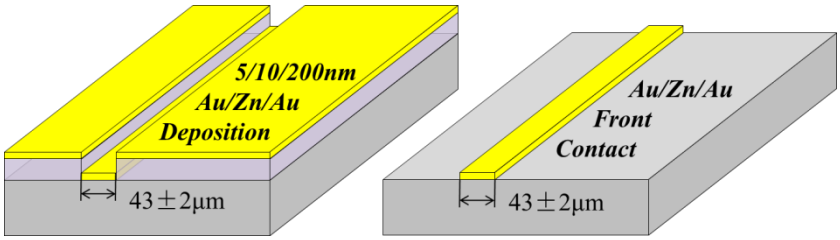

Figure 2-12: Au/Zn/Au front contact deposition

Gold wire and a piece of Zinc are placed in tungsten elements 6cm above the crystal thickness monitor. The chamber was pumped down to a pressure of 2×10^{-6}mbar to proceed. Then Au/Zn/Au layers are deposited with a thickness of 5/10/200nm on both the photoresist coating and the opened stripes, as shown in Fig. 2-12. The metal deposited on the photoresist-coated areas is removed during a lift-off in acetone. The cleanliness is inspected under an optical microscope. Finally, the cleaned sample is annealed in the RTA at 360^{o}C with 30 seconds ramp and 3 seconds dwell.

- **Stage II: Ridge Etching**

This step is similar to the photolithography described above. The sample is spun with SPR 350 positive photoresist and then exposed under UV light with perfect alignment between the deposited contact stripes and the 'RIDGES' mask, followed by 1min MF26A development. The sample is then rinsed in DIW, following by 1min oxygen plasma ash. As in Fig. 2-13, the stripes on mask 'RIDGES' are 50μm wide, 7μm wider than the contact stripes width 43μm, to fully cover the contact area and allow for any misalignment and undercut during wet etch.

An isotropic wet etch is performed to etch down ~1.5μm from the sample surface for the formation of laser ridges. Wet etch using 1:1:1 $HBr/CH_3COOH/K_2Cr_2O_7$, known

locally as the 'one-one-one etchant', has an etch rate of approximately 2-5μm/min at 20°C for most III-V compounds. This rate is too high to control for a target etch depth of only ~1.5μm. For the ease of operation, the etchant is diluted as 2:2:1:1 $HBr/CH_3COOH/K_2Cr_2O_7/DIW$ for a more manageable etch rate.

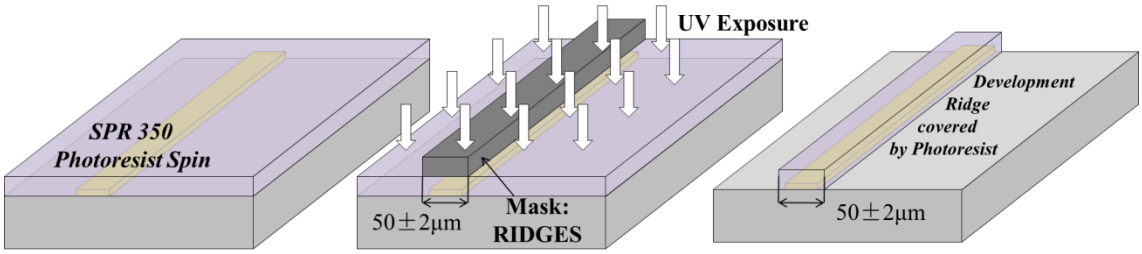

Figure 2-13: Photoresist spin and exposure under 'RIDGES' mask and development

A Veeco DEKTAK 150 is employed for repeatedly checking the etch depth until the target depth is reached. Fig. 2-14 illustrates the wet etching process. Following removal of the resist in EKC830 posistrip, a 2 minute oxygen plasma ash is performed to remove any residual photoresist. The cleaning process is repeated until the sample is clean and no photoresist residue can be observed.

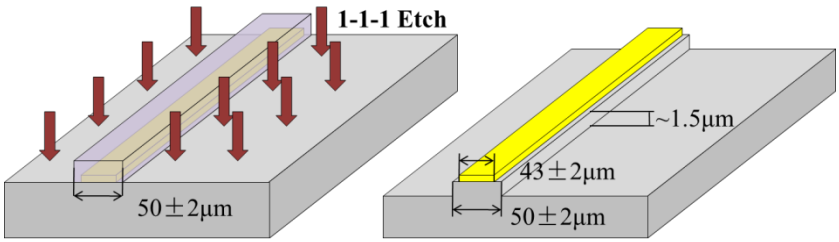

Figure 2-14: 2:2:1:1 $HBr/CH_3COOH/K_2Cr_2O_7/DIW$ etching and resist removal

- **Stage III: Substrate Thinning and Back Contact**

Substrate thinning is important for laser fabrication. For an operating laser, heat is generated in the active region. By thinning the substrate, the active region can be positioned closer to the heat-sink, which increases the ability for heat dissipation, thus improving the overall device performance. Also, a thinner sample allows better cleaving

of devices, especially for short cavity lengths, for which the minimum length that can feasibly be cleaved is ~3 times the substrate thickness. The sample is spun with a thick layer of SPR 350 photoresist to protect the fabricated front features from scratching, which is hard baked at 100^{o}C for 1 minute. The sample is then mounted epi-side-down with wax onto a glass holder for substrate thinning with a Logitech LP50 Lapper Polisher. As in Fig. 2-15, the sample is then evenly grinded to a target thickness of 130-150μm, using 3μm calcined aluminium oxide.

After rinsing in DI water, the sample is removed from its glass holder by dissolving the wax in warm n-butyl acetate. The protective photoresist is removed in warm Acetone, followed by a full 3-stage clean and cleanliness inspection under optical microscope.

Further, 20nm/200nm thick In-Ge/Au back contact matallisation is deposited, again, using the thermal evaporator. The deposition was followed by RTA annealing at 340^{o}C with 30 seconds ramp and 3 seconds dwell. Although not optimum for In-Ge/Au (prefer 420^{o}C), this temperature is chosen as satisfactory to avoid over-diffusing the top Au-Zn-Au contact.

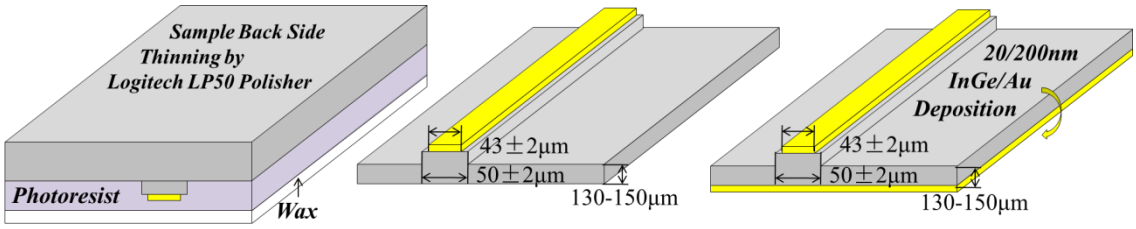

Figure 2-15: Substrate thinning and back contact deposition

- **Final Step: Cleaving / Mounting / Bonding**

The sample is now ready to be cleaved into certain lengths of broad area lasers for characterisation. As in Fig. 2-16, a quick and economical way to package the devices is

to mount them on AlO_2 ceramic tiles with Ag-containing indium paste at its eutectic temperature of 180°C on a hot plate. Then the Au/Zn/Au p-contact is wire-bonded to the lead-outs on the ceramic tile using an Ultrasonic Ball Bonder, such that the leads can be probed during test and not directly to the lasers.

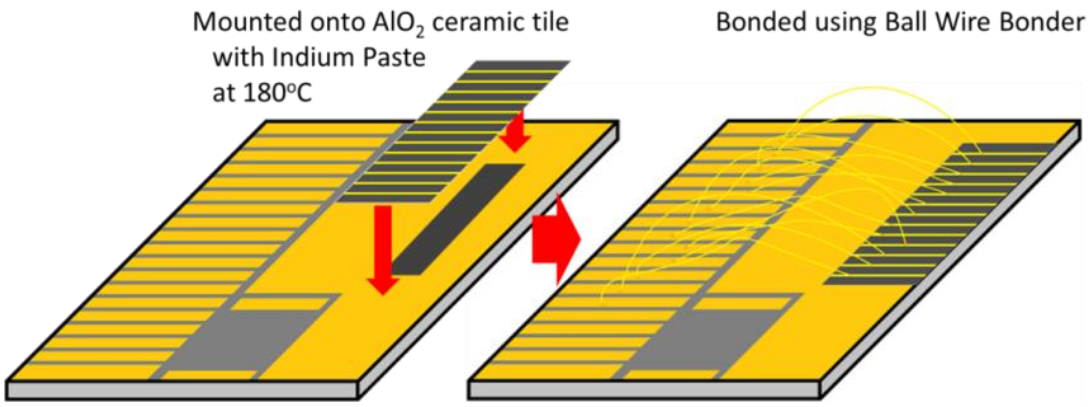

Figure 2-16: Sample packaging on AlO_2 ceramic tile

➢ Standard Fabrication Process II: MESA Diode Fabrication

The fabrication of MESA diodes is similar to the fabrication of broad area lasers. Firstly, the sample is cleaned and cleaved into a suitable size. A thermal evaporator is then employed for back contact In-Ge/Au deposition with a target thickness of 20nm/200nm respectively, followed by RTA annealing at 340°C with 30 seconds ramp and 3 seconds dwell, as in Fig. 2-17 (a).

Then the sample is patterned with 'CONTACT' mask (an array of annular contacts), by photoresist spin, exposure and development. Then a thermal evaporator is again employed for front contact deposition with a target thickness of 5nm/10nm/200nm Au/Zn/Au respectively. After resist removal, annealing is performed using the RTA at 360°C with 30 seconds ramp and 3 seconds dwell, as in Fig. 2-17 (b).

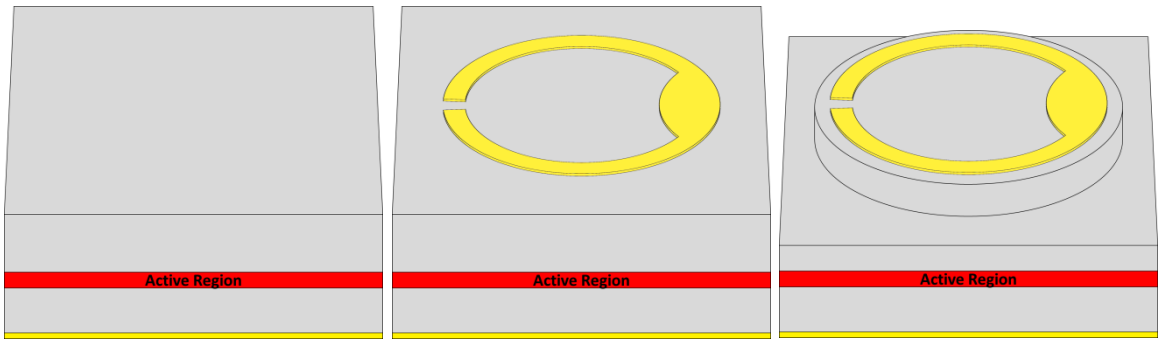

Figure 2-17: Fabrication process of mesa diode (a) back contact deposition, (b) front contact deposition and (c) mesa etching

Finally, the sample is patterned with 'MESA ETCHING' mask (photoresist spin, expose and develop). The sample is etched using a diluted 1-1-1 wet etchant with a target depth of 1~2μm, followed by photoresist removal, as in Fig. 2-17 (c).

The devices are then ready to be cleaved and mounted for characterisation, with the result being an array of electrically contacted cylindrical mesa diodes with an optical access aperture within the top contact. Such devices are useful in electrical characterisation (I-V) and characterisation of spontaneous emission spectra.

➢ Other Fabrication Techniques

In addition to the main fabrication methods described above, there are also a number of other important fabrication processes used in preparation of samples studied in this thesis.

- **PECVD**

Plasma-enhanced chemical vapour deposition (PECVD) is used for dielectric film deposition, e.g. silicon nitride and silicon dioxide. In the fabrication of devices with narrow contact stripes, where we do not wish to bond directly on top of (e.g. devices for

3μm ridge DFBs, as will be described in Chapter 3; devices for 3μm self-aligned stripe structures, as will be described in Chapter 4 and 5), a silicon nitride film was first deposited on the sample surface. Following this, windows were opened in the silicon nitride film on top of the ridge/stripe to form the electrical contact. With this treatment, the silicon nitride film serves as an electrical isolation layer which allows the bond-pad to be deposited close to the contact without shorting to the etched semiconductor surface below.

Also, dielectric deposition can be used for formation of anti-reflection (AR) facet coatings. Furthermore, silicon dioxide and titanium dioxide can be used to enhance the intermixing effect during selective area impurity free vacancy disordering of InGaAs quantum dots, as have been experimented in the preparation work for sampled grating distributed Bragg reflector laser (SGDBR) designs (Chapter 6).

- **AFM**

A Veeco Atomic-force microscopy (AFM), pictured in Fig. 2-18, was employed for characterising the grating resist pattern and the etched grating depth. AFM, as a type of scanning probe microscopy, is very-high-resolution (fractions of a nanometre) and therefore suitable for our requirement of measurement of typically 20nm depths.

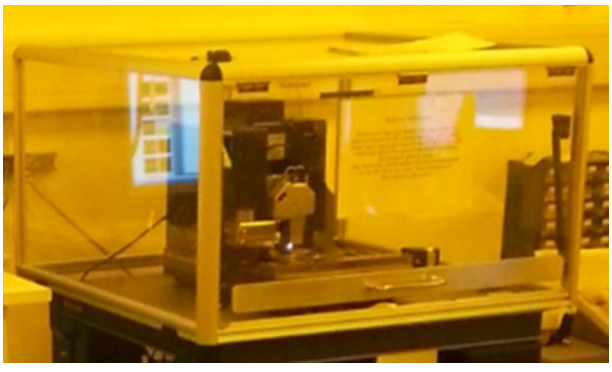

Figure 2-18: Veeco Atomic-force microscopy (AFM)

AMF was employed to measure the nanoscale etch depth in the process of grating fabrication. Fig. 2-19 presents some examples of grating AFM scans showing the etched grating patterns. Although mechanical errors exist in operation, e.g. x-y plane distortion due to sample movement caused by repeated back-and-forth movement of the tip, AFM was an effective and time-efficient method to examine the grating fabrication process.

(a)

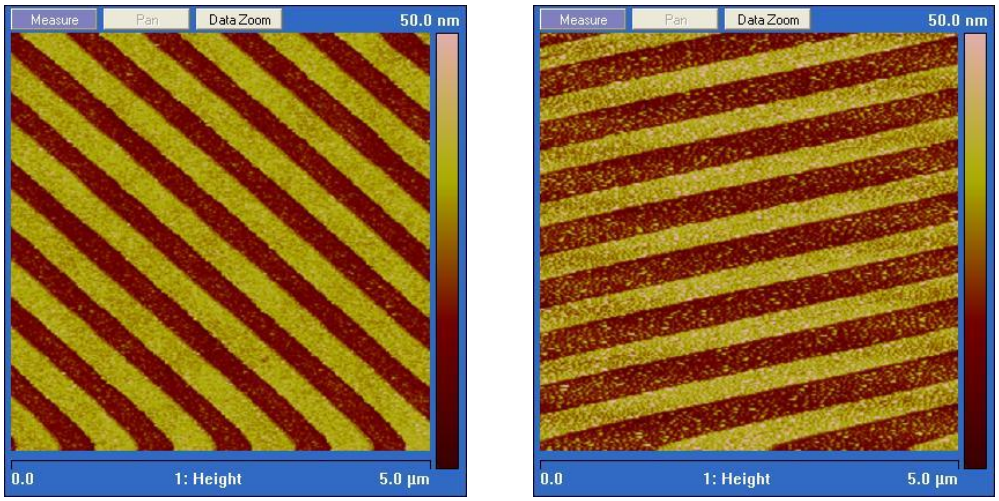

(b)

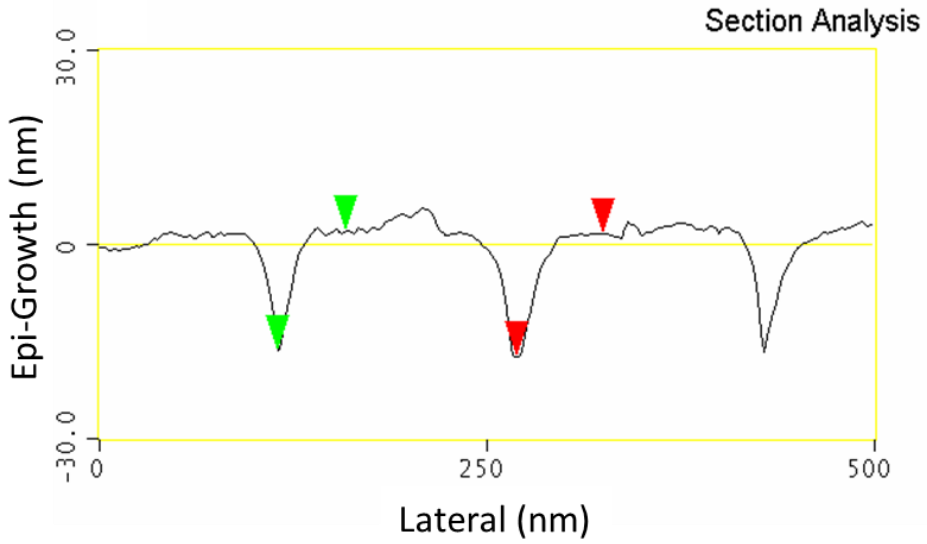

Figure 2-19: (a) Two exemplary grating scans taken by AFM and (b) an example of cross section measurement through the etched grating pattern

Fig. 2-19 (a) shows 2 examples of AFM scans of gratings, the yellow portion corresponds to the un-etched GaAs capping, while the brown portion corresponds to the etched InGaP grooves. A cross-section measurement, as in Fig. 2-19 (b), of the etching depth can determine whether the etching is sufficient or not. Should the grating depth be

insufficient, samples can undergo additional wet chemical etching until the target depth had been reached. In my design, with the top GaAs surface (capping) being robust to this selective etch, which can proceed without the PMMA pattern once the GaAs has been penetrated down into the InGaP layer, as will be described in detail in Chapter 3.

- **Facet Coating**

Facet coating is an important fabrication process for DFB lasers. AR facet coating on at least one side of the device is particularly necessary for the laser cavity to suppress the Fabry–Pérot modes from dominating the DFB mode. Whilst single layer Si_3N_4 or SiO_2 coatings can be applied using PECVD, in order to have high-quality facet coating (i.e. accurate reflectivity), the devices in Chapters 3, 4 and 5 were sent to Helia Photonics, a company (in Livingston, Scotland) specialising in optical coatings for light emitting semiconductor devices. AR (0.1%) and/or HR (95%) coatings were applied to the samples as required specifications, e.g. centred at 1050nm with 25nm bandwidth, based on device information, e.g. effective refractive index at facet and size specifications.

Sometimes, at the starting point of device characterisation, in order to obtain some primary characterisation results rapidly after device fabrication, a Si_3N_4 film was applied to cleaved facets as simple single-layer AR coatings using PECVD. The deposition thickness was calculated as ~125nm for a central wavelength of ~1000nm, using the quarter-wavelength equation, $d=\lambda/4\times n$, where n~2 is the refractive index of Si_3N_4 at 1000nm.

2.2.4 Device Characterisation

In order to quantitatively assess the quality, performance and characteristics of manufactured devices, a characterisation setup, pictured in Fig. 2-20, is available for experimental measurement. For a laser diode, the significant parameters include light output power versus injected current, lasing spectrum profile and far-field beam profile.

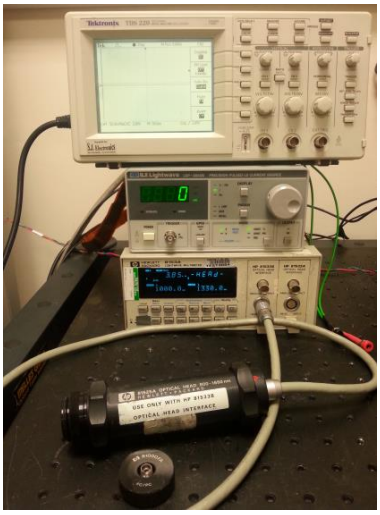

(a)

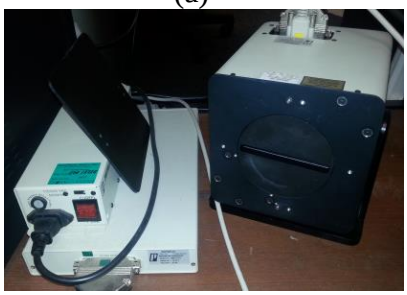

(b)

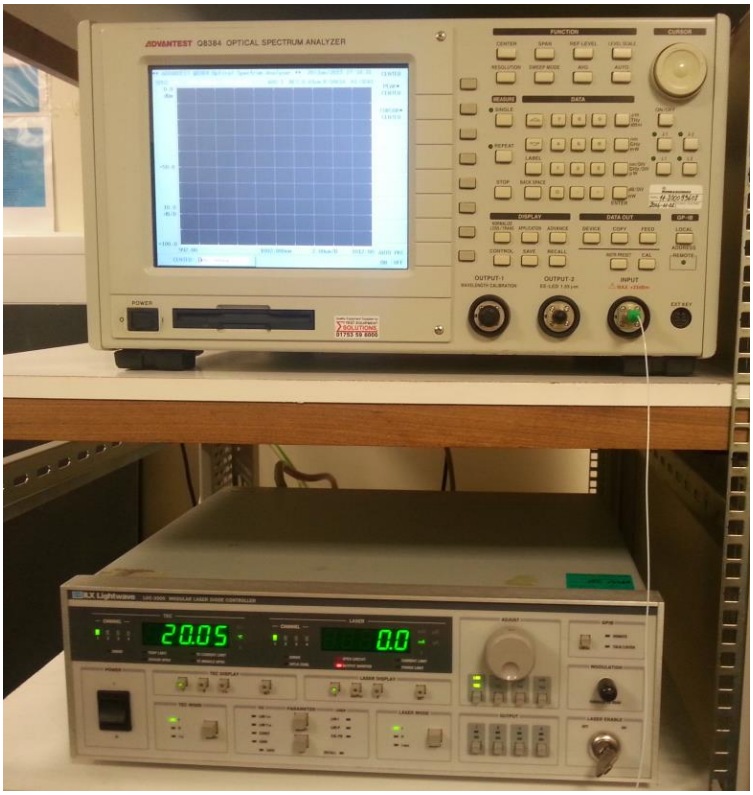

(c)

Figure 2-20: Characterisation setup (a) oscilloscope, pulsed power source and power metre connected to its power head (up to down), (b) far-field beam profiler (c) spectrum analyser and laser diode I/T controller (up to down)

➢ Light Output Power versus Injected Current

Many important characteristics of an optical device are revealed by measuring the light output with increasing current (L-I properties), which for a laser diode reveal

characteristics such as the lasing threshold, slope efficiency and linearity between the growth of power upon the increase of current [14]. A typical L-I curve is shown in Fig. 2-21, together with the I-V characteristic (i.e. the voltage required to generate this current).

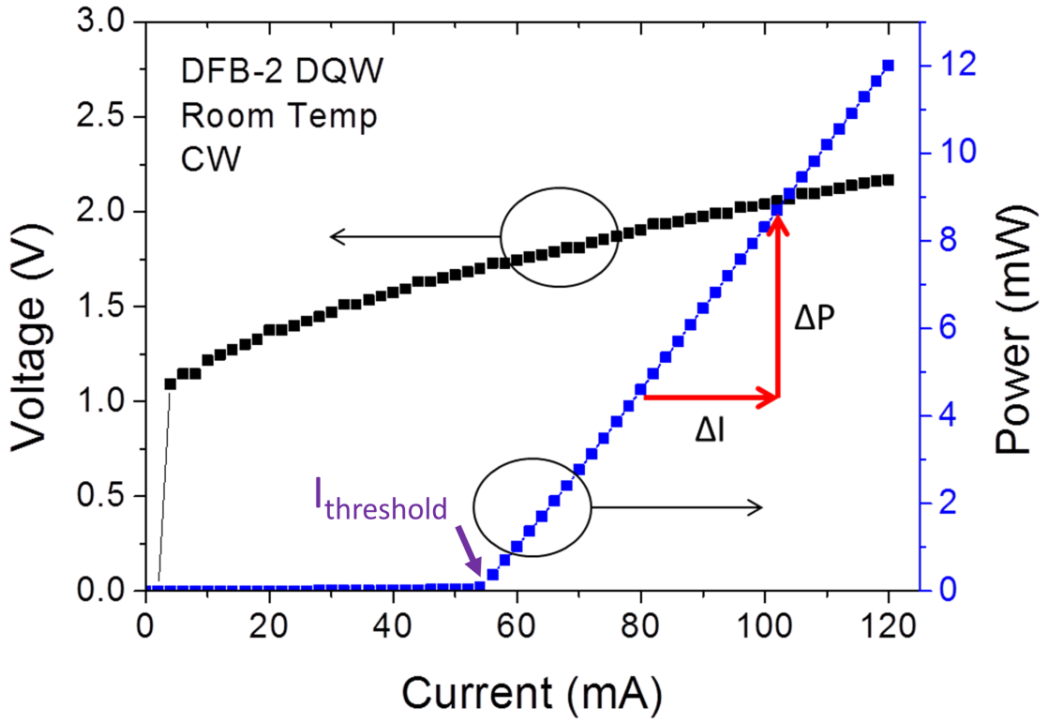

Figure 2-21: Example of L-I-V curve obtained from laser characterisation

- **Cavity Length Dependent Characterisation (η_i, α_i and J_0)**

Many of the performance characteristics of devices are measured, calculated and compared from the LI curves, for instance slope efficiency and threshold current. By measuring a laser structure with different cavity lengths, a cavity-length-dependent characterisation can be performed to (1) reveal the internal quantum efficiencies (η_i) and internal loss (α_i), by plotting the inverse external differential quantum efficiencies (η_d) as a function of the cavity length; (2) calculate the transparency threshold current density, J_0, by plotting the threshold current density, J_{th}, as a function of inversed cavity length [14].

- **Characteristic Temperature (T_0)**

For laser diodes, the device temperature might increase significantly when trying to achieve high output powers, which could impact negatively on lasing operation. For instance, an increase in the threshold current and a decrease in the slope efficiency are typically observed as temperature increases. By measuring a laser device at different operating temperature, a temperature-dependence characterisation can be performed to determine the characteristic temperature, T_0, which should be as high as possible for temperature insensitive operation [14].

➢ Lasing Spectrum Profile

The optical spectrum of a laser depends on its optical cavity and operating conditions (current and temperature) [14]. Ideally, for a DFB laser, the spectrum is composed of a single lasing mode, which is built up in optical feedback from a periodic variation of the structure (grating). This is different from the lasing spectrum of a conventional Fabry–Pérot laser, which is built up via optical feedback from front-back mirrors to form standing wave oscillation with F-P modes at the modes of the standing wave. Fig. 2-22 shows an example of the spectrum recorded from a 0.6mm cavity length DFB laser with 70mA CW pumping applied at room temperature.

The spectrum shows a robust single-mode lasing peak at 1000.8nm with a linewidth of 15.7pm (recorded with a resolution of 10pm) and an SMSR lager than 40dBm.

For different applications, the requirements of the spectrum vary significantly. For a DFB laser diode, not only does the lasing wavelength directly determine the potential of its application, but the side mode suppression ratio (SMSR) and the rate of thermal/current tuning are also important properties to study. Furthermore, due to the

thermal effect on the band gap energy (E_g) of semiconductors, the central wavelength of the gain spectrum red-shifts with an increase in operating temperature.

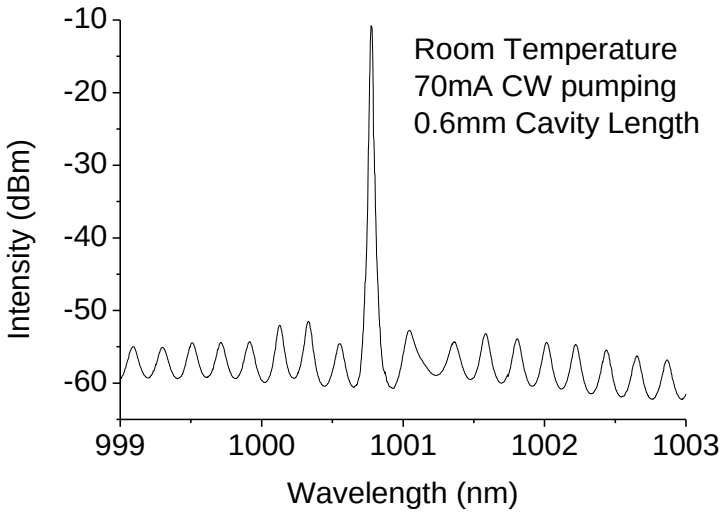

Figure 2-22: Example of the lasing spectrum recorded from a 0.6mm long DFB laser operating with 70mA CW injected current at room temperature

In DFB lasers, the lasing wavelength is stabilised and determined by the grating. Due to the temperature dependence of semiconductor refractive indices, this wavelength also shifts towards long wavelength. When pumped with a CW power source, self-heating of the device also contributes to the wavelength shift.

Controllable and well-defined tunability of a laser provides potential for many applications where a range of lasing wavelengths are needed. By measuring the spectrum of a device under different operating conditions (temperature and pumping current), the degree of thermal and current tunability of a DFB laser can be characterised.

➢ Far-Field Beam Profile

In addition to LI and spectral characteristics, the optical far-field beam profile of the light output of a device is important, both for free space and fibre-coupled applications. The far-field beam profile is measured by capturing the spatial intensity of a laser beam

on a plane perpendicular to the propagation direction. Fig. 2-23 shows an example far-field measurement recorded for a 3mm long DFB laser. The result is displayed in both 3-D and 2-D forms and both illustrate a single lateral mode operation. Axial cross-sections may be obtained, giving both fast- and slow- axis divergence angles, associated with these asymmetric beams.

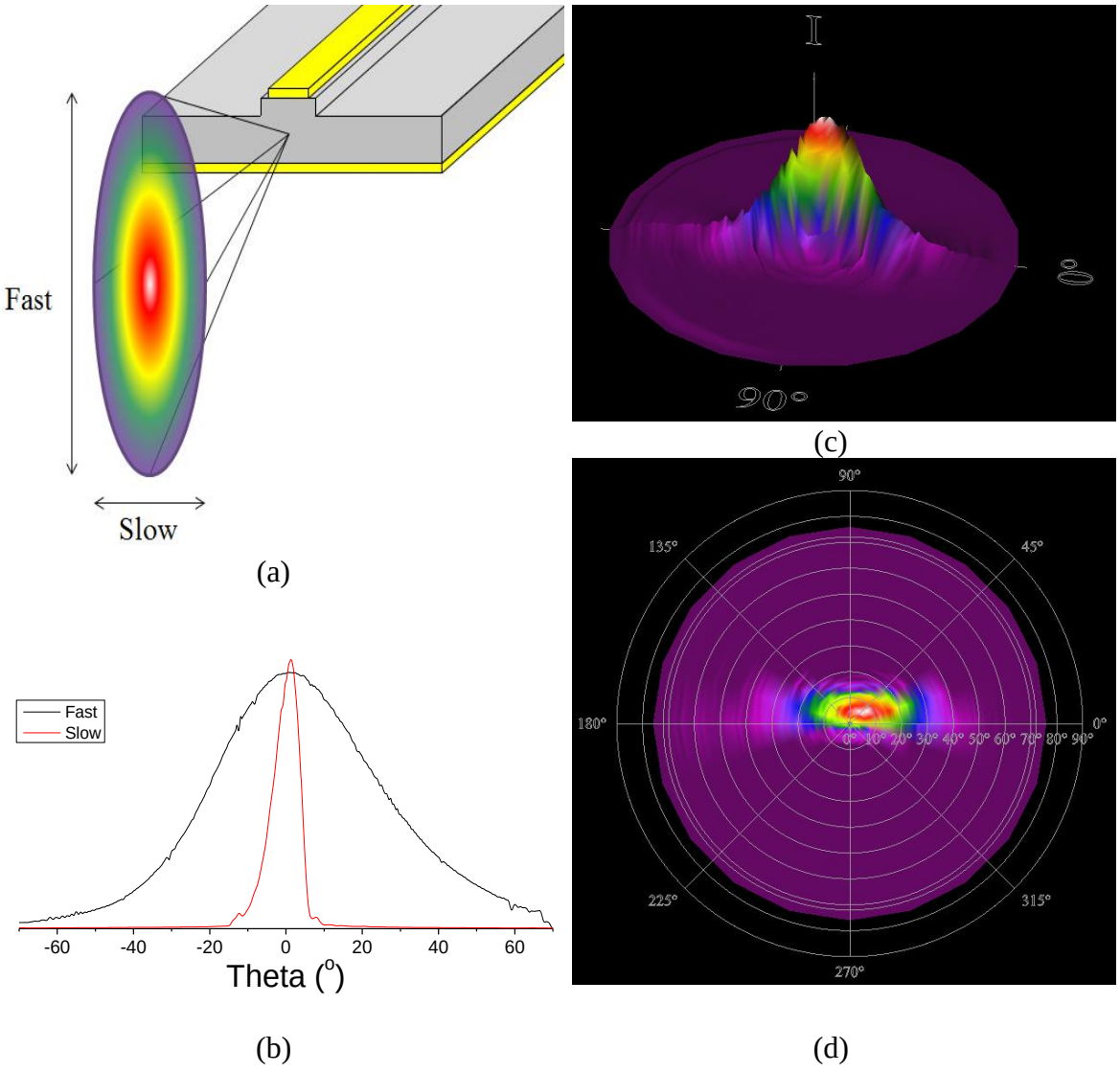

Figure 2-23: Example of beam profile of a ridge DFB laser (a) schematic diagram of divergence of output beam, (b) fast- and slow- section plots, (c) 3-D view and (d) front view

Furthermore, the near-field beam profile of a waveguide can be inferred from that of its resultant far-field. Hence, the measurement of the far-field beam profile of a device is also useful to detect if the device operates via its fundamental optical mode or via higher order lateral modes.

➢ Characterisation Setup Overview

An overall schematic diagram of my characterisation setup is shown in Fig. 2-24. The setup consists of a device driving unit, a probe station on a temperature-controlled platform with 3 detection schemes: (1) light output power measurement, (2) electroluminescence spectrum analysis and (3) far-field beam profile unit. These will be described separately in the following sections.

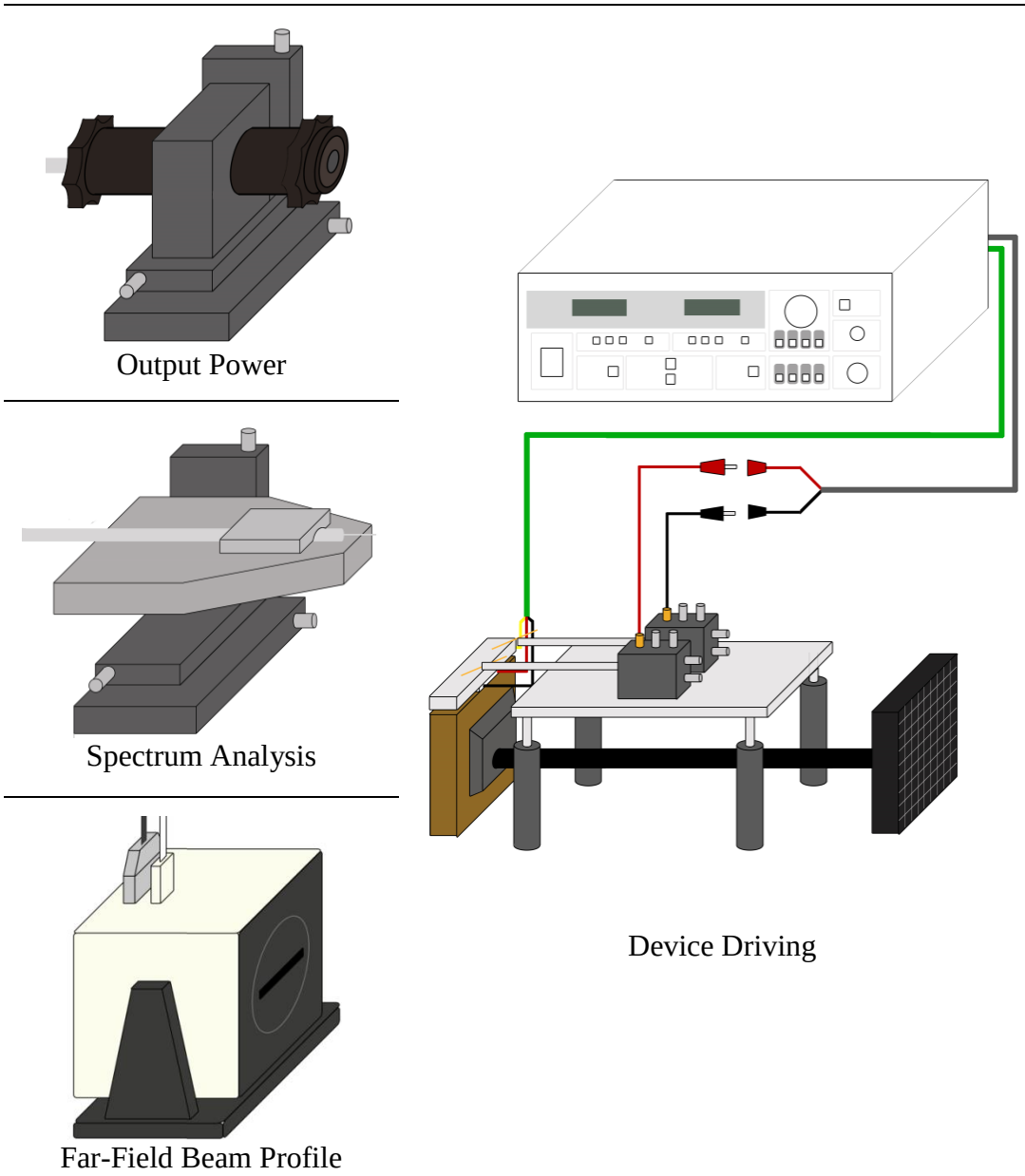

Figure 2-24: Schematic diagram: an overview of device characterisation setup

- **Device Driving Unit**

As illustrated in Fig. 2-25, samples were placed on the temperature controlled copper block, underneath which a Peltier thermo-electric cooling (TEC) element is placed. A Lightwave LDC-3900 Modular Laser Diode Controller controls the temperature by adjusting the driving current of the TEC according to the real-time monitoring of the substrate temperature using a thermistor. The operational temperature range of this setup is 15^{o}C to 75^{o}C. For continuous-wave (CW) operation measurement, the p-contact and n-contact of the device are also connected to the LDC-3900 controller (39440 module installed) through probes. The operational CW driving current range is 0mA to 2000mA with an 8 Watt TEC controller [15].

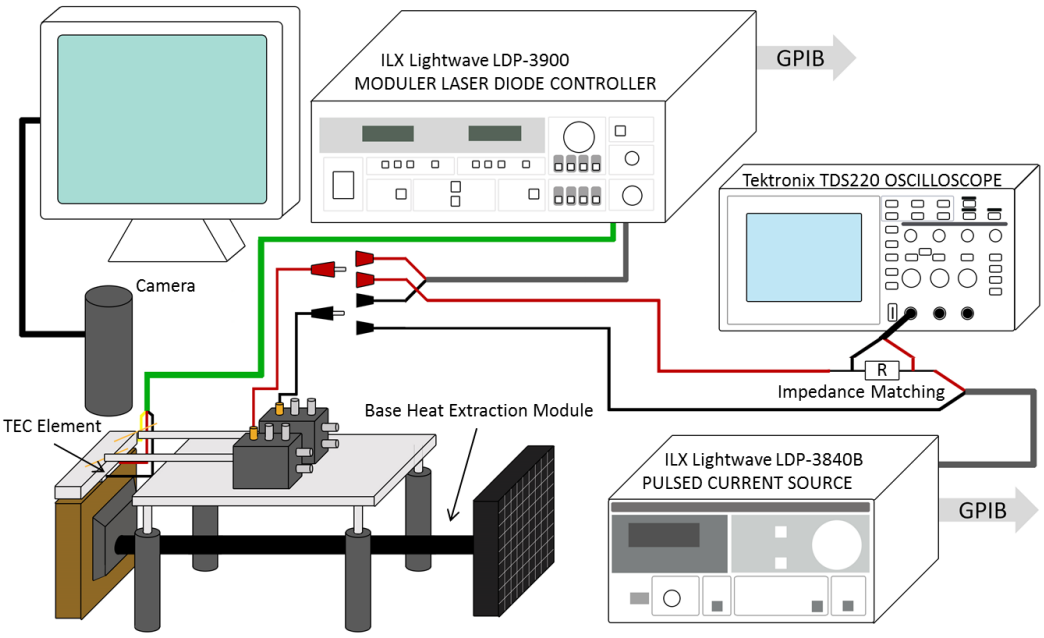

Figure 2-25: Schematic diagram: device temperature control and current driving

As illustrated, a Lightwave LDP-3840B Precision Pulsed LD Current Source is also available as an alternative current source. It is usually used for devices that require a high injection current (>1A) or of high resistance due to growth or fabrication imperfections, where CW pumping causes significant self-heating of the device. In practice, due to transmission line effects, an impedance matching resistor ($R_{mathcing}$ +

R_{device} = 50Ω) is connected in series to achieve good pulsed profile [16] [17]. During measurement, the pulsed wave is monitored by a Tektronix TDS 220 Digital Real-Time Oscilloscope by checking the voltage applied on the impedance matching resistor. The operational driving range is 0mA to 3000mA with a set point resolution of 1mA [16].

- **Light Output Power Measurement**

The light output power of a device is measured through a Hewlett Packard (HP) 81525A Power Head (5mm InGaAs sensor [18]), which is connected via an HP 81533B Power Head Interface to a HP 8153A Lightwave Multimeter.

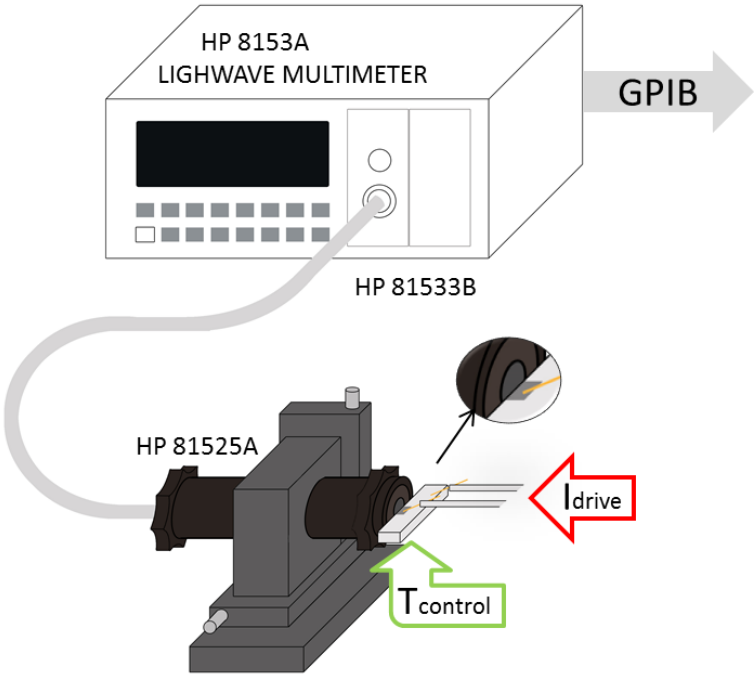

Figure 2-26: Schematic diagram: emission output power measurement

The measurement wavelength range is 800nm to 1650nm and the power range is +3 to -70dBm [18]. The power head is fixed onto a XYZ-stage for the ease of alignment while testing. To plot the light output against current and voltage against current measurement, I used LabVIEW to control both the power meter and the CW (or pulsed) current driver through GPIB cables. In cases when the pulsed current source is used, the

measured value of power is a time-averaged value. Therefore it is automatically multiplied by the inverse duty cycle, for example, if the duty cycle is set to be 1%, the measured power is multiplied by 100. In effect, this represents the power that would be attained in the absence of self-heating.

- **Electroluminescence Spectrum Measurement**

For measurement of the optical emission spectrum, the light wave from the front facet of an operating device is collected by a multimode fibre, which is fixed on an XYZ-stage.

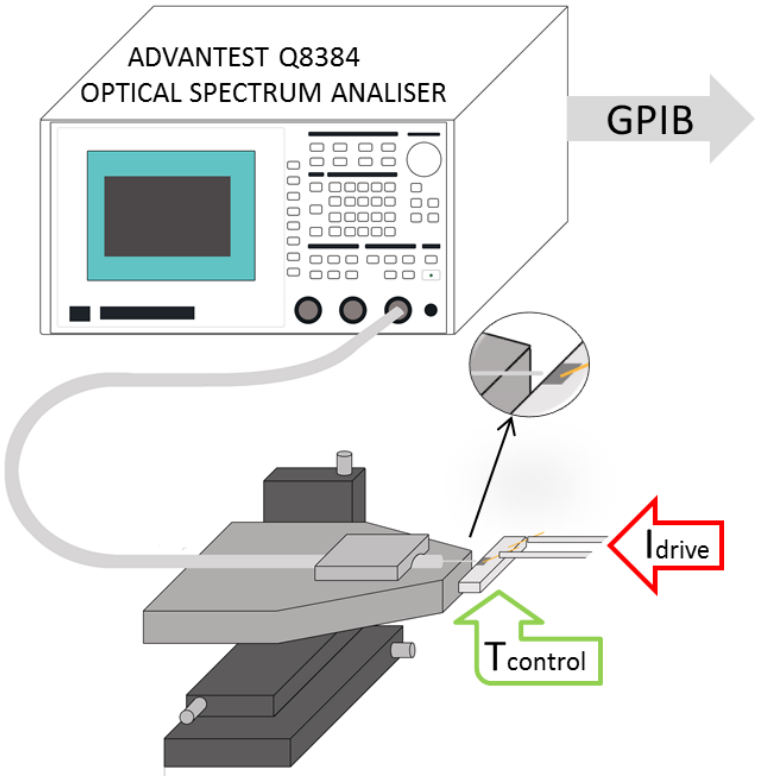

Figure 2-27: Schematic diagram: emmision spectrum investigation

During measurement, the fibre is precisely aligned with its facet being located sufficiently close to the facet of the device under test. The collected light is fed into an Advantest Q8384 Optical Spectrum Analyser (OSA). The available wavelength range is from 600nm to 1700nm with a resolution of 10pm [19].

The OSA is also connected to a PC via a GPIB cable and is remotely controlled using LabVIEW software. Emission spectra can be recorded under different driving currents and/or temperatures.

- **Far-Field Beam Profile Measurement**

A Photon-Inc Goniometric Radiometer LD8900R/IR/10 is employed for far-field beam profile measurement. It is controlled using the supplied PC software through RS-232 controller and Digital I/O Interface 880GSX.

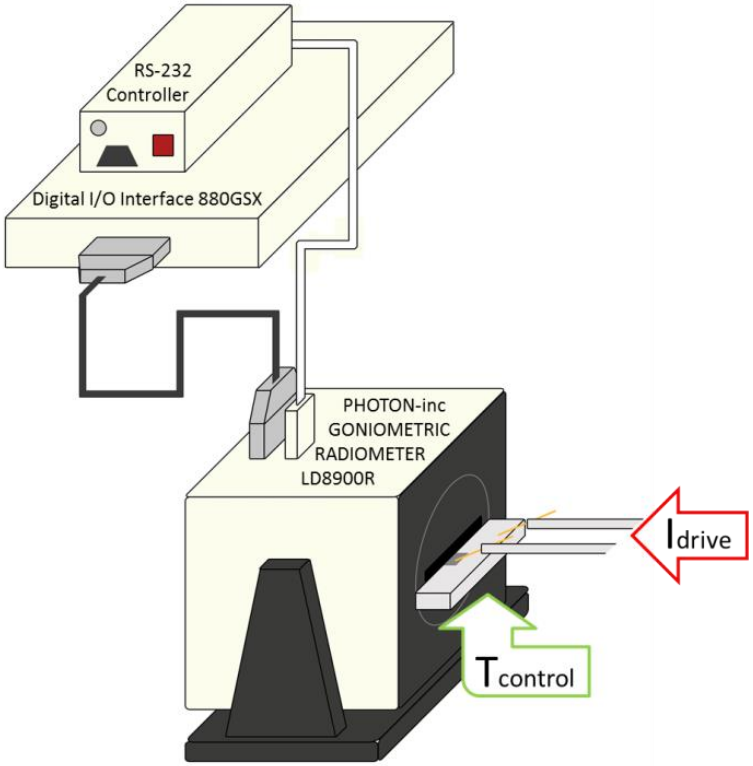

Figure 2-28: Schematic diagram: far-field beam profile measurement

The setup characterises real-time angular radiation intensity of the input light to provide 2-D (horizontal and vertical) or 3-D measurement of the beam profile with a viewing range of $\pm 72^{o}$ (0.055^{o} resolution) [20]. Data is then exported as ".asc" files for further analysis.

2.3 Reference

[1] H. Kogelnik and C. V. Shank, "Coupled-Wave Theory of Distributed Feedback Lasers," *Journal of Applied Physics*, vol. 43, no. 5, pp. 2327–2335, 1972.

[2] G. Morthier and P. Vankwikelberge, *Handbook of distributed feedback laser diodes*. Boston: Artech House, 2013.

[3] F. Rana, "Chapter 13 Distributed Feedback (DFB) Structures and Semiconductor DFB Lasers," class notes for ECE 5330 Semiconductor Optoelectronics, Cornell University, 2011. [Online]. Available: https://courses.cit.cornell.edu/ece533/, Accessed on: 10 December 2012.

[4] K. David, G. Morthier, P. Vankwikelberge, R. G. Baets, T. Wolf and B. Borchert, "Gain-coupled DFB lasers versus index-coupled and phase shifted DFB lasers: a comparison based on spatial hole burning corrected yield," *IEEE Journal of Quantum Electronics*, vol. 27, no. 6, pp. 1714-1723, June 1991.

[5] X. Pan, H. Olesen and B. Tromborg, "Spectral linewidth of DFB lasers including the effects of spatial holeburning and nonuniform current injection," *IEEE* Photonics Technology Letters, vol. 2, no. 5, pp. 312-315, May 1990.

[6] K.-Y. Tu, T. Tamir and H. Lee, "Multiple-scattering theory of wave diffraction by superposed volume gratings," *Journal of the Optical Society of America A*, vol. 7, no. 8, p. 1421-1435, January 1990.

[7] B. J. Stevens, K. M. Groom, J. S. Roberts, P. W. Fry, D. T. D. Childs and R. A. Hogg, "Distributed feedback laser employing buried GaAs/InGaP index-coupled grating," *Electronics Letters*, vol. 46, no. 15, pp. 1076-1077, July 2010.

[8] D. R. Pendse, A. K. Chin, F. P. Dabkowski and J. E. M. Clausen, "Reliability comparison of GaAlAs/GaAs and aluminum-free high-power laser diodes," *Proc. SPIE 3547 Semiconductor Lasers III*, vol. 3547, 1998.

[9] *Fimmwave version 5.2*. Photon Design Ltd. Oxford, OX4 1TW, UK, 2009.

[10] A. S. Sudbo, "Film mode matching: a versatile numerical method for vector mode field calculations in dielectric waveguides," *Pure Applied Optics*, vol. 2, no. 3, pp. 211-233, 1993.

[11] A. S. Sudbo, "Numerically stable formulation of the transverse resonance method for vector mode-field calculations in dielectric waveguides," *IEEE Photonics Technology Letters*, vol. 5, no. 3, pp. 342-344, March 1993.

[12] D. J. Mowbray, "Lecture 14 – Nanostructure based devices – Interband lasers," class notes for PHY6002 Inorganic Semiconductor Nanostructures, University of Sheffield, 2013.

[13] A. Krysa, B. Harrison and D. Morris. *Metalorganic Chemical Vapour Deposition of Arsenide and Phosphide Materials*, 2015. [Online]. Available: http://www.epsrciii-vcentre.com/wp-content/uploads/2015/04/MOCVD_AsP_Capabilities_v1.1.pdf, Accessed on: 10 January 2017.

[14] K. S. Mobarhan, "Test and Characterization of Laser Diodes: Determination of Principal Parameters," *Newport Corporation Technical Publication - Application Note No. 1*, 1995.

[15] ILX Lightwave Corporation, *User's Guide Modular Laser Diode Controller LDC-3900*. [Online]. Available: https://assets.newport.com/webDocuments-EN/images/70011310_LDC-3900_IX.pdf, Accessed on: 10 January 2017.

[16] ILX Lightwave Corporation, *User's Guide Pulsed Current Source LDP-3840B*. [Online]. Available: http://assets.newport.com/webDocuments-EN/images/70037902%20LDP-3840B.PDF, Accessed on: 10 January 2017.

[17] D. Hodgson, K. Noonan, B. Olsen and T. Orosz, "#11 Pulsing a Laser Diode," *ILX Lightwave Application Note*, 2004.

[18] Agilent Technologies, *Agilent 8153A Lightwave Multimeter Technical Specifications*. [Online]. Available: http://cp.literature.agilent.com/litweb/pdf/5962-9321E.pdf, Accessed on: 10 January 2017.

[19] Advantest Corporation, *Q8384 Optical Spectrum Analyser Operation Manual*. [Online]. Available: https://www.advantest.com/documents/11348/146687/pdf_mn_EQ8384_OPERATING_MANUAL.pdf, Accessed on: 10 January 2017.

[20] Photon Ophir Photonics, *Beam Analysis*. [Online]. Available: http://www.ophiropt.com/user_files/laser/beam_profilers/LD-8900.pdf, Accessed on: 10 January 2017.

Chapter 3. GaAs-Based Narrow Ridge Distributed Feedback Lasers

Semiconductor lasers are used as light sources in many of today's optical applications. This is because of their many advantages over alternatives, including their compact size, efficient and reliable operation, and its economic cost. In a traditional Fabry–Pérot laser, the laser oscillation is achieved by the optical feedback from cleaved facets. However, in applications where highly coherent light is needed, such as spectroscopy or fibre optics communication, traditional semiconductor lasers are no longer suitable due to their low spectral stability and purity resulting from the formation of the resonant cavity, where a range of wavelengths are supported simultaneously. For such applications, selection of a single longitudinal mode is required.

In distributed feedback lasers (DFB), optical feedback is obtained from a periodic corrugation along the path of optical propagation. A grating is fabricated through periodic modulation in refractive indices (index-coupled) or gain (gain-coupled), so that a single longitudinal mode is selectively fed back within the broad gain spectrum. In my research, overgrown index-coupled DFB laser structures have been designed, fabricated and characterised. The grating was formed using two materials, GaAs and InGaP, which provide periodical variation of the refractive index.

DFB lasers are potential for applications based on TDLS (tunable laser diode spectroscopy) [1] [2] due to their narrow linewidths and sufficiently high SMSR. The

modulation of a single mode DFB laser can also be used as the signal generation unit in many applications, for example in an all-optical packet switching system [3].

This chapter starts with a description the initial 2×QWs DFB structure [4] in Section 3.1.1. Then, from the initial DFB design, structural modification and simulation are presented in detail in Sections 3.1.2 and 3.1.3. Further, Section 3.2 introduces the preparation work that was conducted prior to DFB lasers being manufactured, including comparison of (1) performance of broad area lasers fabricated from material grown by MOVPE and MBE and (2) performance of mesa diodes and broad area lasers fabricated from MOVPE grown material with 2×, 4× and 6× QWs. Then Section 3.3 describes the four-stage manufacture process of the DFB lasers, followed by characterisation, analysis and discussion in Section 3.4.

3.1 DFB Simulation

The starting point for this study was the DFB structure described in [4]. The initial structure, as described in Table 3-1, consisted of an active region of 2× $In_{0.17}Ga_{0.83}As$ QWs separated by 20 nm GaAs and an InGaP/GaAs grating layer (thickness: 20nm; period: 148nm) grown 470nm above the active region.

In this report, a 1mm long 3μm wide ridge laser with as-cleaved facets (i.e. uncoated) demonstrated a threshold of 62mA with CW injection. At 93mA, the output power reached 7.9mW with an SMSR of 28.3dB. I started this research based on this initial structure.

	Layer	Thickness	Material
Overgrowth	Contact	200nm	GaAs
	Upper Cladding	530nm	$Al_{0.42}Ga_{0.58}As$
	In-Fill	50nm	GaAs
Planar Growth		10nm	GaAs
	Grating	20nm	$In_{0.49}Ga_{0.51}P$
		25nm	GaAs
	Upper Cladding	470nm	$Al_{0.42}Ga_{0.58}As$
	Core: QWs	50nm	GaAs
		7.6nm	$In_{0.17}Ga_{0.83}As$
		20nm	GaAs
		7.6nm	$In_{0.17}Ga_{0.83}As$
		50nm	GaAs
	Lower Cladding	1000nm	$Al_{0.42}Ga_{0.58}As$
	Buffer	500nm	GaAs

Table 3-1: Layer details of the initial DFB structure in [4]

Unlike traditional Fabry–Pérot lasers, the analysis of the optical mode in DFB lasers employs coupled wave theory. Kogelnik and Shank [5] pointed out one problem of AR-coated index-coupled DFB lasers is the degeneracy into dual-mode operation, i.e. on both sides of the Bragg wavelength. One solution to this is the introduction of a λ/4 phase shift. However, such a structure, referred to as a quarter-wave shifted structure, suffers from high spatial hole-burning (SHB) at the phase-discontinuity point [6] [7]. The non-uniform carrier density is a result of non-uniform power density, which further results in unstable single longitudinal mode operation [8] and increase of the linewidth [9]. Although the SHB can be reduced to some extent by modulating the stripe width [10], such structures still suffer from higher complexity with respect to their manufacture.

The purposes behind the study in this chapter were to fine-tune the capability to accurately simulate the waveguide and grating coupling using Fimmwave and to attempt to optimise the lasing performance compared to the original design in [4], with a view to realisation of high power and high performance DFB lasers.

3.1.1 Fimmwave – Waveguide Modelling Software

Fig. 3-2 shows an exemplary simulation of my first DFB structure. As annotated, a grating of a varied thickness was designed to be manufactured in the upper cladding (P-$Al_{0.42}Ga_{0.58}As$) with a separation of varied distance above the active region. In terms of waveguide design, the grey areas were the areas to be etched away in order to form the ridge. The ridge width was fixed to be 3µm in order to achieve single lateral mode operation. The etching depth was designed to be ~1.5µm inbetween grating and active region. The contour plotting represents the intensity profile of the simulated guided optical mode.

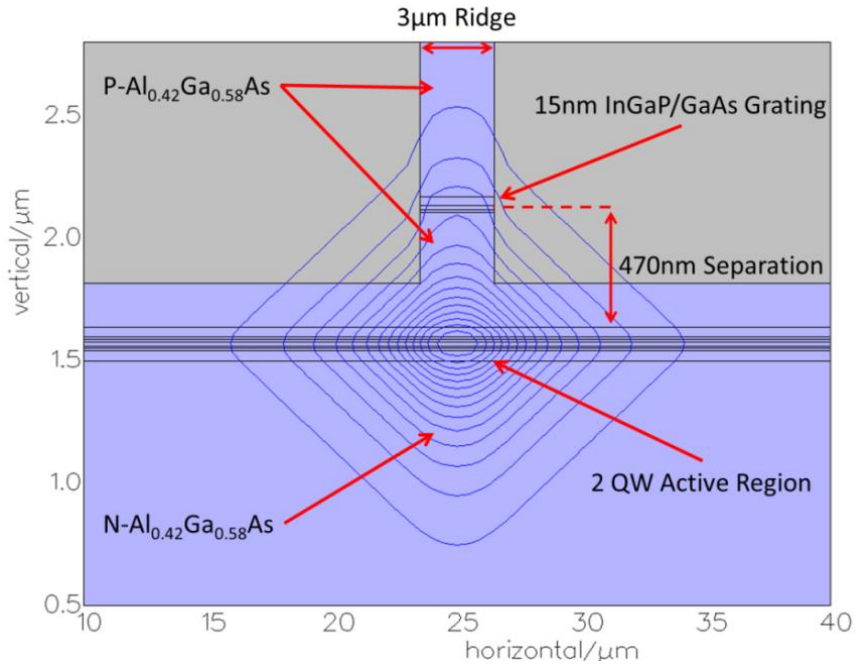

Figure 3-1: DFB-1: 2×QWs, 470nm separation and 15nm grating thickness

One important parameter that can be obtained from waveguide simulation is the confinement factor in the grating layer, which allows the calculation of its coupling coefficient (*K*) through the equation:

$$\Gamma_g = \frac{K\lambda_B}{2(n_1 - n_2)}$$

λ_B is the DFB wavelength, and n_1 and n_2 are the refractive indices of GaAs and InGaP (3.51 and 3.15 at 1000nm respectively). The simulated confinement factor for the initial structure was 0.001358, corresponding to a K~10cm^{-1}, which makes KL=1 for a 1mm device.

3.1.2 Strain-Balanced QW Design

As mentioned at the beginning of this section, the aim of the design was not only to fine-tune the capability of tailoring the waveguide using Fimmwave, but also seeking optimisation (in terms of power and SMSR) of the original DFB structure. One way to achieve high power lasing is to cleave longer devices. But this would limit the performance (longer grating means higher possibility of defect incorporation and reduces efficiency) and application potential (many applications are not suitable for long devices, for example high-speed modulation) of my design. Therefore, in addition to variation of the grating thickness and distance from the active region for 2×QWs designs, additional QWs were added to my structure in order to achieve higher gain in the core. So I included another 2 structures into the overall design theme, which had 4× and 6× QWs in the active region respectively. Furthermore, it was expected that a higher differential gain offered by additional number of QWs could potentially support a higher direct modulation speed.

However, when growing $In_{0.17}Ga_{0.83}As$ QWs within GaAs separations (barriers), the mismatch in lattice constants between the two materials causes strain in the layers. When growing 2×QWs in the structure, the effect of the strain is not significant.

However, when stacking 4× and 6× QWs, the strain effect significantly influences the quality of growth [13]. Therefore, instead of only using GaAs spacer layers between the QWs, the 10nm of GaAs on either side of the $In_{0.17}Ga_{0.83}As$ QWs was substituted with $GaAs_{0.885}P_{0.115}$. The lattice constant of $In_{0.17}Ga_{0.83}As$ is higher, which is higher than that of GaAs than that of $GaAs_{0.885}P_{0.115}$. Therefore, to some extent, by sandwiching $In_{0.17}Ga_{0.83}As$ with $GaAs_{0.885}P_{0.115}$ layers we can balance the induced strain.

In the process of growing lattice-mismatched materials, the accumulation of strain is positively correlated to the product of growth thickness (d) and strain rate (ε). In my design, as illustrated in Fig. 3-2, in each repeating unit, a 7.6nm InGaAs QW is sandwiched by two 10nm GaAsP barriers. Fig. 3-3 presents the schematic diagram of the energy band diagram of this structure.

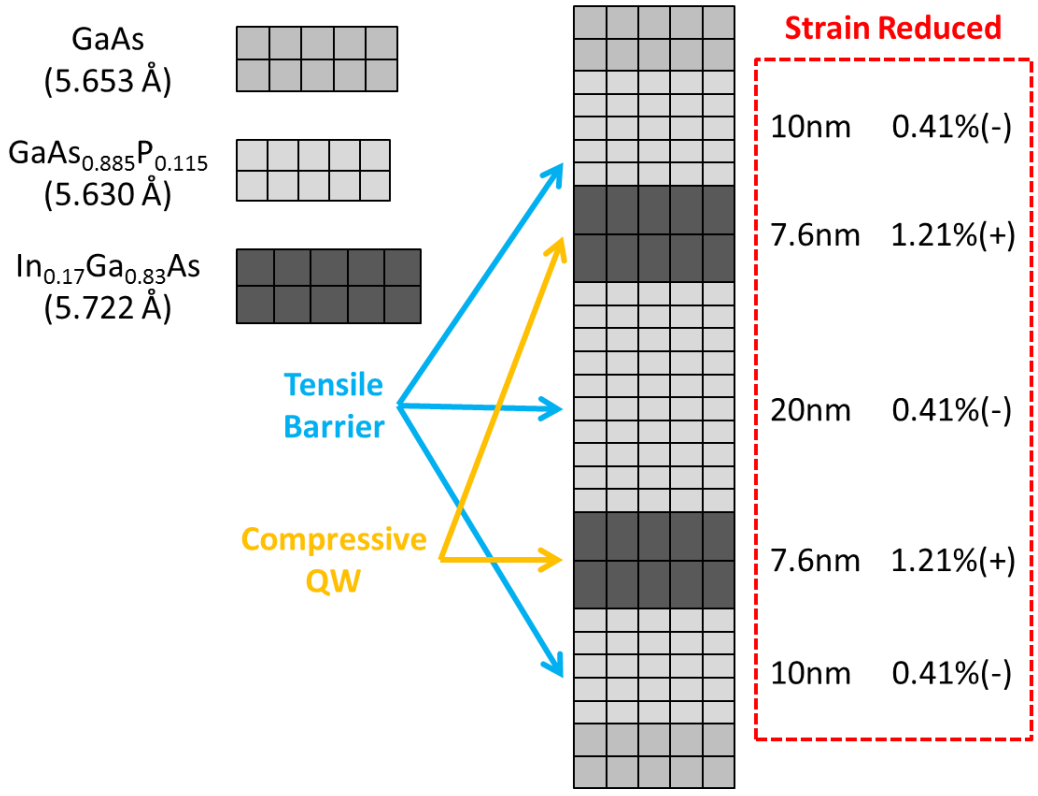

Figure 3-2: Compensation of compressive strain induced by InGaAs QWs

The lattice constant of GaAs is 5.653Å and that of $In_{0.17}Ga_{0.83}As$ is approximately 5.722Å, where the strain rate, $\varepsilon_{(InGaAs \rightarrow GaAs)}$, is ~ 1.21%(+). The lattice constant of

$GaAs_{0.885}P_{0.115}$ is approximated to be 5.630Å and its strain rate to GaAs, $\varepsilon_{(GaAsP \rightarrow GaAs)}$, is then ~ 0.41%(-). Therefore, for each unit, the determining factor of compressive strain induced by InGaAs QW is: $d_{(InGaAs)} \times \varepsilon_{(InGaAs \rightarrow GaAs)} = 9.2(+)$, whilst that of the tensile strain induced by GaAsP barriers is: $d_{(GaAsP)} \times \varepsilon_{(GaAsP \rightarrow GaAs)} = 8.2(-)$.

This mathematically shows the compensation (9.2 ~ 8.2) of strain effect in the structure design. Since the structure is still slightly compressively strained (9.2 > 8.2), one can expect that when stacking more number of QWs (2× → 4× → 6×), the effect of strain will become more significant, thereby influencing the properties of the devices.

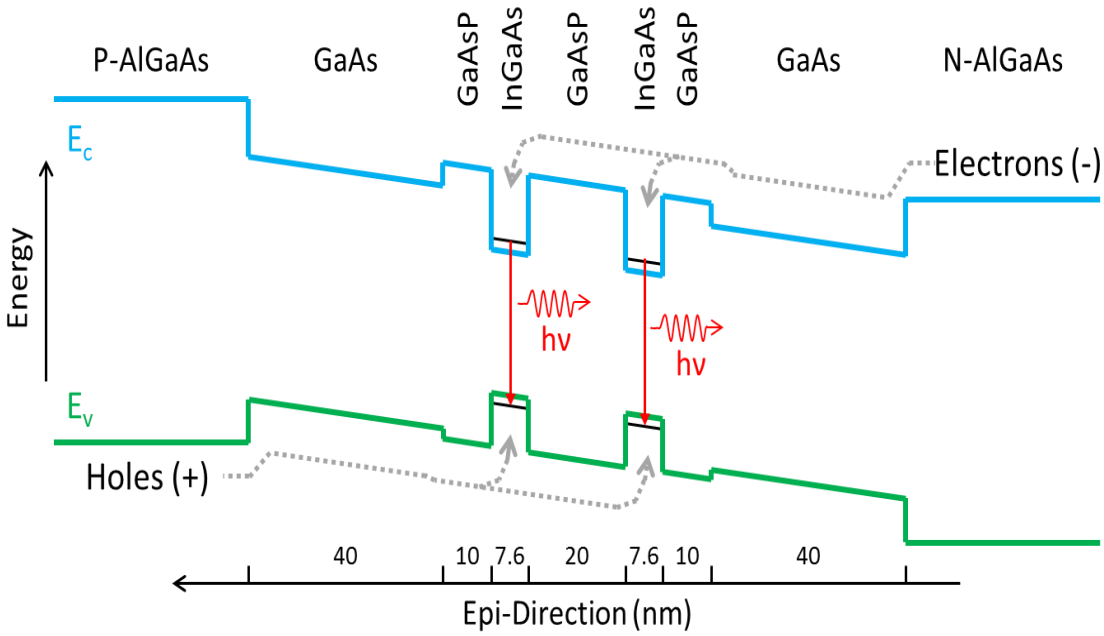

Figure 3-3: Energy band diagram of the strain-balance structure design

3.1.3 Design and Simulation

In order to control the variables in the complete set of structures, I modified the original structure from [4] and added GaAsP strain-balancing layers for all the 2×, 4× and 6× QWs structure designs, as illustrated in Fig. 3-4.

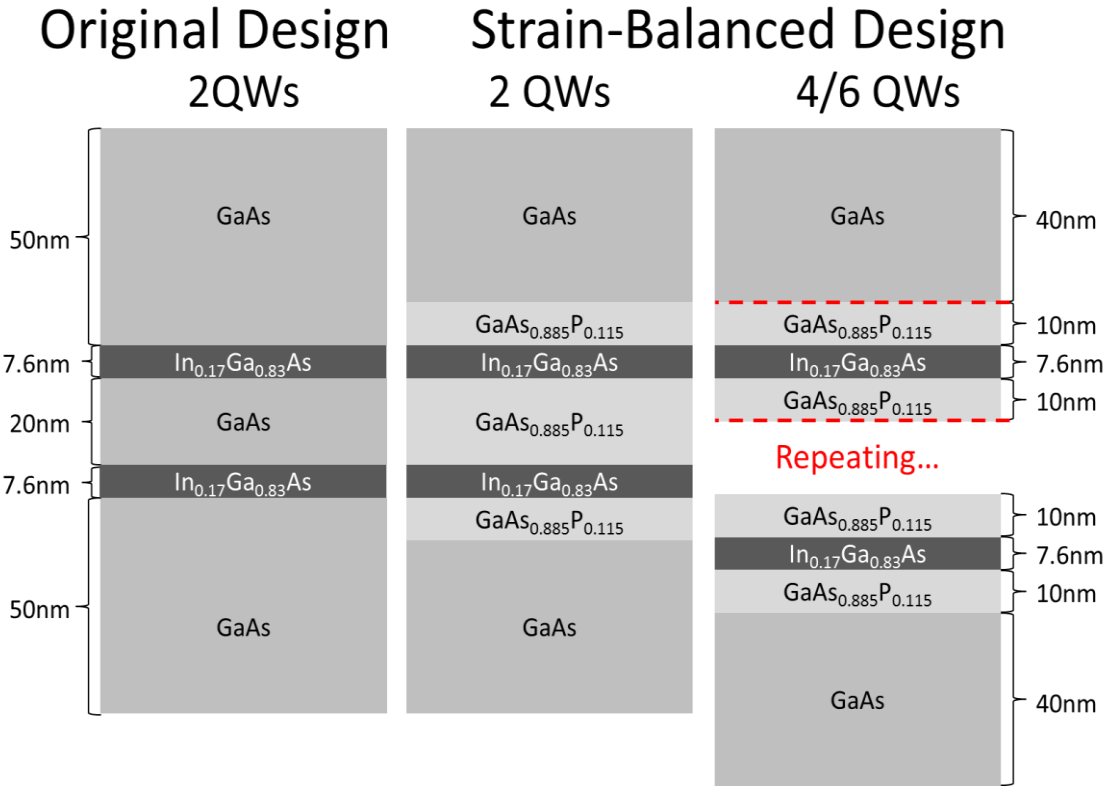

Figure 3-4: Strain-balanced design for 2×, 4× and 6× QWs active region

Based on this initial structure, I simulated 5 DFB structures with variation in the following 3 aspects: (1) thickness of grating (DFB1~DFB3), (2) separation between grating and active region (DFB1~DFB2) and (3) number of quantum wells in the active region (DFB2, 4, 5). Table 3-2 shows the layer details of the 5 DFB structures.

By adjusting (1) and (2), coupling in the structure can be modified. Adjusting (3) will affect the gain, as well as the coupling, and hence grating thickness and space for these structures were designed to maintain a constant confinement factor in the grating. For example, the 3 variations designed for the initial structure were: 15nm grating, 470nm separation and 2 QWs.

DFB 2 and DFB 3 are both based on DFB 1, the initial structure, with one variable changed in each. As illustrated, DFB 2 has 500nm separation instead of 470nm resulting in a decrease of confinement factor in the grating, Γ_g, from 0.001358 (DFB 1) to 0.000963 (DFB 2). DFB 3 has 20nm grating thickness instead of 15nm causing an

increase of confinement factor from 0.001358 (DFB 1) to 0.001694 (DFB 3). Fig. 3-5 illustrates the waveguide simulation of DFB 2 and DFB 3.

Layer	Thickness	Material	DFB1	DFB2	DFB3	DFB4	DFB5
Contact	300nm	GaAs	-	-	-	-	-
Upper Cladding	850nm	$Al_{0.42}Ga_{0.58}As$	-	-	-	-	-
In-Fill	40nm	GaAs	-	-	-	-	-
	12nm	GaAs	-	-	-	-	-
Grating	(varied)	$In_{0.49}Ga_{0.51}P$	15nm	15nm	20nm	20nm	25nm
	12nm	GaAs	-	-	-	-	-
Upper Cladding	(varied)	$Al_{0.42}Ga_{0.58}As$	470nm	500nm	470nm	400nm	340nm
Barrier	40nm	GaAs	-	-	-	-	-
Core: QWs	10nm	$GaAs_{0.885}P_{0.115}$	Repeat ×2	Repeat ×2	Repeat ×2	Repeat ×4	Repeat ×6
	7.6nm	$In_{0.17}Ga_{0.83}As$					
	10nm	$GaAs_{0.885}P_{0.115}$					
	…						
Barrier	40nm	GaAs	-	-	-	-	-
Lower Cladding	1200nm	$Al_{0.42}Ga_{0.58}As$	-	-	-	-	-
Buffer	500nm	GaAs	-	-	-	-	-
Confinement Factor in Grating ($\times 10^{-3}$)			1.358	0.963	1.694	0.962	0.936
Confinement Factor in QWs ($\times 10^{-3}$)			25.397	21.628	25.048	44.526	62.429

Table 3-2: Layer details of five simulated DFB structures, DFB 1, 2, 3 compare Γ_g, whilst DFB 2, 4, 5 compare increasing QW number

The confinement in the QWs of DFB 1, 2 and 3 had similar values, 0.025397, 0.021628 and 0.025048 respectively. Because the only structural difference between DFBS 1 and 3 was the 5nm thicker grating in DFB 3, therefore the lateral and vertical confinement conditions were similar, so that they have approximately the same confinement factor in the QWs. As to DFB 2, this structure had 30nm thicker AlGaAs between the grating and the active region, which broadened the optical mode in the lateral direction. This was because the ridge waveguide was etched to a depth 30nm higher than DFB 1, which resulted in a slightly weaker lateral confinement of the optical mode.

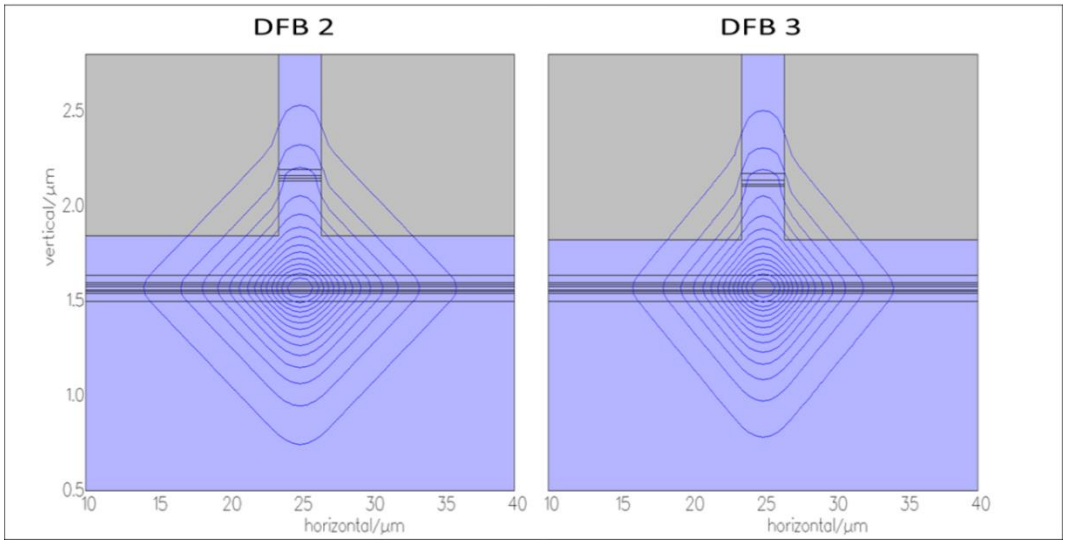

Figure 3-5: Waveguide simulations of DFB 2, where Γg decreased from 0.001358 (DFB 1) to 0.000963, and DFB 3, where Γg increased from 0.001358 (DFB 1) to 0.001694

As for structures with 4×QWs and 6×QWs (Fig. 3-6), these structures were designed to maintain Γ_g such that the only difference should be a result of greater gain being available in structures with more QWs.

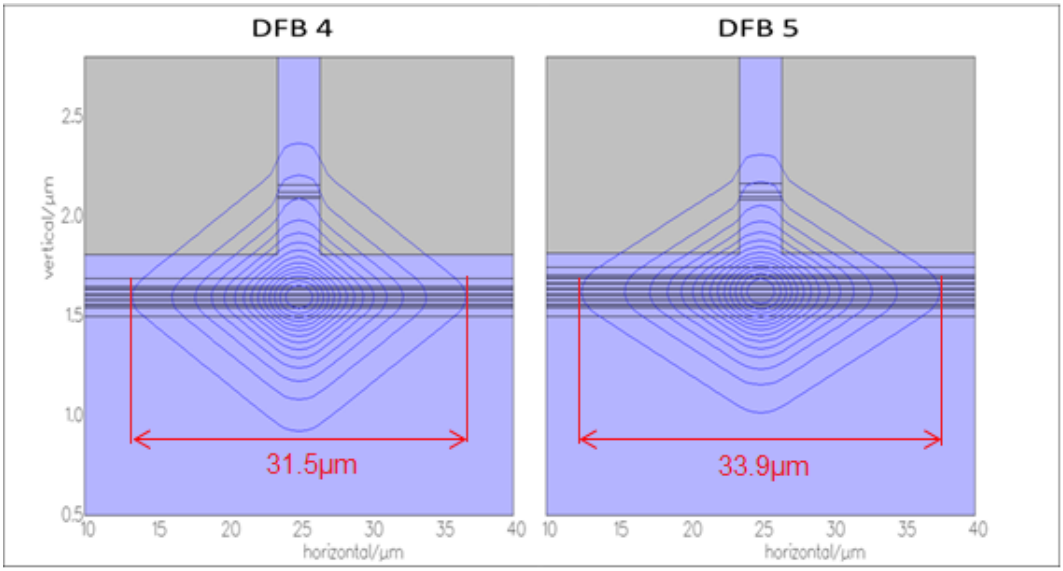

Figure 3-6: Waveguide simulations of DFB 4 and DFB 5

By stacking more QWs, the vertical confinement of the waveguide becomes stronger, which results in the optical mode shrinking away from the grating layer when increasing the number of QWs in the active region from 2 (DFB 2) to 4 (DFB 4) to 6 (DFB 5).

This also gives rise to a slight decrease of the lateral confinement. This can be seen from the decrease of the width of the outermost contour plot in Fig. 3-6. The outermost width of DFB 2 was 29.4μm, which increased to 31.5μm for 4×QWs and further increased to 33.9μm for 6×QWs.

In order to match the confinement factor in the grating layer with DFB 2 (the structure with the lowest confinement factor in the three 2×QWs designs), a thinner AlGaAs spacing and a thicker GaAs/InGaP grating were incorporated into the design and simulated. In the final structure, the waveguides containing 4× and 6× QWs had a confinement factor in the grating of 0.000962 and 0.000936 respectively, which matched with that of DFB 2 (0.000963). The confinement factors in the active region were 0.04526 and 0.062429 for 4× and 6× QWs respectively, which were roughly doubled and tripled compared to that of DFB 2 (0.021628).

3.1.4 Summary

In summary, DFB 1 was based on the initial DFB structure reported in [4]. For DFBs 2 and 3, modifications were made in the distance between grating and active region and the thickness of grating to tailor the confinement factor in the grating layer. Furthermore, with the expectation to manufacture high-power DFB lasers, a greater number of QWs were introduced into DFBs 4 and 5. In order to maintain consistency between structures, the confinement factor in the grating layer of DFBs 2, 4 and 5 were designed to be approximately equal.

3.2 Preparation Works

➢ MOVPE and MBE

Before the manufacture of DFB ridge lasers, the ability of the III-V Centre to produce 980nm lasers was examined. General laser performance was compared between samples grown by MOVPE and by MBE by fabricating and characterising broad area lasers. Table 3-3 presents the detailed layer structure of the 2× InGaAs/GaAs QWs grown by both methods on n-doped GaAs substrate with 3^{o} off to (110) orientation.

Layer	Thickness	Material	Doping	Concentration
Contact	300nm	GaAs	p	2.00E+19
Upper Cladding	600nm	$Al_{0.42}Ga_{0.58}As$	p	1.00E+18
	600nm	$Al_{0.42}Ga_{0.58}As$	p	5.00E+17
Active Region	50nm	GaAs	-	-
	7.6nm	$In_{0.17}Ga_{0.83}As$	-	-
	20nm	GaAs	-	-
	7.6nm	$In_{0.17}Ga_{0.83}As$	-	-
	50nm	GaAs	-	-
Lower Cladding	600nm	$Al_{0.42}Ga_{0.58}As$	n	5.00E+17
	600nm	$Al_{0.42}Ga_{0.58}As$	n	1.00E+18
Buffer	500nm	GaAs	n	1.00E+18

Table 3-3: Layer structure of 2× InGaAs/GaAs QWs grown by MBE and MOVPE

➢ Two, Four and Six QWs

The starting point for the research was the initial 2×QWs DFB design, where 2×QWs offer more gain than a single QW, it leads that to grow more QWs should result in even higher gain in active region, thus achieving higher power DFB lasers.

In order to investigate and compare general properties prior to the real manufacture of 2×, 4× and 6× QWs DFB lasers, a set of structures comprising 2×, 4× and 6× QWs

were grown, so that, by fabricating these structures into devices (lasers and/or mesa diodes), their optical properties could be studied and compared prior to their integration into DFB lasers (e.g. what cavity lengths are required and the implications for *K* design). The growth involved strain-balancing design as described in Section 3.1.3. The active region described in Table 3-3 was replaced by the structure shown in Table 3-4.

Layer	Thickness	Material	2×QWs	4×QWs	6×QWs
Active Region	40nm	GaAs	-	-	-
	10nm	$GaAs_{0.885}P_{0.115}$	Repeat ×2	Repeat ×4	Repeat ×6
	7.6nm	$In_{0.17}Ga_{0.83}As$			
	10nm	$GaAs_{0.885}P_{0.115}$			
	40nm	GaAs	-	-	-

Table 3-4: Active region of MOVPE grown 2×, 4× and 6× QWs

➢ Mesa Diode and Broad Area Lasers

The operation of a laser depends on many factors including waveguide design, mirror reflectivity and resonant cavity. Therefore, before the fabrication of lasers, mesa diodes, as in Fig. 3-7 (a), were first manufactured from these samples to check their electrical properties and compare the spontaneous emission.

As described in detail in Chapter 2, to fabricate mesa diodes, the samples were first deposited with the In-Ge/Au n-contact contact, followed by 340 ℃ annealing. After, Au/Zn/Au p-type contact was deposited and annealed at 360 ℃. The devices were finished by 1-1-1 etching (1:1:1 of $C_2H_4O_2$, HBr and $K_2Cr_2O_7$) to form the mesa of a depth of 1.4μm.

Broad area lasers were also fabricated to compare the lasing characteristics. As described in Chapter 2, a broad area laser is a standard and quick-to-make laser structure, which is usually fabricated from designed wafer structures for

electroluminescence characterisation of their lasing properties, for example the EL spectrum and LIV characteristics. They allow rapid feedback of material growth success and are also beneficial for length dependent laser characterisation since the influence of process-induced uniformity is minimised. Fig. 3-7 (b) shows s schematic diagram of a standard broad area laser with parameters annotated.

(a)

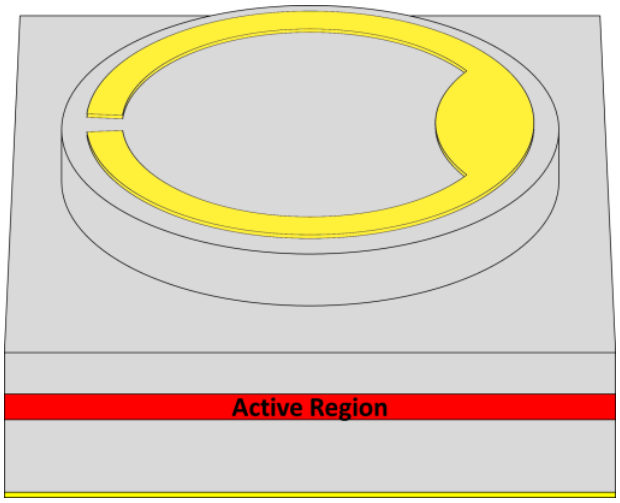

(b)

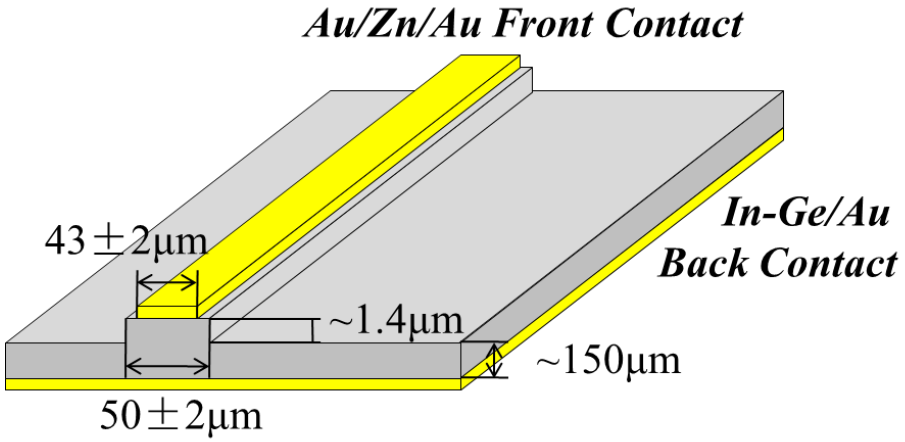

Figure 3-7: Schematic diagram of (a) a mesa diode and (b) a broad area laser

Broad area lasers (50μm wide) were processed from these materials in order to characterise their performance. Their fabrication process is described in detail in Chapter 2, but comprise a 1.4μm deep wet etch and application of Au/Zn/Au p-contact to the ridge and substrate thinning to ~150μm, followed by In-Ge/Au n-contact metallisation, prior to cleaving.

3.2.1 MBE and MOVPE Comparison: Broad Area Lasers

As both growth methods (MBE and MOVPE) are available at the III-V Centre, we firstly grew the same standard 2× InGaAs/GaAs QWs structure by both methods to determine which would be most appropriate for DFB planar growth, given the long waiting list for growth and hence the long lead time associated with the III-V centre's MOVPE reactors. The two materials were fabricated together into broad area lasers and length dependent LI characteristics were measured. Fig. 3-8 plots the length dependent CW measurement of the two laser sets.

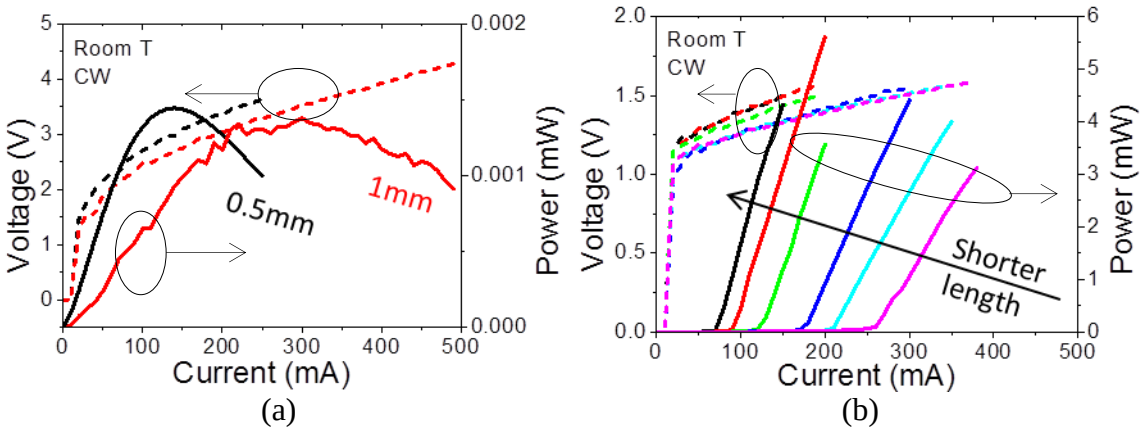

Figure 3-8: CW measurement of broad area laser grown by (a) MBE (0.5/1mm) and (b) MOVPE (0.75/1/1.5/2/2.5/3mm)

The results indicate that the samples grown by MBE could not lase under CW current injection at room temperature, likely as a result of their high resistance. According to the measurement, a 1mm long MOVPE grown laser had a resistance of ~ 1.88Ω and that of a 1mm MBE grown laser was 4.12Ω. In comparison, the cavity length dependent characterisation of the samples grown by MOVPE exhibited a more typical laser performance. There is no particular reason why MOVPE should be better than MBE for these structures, but the quality of AlGaAs that can be achieved is a likely factor. Fig. 3-9 shows the temperature dependent characterisation of the MOVPE-grown

lasers. The calculated characteristic temperature T_0 is 55.835°C. Whilst this is low in real terms compared with published values for comparable structures, these are bare, un-mounted, non-heat-sunk bars.

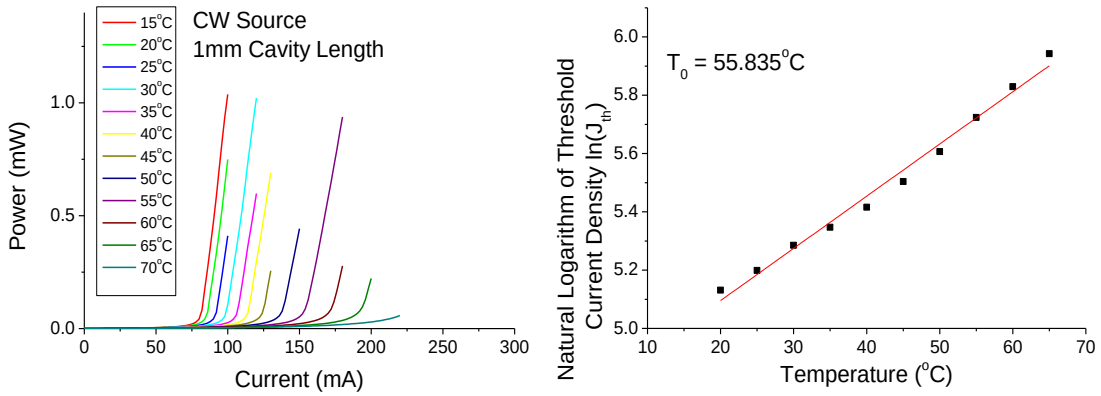

Figure 3-9: CW temperature dependent characterisation of a 1mm MOVPE grown broad area laser

That the performance of the MOVPE-grown lasers was so far superior to those grown by MBE affirmed our decision to continue the growth campaign by MOVPE.

3.2.2 Comparison of 2×, 4× and 6× QWs Mesa Diodes

Fig. 3-10 plots the L-I measurement of fabricated mesa diodes with 2×, 4× and 6× QWs. The light output was measured by placing the power head vertically 1mm above the contacted mesa, which was further aligned by injecting a test current to the device and adjusting the x-y location to optimise the coupling efficiency and therefore attain the highest power value. The spontaneous emission produced by mesa diodes containing 6×QWs sample is larger than that of 4×QWs, which is larger than those with 2×QWs. Gain is not directly related to spontaneous emission, the result accords with expectation. The spontaneous emission output power of a mesa is related to current by the equation [14]:

$$P_{sp} = \eta_c \eta_i \eta_r \frac{h\nu}{q} I, \quad where \quad \eta_r = \frac{R_{sp}}{R_{sp} + R_{nr} + R_l}$$

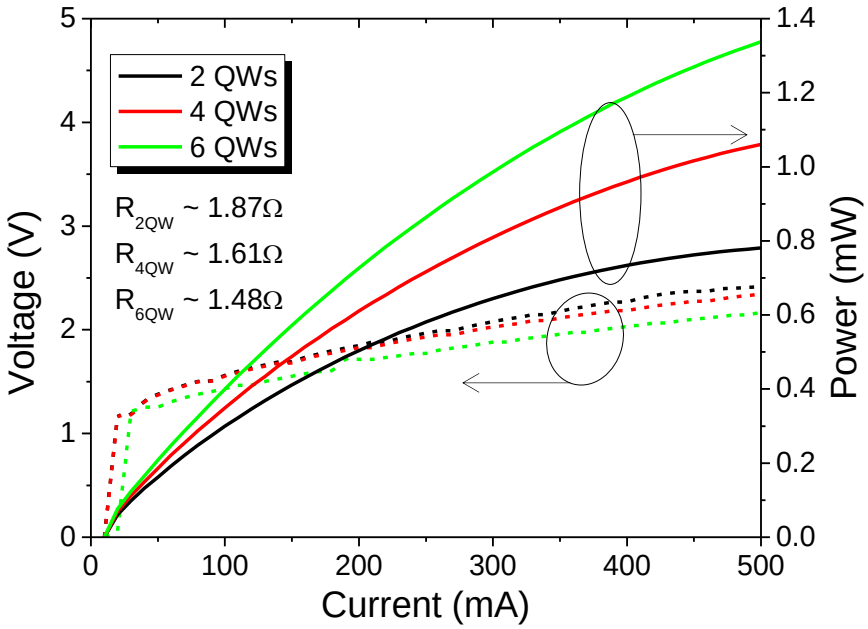

Figure 3-10: Measurement of the spontaneous emission and voltage from 2×, 4× and 6× QWs mesa diodes as a function of current

Therefore, a change in L-I relationship must be due to change in η_c and/or η_i and/or η_r. η_c is net collection efficiency, and is considered to be kept constant. η_r is radiative efficiency, defined to simplify the uncertain dependence of non-radiative recombination rate (R_{nr}) and carrier leakage (R_l) on I, but usually depends on carrier density (N) [14].

η_i is internal quantum efficiency, which represents the fraction of injected current in the active region. The different number of QWs should not affect η_i, but the measured device resistance shows that $R_{2QW} > R_{4QW} > R_{6QW}$, which would cause the local temperature inside the 2×QWs mesa to be higher than for 4×QWs mesa, and higher than 6×QWs mesa. This might result in a decrease of η_i from 6× to 4× to 2× QWs.

This hypothesis can be validated by revealing the relative difference ratio (%) in both output power and in resistance. Fig. 3-11 plots the output power difference ratios from the 4×QWs (●) and 6×QWs (▲) mesas to that of the 2×QWs mesa, i.e. setting 2×QWs as the reference, as a function of current. Both curves show that the ratio increases with

a near-linear profile against the increase in current injection. By applying linear fitting for both, an intercept of 11.1% was calculated for the curve (4× to 2× QWs) and 24.7% for the curve (6× to 2× QWs). The intercept of the linear fitting represents a theoretical output power difference ratio at 0mA current injection, where the self-heating effect can be neglected.

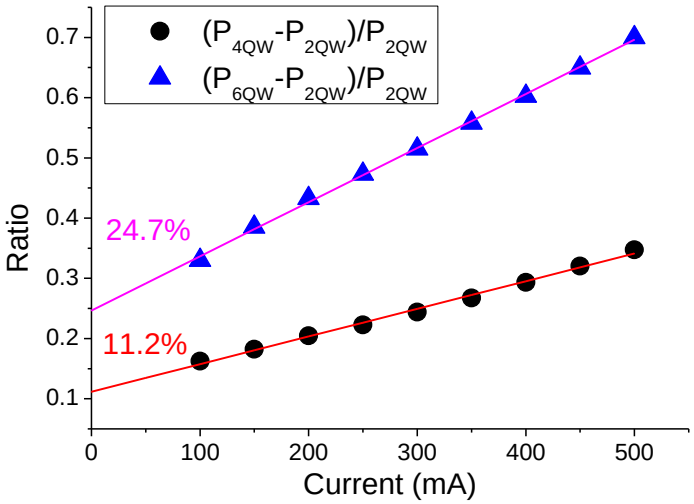

Figure 3-11: The relative difference ratios from 4× and 6× QWs mesa to 2×QWs mesa, plotted as a function of injection current, together with their linear fitting

Also, the relative difference ratios in resistance from the 4× and 6× QWs mesas to that of the 2×QWs mesa can be calculated as follows:

$$(R_{4QW} - R_{2QW}) / R_{2QW} = -16.1\%;\ (R_{6QW} - R_{2QW}) / R_{2QW} = -26.4\%$$

Therefore, with the 2×QWs mesa being the reference here, the 4×QWs mesa exhibited 16.1% lower resistance, whilst exhibiting a characteristic output power increase of 11.2%; and the 6×QWs mesa exhibited 26.4% lower resistance, whilst exhibiting a characteristic output power increase of 24.7%.

This calculation validated the hypothesis above that the difference in device resistance contributed to the difference of measured L-I properties.

3.2.3 Comparison of 2×, 4× and 6× QWs Broad Area Lasers

2×, 4× and 6× QWs broad area lasers were fabricated following the same process as in 3.4.1, with all samples mounted on ceramic tiles and tested as-cleaved without the application of facet coatings.

➢ Laser Characterisation

One important parameter to be calculated in the laser characterisation is the internal quantum efficiency (η_i), which determines the L-I properties of a laser. Firstly, we calculate the external differential quantum efficiency (η_d) as a function of cavity length, extracted from the linear fitting of an L-I curve by the given equation [15]:

$$\eta_d = 2\frac{\Delta P}{\Delta I}\left[\frac{q\lambda}{hc}\right]$$

$h = 6.6262\times10^{-34}$ J.sec; $c = 2.99\times10^{8}$ m/sec; $q = 1.6022\times10^{-19}$ C; $\lambda = 1\times10^{-6}$ m;

If we then plot the inverse external differential quantum efficiency ($1/\eta_d$) as a function of cavity length (L), the intercept of the linear fit on the $1/\eta_d$ axis is then $1/\eta_i$.

Another important parameter to be calculated is the transparency threshold current density (J_0), which can be regarded as the theoretical threshold current density of laser with infinite optical cavity length (i.e. no mirror loss) [15]. This is obtained by plotting the threshold current density (J_{th}) as a function of inverse cavity length ($1/L$). The intercept of the linear fit with the J_{th} axis is then J_0.

The following section presents the experimental results obtained from 2×, 4× and 6× QWs broad area lasers, characterised in this way.

- **Characterisation of 2×QWs Broad Area Laser**

Fig. 3-12 plots the L-I curve of 2×QWs broad area lasers with cavity length of 0.5, 1, 1.5 and 2mm. Measurements were performed at room temperature using a CW current source. CW lasing was observed down to the shortest cavity length cleaved with I_{th} ~ 70mA (J_{th} ~ 280A/cm^2). Table 3-5 presents the characteristics obtained from analysis of the measurement of the 2×QWs broad area lasers in Fig. 3-12. From this table η_d and J_{th} are plotted as a function of cavity length in Fig. 3-13. The internal quantum efficiency (η_i) is calculated to be 64.53% and the transparency threshold current density (J_0) is 166.56A/cm^2.

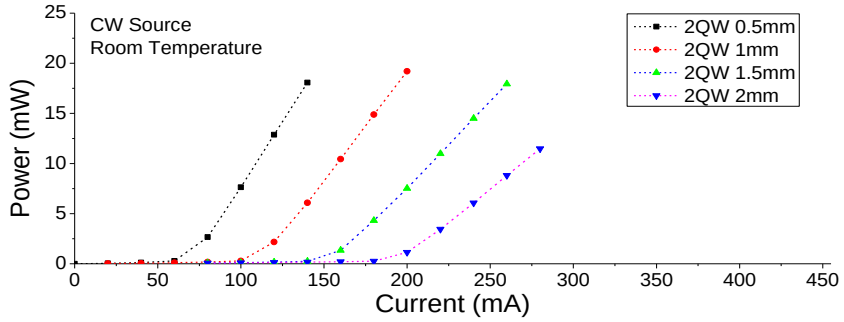

Figure 3-12: L-I curve of 2×QWs broad area laser

2×QWs BA Lasers		0.5mm	1mm	1.5mm	2mm
Area	cm^2	0.00025	0.0005	0.00075	0.001
2×Slope Efficiency	W/A	0.512	0.429	0.335	0.268
η_d	-	0.414	0.347	0.271	0.217
Threshold Current	mA	69.7	110.8	153.6	194.5
Threshold Current Density	A/cm^2	278.9	221.5	204.8	194.5

Table 3-5: Experimental results of 2×QWs broad area laser

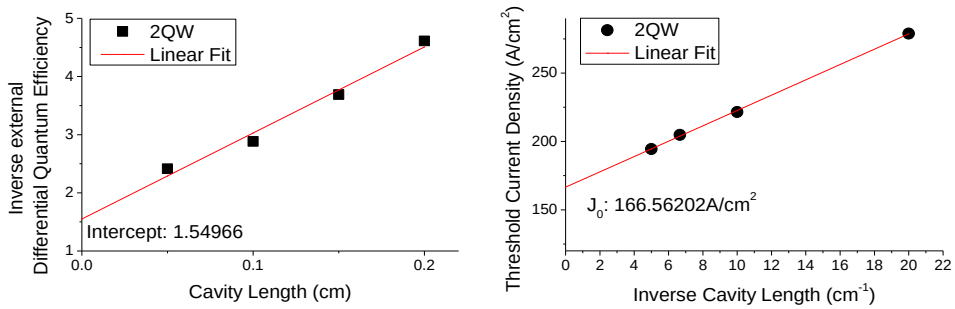

Figure 3-13: Characterisation of 2×QWs broad area laser

- **Characterisation of 4×QWs Broad Area Laser**

Fig. 3-14 plots the L-I curve of 4×QWs broad area lasers with cavity lengths of 0.5, 1, 1.5 and 2mm. Measurements were performed at room temperature using a CW current source. CW lasing was observed down to the shortest cavity length cleaved with I_{th} ~ 86mA (J_{th} ~ 343A/cm^2). Table 3-6 presents the characteristics obtained from analysis of the measurement of the 4×QWs broad area lasers in Fig. 3-14. From this table η_d and J_{th} are plotted as a function of cavity length in Fig. 3-15. The internal quantum efficiency (η_i) is calculated to be 49.09% and the transparency threshold current density (J_0) is 203.49A/cm^2.

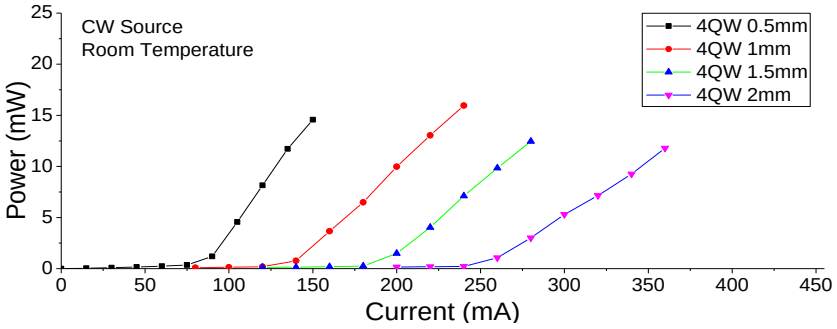

Figure 3-14: L-I curve of 4×QWs broad area laser

4×QWs BA Lasers		0.5mm	1mm	1.5mm	2mm
Area	cm^2	0.00025	0.0005	0.00075	0.001
2×Slope Efficiency	W/A	0.477	0.307	0.277	0.212
η_d	-	0.386	0.248	0.224	0.171
Threshold Current	mA	85.8	135.9	189.6	250.9
Threshold Current Density	A/cm^2	343.4	271.8	252.7	250.9

Table 3-6: Experimental results of 4×QWs broad area laser

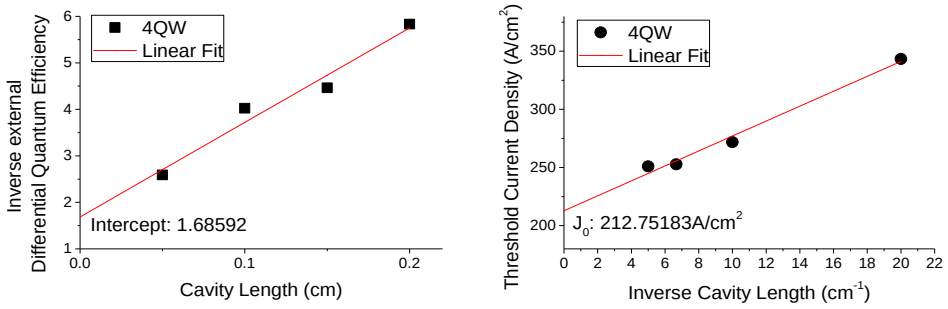

Figure 3-15: Characterisation of 4×QWs broad area laser

- **Characterisation of 6×QWs Broad Area Laser**

Fig. 3-16 plots the L-I curve of 6×QWs broad area lasers with cavity length of 0.5, 1, 1.5 and 2mm. Measurements were performed at room temperature using a CW current source. CW lasing was observed down to the shortest cavity length cleaved with I_{th} ~ 123mA (J_{th} ~ 492A/cm^2). Table 3-7 presents the characteristics obtained from analysis of the measurement of the 6×QWs broad area lasers in Fig. 3-16. From this table η_d and J_{th} are plotted as a function of cavity length in Fig. 3-17. The internal quantum efficiency (η_i) is calculated to be 52.13% and the transparency threshold current density (J_0) is 371.73A/cm^2.

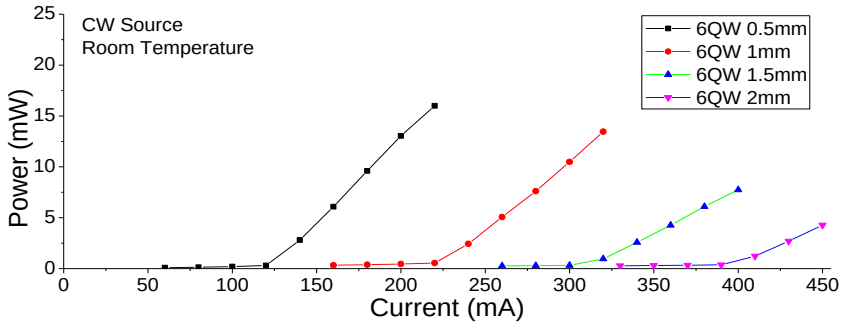

Figure 3-16: L-I curve of 6×QWs broad area laser

6×QWs BA Lasers		0.5mm	1mm	1.5mm	2mm
Area	cm^2	0.00025	0.0005	0.00075	0.001
2×Slope Efficiency	W/A	0.333	0.275	0.173	0.153
η_d	-	0.270	0.222	0.140	0.124
Threshold Current	mA	123.0	223.1	310.2	394.2
Threshold Current Density	A/cm^2	491.8	446.2	413.6	394.2

Table 3-7: Experimental results of 6×QWs broad area laser

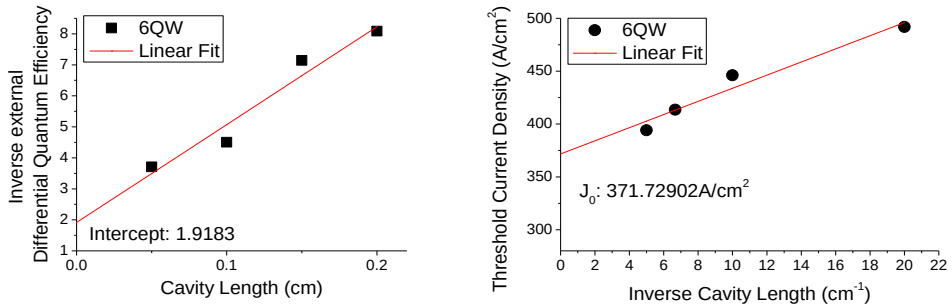

Figure 3-17: Characterisation of 6×QWs broad area laser

➢ Discussion and Comparison

- **Device Resistance**

Fig. 3-18 illustrates the resistance calculated from length-dependent electrical (I-V) characterisation showing that the 2×, 4× and 6× QWs devices have similar resistance for all cavity lengths. This is expected, since the devices were fabricated together under identical process parameters. No additional resistance or leakage was contributed by the additional QWs growth.

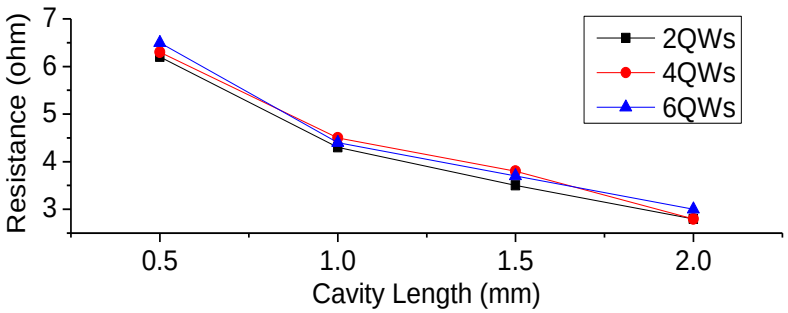

Figure 3-18: Length dependent resistance of 2×, 4× and 6× QWs lasers

- **Estimation of Minimum Saturated Gain**

For the 2×QWs laser set, lasing is observed for cavity lengths down to the shortest available (due to cleaving limitation) of 500μm. With the assumption of no other losses in the cavity, the gain coefficient is given by the threshold condition equation [16]:

$$g = \frac{1}{2L}\ln\frac{1}{R^2}$$

The reflectively (R) on both as-cleaved facets were approximated as 0.31, which is a typical value for GaAs/AlGaAs laser [15]. Such that a saturated gain coefficient was estimated to be higher than 23.4cm^{-1}. This indicates its potential applicability to the DFB laser, and any subsequent integrated devices. Further gain, through greater number of QWs is therefore only really necessary should subsequent device processing have a

deleterious impact on gain, or generate excessive waveguide losses. Analysis of these materials, containing greater number of QWs, is therefore necessary to ensure that there are no additional issues, such as excess strain commensurately higher defect density, associated with the growth of additional QWs.

- **L-I Characterisation Comparison**

Laser characterisation for the 2×, 4× and 6× QWs lasers are summarised in Table 3-8. These results demonstrate that the transparency threshold current density, J_0, increases significantly along with the increase in the number of quantum wells. It can be expected that this increase is due to the increase in the number of available electronic states to fill and non-uniform carrier injection into the QWs, resulting in a higher injected current needed to reach the transparency condition. This matches the result of [17], where 3×, 5× and 7× $Ga_{0.5}In_{0.5}P/(Al_{0.7}Ga_{0.3})_{0.5}In_{0.5}P$ QWs lasers were studied. The result also matches with the research reported in [18], where 1×, 2× and 3× $GaAs/Al_{0.22}Ga_{0.78}As$ (7nm/5nm) QWs lasers were studied. However in their measurement of short devices (<200μm), a larger number of quantum wells resulted in lower threshold current density, which was attributed to the mirror loss term increasing with a decrease in cavity length, such that the optical gain of their 1× QW device was easily saturated.

	2×QWs	4×QWs	6×QWs
Transparency Threshold Current Density	166.6A/cm^2	212.8A/cm^2	371.7A/cm^2
Internal Quantum Efficiency	64.50%	59.30%	52.10%

Table 3-8: Comparison of 2×, 4× and 6× QWs laser characterisation

Table 3-8 also shows that, under CW pumping, lasers with 2×QWs have higher internal quantum efficiency (64.53%) than that of 4×QWs (59.3%), than that of 6×QWs

(52.1%). I suggest that this is mainly due to heating in the device induced by the CW pumping current. Due to the increasing current needed to reach the lasing condition, as discussed above, the self-heating effect caused by the large CW current becomes more significant. For example, the CW threshold current of a 1mm long laser was 110.8mA for a 2×QWs laser, 135.9mA for a 4×QWs laser, and 223.1mA for a 6×QWs laser. In order to verify this assumption, a selection of devices was re-measured under pulsed current injection with 5μs pulse width and 5% duty cycle. Fig. 3-19 plots the L-I characteristic for a range of cavity length from 0.5-2mm using pulsed current injection.

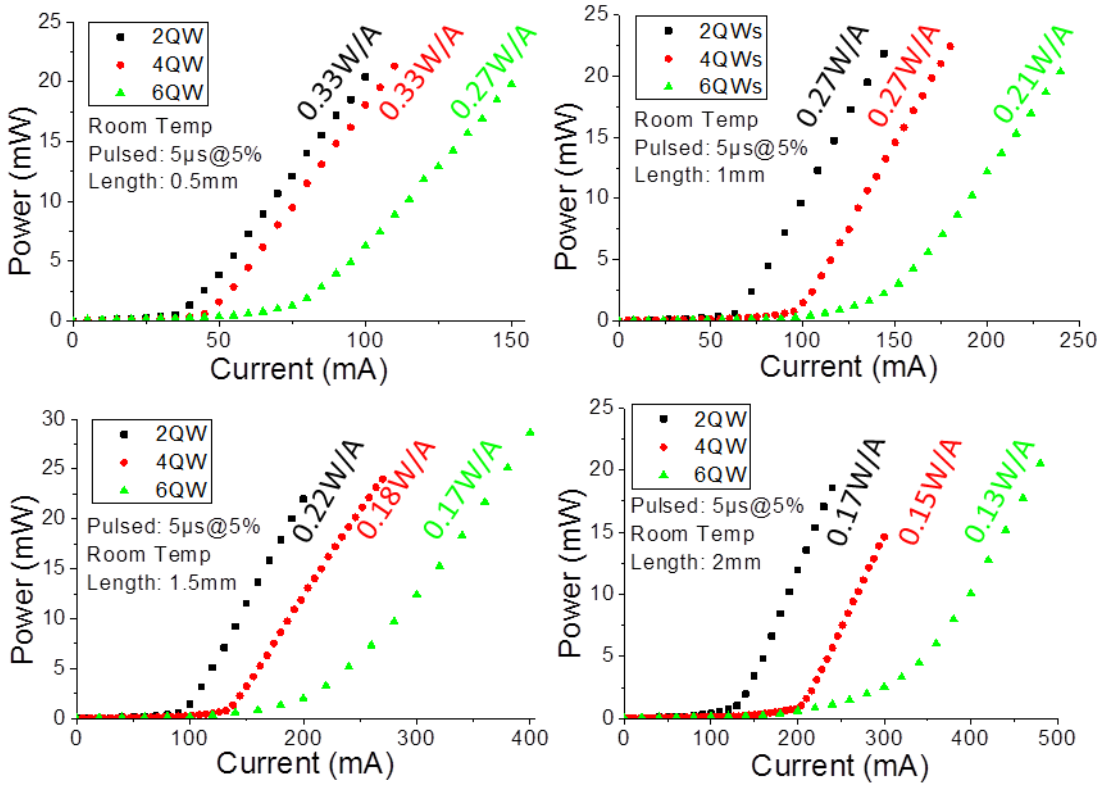

Figure 3-19: L-I plots of 0.5/1/1.5/2mm lasers with 2×, 4× and 6× QWs measured with pulsed current source (pulse: 5μs-5%)

Table 3-9 summarises the threshold currents extracted from these plots. Because of the significant reduction in heating resulting from the pulsed operation, a decrease in lasing threshold current is observed, compared with the CW measurement. Taking the 1mm devices as an example, for 2×QWs: 110.8mA dropped to 63.4 mA; 4×QWs: 135.9mA dropped to 96.1 mA; 6×QWs: 223.1mA dropped to 142.4 mA. It should be

pointed out that for pulsed current injection there is an underlying background DC bias, contributing several mAs to the current injection in all cases. Since this is small, and identical between measurements, it does not affect the discussion here.

	Threshold Current (mA)				Slope Efficiency (W/A)			
Length(mm)	0.5	1	1.5	2	0.5	1	1.5	2
2×QWs	38.1	63.4	97.5	130.9	0.33	0.27	0.22	0.17
4×QWs	46.5	96.1	132.5	201.6	0.33	0.27	0.18	0.15
6×QWs	77.3	142.4	239.2	322.5	0.27	0.21	0.17	0.13

Table 3-9: Threshold current and slope efficiency (single facet) of 0.5/1/1.5/2mm lasers with 2×, 4× and 6× QWs measured using pulsed current source (pulse: 5μs-5%)

As shown in Fig. 3-19, as well as listed in Table 3-9, the relationship between the measured slope efficiency and the number of QWs is in agreement with the assumption above. First of all, all 12 values (4 lengths × 3 structures) of slope efficiency increase significantly from those measured under CW operation (note efficiency is per facet in Table 3-9), which was a result of the reduced self-heating from pulsed current injection compared to CW. For low threshold current devices, i.e. 0.5mm and 1mm devices of 2× and 4× QWs, devices of identical cavity length operated with approximately the same slope efficiency, 0.33W/A (0.5mm) and 0.27W/A (1mm) for both 2× and 4× QWs, matching observations made in [17].

For devices operating with higher threshold currents some self-heating still contributes to a reduction in slope efficiency. However, this is much less significant compared to that resulting from CW operation. For example, the measured CW slope efficiency of a 2mm-long 2×QWs 2mm laser was 0.1341, whilst for a 2mm-long 6×QWs laser it was 0.07646, which indicates a reduction ratio of (0.1341-0.07646)/0.1341 ≈ 43%, while the measured pulsed slope efficiencies were 0.17 and 0.13, indicating a reduction ratio of only (0.17-0.13)/0.17 ≈ 24%.

3.2.4 Summary

This section described the comparison made (a) between MOVPE-grown and MBE-grown broad area lasers (Section 3.2.1), where the MOVPE-grown lasers demonstrated better performance, and (b) among 2×, 4× and 6× strain-balanced InGaAs QWs as mesa diodes (Section 3.2.2) and broad area lasers (Section 3.2.3). Length dependent characterisation of broad area lasers fabricated from these structures revealed that, for the 2×QWs structure, lasers with cavities as short as 0.5mm cavity length demonstrated lasing. The characterisation demonstrated an increase in transparency threshold current density due to the increasing number of states to fill, and a reduction in internal quantum efficiency was observed from 2× to 4×, then to 6× QWs. This was attributed to an increase in the threshold current, which generated more self-heating during device operation.

3.3 DFB Fabrication

Following the previous study, the device manufacture follows a four-step process: (I) planar wafer growth, (II) grating patterning and etching, (III) over-growth and (IV) device fabrication. This section describes these four steps in detail.

Fig. 3-20 is a schematic illustration of the general DFB laser cross-section. The front view is a slice through the grating (i.e. light propagating along the width of the page), of the layer structure after regrowth and prior to fabrication. As shown in this schematic, the InGaP/GaAs grating layer was formed within the upper cladding layer to a distance above the InGaAs QW active region defined by the required grating coupling strength.

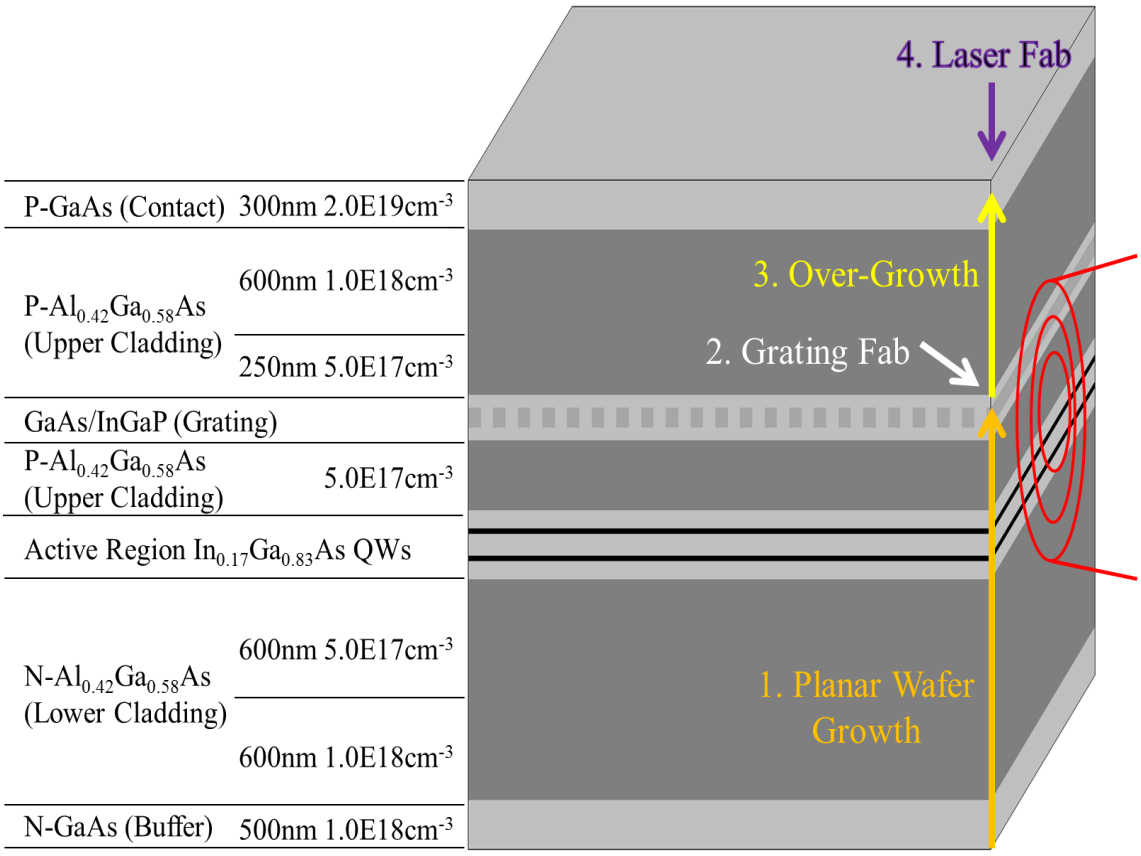

Figure 3-20: Schematic diagram of the layer structure after overgrowth

3.3.1 Planar Growth

Epitaxial growth was performed by Metal-Organic Vapour Phase Epitaxy (MOVPE) in the EPSRC National Centre for III-V Technologies. On an n-doped GaAs substrate which was mis-oriented by 3 ° to the (110) direction, 1200nm n-doped (lower 600nm: $1.0\times18cm^{-3}$; upper 600nm: $5.0\times17cm^{-3}$) $Al_{0.42}Ga_{0.58}As$ lower cladding layer was grown above a 500nm GaAs (n-doped $1.0\times18cm^{-3}$) buffer layer. Above this, partially strain-balanced quantum wells (QWs) emitting ~990nm were grown within a waveguide structure comprising: 2×, 4× and 6× 7.6nm $In_{0.17}Ga_{0.83}As$ QWs separated by 20nm $GaAs_{0.885}P_{0.115}$ strain balancing layers with 10nm $GaAs_{0.885}P_{0.115}$ and 40nm GaAs grown on either side. For each structure, a certain thickness of p-doped ($5.0\times17cm^{-3}$) $Al_{0.42}Ga_{0.58}As$ was grown above the core prior to growth of the grating layer, the thickness of which, like the grating thickness, is a simulation result to match the coupling requirement for $KL \sim 1$.

3.3.2 Grating Patterning and Etching

After growth, the samples were patterned in ~50nm PMMA by electron beam lithography with a range of grating periods with mark to space ratio of approximately 50:50. Ten continuous grating periods were patterned from 144nm to 162nm with a 2nm step. This was aimed to allow for uncertainty in calculation of n_{eff} and to allow for red-shift of gain due to thermal effects. By estimation (assuming $n_{eff} = 3.33$), this grating period range could achieve a range of Bragg wavelength (λ_B) from ~960nm to ~1080nm to fully cover the intrinsic gain peak and operational red-shift of our structures (7.6nm

$In_{0.17}Ga_{0.83}As$ QWs), thereby ensuring the existence of grating periods that are located close enough to receive sufficient gain to reach DFB lasing condition. Fig. 3-21 illustrates the features along the patterned grating stripe of the samples. As to the method of grating fabrication, in order to precisely achieve the designed structure, it is necessary to achieve precise control over the depth of the grating etch. In wet etching alone, it is difficult to control the mark to space ratio due to lateral etching. If using dry etching only, the etching rate is difficult to control precisely, considering the variation of equipment usage (changes relating to previous used recipes, last chamber cleaning time, sample size, etc.) and resulting variation in etching rate. Precision in grating etch was attained through use of a two-step etching process, which combined dry etch and wet etch, since neither of these used alone could guarantee the required level of precision. For this method, the first order DFB grating layer comprised an InGaP layer (lattice matched to GaAs) sandwiched between two 12nm thick GaAs layers.

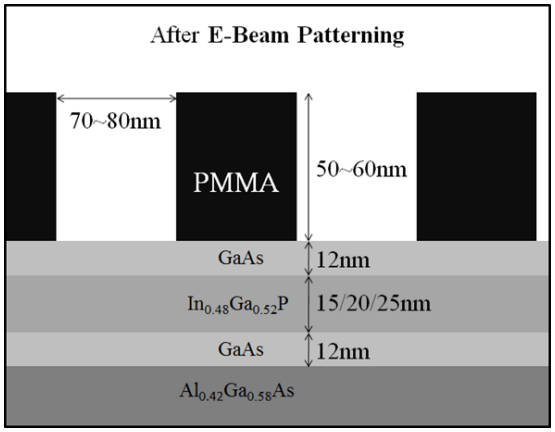

Figure 3-21: E-beam patterning

➢ Step I: ICP Dry Etch – etch into InGaP layer

The first step is to etch the exposed GaAs using an Oxford Plasma-Lab ICP (Inductively Coupled Plasma) Etch System using the Argon recipe: RF power = 250W, ICP power = 0W, pressure = 4mTorr and Argon = 10sccm. The etch process etches

through the upper 12nm GaAs and terminates some depth (~10nm) within the InGaP layer. The target etch depth was set to 20~25nm to ensure that the top GaAs is consistently penetrated but that the lower GaAs layer is not reached. Fig. 3-22 illustrates this process. The red arrows represent the Argon etch process and the yellow arrows illustrate the etched areas.

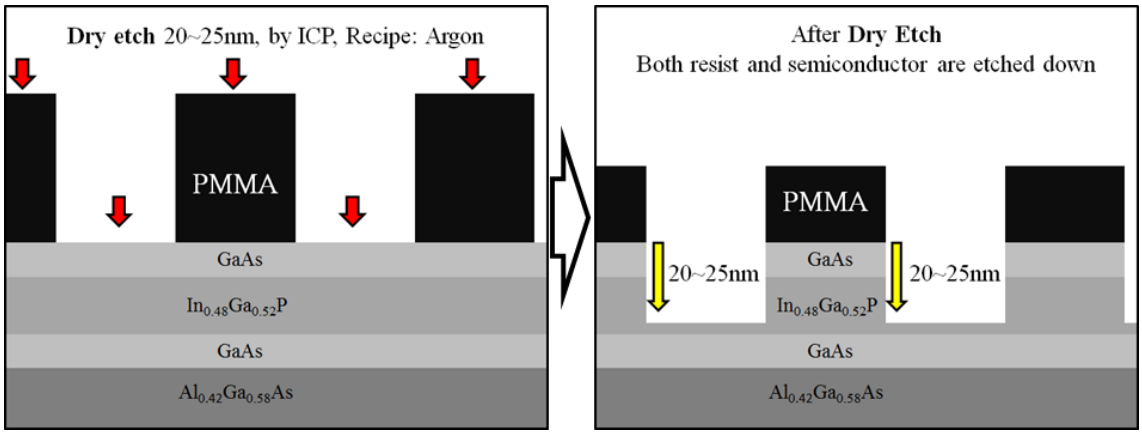

Figure 3-22: ICP dry etch -- through upper-GaAs layer into InGaP layer

➢ Step II: PMMA Removal

After etching, Acetone is used to fully remove the PMMA resist, followed by a 1.5-minite O_2 plasma ash, revealing the grating structure as shown in Fig. 3-23. The cleanliness was inspected under an optical microscope to ensure the complete removal of the PMMA resist.

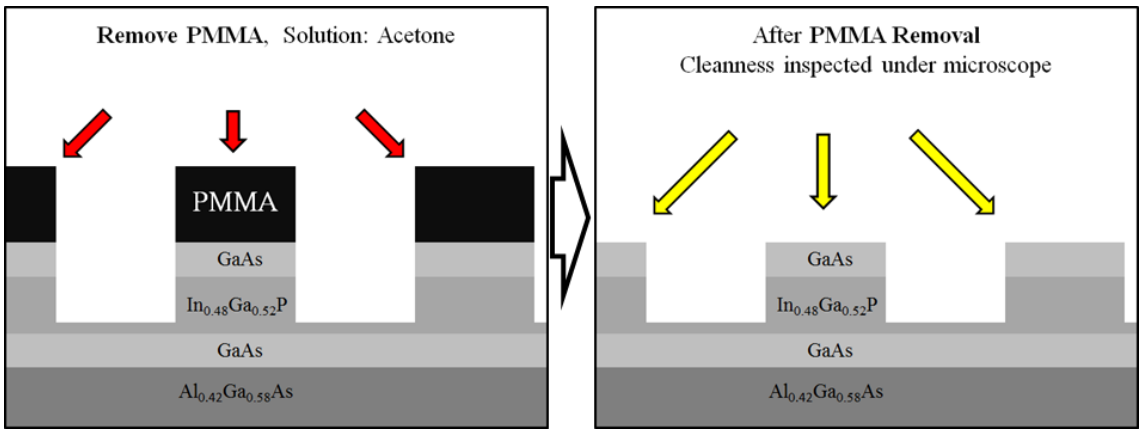

Figure 3-23: Removal of PMMA

➢ Step III: Selective Wet Etch – etch down to lower GaAs

The third step is to selectively etch the remaining depth of InGaP in the exposed area of the grating pattern, terminating at the lower GaAs/InGaP interface. The etchant 1:1 HCl/H_3PO_4 solution is chosen for its high etching selectivity of InGaP over GaAs, so that the lower GaAs layer acts as an etching-stop layer in this process to protect the $Al_{0.42}Ga_{0.58}As$ layer underneath from being exposed. Fig. 3-24 illustrates this process. The red and yellow arrows represent the etching process and indicate the etched thickness respectively. This same wet etchant was used in processing the self-aligned stripe structure described in [19], and as demonstrated, the etching proceeded with a 45^o angle, pinned laterally by the GaAs layer above.

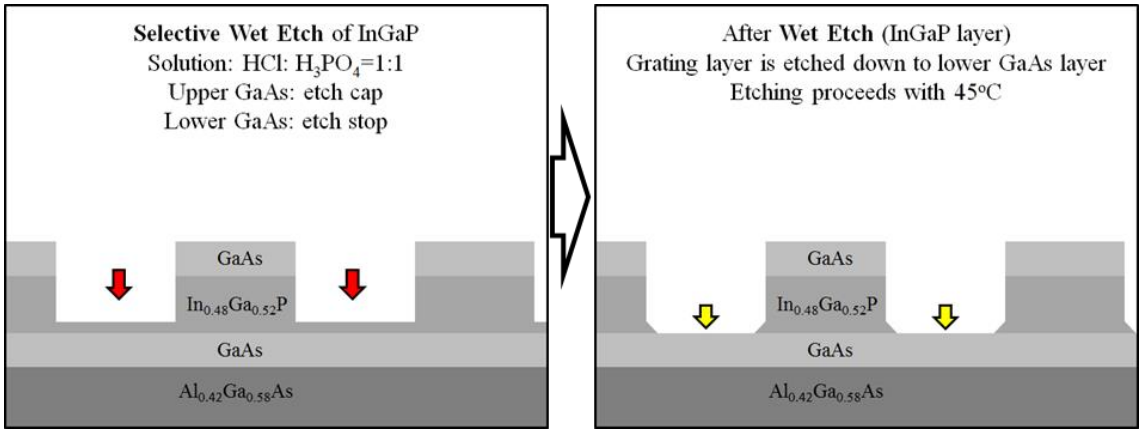

Figure 3-24: 1:1 HCl/H_3PO_4 solution wet etch the remaining InGaP

➢ Grating Etch Measurement

The grating etch was measured using AFM to characterise the grating etch. Samples were inspected and Fig. 3-25 shows the measurement of DFB 1, which had a 15nm deep grating. The measured ~27nm etch depth matched the sum of GaAs capping thickness (12nm) and the grating etched thickness (15nm), which indicated successful etch of the gratings, down to the lower GaAs etch-stop layer.

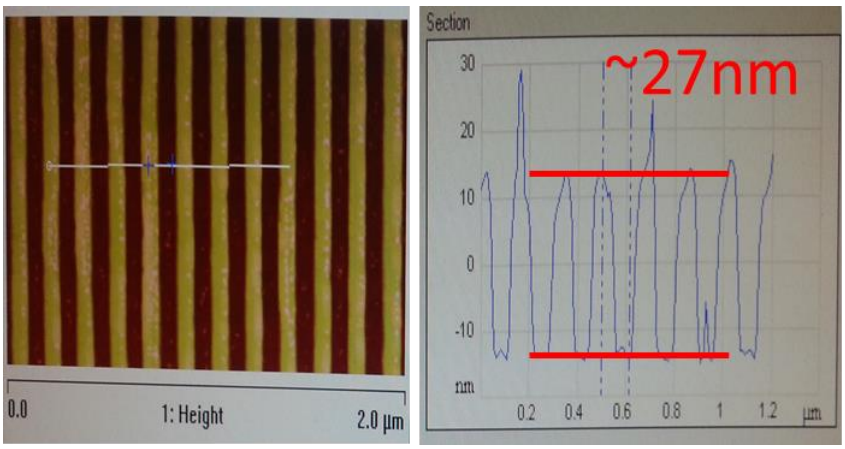

(a) (b)

Figure 3-25: AFM scan of etched grating pattern of DFB 1, ~27nm etch depth measured. The height profile in (b) is taken at the cross-section marked by the while line in (a)

3.3.3 Over-Growth

Following grating etch and clean-up of the PMMA mark, the wafer was then returned to the MOVPE reactor for overgrowth. Immediately prior to loading into the chamber, a wash in 1% diluted HF is performed to assist removal of native oxide and any further residual contamination. Fig. 3-26 illustrates the overgrowth process and the formation of the buried 1st order rectangular 50/50 GaAs/InGaP grating.

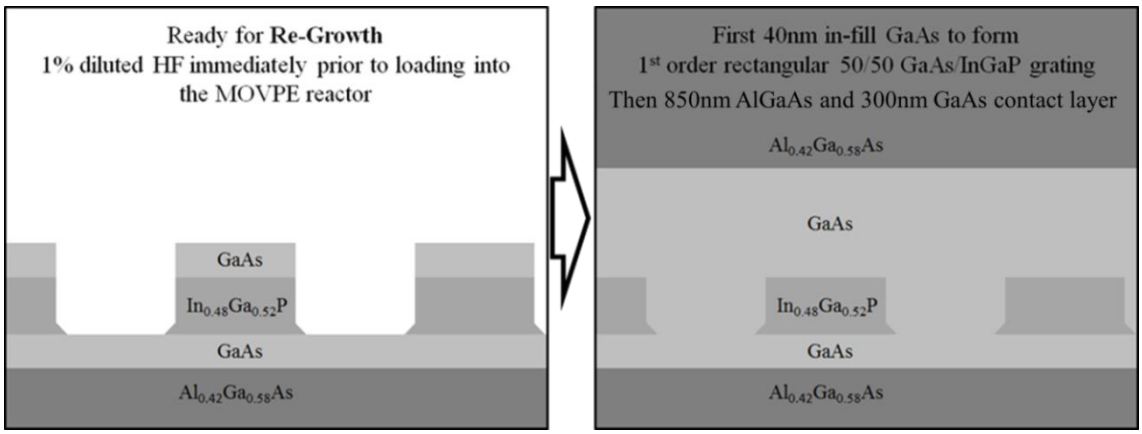

Figure 3-26: 1:1 Formation of InGaP/GaAs buried grating structure

As shown in the figure, 40nm p-doped (5.0×18cm^{-3}) GaAs was first overgrown to in-fill and planarise the grating, followed by 850nm p-doped (lower 250nm: 5.0×17cm^{-3},

upper 600nm: $1.0\times18cm^{-3}$) $Al_{0.42}Ga_{0.58}As$ upper cladding, and a 300nm p-doped ($2.0\times19cm^{-3}$) GaAs contact layer to complete the structure. The grating is formed in the upper cladding layers with a thickness and distance above the active region as determined by the simulation in Section 3.1.3.

3.3.4 Laser Fabrication

The fabrication of narrow ridge 3μm-wide DFB lasers consisted of 4 main steps, namely (1) trench etching; (2) dielectric deposition and contact window opening; (3) p-contact and bond-pad deposition; (4) back thinning and n-contact deposition.

➢ Step I: Trench Photolithography and Etching

To assist in the description of the device fabrication process, Fig. 3-27 (a) shows a pictorial representation of the epitaxial structure of the overgrown wafer, as in Fig. 3-20, but with the front view being perpendicular to grating. SPR 350 photoresist was spun onto the samples at 4000rpm for 30 seconds, followed by 1 minute bake on 100^{o}C hot plate. For better alignment, photoresist edge beads were removed. Mask patterns were aligned to stripe patterns (grating), exposed and developed in MF26A for 1 minute and rinsed in DI water, as Fig. 3-27 (b).

In order to ensure complete removal of the resist in the exposed area, 1 minute oxygen plasma ash was performed. To make the remaining photoresist more resistant against the following ICP etching, samples were hard baked at 100^{o}C on a hot plate for another 1 minute.

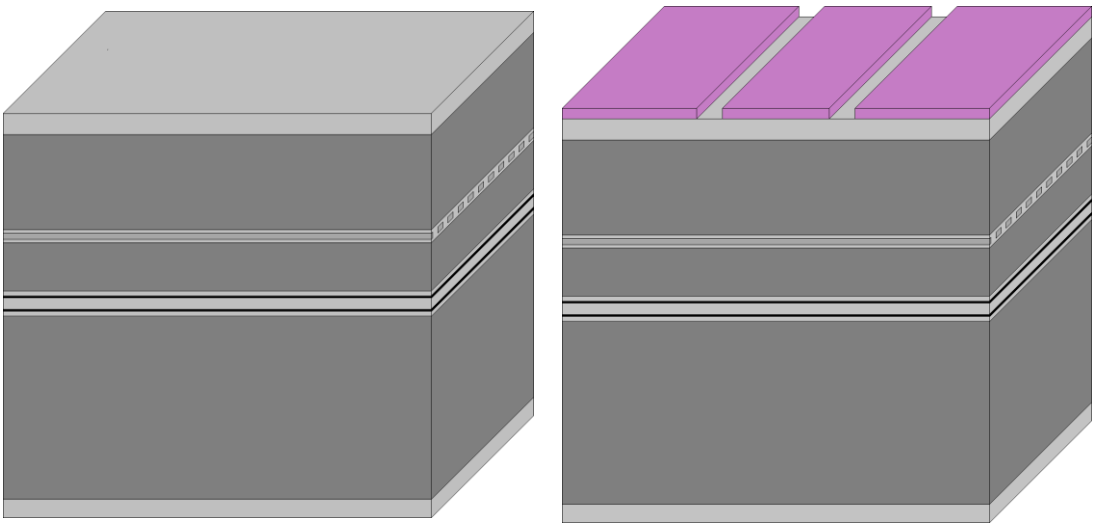

(a) (b)

Figure 3-27: Photolithography for trench etching

ICP etching was employed for trench etching with the following settings: SiCl4 = 5sccm, RF = 100W, ICP = 250W, Pressure = 2 mTorr and Temperature = 20^{o}C. The target was to etch down to 150-250nm above active region depending on each sample.

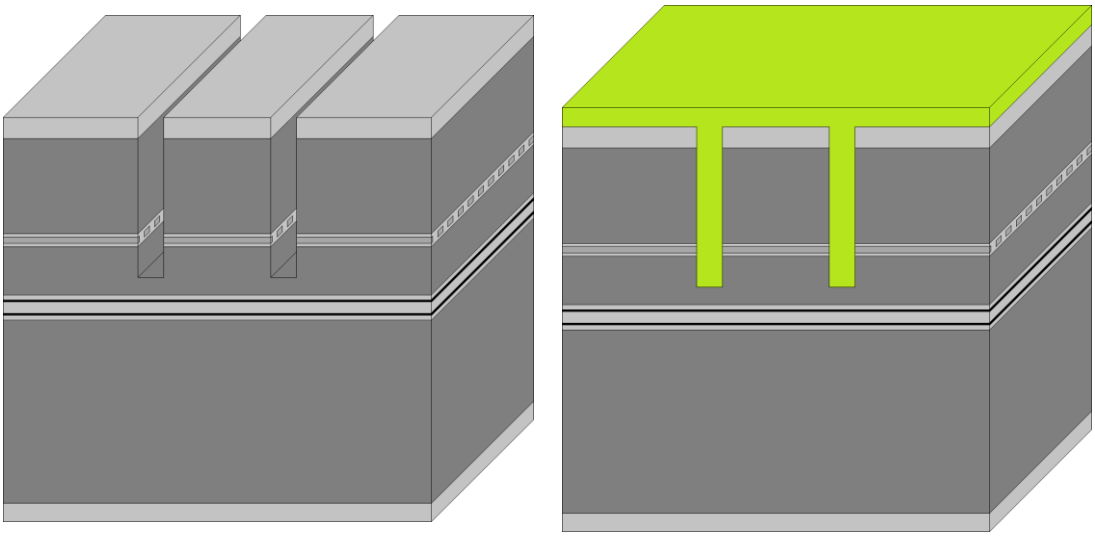

(a) (b)

Figure 3-28: Trench etching and Si_3N_4 deposition

Then a 30s wet etch in 20:1 Citric acid / H_2O_2 was performed to smooth any roughness/damage, followed by 3 minute oxygen plasma ash. The samples were then placed in warm acetone to remove the photoresist. After cleaning, another 2 minute oxygen plasma ash was performed to remove any residual photoresist, resulting in structure in Fig. 3-28 (a).

➢ Step II: Silicon Nitride Deposition and Window Etching

The next step was dielectric deposition to provide an electrical insulating layer to enable remote bandpads to be deposited adjacent to each ridge. Plasma-enhanced chemical vapour deposition (PECVD) was employed to deposit 550nm thick Si_3N_4 onto samples, as shown in Fig. 3-28 (b). Then, similar to Step I, Si_3N_4 coated samples were spun with SPR350 photoresist and aligned to the contact window mask. After exposure, development and oxygen plasma ash, as in Fig. 3-29 (a), samples were ready for dielectric etching.

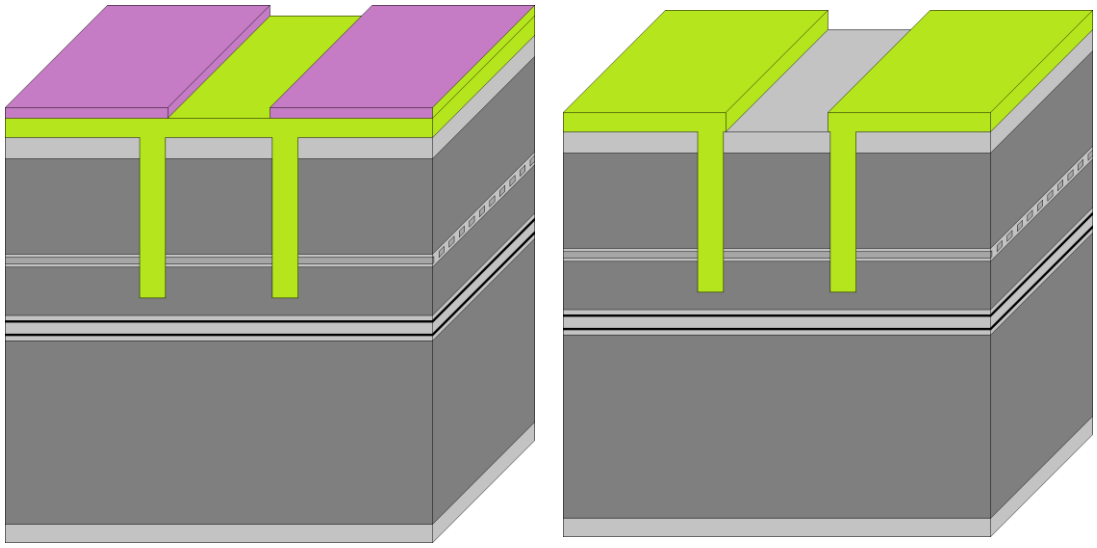

(a) (b)

Figure 3-29: Contact window photolithography and etching

The reactive ion etcher (RIE) was employed to etch the contact window area. The process recipe was: CHF_3 = 35sccm, O_2 = 5sccm, chamber pressure = 35mTorr and RF power = 60W. The etch process was monitored using End Point laser reflectometry. After the curve became flat to indicate the Si_3N_4 was etched through, 30 extra seconds etching time was given to ensure the complete removal of Si_3N_4 in defined area, particularly at edges and in case of non-uniformity. After etching, samples were performed with 5 minute oxygen plasma ash, before the samples were placed in warm

acetone to remove the photoresist**.** It was inspected to ensure that all the resist had been removed and that the dielectric etch was successful.

➢ Step III: P-Contact and bond pad photolithography and deposition

Samples were then spun with PMGI and photoresist SPR 350. The P-contact mask was aligned to the etched contact window pattern. The exposure and development processes were similar to those described above. After 1 minute oxygen plasma ash, samples were ready for metal deposition, as in Fig. 3-30 (a).

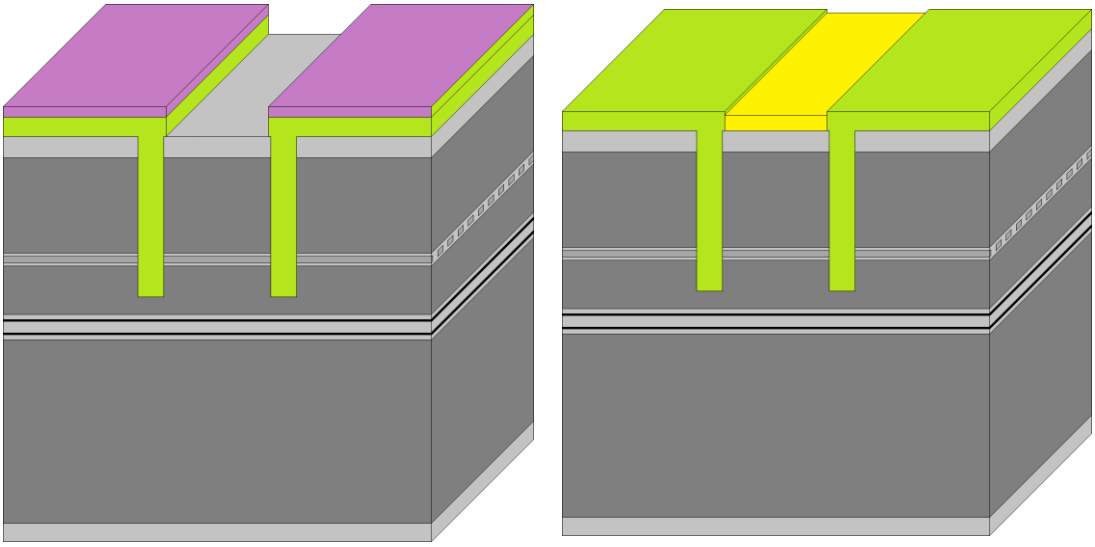

(a) (b)

Figure 3-30: P-Contact photolithography and deposition

For the deposition of Au-Zn-Au P-contact, a thermal evaporator was employed. In the preparation for evaporation, 200mg of gold wire and a 10mg piece of Zinc were placed in tungsten elements. Samples were rinsed in 19:1 H_2O : Analar Ammonia solution for 30 seconds to remove surface oxide, then rinsed in DI water and blown dry. When loading, both heating elements were fixed 6cm above the crystal thickness monitor. Samples were then placed in the chamber underneath the heating elements, close to the crystal thickness monitor. The chamber was pumped down to a pressure of

2×10^{-6}mbar to proceed. The contact deposition included 5nm gold, then 10nm zinc and then 200nm gold. After lifting off and cleaning, to realise the structure picture in Fig. 3-30 (b), the samples were put into the rapid thermal annealer (RTA). The annealing process was set to be 30 seconds ramp and 3 seconds dwell at 360^{o}C.

For the deposition of band pads, the photolithography and metallisation was as above but 200mg of gold wire and 10mg of titanium wire placed in tungsten elements at either side of the sample. The bond pad deposition included 15nm titanium and then 150nm gold from each side of the sample, which is a process usually used in order to coat any sidewalls successfully, resulting in the structure pictured in Fig. 3-31.

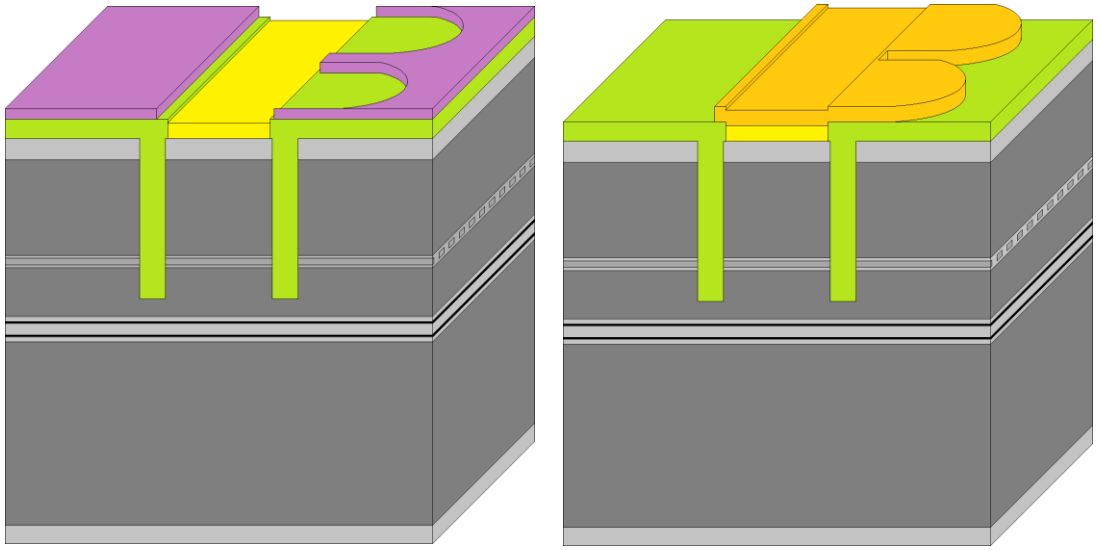

(a) (b)

Figure 3-31: Bond pad photolithography and deposition

➢ Step IV: Back thinning and n-contact deposition

A Logitech LP50 lapper/polisher was employed for substrate thinning. This process is necessary for better heat extraction thereby a higher pumping current limit for high power operation and to allow cleaving of small cavity lengths. In preparation, samples were first spun with a thick layer of photoresist to protect the fabricated feature from

scratches. Then, samples were mounted upside down onto the glass holder of the Logitech LP50 using specialist wax. The lapping media was a 1:9 ratio of 3µm aluminium oxide particles: water. The samples were thinned to around 130µm. After rinsing in DI water, samples were removed from glass holder in warm n-butyl acetate, followed by removal of the protective resist in Acetone and 3-stage cleaning. 20nm/300nm In-Ge/Au back contact was then deposited using a thermal evaporator, followed by RTA annealing at 340^{o}C with 3 seconds dwell.

➢ Step V: Cleaving, AR/HR Coating, Mounting and Bonding

The fabricated samples were cleaved into 1, 2 and 3mm long devices and anti-reflection and high-reflection coatings, with reflectivities of R < 0.1% (AR) and R > 95% (HR) at 1014nm with 25nm bandwidth, were applied to either side of the facets by Helia Photonics. Lastly, some devices were mounted epi-side-up on C-mount or AlO_2 ceramic tiles with InAg paste and bonded using a K&S Ultrasonic Ball Bonder for characterisation purposes.

3.4 DFB Characterisation

Since this research was aimed at high power DFB lasers, the full set of 5 structures was bar-tested (i.e. probed and characterised for L-I, spectrum, resistance etc.) to screen out any poor performing DFB designs and identify suitable devices for further study.

Fig. 3-32 plots the achieved wavelength range of CW-pumped DFB lasers under room temperature operation for this set of designs, in accordance with the grating period. According to the measurements performed over all the 5 DFB designs, devices with 4 out of 10 grating periods (i.e. 150nm, 152nm, 154nm and 156nm) were observed single-mode DFB operation.

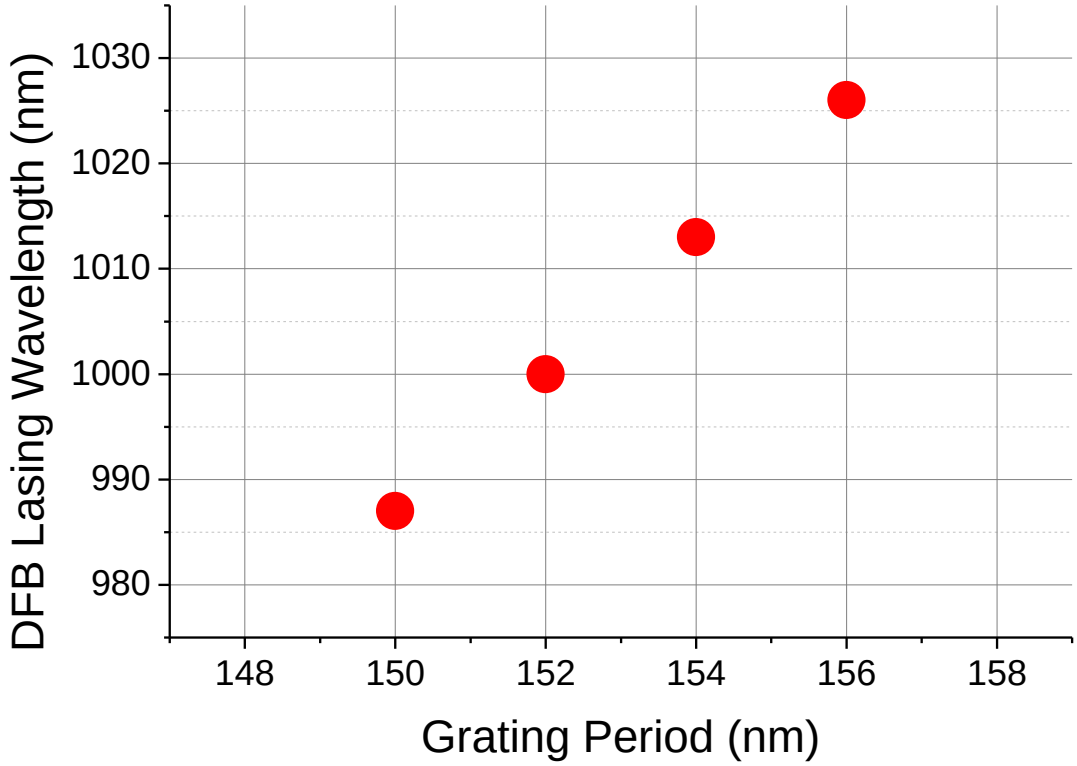

Figure 3-32: DFB wavelength resulting from the grating period, which is averaged from the characterisation of the 5 structures to represent this set of devices for illustration purpose)

In my DFB designs, the Bragg wavelength (λ_B) is determined by grating period (Λ), whilst the ability to lase vis DFB modes depends on the detuning level, i.e. the distance

between the centre of the amplified spontaneous emission (ASE) spectrum and the selected wavelength. Based on the overall measurement, the ASE spectral peak shifted from ~990nm (low current and low substrate temperature) to ~1040nm (high current and high substrate temperature), which allowed DFB laser operation from grating periods of 150/152/154/156nm, as noted in Fig. 3-32 by red dots lasing at ~987/1000/1013/1026nm respectively. This result will be discussed in more detail in Section 3.4.4, together with a discussion of wavelength tunability.

From the calculation of the fit to this plot, an effective refractive index of the fabricated GaAs/InGaP grating was estimated as ~3.29, which was approximately the same (1.2% lower) as the theoretical estimation, 3.33, as used in the Fimmwave waveguide simulation. This slight difference could be caused by the 45^{o} etching angle during the selective wet etch (etchant: HCl/H_3PO_4) at the very bottom of the structure, which resulted in slightly more InGaP than GaAs being present in what was designed as a 50/50 rectangular grating, together with a slight variation in mark-to-space of the pattern generated by EBL.

3.4.1 Characterisation of Two 1mm Long Representative Devices

The L-I bar-test measurement revealed that DFB2 and DFB4 performed better in terms of resistance, threshold, slope efficiency and spectrum. Therefore, two 1mm-long devices of each of DFB 2 and DFB 4 were firstly mounted on C-mounts and measured at room temperature under CW operation due to their possibility for attaining high power performance.

A C-mount is illustrated in Fig. 3-33 with the top-view optical microscope image of a mounted 1mm DFB laser, where the sample is mounted epi-side-up to the plated CuW submount with the P-bond-pads wired to the side stripe.

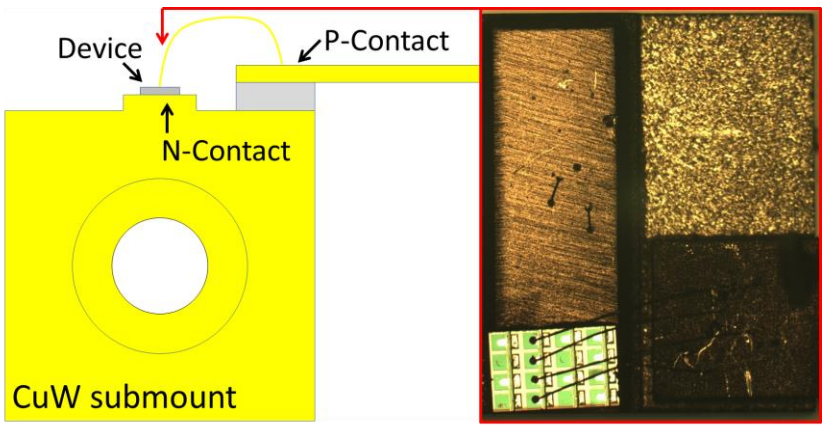

Figure 3-33: Illustration of a C-mount and the top-view of a mounted DFB laser

These 2 devices were representative of the set of lasers in each bar. Since the temperature-induced wavelength shift of the ASE spectral peak changes more rapidly than that of the DFB peak, the 152nm grating period was selected because the corresponding Bragg wavelength was experimentally measured to be slightly on the longer wavelength side of the gain peak. Therefore, when pumped to high currents such as require for high power, the resultant rise in temperature brings the gain peak into resonance with the Bragg wavelength.

➢ Representative Device 1: DFB-2 (2×QWs)

Fig. 3-34 shows the L-I-V measurement of a 1mm device with 152nm grating period of DFB 2 structure. It was mounted on a C-mount using indium-based paste and tested at room temperature (~17^{o}C) using a CW current source.

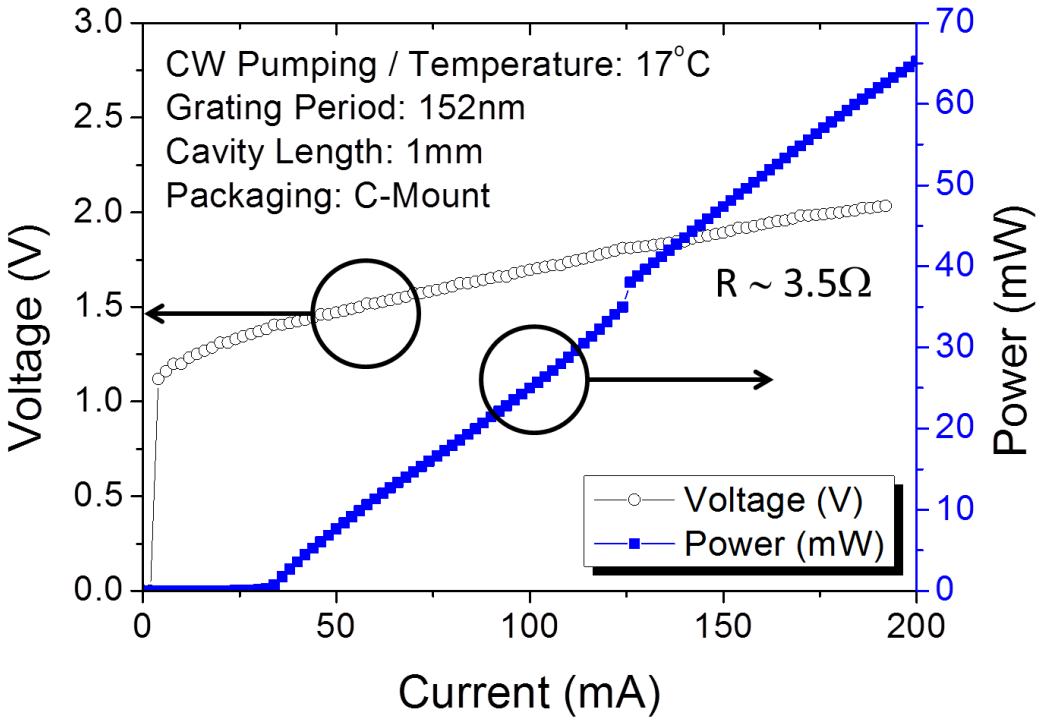

Figure 3-34: L-I-V measurement of a 1mm representative device of DFB 2

Fig. 3-35 present the electroluminescence spectral recorded with injected current from 40mA to 200mA. In the figure, (a) shows a single peaked response from 40mA to 100mA and a dual mode response since 120mA to 200mA; (b) shows a colour-filled-contour version of these spectra graphically presenting the appearance of the second mode by showing the change in spectral intensity as a function of current; (c) plots the extracted peak wavelength and SMSR as a function of the injected current, where the peak in the SMSR of ~37dBm was recorded at 60mA before reducing with the increasing current.

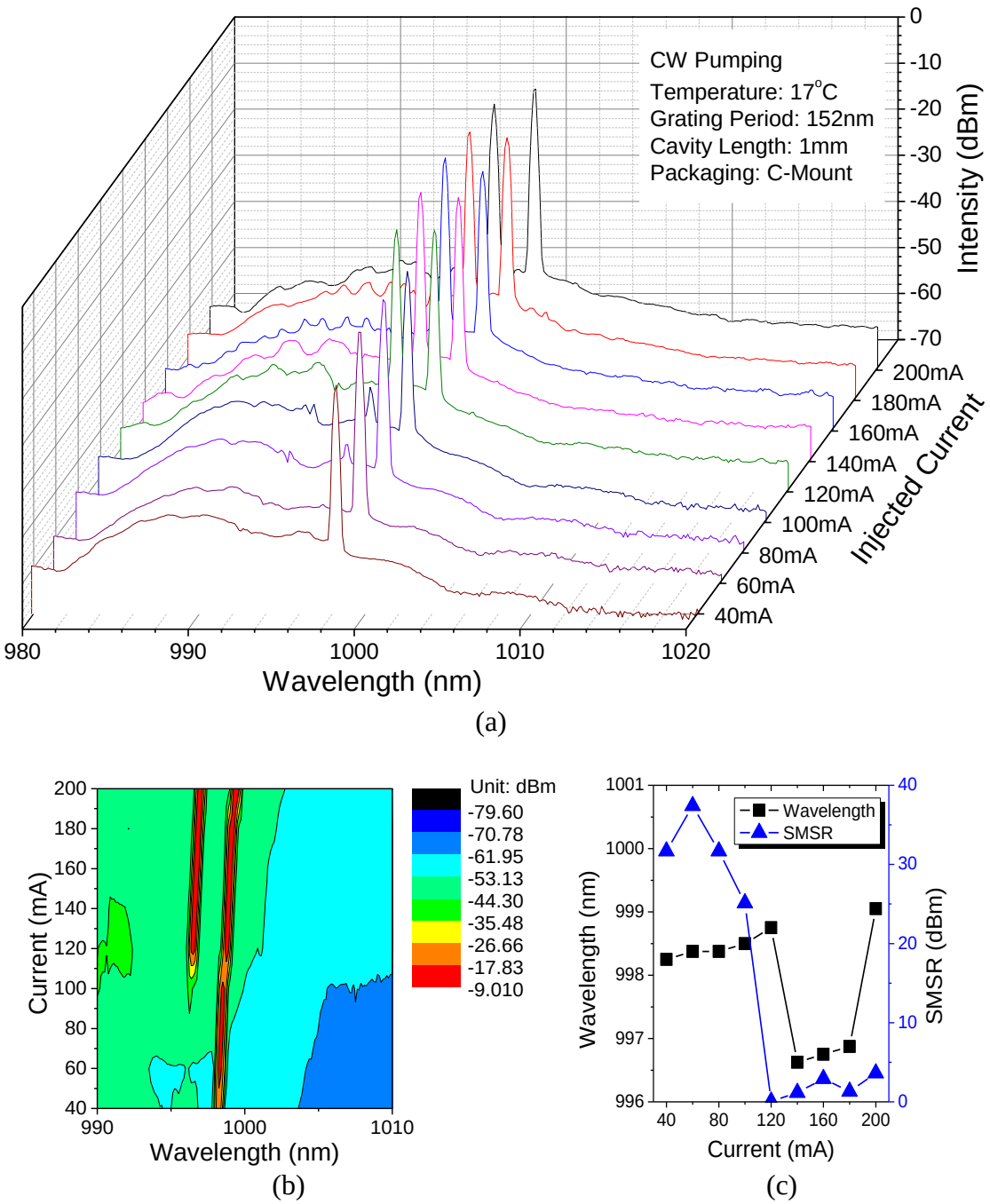

Figure 3-35: (a) EL spectra recorded with current injection from 40mA to 200mA, (b) Colour-fill contour plot of the recorded spectra and (c) the peak wavelength and SMSR plotted as a function of injected current. The plots show that a second mode appears within the current injection range of 100-120mA

These plots (Fig. 3-34 and 3-35) show that the device starts lasing with a threshold of ~30mA. As shown in Fig. 3-35 (a) and (b), the device exhibits a single lasing mode upon lasing at ~998nm from a current of 40mA up until 100mA, before a 2nd mode at ~996nm appears since 120mA. With more injected current, both modes exist simultaneously. Fig. 3-35 (c) plots the wavelength shift and SMSR as a function of

current. The plot shows that the device operates with an SMSR higher than 25dBm from 40mA to 100mA. In this range, the laser demonstrates single mode lasing with an output power reaching ~25mW at 100mA and with an SMSR larger than 25dBm. Above 100mA, the power continues to rise (e.g. 65mW at 200mW) however, with power split over 2 lasing modes.

➢ Representative Device 2: DFB-4 (4×QWs)

Fig. 3-36 shows the L-I-V measurement of a 1mm device with 152nm grating period of DFB 4 structure. It was mounted on a C-mount using indium-based paste and tested at room temperature (~17°C) using a CW current source. This device behaves very similarly to DFB2 above, but with slightly higher power available.

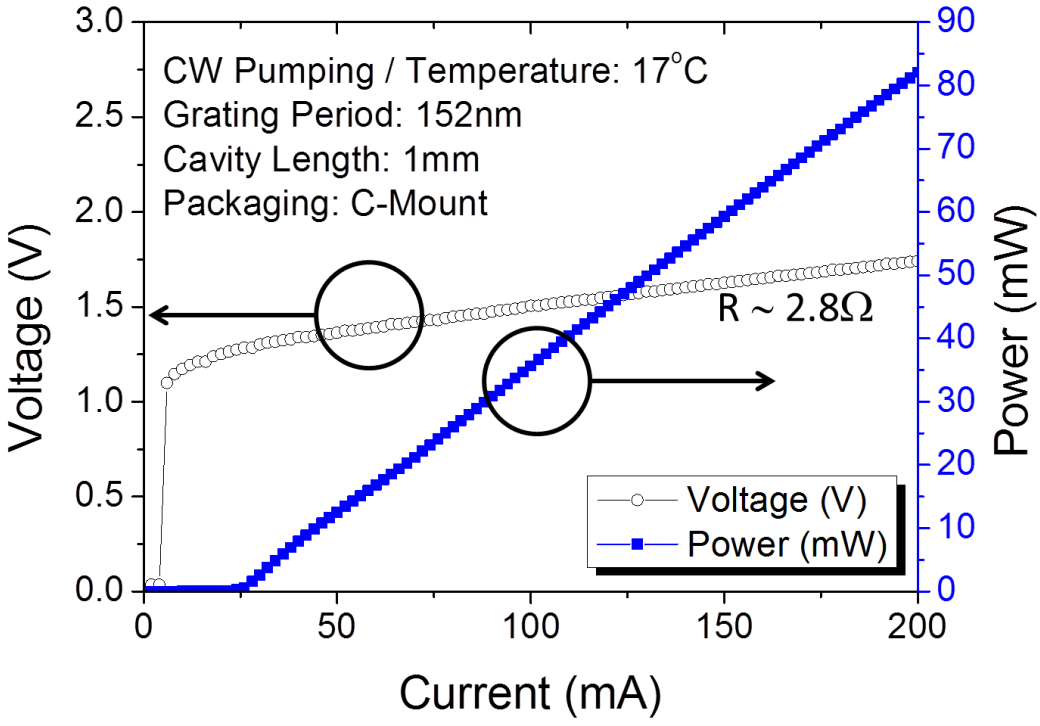

Figure 3-36: L-I-V measurement of a 1mm representative device of DFB 4

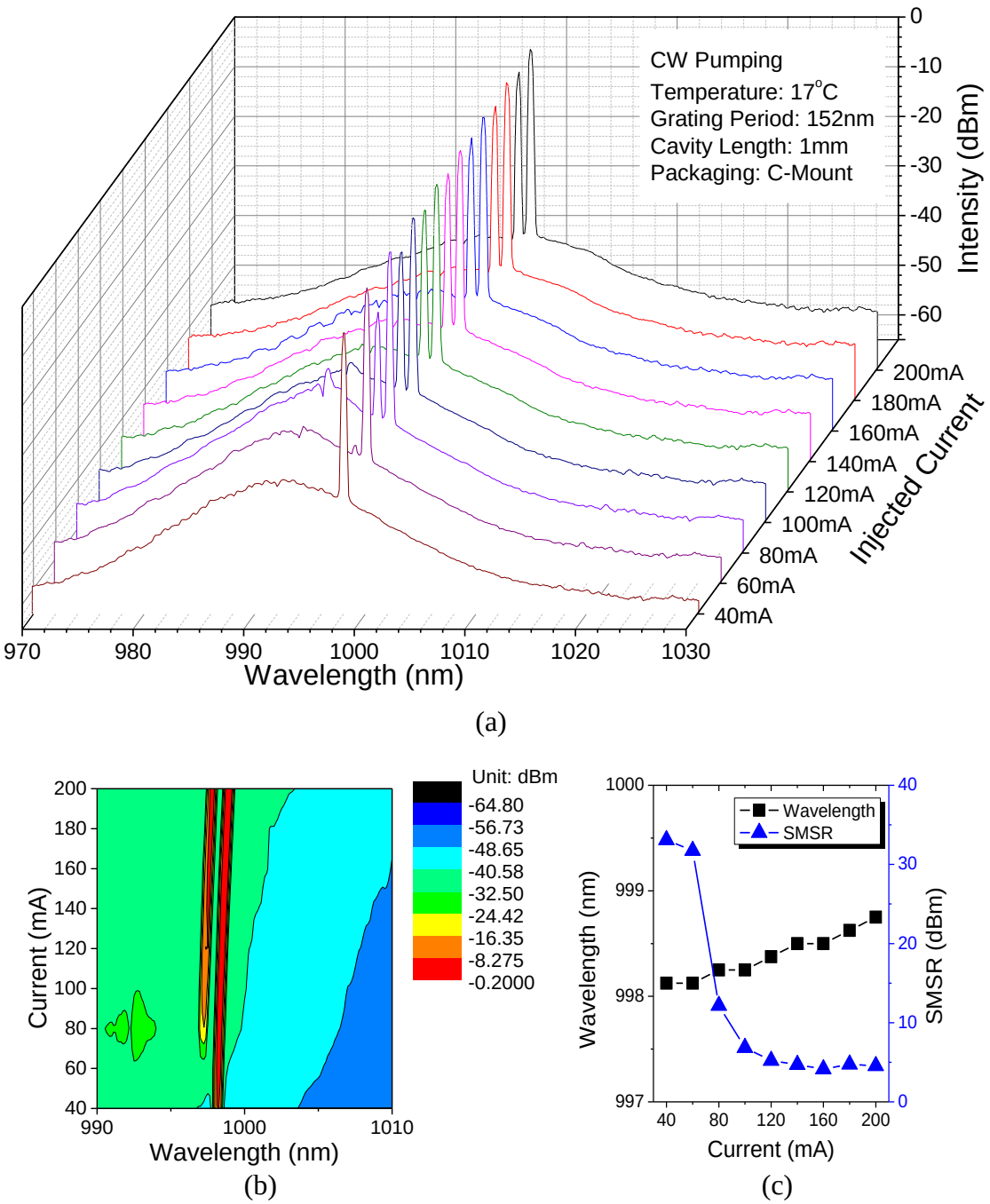

Figure 3-37: (a) EL spectra recorded with current injection from 40mA to 200mA, (b) Colour-fill contour plot of the recorded spectra and (c) the peak wavelength and SMSR plotted as a function of injected current. The plots show that a second mode appears within the current injection range of 60-80mA

Fig. 3-37 (a) present the electroluminescence spectra recorded with injected current from 40mA to 200mA, showing a single peaked response from the lasing threshold to 60mA and a dual mode response between 80mA to 200mA; (b) presents a colour-filled-contour version of (a) plotting the spectral intensity as a function of current and wavelength which graphically shows the appearance of the second mode; (c) plots the

extracted peak wavelength and SMSR as a function of the injected current, where the peak in the SMSR drops from ~33dBm at the current of 40mA to ~4dbm at the current of 120mA, which corresponding to the appearance of the second mode at the current of 80mA.

These plots (Fig. 3-36 and 3-37) show that the device starts lasing with a threshold of ~25mA. Upon lasing, the device exhibits a single lasing mode at 998nm, as shown in Fig. 3-37 (a) and (b), up until a current of ~70mA, where a 2nd mode appears. With more injected current, both modes exist simultaneously. As shown in Fig. 3-37 (c), the device operates with an SMSR higher than 30dBm from 40mA to 60mA, and drops to <15dBm at 80mA due to the appearance of the second mode. In this range, the laser demonstrates single mode lasing with an output power of ~17mW at 60mA with an SMSR ~ 32dBm. Above 80mA, the SMSR continues to reduce and maintains as low as 4dBm from 120mA to 200mA, where the 2 modes exist simultaneously, whilst the power increases approximately linearly as a function of the injected current up to 82mW at 200mA however, with power split over 2 lasing modes.

➢ Discussion

Within the range of injection currents corresponding to single mode operation, both representative devices perform much better than the 1mm DFB laser reported in [4], in which a CW threshold of 62mA with an output power of 7.9mW at 93mA with an SMSR of 28.3dB was demonstrated. Compared to this initial realisation, the threshold current is reduced to ~25mA (DFB 2) and ~30mA (DFB 4). Furthermore, the single mode output power obtained with high SMSR~30dBm is larger, with ~18mW at 80mA (DFB 2) and ~17mW at 60mA (DFB 4) versus only 7.9mW at 93mA in [4]. The laser in

[4] exhibited single mode operation over a small range of currents due to there being no AR coat and multiple stich errors between the 10 E-beam lithography write-fields required, and it was expected that the present design could provide a remedy to this, with single-mode operation over a much broader range of currents. The existence of a 2nd mode in both Fig. 3-35 and 3-37 could be because of the DFB mode hopping phenomenon or multiple lateral modes. For the DFB mode hopping phenomenon, the DFB lasing mode hops from one wavelength to another (usually from one mode to the next longer wavelength mode) due to the shift in the gain peak. However, longitudinal DFB modes tend to shift from one mode to another with the increasing current or temperature, rather than lase simultaneously as is observed here. The dual-mode operation observed from both DFB 2 and DFB 4 devices is indicative of two lateral modes competing in the waveguide. In order to further confirm this suspicion, the far-field beam profile of light exiting the facet of DFB 2 was measured.

➢ Examination of Far-Field Beam Profile

The far-field beam profile measurement was performed using a Photon-Inc Goniometric Radiometer LD8900R, as described in Chapter 2, by placing the device such that its facet is positioned 1mm away from the light entrance slit of the equipment. Fig. 3-38 (a) illustrates the fast/slow axis as the light exiting the facet.

Fig. 3-38 (b) and (c) plots the far-field profile measured at 60mA, 130mA and 160mA CW current pumping using the cross-sectional profiling mode and 3-D profiling mode respectively. As shown, at 60mA, the beam profile shows a single lateral mode. However, with increasing current, a second lateral mode appears in the beam profile recorded at 130mA. As more current is injected (from 130mA to 160mA), the second

mode grows stronger. One can expect that the appearance of this second lateral mode could be the reason for the appearance of the second peak in the emission spectrum. This measurement of the far-field beam profile of the representative device 1 (DFB2) provides further evidence to support the hypothesis that a second lateral mode is propagating in the waveguide

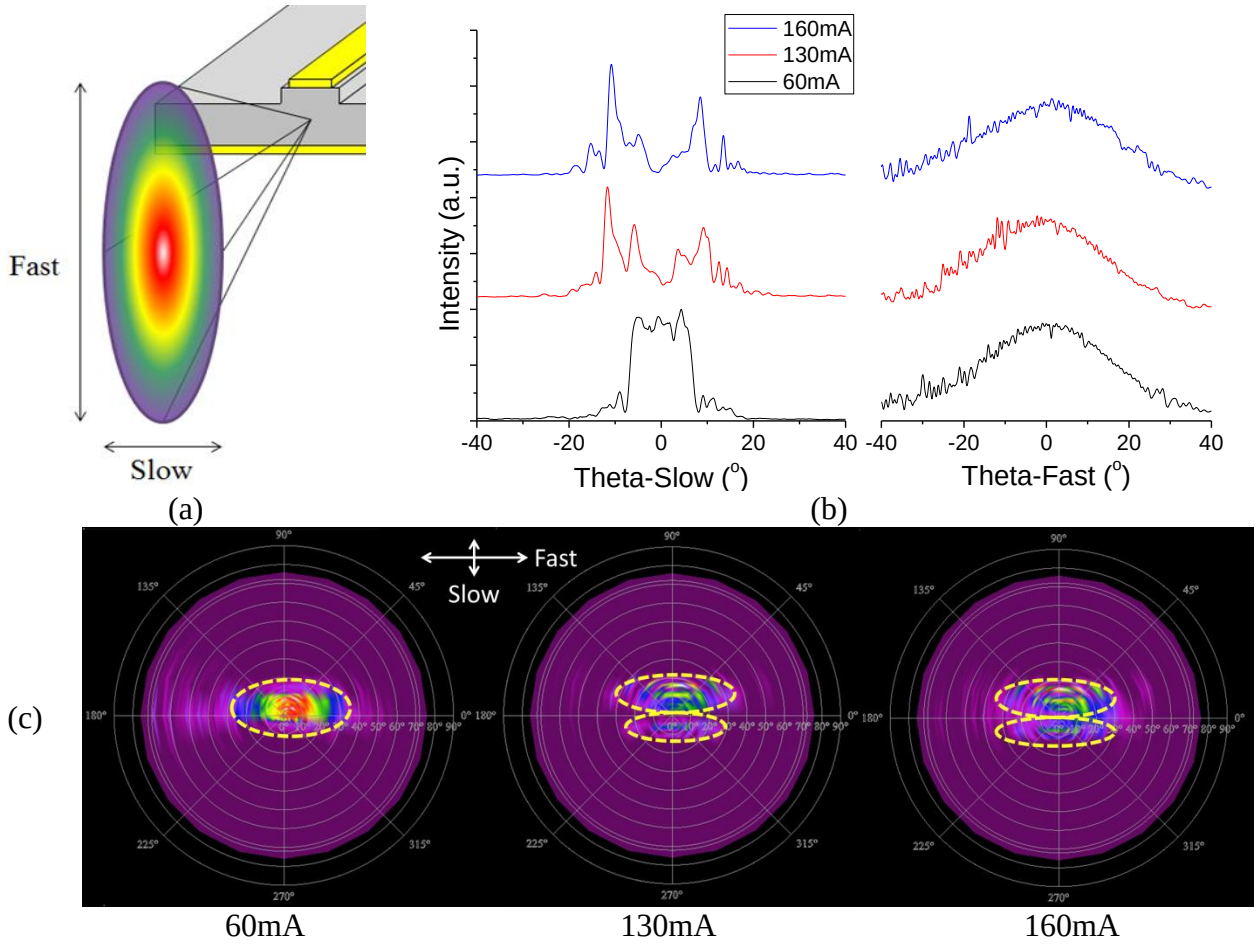

Figure 3-38: (a) Illustration of the fast/slow axis of the far-field beam profile measurement; (b) the far-field beam profiles recorded with injected current of 60/130/160mA; (c) 3-D view of the beam profiles recorded

The simulation activity in Section 3.1.3 resulted in an etch depth being defined for which only the fundamental optical mode is supported. However, upon examination of the fabricated laser structures, it became apparent that the etch depth was not as it was designed to be. When forming the 3μm ridge, the devices had been accidentally over-etched.

During fabrication, instead of a trench-etch depth of 1.5µm, terminating inbetween the grating layer and active region as designed, the ridge had been etched to a depth of 2.5µm, through the active region and terminating some distance into the lower cladding. In order to verify the effect that this over-etch would have on the beam profile, the waveguide was re-simulated using this revised etch depth.

3.4.2 Re-Simulation of Over-Etched Ridge Waveguide

The simulation of optical modes is shown in Fig. 3-39 for an etch depth of 2.5µm. In contrast to Fig. 3-3, 3-5 and 3-6, this waveguide may support 2 lateral optical modes.

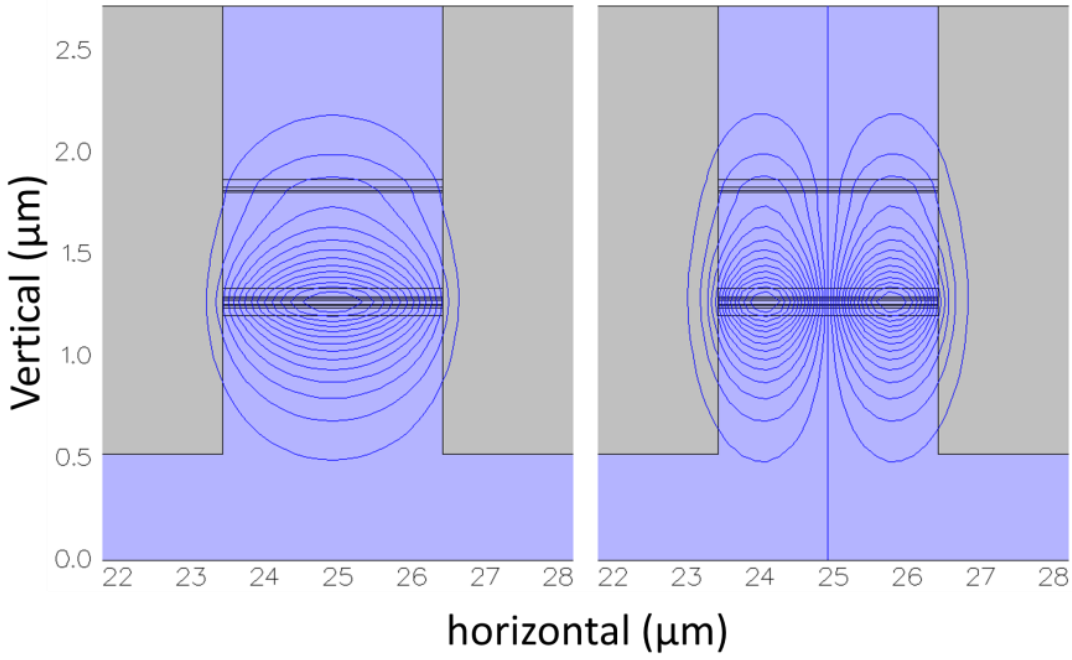

Figure 3-39: Re-Simulation of the Actual Ridge Structure

Therefore, during characterisation of these devices, it is possible that there were 2 competing lateral modes propagating in the laser cavity as observed in the far-field profile in Fig. 3-38. One lateral mode enjoys a relatively lower threshold such that the devices start lasing on a single mode. With increasing pumping current, at some point,

the second mode reaches threshold and also begin to lase, resulting in a dual-mode laser.

From the far-field beam profile examination shown in Fig. 3-38 (b) in Section 3.4.1, it is suggested that the laser starts lasing via the fundamental mode, and then switches to 2 competing lateral modes. It is noted that the mode profile observed from the slow-axis profile at 60mA was not the expected Gaussian-like profile. This was because the transition from lasing via the fundamental mode to lasing via multiple lateral modes starts soon after the lasing threshold is overcome for this 1mm device. A later far-field examination of a 3mm-long DFB laser shows the Gaussian-like distribution, where a longer cavity introduces a greater difference in threshold gain between the two modes, resulting in single mode operation over a broader range of currents.

3.4.3 Characterisation of Longer Devices

Sections 3.4.1 and 3.4.2 demonstrate that the over-etched waveguides could support multiple lateral modes. Therefore, in real operation, due to imperfections in the waveguide, two modes are in competition in the waveguide. One of the two modes enjoys a relatively lower threshold such that lasing commences via this single mode. With increasing current, the other mode also reaches threshold and the laser then operates in a dual-mode manner. Due to this mechanism, a longer cavity length could theoretically increase the difference between the thresholds of the two modes, such that the device operates single mode over a wider range of currents.

A 3mm long DFB 4 device was mounted on a C-mount for measurement. Fig. 3-40 plots the CW L-I-V characteristics measured from this device. A device resistance was

calculated as 1.15Ω from the I-V plot. The threshold current and slope efficiency were extracted from this data as 55mA and 0.325mW/mA respectively.

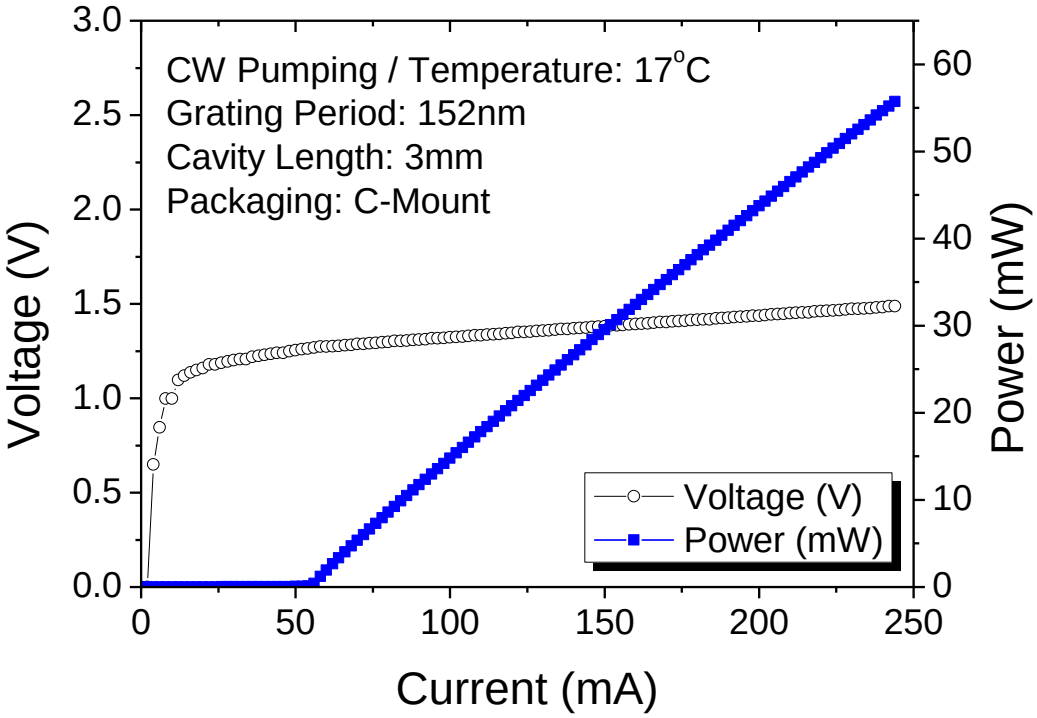

Figure 3-40: L-I-V measurement of a 3mm representative device of DFB 4

Fig. 3-41 (a) and (b) presents the EL spectra recorded from the device at the CW injection current range of 60 to 250mA, demonstrating single mode operation in this current range. Fig. 3-41 (c) plots the lasing wavelength and SMSR as a function of current measured from 60mA to 250mA. The device starts lasing via a single DFB mode from 70mA (at 997.8nm with >35dBm SMSR) and continues to operate in this way until a current of 250mA (at 998.3nm with >44dBm SMSR). This measurement provides strong evidence to support the assumption that longer length laser cavities help to expand the threshold difference between the supported lateral modes, resulting in extension of the single mode operation to higher currents (hence to correspondingly higher output power).

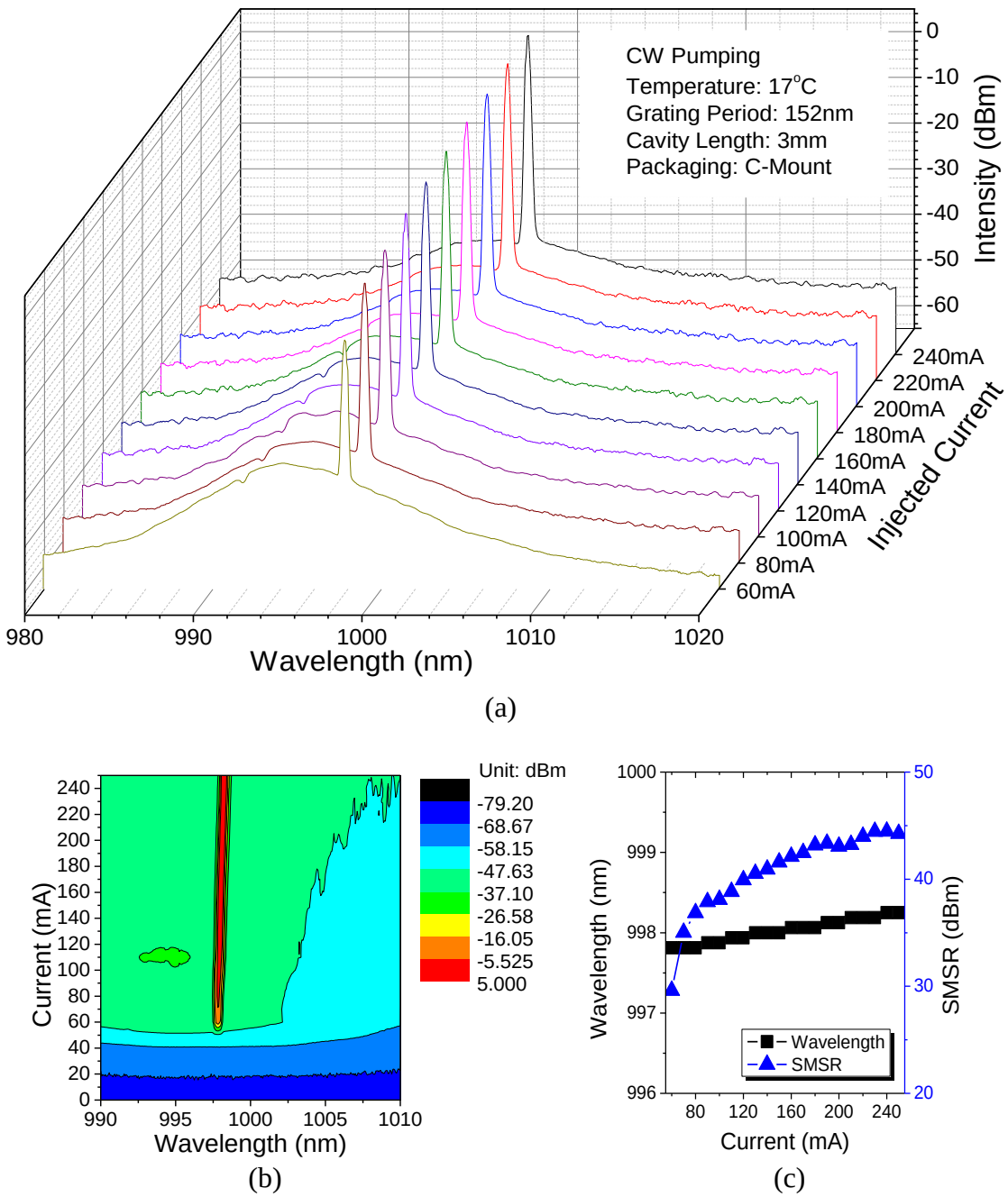

Figure 3-41: (a) EL spectra recorded with current injection from 60mA to 240mA, (b) Colour-fill contour plot of the recorded spectra and (c) the peak wavelength and SMSR plotted as a function of injected current. The device demonstrates single-mode DFB operation up until 250mA

Fig. 3-42 presents the experimentally measured far-field beam profile of this 3mm DFB laser (solid lines), which was taken with a current injection of 60mA. The Gaussian-like distribution of measured divergence in both fast and slow axis is in agreement with the previous assumption that the devices operate via the fundamental mode upon reaching the threshold. Correspondingly, the measurement was compared to

the simulated profile of the supported fundamental mode extracted from the waveguide modelling.

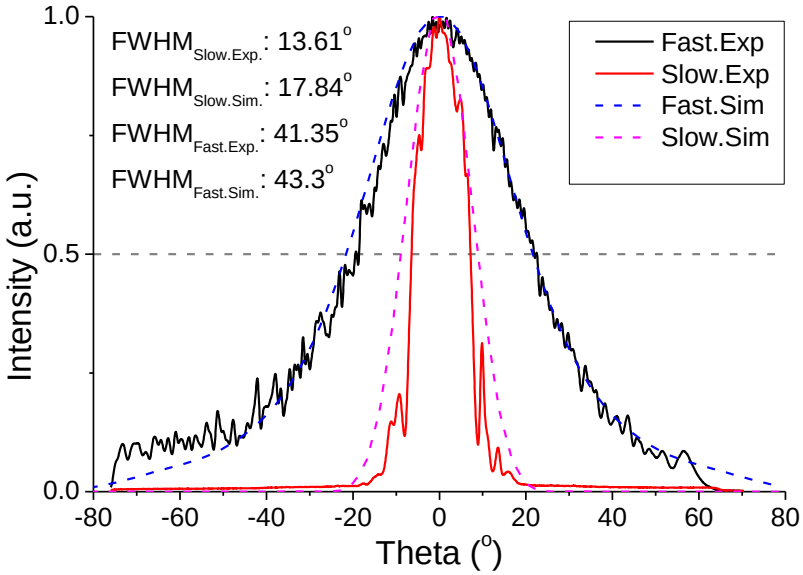

Figure 3-42: Comparison of far-field beam profile between experimental (solid lines) measurement and simulation result (dotted lines)

This comparison shows that the experimentally measured vertical divergence (fast-axis) matches that simulated, with FWHMs of 41.35° and 43.75° respectively. However, the measured lateral divergence is narrower than that simulated, with FWHMs of 13.61° and 17.84° respectively. This could be a result that, the fundamental mode was modelled in an individual manner in the simulation, while in the real operation, the competition between modes exists although the laser operates via a single mode upon reaching the threshold.

3.4.4 Thermal and Current Tuning Measurement

Another important characteristic of DFB lasers is the tunability, as required for spectroscopic applications. Furthermore, tunability of DFBs in this range could be useful in realisation of tunable THz sources by difference frequency generation, and also in frequency doubled applications, e.g. display. A typical $\Delta\lambda$ of thermal tuning of a DFB laser is a few nanometres with a tuning rate of 0.08-0.1 nm/^{o}C [20]-[22].

The DFB lasers were therefore characterised as a function of temperature (thermal tuning) and current (current tuning) to investigate their tunability. A 1mm long DFB laser (DFB 2, grating period: 154nm) was cleaved. By increasing the operating temperature of a DFB laser, the operational wavelength shifts to longer wavelength (red-shift) due to the changes in refractive indices within the grating structure. Besides controlling substrate temperature, the self-heating mechanism induced by increasing the pumping current is another method sometimes used for red-shifting the emission. The device was mounted with indium-containing paste on an AlO_2 ceramic tile and bonded with gold wires. Compared to a C-mount, ceramic tiles exhibit poorer thermal conductivity. As the sample was tested at elevated temperature, a grating period of 154nm was chosen instead of 152nm, in order to better match the red-shifted gain spectrum.

➢ Thermal Tuning

The EL spectrum of DFB 2 is shown in Fig. 3-43, recorded at a fixed CW pumping current of 60mA over a range of temperature from 25^{o}C to 65^{o}C. A single laser peak is observed over this temperature range and a wavelength shift of 4.5nm is measured,

corresponding to a tunability of 0.1125nm/^{o}C. Compared to the values reported in [20]-[22], this is a relatively high tuning rate, which could result from the additional self-heating generated by CW pumping of a poorly heat-sunk device. In any case, the single mode is maintained throughout the complete tuning range, demonstrating its suitability for use in its intended applications.

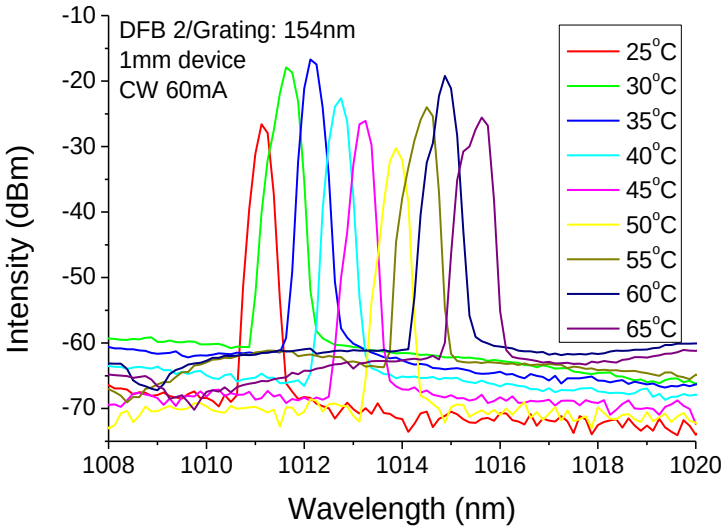

Figure 3-43: Thermal tunning with 60mA CW Current Pumping

Fig. 3-44 plots the peak wavelength of the DFB mode and the spontaneous emission peak, which is representative of the gain peak, as a function of temperature. The gain peak is observed to shift much more rapidly than the DFB mode, at a rate of ~0.725nm/^{o}C.

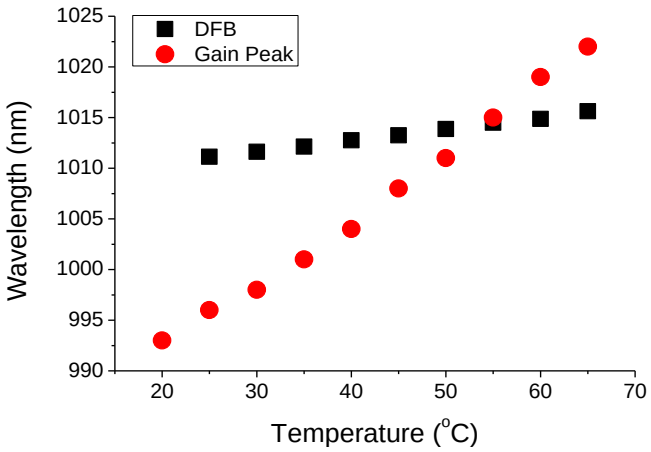

Figure 3-44: Wavelength shift of DFB peak and gain peak against temperature

This is as expected since the E_g has a greater dependence on temperature than the refractive index in the grating does. Hence the operating temperature is an important condition in DFB design, due to the requirement to match λ_B with λ_{gain}.

➢ Current Tuning

Current tuning in DFB laser is a result of current-induced local temperature increase inside the device and its subsequent effect on the refractive index profile of the grating. Fig. 3-45 plots the current tuning of the same DFB laser (DFB 2, 154nm grating period, 1mm length) tested at a fixed heat-sink temperature of 25°C over a range of CW pumping currents from 40mA to 100mA. A wavelength shift of 1.375nm is measured over this current range for the single laser mode, corresponding to a current tuning of 0.023nm/mA.

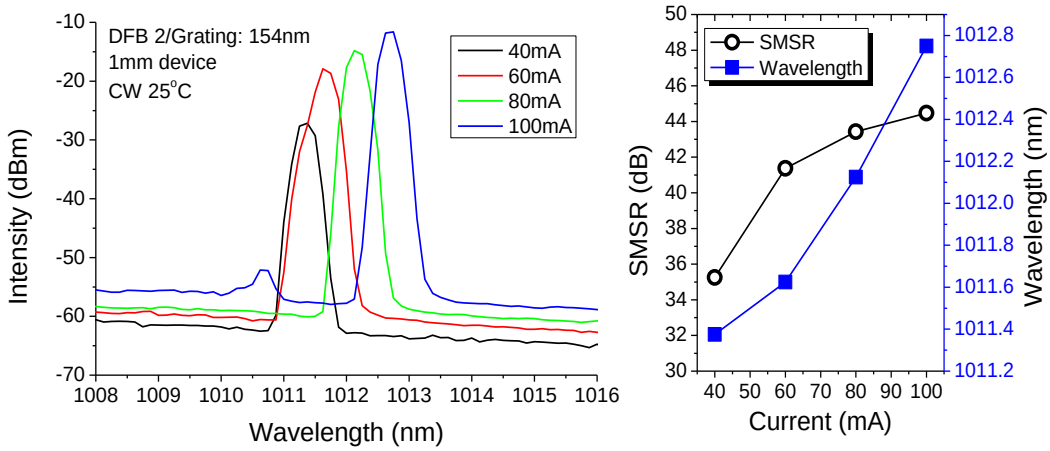

(a) (b)

Figure 3-45: (a) CW current tunning with heat-sink temperature fixed at 25°C and (b) extracted SMSR and DFB peak against injected current

The SMSR for this laser is plotted in Fig. 3-45 (b) as a function of current, together with the peak wavelength. As the current is increased above the laser threshold current, the SMSR is observed to increase, together with an increase in the peak wavelength. The rate of red-shift in lasing wavelength increases with increasing current, and

commensurately, as the current is increased, the rate of increase in SMSR diminishes, saturating at a very high 44dB.

3.4.5 Overall Summary of DFB Tuning Measurement

Measurement of the peak wavelength of different period DFB lasers were synthesised in order to enable construction of a wavelength map. Fig. 3-46 summarises the full extent of DFB laser tunability through both thermal and CW current tuning. This plot aims to identify the lasing wavelength attainable under different heat-sink temperatures and pumping currents of the whole set of DFB lasers.

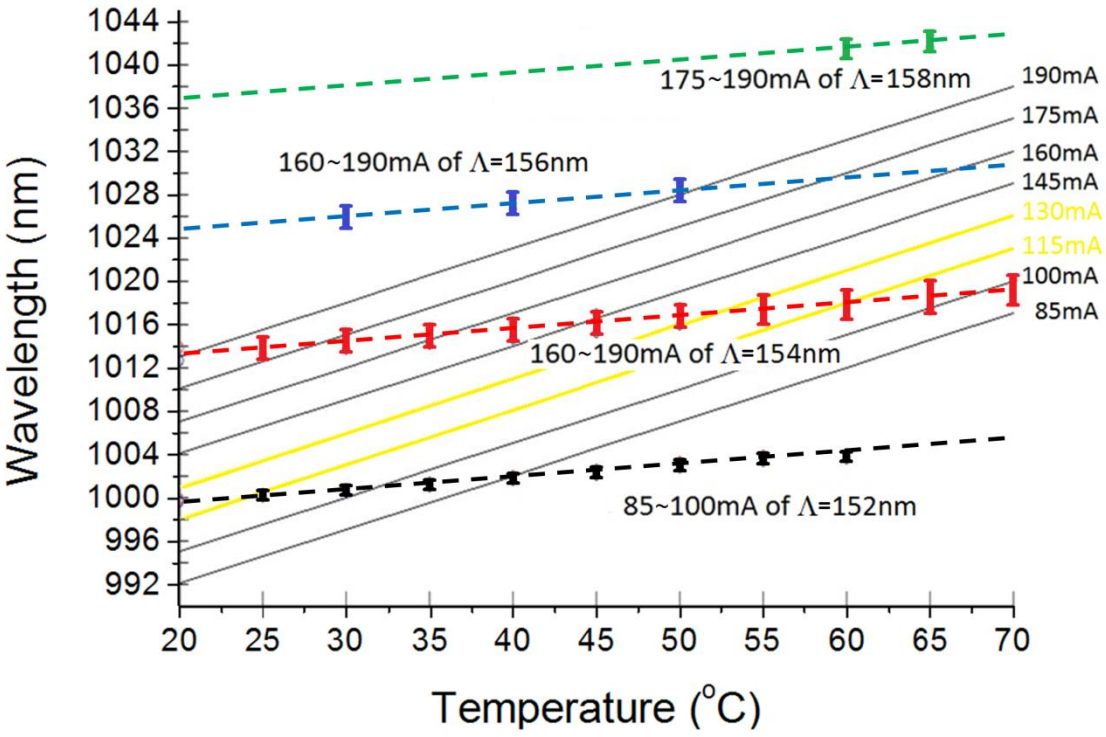

Figure 3-46: Summary of DFB tuning measurement of temperature and CW pumping current, where the recorded DFB wavelength shifts of 4 different grating periods are compared to that linearly apporximated for the gain peak

The black and yellow solid lines represent a linear approximation to the wavelength shift of the gain peak with temperature at different pumping currents (85-190mA). The

yellow lines represent an estimation of pumping currents, 115mA and 130mA, which were not actually measured but seen as a guide. The dashes represent the DFB lasing wavelengths measured at different temperature, with different grating periods highlighted by different colours, where the smaller current tuning effect result in a vertical dash of wavelength points as a function of current at each current. Hence the vertical range of a dash illustrates the current tuning at a certain heat-sink temperature over the annotated current range.

For example, for a device with a 154nm grating period (red dashes), when operating with a current injection of 160mA under 40^{o}C heat-sink temperature, the DFB lasing wavelength would be at ~1015nm, being approximately on the gain peak at ~1017nm. For a device with a 156nm grating period (blue dashes), the lasing wavelength under the same condition would be on the red side of the gain peak in the range of 1024~1026nm.

3.4.6 Comparison of Experimental and Simulated Coupling Coefficients

As outlined in Section 3.1, the purpose of the different DFB structural designs was to fine-tune the ability to simulate and design DFB lasers according to the required cavity length. According to the theory introduced in Section 2.1.2, the coupling coefficient (K) of a DFB laser with a uniform grating (non-λ-shifted) at a given cavity length (L) can be approximated from measurement (K_{meas}) of the longitudinal mode spacing (Δv_{long}) and the spacing between the two DFB modes (Δv), which is related to the stopband by the equation:

$$K_{meas} = \frac{\pi \times \Delta v}{2 \times L \times \Delta v_{long}}$$

Fig. 3-47 shows an example of how the coupling coefficient is calculated from measurement of a 1mm DFB1 laser with $\Delta\nu$ obtained from the plot of the central wavelength region and $\Delta\nu_{long}$ obtained from the F-P modes. As annotated on the figure, $\Delta\nu$ and $\Delta\nu_{long}$ were measured as 1.27cm^{-1} and 1.80cm^{-1} respectively, from which a K_{meas} of 22.23cm^{-1} was then approximated.

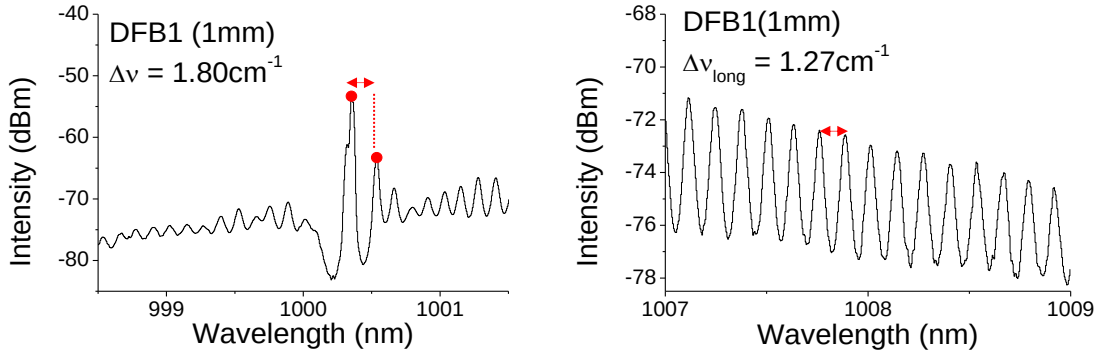

Figure 3-47: The $\Delta\nu_{long}$ and $\Delta\nu$ measurements of a 1mm long DFB1 laser

The coupling coefficient (K) for a 50/50 rectangular grating is linked to the Bragg wavelength (λ_B), optical confinement factor in grating layer (Γ_g), and the refractive index difference between the grating materials (n_1 - n_2) by the equation:

$$\Gamma_g = \frac{K\lambda_B}{2(n_1 - n_2)}$$

Therefore a set of simulated coupling coefficients (K_{simu}) can be calculated for DFB 1-5 from the measured DFB lasing wavelength (λ_{meas}) and the re-simulated grating confinement factor ($\Gamma_{re\text{-}simu}$), where a 2.5μm etching depth (as actually fabricated) is used instead of the 1.5μm as originally designed, using the equation:

$$K_{simu} = \frac{2\times\Gamma_{re-simu}\times(n_{\mathrm{GaAs}} - n_{\mathrm{InGaP}})}{\lambda_{meas}}$$

$where\ n_{GaAs} \sim 3.51\ and\ n_{InGaP} \sim 3.15$

Table 3-10 summarises the measurements of $\Delta\nu_{long}$ and $\Delta\nu$ from DFBs 1 to 5, from which a K_{meas} was approximated for each laser. There was no specific reason for

choosing different cavity length lasers, since this would not influence the comparison because the related equations are independent on cavity length. A comparison can then be made between K_{meas} and K_{simu} for each DFB laser.

	L	$\Delta\nu_{long}$	$\Delta\nu$	$\boldsymbol{K_{meas}}$	$\Gamma_{re\text{-}simu}$	$\boldsymbol{K_{simu}}$
Unit	(cm)	(cm^{-1})	(cm^{-1})	(cm^{-1})	($\times10^{-3}$)	(cm^{-1})
DFB1	0.1	1.27	1.80	**22.23**	2.90	**20.87**
DFB2	0.2	0.66	1.30	**15.49**	2.02	**14.54**
DFB3	0.1	1.29	2.75	**22.53**	3.18	**22.89**
DFB4	0.3	0.45	1.08	**12.69**	2.11	**15.19**
DFB5	0.1	1.27	1.42	**17.51**	2.17	**15.64**

Table 3-10: Coupling coefficient measurement

The re-simulated coupling coefficient of the 5 over-etched DFB structures matches with the experimentally obtained coupling coefficients within 16.5%, especially for DFB1 (+6.5%), DFB2 (+6.5%) and DFB3 (-1.6%). A slightly larger difference was observed for DFB4 (-16.5%) and DFB5 (+12.0%). As a reminder of the difference between these structures, if DFB 1 is the control structure, DFB 2 has larger AlGaAs spacer and DFB 3 has thicker grating layer compared to DFB1. So DFB 1 should have a larger *K* than DFB 2 but less than DFB 3. DFBs 4 and 5 were designed (originally) to have *K* approximately equal to DFB 2, despite containing more QWs.

For this batch of devices, because of the AR/HR (<0.1% and >95% at 1014nm with 25nm bandwidth) coatings, there will be reflections and hence the DFB laser becomes phase-shifted due to the facet phase issue. As pointed out in [23], the measurement of the value of *KL* is theoretically established from the stopband (calculated from the wavelengths of the two DFB modes). However, errors in their measurement can arise due to alteration of the spectrum caused by facet reflections and facet-to-grating phase variability. For the estimation of the stopband for a low-facet-reflectivity (0.05%) DFB laser with *KL*~1, accuracy is typically of ±25% [23]. In [23], it was demonstrated by performing a mathematical calculation of a laser with *KL*~2.1, that the frequency at

which to measure the stopband and the corresponding obtained width are measured depends on the variation of facet phase. In a critical condition, a "random-phased" DFB laser with no shift in its grating can operate as a λ/4-shifted (or 2×λ/8-shifted) DFB laser. Instead of having two modes on either side of the Bragg wavelength, such lasers have only one lasing mode exactly at the Bragg wavelength. As an example, Fig. 3-48 (a) plots the spectrum recorded from a 1mm long DFB3 laser. The stopband of such a spectrum was approximated by measuring the spacing between the troughs at either side of the main spike, as annotated by the red dots.

For the purpose of illustration, Fig. 3-48 (b) plots 2 spectral examples of DFBs with low facet reflectivity taken from the DFB sections of the self-aligned stripe master oscillator power amplifier (SAS-MOPA) devices (discussed further in Chapter 5), in which the MO (DFB) sections have one end monolithically integrated with a subsequent semiconductor optical amplifier (SOA) section, and the DFB side cleaved facet is AR-coated to 0.1% (at 1050nm). Both spectra show a clear dual-mode sub-threshold profile, making extraction of the key parameters for coupling calculation more straightforward.

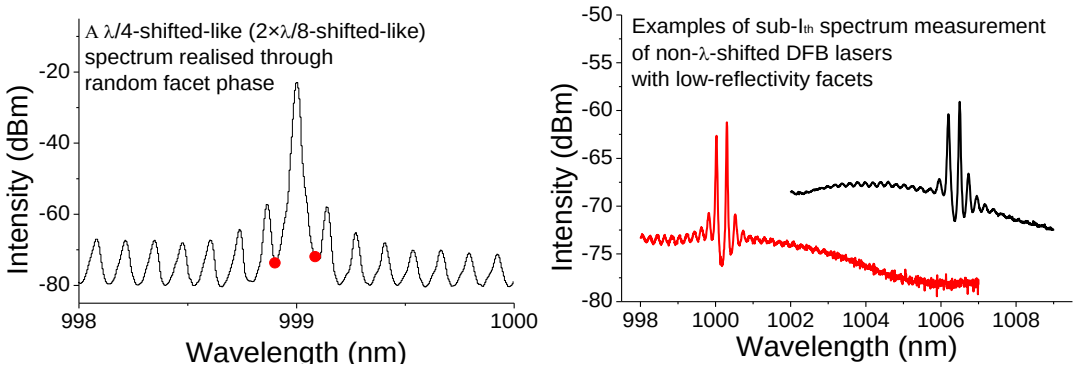

Figure 3-48: Spectrum measurement: (a) a 1mm non-λ-shifted DFB3 laser demonstrated a λ/4-shifted-like (or 2×λ/8-shifted-like) DFB spectrum and (b) examples of sub threshold spectrum of non-λ-shifted DFB lasers with low facet reflectivity

Therefore the measurement-to-simulation comparison demonstrated a high level of consistency within a relatively small error range of (-16.5%, +12.0%), and is, perhaps, as strong a correlation as we could hope for, given the facet coating scheme employed.

3.5 Conclusion

In this chapter, a set of 5 GaAs-based strain-balanced InGaAs QW DFB structures have been designed, manufactured and characterised. The original purpose of this batch of designs was to enable the manufacture of high output power DFB lasers (hundreds of mWs) based on the original design reported in [4], with lower threshold current density, higher slope efficiency and improved output spectrum with respect to the SMSR. An AR/HR coated 3μm wide 3mm long DFB laser containing 4×QWs demonstrated a CW threshold of 54mA (J_{th} ~ 600A/cm^2) with a slope efficiency of 0.33mW/mA. The laser operated via a single mode at ~998nm with an SMSR>35dBm over a current range of 70mA to 250mA. An output power of 54.68mW with 44.46dB SMSR was measured at 240mA.

In Section 3.1, five different DFB structures were designed through Fimmwave simulation. Section 3.2 described the preparation work carried out prior to the manufacture of DFB lasers, including a comparison made between MOVPE-grown and MBE-grown broad area lasers and a comparison of devices with 2×, 4× and 6× QWs.

According to the simulation, the designed waveguide with ~1.5μm ridge etch depth would support operation via the fundamental lateral mode. Unfortunately, during fabrication, the devices were accidentally over-etched through the active region to a depth of ~2.5μm, resulting in a significant change to the waveguide, and dual-lateral-mode operation being supported, as measured and re-simulated in Sections 3.4.1-3.4.2. This mistake directly limited the potential for high power single mode performance for

the whole batch of structures. Study of two representative devices with high power potential exhibited a single lasing mode from threshold up until a higher current where a 2nd mode appeared and both modes existed simultaneously with more injected current. Within the single mode operation current range, the two devices demonstrated a threshold of ~30mA and ~25mW output power at 100mA with SMSR~25dB and a threshold of ~25mA with ~17mW output power at 60mA with SMSR~32dB (Section 3.4.1) respectively. Both were considerable improvements over the device reported in [4]. A 3mm 4×QWs DFB device demonstrated a CW threshold of 54mA and a current range of 70mA to 250mA for ~998nm single mode lasing with SMSR>35dB (Section 3.4.3).

Wavelength tuning was studied in Section 3.4.4 for a representative sample mounted on a ceramic tile. A thermal tunability of 0.1125nm/^{o}C was measured in CW operation for a wavelength shift of ~5nm over the temperature range from 20^{o}C to 60^{o}C. Furthermore, current tuning was measured with a rate of 0.023nm/mA, which approximately corresponds to a self-heating rate of 0.2^{o}C/mA.

Coupling coefficients (K_{meas}) were approximated for each DFB structure through measurement of the longitudinal mode spacing and DFB stopband. These were compared to the simulated coupling coefficients (K_{simu}), calculated from the re-simulated optical confinement factor in grating layer for each of the over-etched waveguides. Good agreement, with clear experimental limitations, was discussed in Section 3.4.6, verifying the validity of the simulation in future design.

3.6 Reference

[1] P. Werle, “A review of recent advances in semiconductor laser based gas monitors,” *Spectrochimica Acta Part A: Molecular and Biomolecular Spectroscopy*, vol. 54, no. 2, pp. 197–236, 1998.

[2] J. Seufert, M. Fischer, M. Legge, J. Koeth, R. Werner, M. Kamp and A. Forchel, “DFB laser diodes in the wavelength range from 760 nm to 2.5 μm,” *Spectrochimica Acta Part A: Molecular and Biomolecular Spectroscopy*, vol. 60, no. 14, pp. 3243–3247, 2004.

[3] P. Wai, L. Chan, L. Lui, L. Xu, H. Tam and M. Demokan, “All-optical header processing using control signals generated by direct modulation of a DFB laser,” *Optics Communications*, vol. 242, no. 1-3, pp. 155–161, 2004.

[4] B. J. Stevens, K. M. Groom, J. S. Roberts, P. W. Fry, D. T. D. Childs and R. A. Hogg, "Distributed feedback laser employing buried GaAs/InGaP index-coupled grating," *Electronics Letters*, vol. 46, no. 15, pp. 1076-1077, July 22 2010.

[5] H. Kogelnik and C. V. Shank, “Coupled-Wave Theory of Distributed Feedback Lasers,” *Journal of Applied Physics*, vol. 43, no. 5, pp. 2327–2335, 1972.

[6] A. J. Lowery and D. Novak, "Performance comparison of gain-coupled and index-coupled DFB semiconductor lasers," *IEEE Journal of Quantum Electronics*, vol. 30, no. 9, pp. 2051-2063, Sep 1994.

[7] K. David, G. Morthier, P. Vankwikelberge and R. Baets, "Yield analysis of non-AR-coated DFB lasers with combined index and gain coupling," *Electronics Letters*, vol. 26, no. 4, pp. 238-239, 15 February 1990.

[8] G. Morthier, P. Vankwikelberge, K. David and R. Baets, "Improved performance of AR-coated DFB lasers for the introduction of gain coupling," *IEEE Photonics Technology Letters*, vol. 2, no. 3, pp. 170-172, March 1990.

[9] X. Pan, H. Olesen and B. Tromborg, "Spectral linewidth of DFB lasers including the effects of spatial holeburning and nonuniform current injection," *IEEE Photonics Technology Letters*, vol. 2, no. 5, pp. 312-315, May 1990.

[10] Y. Nakano and K. Tada, “Analysis, design, and fabrication of GaAlAs/GaAs DFB lasers with modulated stripe width structure for complete single longitudinal mode oscillation,” *IEEE Journal of Quantum Electronics*, vol. 24, no. 10, pp. 2017–2033, 1988.

[11] F. Rana, “Chapter 13 Distributed Feedback (DFB) Structures and Semiconductor DFB Lasers,” class notes for ECE 5330 Semiconductor Optoelectronics, Cornell University, 2011. [Online]. Available: https://courses.cit.cornell.edu/ece533/, Accessed on: 10 December 2012.

[12] S. Adachi, “GaAs, AlAs, and AlxGa1−xAs: Material parameters for use in research and device applications,” *Journal of Applied Physics*, vol. 58, no. 3, 1985.

[13] F. Bugge, U. Zeimer, H. Wenzel, R. Staske, B. Sumpf, G. Erbert, M. Weyers and G. Tränkle, “Laser diodes with highly strained InGaAs MQWs and very narrow vertical far fields,” *Physica Status Solidi (c)*, vol. 3, no. 3, pp. 423–426, March 2006.

[14] L. A. Coldren, S. W. Corzine and M. Mashanovitch, *Diode lasers and photonic integrated circuits*. Hoboken, NJ: Wiley, 2012.

[15] K. S. Mobarhan, "Test and Characterization of Laser Diodes: Determination of Principal Parameters," *Newport Corporation Technical Publication - Application Note No. 1*, 1995.

[16] W. T. Silfvast, "Module 1.5 Lasers," in *Fundamentals of Photonics*, 1st ed., A. H. Guenther, L. S. Pedrotti and C. Roychoudhuri, Ed. Storrs, CT: University of Connecticut, 2000, pp. 169-210.

[17] T. I. Alam, M. A. Rahim and R. Basak, "Effects of Variation of Quantum Well Number on the Performance of a Designed 635nm $Ga_{0.5}In_{0.5}P/(Al_{0.7}Ga_{0.3})_{0.5}In_{0.5}P$ Multiple Quantum Well Red Laser," *International Journal of Multidisciplinary Sciences and Engineering*, vol. 4, no. 2, February 2013.

[18] A. Kurobe, H. Furuyama, S. Naritsuka, N. Sugiyama, Y. Kokubun and M. Nakamura, "Effects of well number, cavity length, and facet reflectivity on the reduction of threshold current of GaAs/AlGaAs multiquantum well lasers," *IEEE Journal of Quantum Electronics*, vol. 24, no. 4, pp. 635-640, April 1988.

[19] K. M. Groom, B. J. Stevens, P. J. Assamoi, J. S. Roberts, M. Hugues, D. T. D. Childs, R. R. Alexander, M. Hopkinson, A. S. Helmy and R. A. Hogg, "Quantum Well and Dot Self-Aligned Stripe Lasers Utilizing an InGaP Optoelectronic Confinement Layer," *IEEE Journal of Selected Topics in Quantum Electronics*, vol. 15, no. 3, pp. 819–827, 2009.

[20] T. Zhai, S.-Y. Tan, D. Lu, W. Wang, R.-K. Zhang and C. Ji, "High Power 1060 nm Distributed Feedback Semiconductor Laser," *Chinese Physics Letters*, vol. 31, no. 2, p. 024203, 2014.

[21] M. Aoki, M. Komori, A. Taike, R. Yamabi and K. Uomi, "Low-power-consumption thin-film heater-loaded wavelength-tunable DFB laser," *Fifth Asia-Pacific Conference on ... and Fourth Optoelectronics and Communications Conference on Communications*, Beijing, China, vol. 2, pp. 1548-1549, 1999.

[22] W. Wei, H. Deng and J. J. He, "GaAs/AlGaAs-Based 870-nm-Band Widely Tunable Edge-Emitting V-Cavity Laser," *IEEE Photonics Journal*, vol. 5, no. 5, pp. 1501607-1501607, October 2013.

[23] J. E. Carroll, J. Whiteaway and D. Plumb, *Distributed feedback semiconductor lasers*. London, UK: The Institution of Electrical Engineers, 1998.

Chapter 4. GaAs-Based Self-Aligned Stripe Distributed Feedback Lasers

GaAs-based distributed feedback (DFB) lasers provide a robust, portable and low cost solution to enable a broad range of potential applications in spectroscopy, gas sensing, THz generation, and display.

Research has been conducted on GaAs-based DFB lasers covering a wide range of lasing wavelengths, from 750nm-880nm AlGaAs-GaAs DFB lasers [1] [2] to 900nm-1100nm InGaAs/GaAs DFB lasers [3], then to 1.3μm-1.5μm GaInAsN-GaAsN-AlGaAs DFB lasers [4]. DFB lasers are typically available on GaAs as ridge lasers, as described in Chapter 2, with either laterally loss-coupled gratings [5] [6] and more recently using buried index-coupled grating approaches incorporating combinations of GaAs, AlGaAs and InGaP [3].

However, ridge waveguides suffer from surface recombination, carrier spreading and poor fibre coupling efficiencies. In comparison, buried hetero-structures (BH) allow small lateral sizes, low threshold currents, good thermal management, and excellent fundamental mode stability [7]. Furthermore, BH lasers can also be designed to support direct modulation [8]. For these reasons, BH DFB laser arrays can be used to form widely tunable laser sources [9]. They are typically used in directly modulated InP telecoms lasers [10].

The history of buried heterostructure lasers dated back to the 1970s. A GaAs/$Al_xGa_{1-x}As$ buried heterostructure laser lasing at ~817nm was realised and reported in [11], where a 2-step liquid-phase-epitaxial (LPE) technique allowed $Al_xGa_{1-x}As$ to

completely surround the filamentary GaAs active region. In this structure, the optical confinement was realised through the index difference between GaAs and AlGaAs and the electrical confinement was realised by the n-p-n-p structure. In [11], with comparison to a ridge waveguide laser, the BH laser demonstrated better characteristics and a lower sensitivity to temperature. A latter design, as reported in [12], realised DFB operation at ~830nm though embedding a corrugated structure into the p-AlGaAs in the same structure as described in [11], grown with the same 2-step LPE technique.

In BH laser structures, single lateral mode operation is easier to achieve than in ridge lasers [13]. This is because that a much smaller index-step for wave-guiding in BH structures tends to release, rather than capture, higher order modes. Also, in BH structures, narrower active regions can be preceded as not needing to contact to the top directly. BH DFB lasers are commonplace on InP [8], where DFB gratings are incorporated within the buried heterostructure laser to realise rapidly modulated telecoms lasers. However, they are not commonly available on GaAs and approaches to their realisation include regrowth over potentially oxidised aluminium-containing layers, etch/regrowth in the same reactor [7] [14], or use of InGaP cladding [15].

This chapter presents the development of self-aligned-stripe (SAS) DFB lasers, starting with the waveguide design and simulation (Section 4.1), in which the original design concept and structural details are firstly presented. After, I describe the structural modifications that were required according to need for regrowth of thicker GaAs. Then the growth and fabrication processes are described in detail in Section 4.2, followed by the characterisation and discussion of several representative devices in Section 4.3.

4.1 Structural Design of SAS-DFB

The self-aligned stripe (SAS) fabrication method allows a stripe-geometry to be realised by overgrowth upon a stripe-etched current blocking layer in a 2-stage growth process. The current blocking layer is located above the active region with a distance of hundreds of nanometres by p-doped AlGaAs to form the p-n-p-n blocking structure.

In the previous research reported by our group, a GaAs/InGaP regrowth process was used to enable SAS lasers to be manufactured on GaAs [16], as in Fig. 4-1 (a).

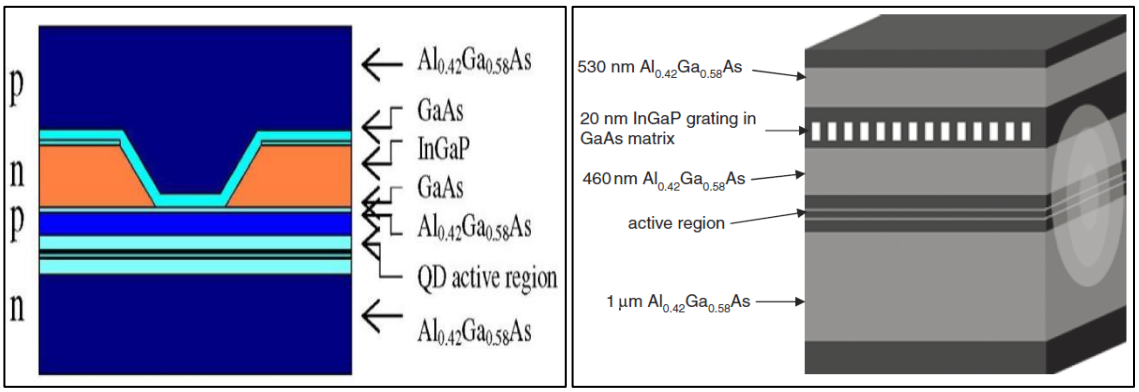

(a) (b)

Figure 4-1: Previous work (a) SAS laser [16] and (b) DFB laser [3]

In our GaAs-based SAS process, no aluminium is exposed to atmosphere prior to regrowth. Furthermore, since $Al_xGa_{1-x}As$ is lattice matched to GaAs for all compositions of x, this permits a significant amount of flexibility in waveguide design, and provides attractive benefits for future GaAs based photonic integrated circuits design [17]. In a discrete optical system, the requirement for the DFB laser source to operate via its fundamental transverse optical mode for high efficiency coupling in successive components severely limits the width of the laser active region and commensurately its output power [18]. Our previous DFB [3] and SAS laser [16]

designs describe structures realised with a single overgrowth and not specifically designed to be integrated together. In this chapter, we demonstrate the realisation of SAS-DFB lasers emitting at ~1000nm, based on a three-stage growth process (i.e. 2 overgrowths).

4.1.1 Advantage and Novelty

In general, SAS lasers provide many advantages with respect to device performance comparing to ridge lasers, e.g. more stable single lateral mode operation, narrower active regions, better direct modulation performance, etc. In my SAS DFB design, one core advantage is its excellent flexibility in terms of waveguide design to support device optimisation. Fig. 4-2 (a) summarises 12 available variables that can be utilised to support designing of a SAS DFB waveguide structure.

First of all, positions of the overgrown grating and the self-aligned stripe can be adjusted within nearly the entire upper cladding region (①-②) to achieve certain profile and/or parameters of the guided optical mode. In addition, further modification of the waveguide can be achieved via designing structural dimensions of the SAS geometry (③-⑦) and the grating sequence (⑧-⑪). Furthermore, the Al composition of AlGaAs cladding (⑫) can also be adjusted.

In this project, the SAS geometry was designed to be grown immediately above the overgrown GaAs/InGaP grating layer, as illustrated in Fig. 4-2 (b), which means that the lower etch-stop GaAs layer of the SAS section ($t_{GaAs\text{-}1}$) also performed as the in-fill overgrown GaAs layer ($t'_{GaAs\text{-}overgrowth}$) for the formation the grating matrix.

(a)

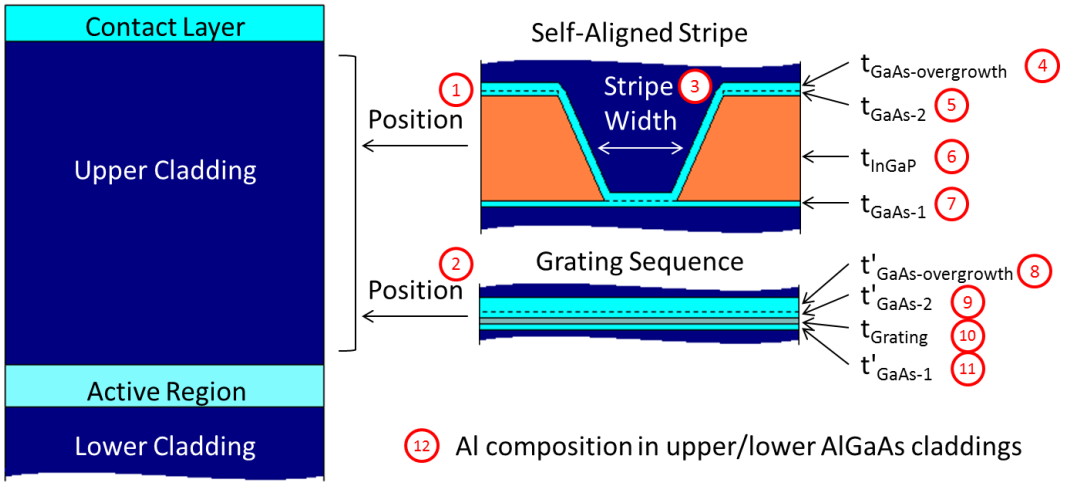

(b)

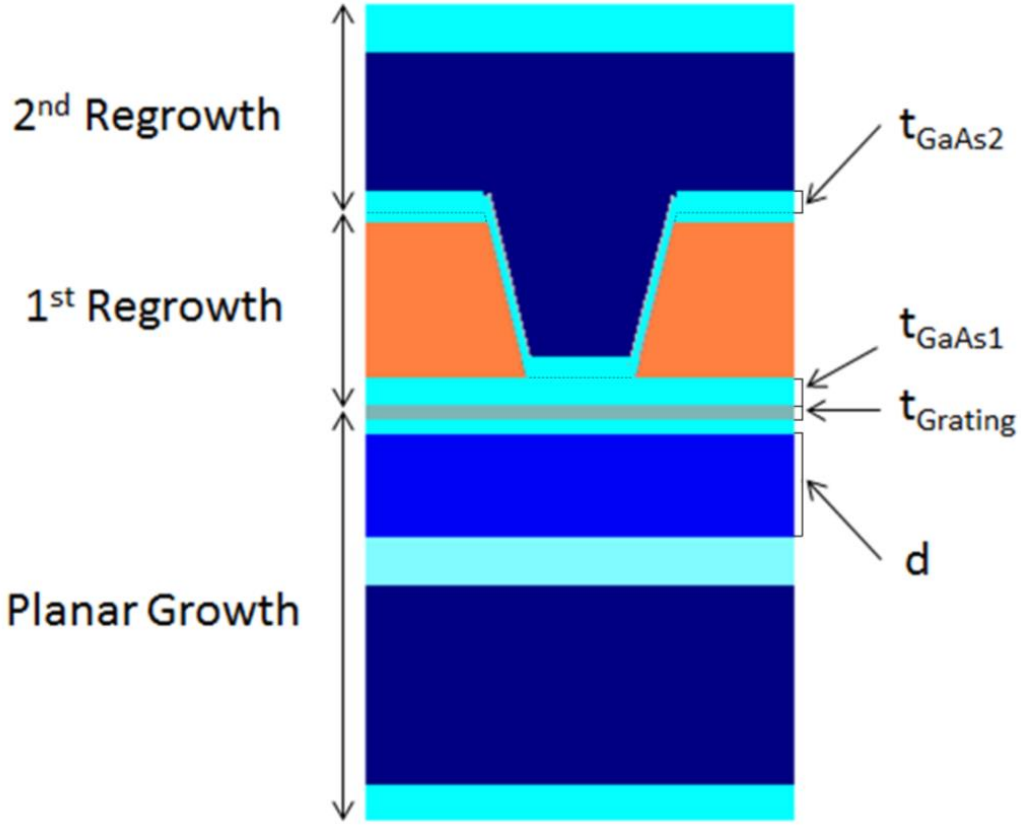

Figure 4-2: Schematic diagram of (a) the design concept of SAS DFB lasers showing 12 variables that can be tailored and (b) the waveguide structure designed in this project

This design consists of a 3-stage growth process: the planar growth (lower cladding, QWs, partial upper cladding and grating layer), the 1st overgrowth (in-fill GaAs to form the grating and n-InGaP blocking layer) and the 2nd overgrowth (in-fill GaAs to form the SAS, the remainder of the upper cladding layers and contact layer).

4.1.2 Original Design and Simulation

In the initial structural design stage, Fimmwave software, by Photo-Design, was again used to simulate the waveguide and calculate overlaps in the structures, using refractive indices at 1000nm of 3.51 for GaAs, 3.3 for $Al_{0.42}Ga_{0.58}As$, 3.14 for $Al_{0.7}Ga_{0.3}As$, and 3.15 for InGaP. The aim of the simulation activity is to help design the structure in terms of optimising confinement factors, as well as the mode profile. Because the grating is to be fabricated as a 50/50 mark-to-space ratio square-shaped GaAs/InGaP grating, the refractive index of grating layer is then calculated as 3.335. The basic concept was to achieve optical confinement in the grating as KL=1, as discussed in chapter 2, whilst also maintaining strong optical confinement with the QWs.

Based on the previously designed SAS laser and DFB structures, two structures, one comprising 2×QWs and one with 4×QWs, are simulated. Essentially, the design is an amalgamation of the GaAs DFB laser in [3] with the GaAs SAS laser structure in [16], placing the grating layers immediately below the n-doped InGaP optoelectronic confinement layer, as shown in Fig. 4-2 (b).

I applied the optimised thickness (600nm) and width (3μm) of the InGaP optoelectronic confinement layer as described in [16], whilst the four main variables that I used to modify the waveguide are highlighted in the figure:

- **d:** the separation between grating and active region (partial upper cladding)
- **$t_{Grating}$:** thickness of grating
- **t_{GaAs-1}:** in-fill GaAs in 1st overgrowth
- **t_{GaAs-2}:** in-fill GaAs in 2nd overgrowth

Table 4-1 shows the resultant original designs for the 2× and 4× QWs SAS-DFB laser structures.

	Thickness(nm)	Material	Doping (cm^{-3})		2×QWs	4×QWs
2nd Regrowth	300	GaAs	P	1.0×10^{19}	--	--
	750	$Al_{0.42}Ga_{0.58}As$	P	1.0×10^{18}	--	--
	750	$Al_{0.42}Ga_{0.58}As$	P	5.0×10^{17}	--	--
	20	$Al_{0.42}Ga_{0.58}As$	P	5.0×10^{17}	--	--
	60	GaAs	P	5.0×10^{17}	--	--
1st Regrowth	20	GaAs	P	5.0×10^{17}	--	--
	600	$In_{0.5}Ga_{0.5}P$	N	5.0×10^{17}	--	--
	45	GaAs	P	1.0×10^{18}	--	--
Planar Growth	10	GaAs	P	5.0×10^{17}	--	--
	7.5	$In_{0.5}Ga_{0.5}P$	P	5.0×10^{17}	--	--
	15	GaAs	P	5.0×10^{17}	--	--
	--	$Al_{0.42}Ga_{0.58}As$	P	5.0×10^{17}	510nm	300nm
	50	GaAs	Un-doped		--	--
	10	$GaAs_{0.885}P_{0.115}$	Un-doped		Repeat ×2	Repeat ×4
	7.6	$In_{0.17}Ga_{0.83}As$	Un-doped			
	10	$GaAs_{0.885}P_{0.115}$	Un-doped			
	50	GaAs	Un-doped		--	--
	750	$Al_{0.42}Ga_{0.58}As$	N	5.0×10^{17}	--	--
	750	$Al_{0.42}Ga_{0.58}As$	N	1.0×10^{18}	--	--
	500	GaAs	N	1.0×10^{18}	--	--

Table 4-1: Layer structures design of SAS-DFB 2× and 4× QWs

Fig. 4-3 shows the simulated guided optical mode profile of both designs. The blue contour lines indicate the optical mode intensity superimposed over the simplified waveguide dimensions, to indicate the overlaps. As can be seen from the 2×QWs design, Fig. 4-3 (a), an inevitable guided mode exists around the overgrowth GaAs layers. This was because, in 2×QWs design, the average refractive index of the active region was not sufficiently higher than that of the grating area, which had 2 in-fill GaAs from both 1st and 2nd regrowth. Effort had been given to minimise the value by:

- Reducing the 2nd in-fill GaAs from 100nm (as reported in [16]) to 60nm
- Increasing the separation between grating and active region to 510nm

It can also be found that the effect of stacked in-fill GaAs was less obvious in 4×QWs design, Fig. 4-3 (b), because the active region had relatively higher capability of confining optical wave with 2 additional high-refractive-index QW layers.

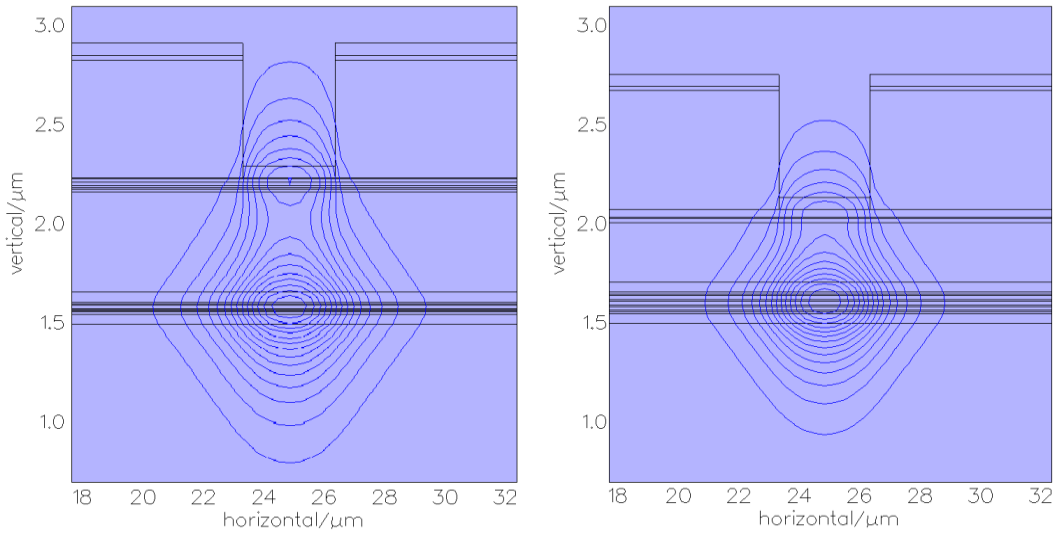

Figure 4-3: Mode profile of 2× and 4× QWs SAS-DFB lasers

4.1.3 Design Modification

➢ Requirement for thicker in-fill GaAs in the first overgrowth

In order to infill and planarise the grating, the GaAs layer was grown at a higher temperature than is typically used for GaAs. This imposes a minimum thickness limitation on the GaAs layer in order to adequately planarise the surface prior to InGaP growth. Thinner GaAs layers (45nm), such as those used previously [3] and incorporated in our initial design from Section 4.1.2, were defective in planar areas on test overgrowth samples.

Although higher quality overgrowth was observed in the grating areas, this would not be suitable for future integrated devices, which would require components to be

processed within these planar areas. Overgrowth quality was significantly improved by using a thicker GaAs planarisation layer (100nm). A dark-field 002 transmission electron micrograph (TEM), recorded for a cross-section along the grating, is also shown in Fig. 4-4 (a), demonstrating high quality infill and planarisation of the InGaP grating with subsequent n-doped InGaP growth above, using the modified thickness of 100nm GaAs for infill and planarisation.

(a)

(b)

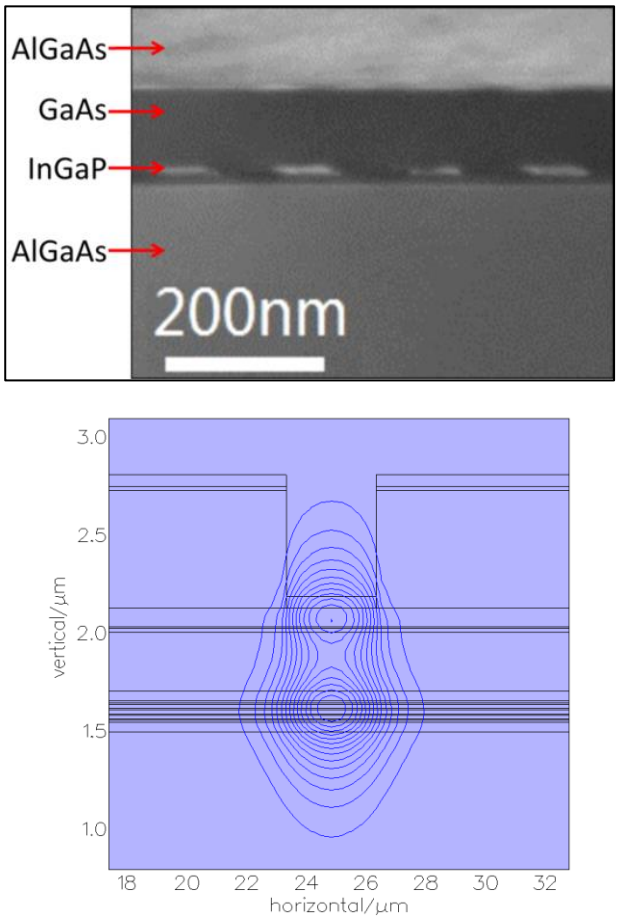

Figure 4-4: (a) Dark-field 002 TEM of cross section along grating and (b) Additional guided mode due to increased GaAs planarisation layer (45nm to 100nm)

The requirement to grow 100nm GaAs in the first regrowth stage resulted in an inevitable change in the simulated optical mode profile for 2× and 4× QWs structures, which also resided in an additional guided mode some distance above the active region for 4×QWs design as well, as illustrated in Fig. 4-4 (b), when using the same cladding layer composition as originally designed.

This therefore required a re-design of the layer structure to ensure that appropriate optical confinement can be achieved in both the grating and in the QWs. One strategy could be a re-design of both the upper and lower cladding compositions, and therefore growth of a new planar wafer. Another strategy would be to make use of the tailor-ability of $Al_xGa_{1-x}As$, which is virtually lattice-matched to GaAs for all compositions, x. We are therefore afforded full flexibility for a choice of Al_x composition to use in the upper cladding layers. Additionally, a change could also be made to the thickness of GaAs that is grown first in the second overgrowth step. Therefore, it was entirely feasible that sufficient modification to the optical wave-guiding could be achieved by changing only the layers in the subsequent 2^{nd} regrowth step, rather than necessitating growth of a new starting wafer with different lower cladding composition.

Since the simulation of the 4×QWs SAS waveguide showed a better mode profile, the modification of the structure was mainly based on the simulation of the 4×QWs SAS.

➢ Structure tailoring of second overgrowth

The ability to tune the Al_x composition in the overgrown cladding layers is a unique attribute of the GaAs/InGaP SAS design as compared to alternative strategies for buried waveguides, such as Al-free approaches. In this work, full tailoring of the optical mode was possible through optimisation of two main variables in the subsequent second overgrowth stage: Al_x composition / GaAs thickness.

Fig. 4-5 (a) plots the optical confinement factor in both the grating and in the QWs, simulated as a function of Al_x composition with the GaAs thickness fixed at 60nm (as per our original design). This demonstrated that confinement in the grating could be

reduced towards our target value through use of higher composition Al_x in the upper cladding layers. Above x ~0.4, optical confinement in the QWs was sufficiently high and approximately constant. An Al_x composition of x=0.7 was deemed to be an appropriate upper limit for ease of device fabrication and also taking into account the potential reliability issues associated with higher Al compositions.

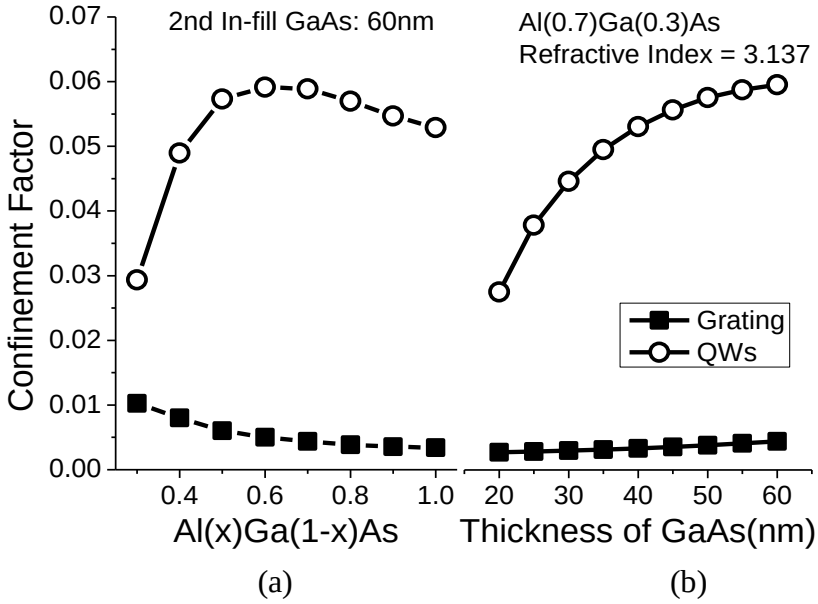

Figure 4-5: Simulated optical confinement factors in the grating and quantum wells as a function of (a) Al_x composition in $Al_xGa_{1-x}As$ for fixed 2nd regrowth GaAs thickness of 60nm, (b) thickness of 2nd regrowth GaAs for fixed Alx composition of $Al_{0.7}Ga_{0.3}As$

Fig. 4-5 (b) plots the same simulation as a function of the thickness of GaAs grown in the second regrowth stage with the composition of Al_x fixed at x=0.7, as decided from Fig. 4-5 (a). When decreasing the thickness from 60nm, as designed, the confinement factor in the grating layer reduced gradually, as did the confinement factors in the QWs. At 40nm thick GaAs, our target value of optical confinement factor in the grating was reached whilst also exhibiting a reasonably high optical confinement factor in QWs.

4.1.4 Final Structure Design

Table 4-2 outlines the optical confinement and optical far-fields simulated for both the original design and the modified design with (1) 45nm and (2) 100nm of in-fill and planarisation GaAs grown above the InGaP grating. Fig. 4-6 (a) compares the original and modified structure at the cross-section of the etched stripe.

	(1) Intended 45nm GaAs planarisation	(2) Now with 100nm GaAs planarisation
Upper $Al_xGa_{1-x}As$	x=0.42	x=0.7
2nd GaAs in-fill	60nm	40nm
$\Gamma_{Grating}$	0.0033	0.0031
Γ_{QWs}	0.0526	0.0531
Far-field FWHM-Slow	9.7°	6.9°
Far-field FWHM-Fast	43.1°	46.1°

Table 4-2: Parameters used in the (1) original and (2) modified design together with the expected resultant optical properties

As can be seen, the confinement factor in both the grating layer ($\Gamma_{Grating}$) and the active region (Γ_{QWs}) could be maintained at similar values as for the original design, as presented in Table 4-1 (column "4×QWs"). Furthermore, as described in Section 4.1.3, without any modification to the 2nd overgrowth for the required thicker GaAs planarisation layer (45nm to 100nm), the simulated mode profile shown in Fig. 4-4 (b) demonstrated the occurance of an additional guided mode. After the modification, the simulated optical profile of this modified design, as shown in Fig. 4-6 (b), exhibited improved profile compared to that shown in Fig. 4-4 (b). Also, with these parameters included in the design, an optical far-field of 46.1 °(fast) and 6.9 °(slow) was simulated. These values were similar to those achievable using our original design (43.1 °, 9.7 °). The narrower horizontal (slow axis) divergence was a result of a change in the shape of

the mode as it interacts with the SAS, but was not expected to present any obvious change in device performance.

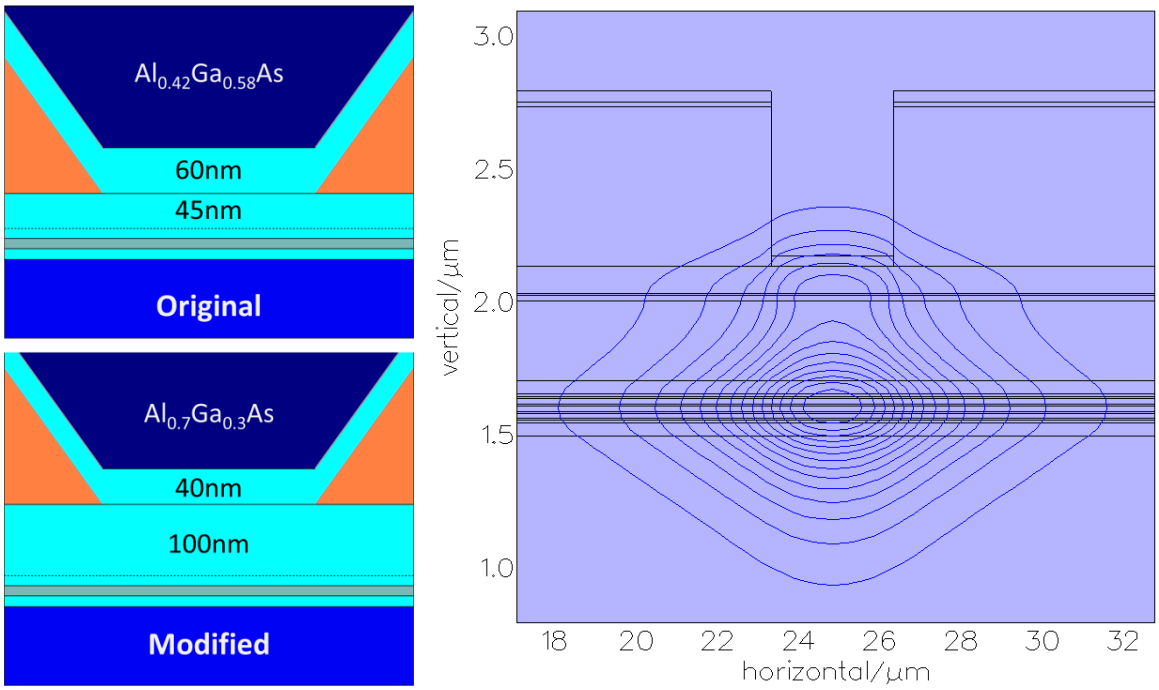

(a) (b)

Figure 4-6: (a) Schematic diagrams of original and modified stripe structure and (b) single fundamental mode profile enabled using new parameters

Therefore, as a direct consequence of the thicker GaAs grating in-fill and planarisation layer, necessary for high quality InGaP growth, the use of thinner GaAs and higher Al composition AlGaAs in the upper cladding layer can be viewed as a positive solution to regain the required optical confinement factors.

4.2 Growth and Fabrication

This section describes the fabrication process for realisation of SAS-DFB lasers. The sample underwent a 3-stage growth process. Between the 1st and 2nd growth, an InGaP/GaAs grating was formed within the upper cladding layer and immediately below the optoelectronic confinement layer (where the buried stripe was to be etched).

Between the 2nd and 3rd growth, a 3μm wide SAS was formed above the grating by etching through the 600nm n-InGaP blocking layer. A schematic diagram of this SAS-DFB laser is shown in Fig. 4-7.

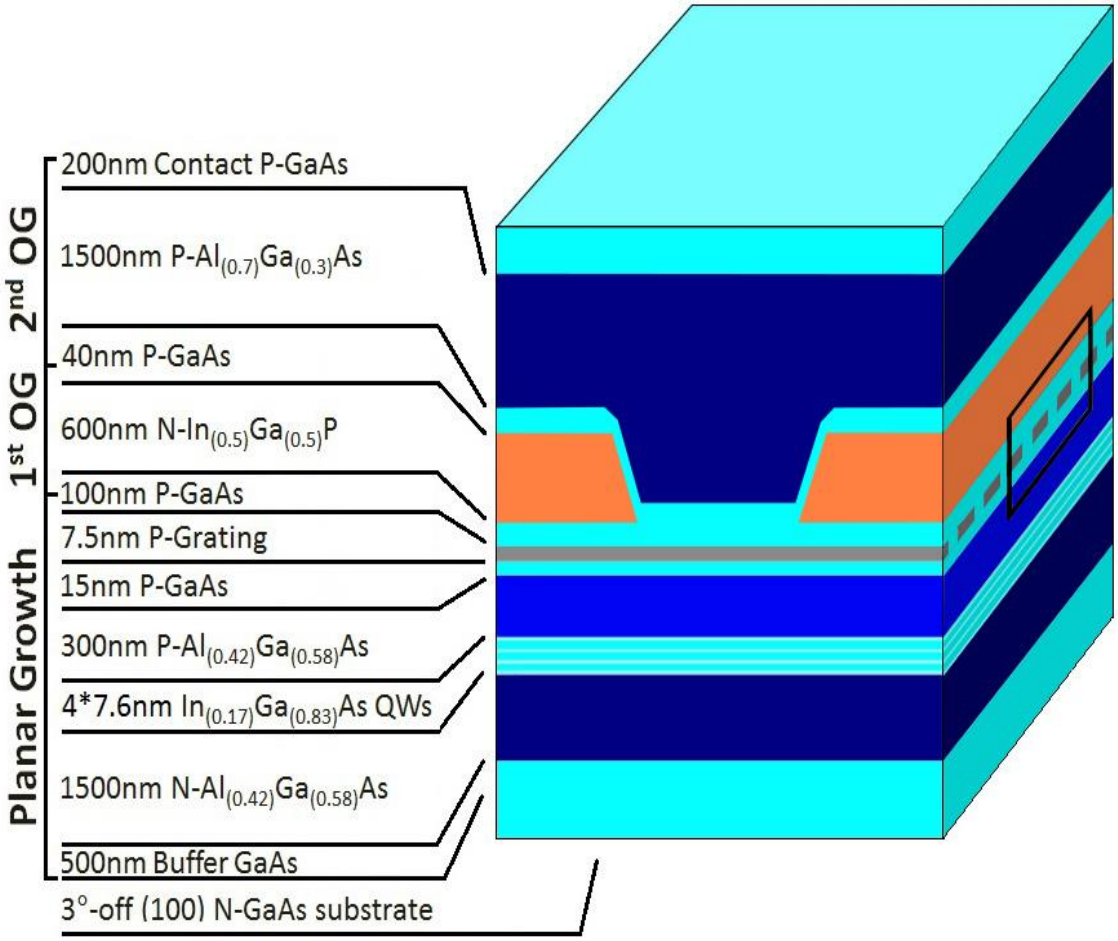

Figure 4-7: Schematic diagram of the layer structure that defines the SAS-DFB laser, the box showing the formed 50/50 mark-to-space ratio overgrown grating

4.2.1 Sample Growth

As mentioned, a three-stage growth process has been applied. In order to realise this structure, the following fabrication scheme was used.

➢ Stage I: Planar Growth and Grating Etching

An n-doped $Al_{0.42}Ga_{0.58}As$ lower cladding layer was grown using MOVPE (metal-organic vapour phase epitaxy) above a 500nm GaAs buffer layer on an n-doped GaAs substrate which was mis-oriented by 3° to the (110) direction. Above this, partially strain-balanced quantum wells (QWs) emitting ~990nm were grown within a waveguide structure comprising 2 × and 4 × 7.6nm $In_{0.17}Ga_{0.83}As$ QWs separated by 20nm $GaAs_{0.885}P_{0.115}$ strain balancing layers. 50nm GaAs was grown on either side to complete the waveguide core. 300nm p-doped $Al_{0.42}Ga_{0.58}As$ was grown above the core prior to growth of the grating layer. The first order DFB grating layer comprised a 7.5nm thick InGaP layer (lattice matched to GaAs) sandwiched between 15nm and 10nm thick GaAs layers.

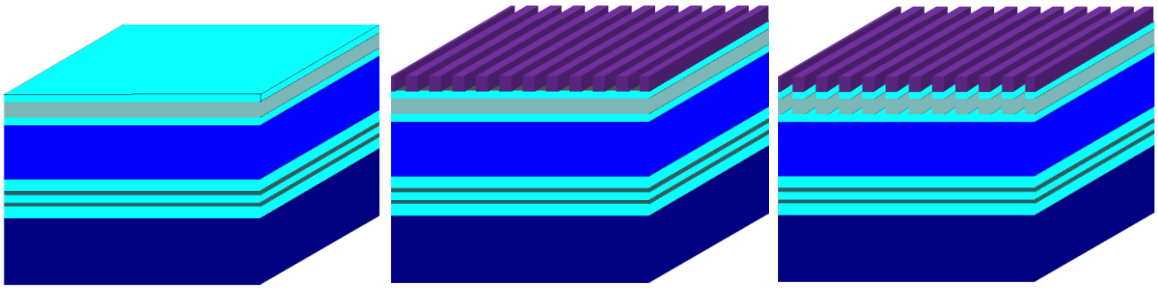

(a) (b) (c)

Figure 4-8: Schematic diagrams of (a) planar growth, (b) electron beam lithography and (c) grating etching

Following patterning by electron beam lithography (the same process as for ridge DFB lasers in chapter 3) grating with periods of 148nm, 149nm and 150nm were

formed by first dry etching through the GaAs top layer using an argon reactive ion etch process, before wet etching through the InGaP using HCl/H_3PO_4. In this method, this wet etch is highly selective and terminates abruptly at the lower GaAs layer, whose role is to protect the underlying p-doped $Al_{0.42}Ga_{0.58}As$ layer from being exposed to atmosphere. This etch was laterally pinned by the previous GaAs dry etch process and can be performed either with or without removal of the patterned PMMA, using the upper GaAs layer as the etch mask.

➢ Stage II: First Overgrowth

Following etching, the PMMA was removed and a simple clean process was performed, including O_2 plasma ash, before a wash in 1% diluted HF immediately prior to loading into the MOVPE reactor. The wafer was then returned to the reactor for overgrowth. 100nm p-doped GaAs was overgrown to infill and planarise the index-coupled DFB grating, before 600nm n-doped InGaP (lattice-matched to GaAs) optoelectronic confinement layer, and 20nm of GaAs completed the overgrowth.

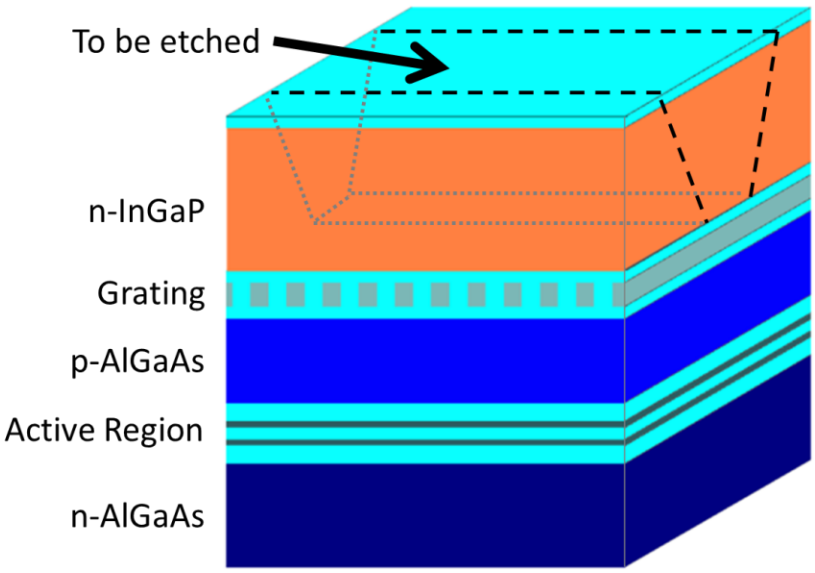

Figure 4-9: Schematic diagram of the structure following the first overgrowth, the dotted line represents the stripe to be etched in the next stage

Fig. 4-9 shows a schematic diagram of the sample after the 1st overgrowth. As illustrated, the GaAs/InGaP grating was formed to a distance (510nm for 2×QWs design and 300nm for 4×QWs design) above the active region. The dotted lines represent the stripe to be etched in the next stage for the formation of the SAS.

➢ Stage III: Stripe Etching and Second Regrowth

As shown in Fig. 4-10, 3μm wide SAS patterns were defined using standard UV optical lithography. A stripe was etched into the n-doped InGaP layer by first dry etching through the top GaAs layer using a $SiCl_4$/Ar based inductively coupled plasma (ICP) process and then wet etching through the InGaP layer, down to the lower GaAs etch stop layer, again using HCl/H_3PO_4.

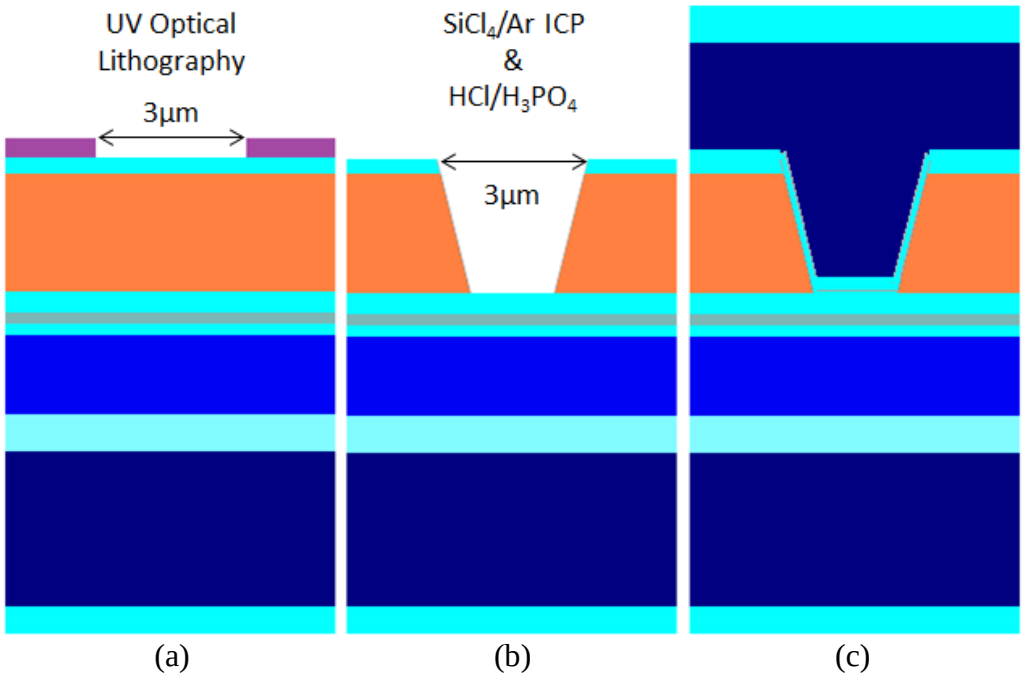

Figure 4-10: Schematic diagrams of fabrication of 3μm wide self-aligned stripes

Following photoresist removal and a simple HF clean, a second overgrowth of 40nm p-doped GaAs, 1500nm p-doped $Al_{0.7}Ga_{0.3}As$ and a 200nm GaAs contact layer completed the structure.

4.2.2 Device Fabrication

Fig. 4-11 (a) shows a pictorial representation of the epitaxial structure of the wafer. As illustrated, the buried hetero-structure was formed along with the grating.

The in-fill GaAs and $Al_{0.7}Ga_{0.3}As$ formed the SAS in the etched 600nm n-doped InGaP blocking layer with GaAs/InGaP 50/50 square-shaped grating layer immediately beneath the stripe.

➢ Trench Etching

To define the pattern for etching of the isolation trenches, SPR 350 photoresist was spun onto the samples at 4000rpm for 30 seconds, followed by 1 minute hard bake at 100^{o}C. After exposure, the samples were developed in MF26A for 1 minute and rinsed in DI water, as Fig. 4-11 (b). Then 1 minute oxygen plasma ash was performed to ensure the complete removal of the resist in the exposed areas.

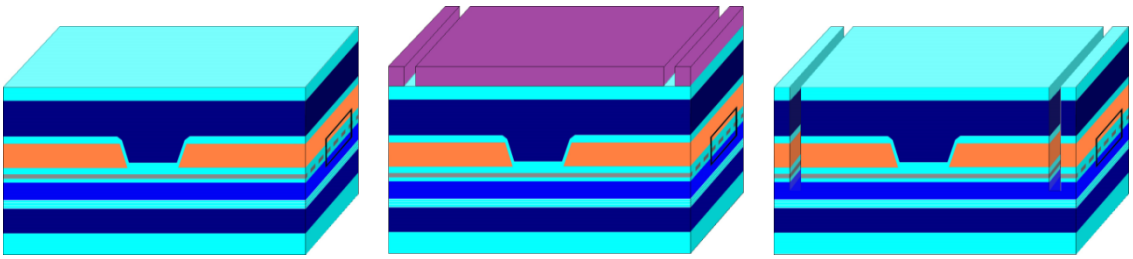

(a) (b) (c)

Figure 4-11: Isolation trenches wet etching to form 100μm wide electrically isolated devices

Then, the patterned samples were wet etched to a trench depth of ~2.5μm using a 1:1:1 mixture of acid HBr, $C_2H_4O_2$ and $K_2Cr_2O_7$, shown in Fig. 4-11 (c). The samples were again rinsed in DI water and blown dry, followed by a resist lift-off process in warm acetone. After 3-stage cleaning, a 2 minute oxygen plasma ash was used to remove any residual photoresist.

The cleaning process was repeated until the samples were clean, as verified by inspection under an optical microscope.

➢ Si_3N_4 Deposition and Window Etching

The next step was dielectric deposition. Plasma-enhanced chemical vapor deposition (PECVD) was employed to deposit 500nm thick of Si_3N_4 film onto the samples, serving the purpose as an electrically insulting layer to allow the later Ti/Au bond pad to be deposited close to the stripe, as shown in Fig. 4-12 (a).

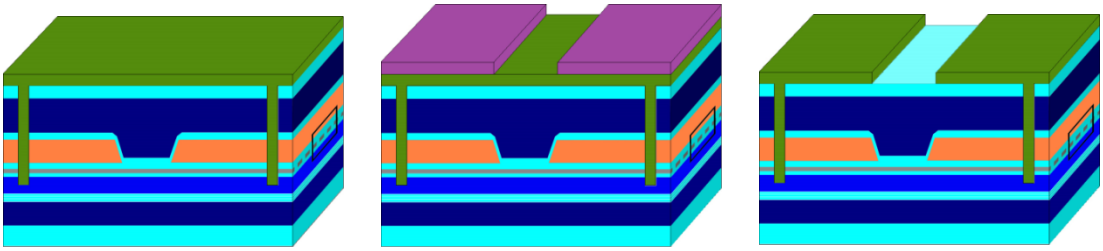

(a) (b) (c)

Figure 4-12: Deposition of 500nm thick SiN dielectric layer and window etching

The samples were then patterned to expose a window area above the SAS, suing a similar process to that described above (photoresist spin, edge bead removal, exposure, development, photoresist lift-off), shown in Fig. 4-12 (b). A reactive ion etcher (RIE) was used to etch the Si_3N_4 to open the defined window areas.

The process recipe included 35sccm of CHF_3 and 5sccm of O_2 with a chamber pressure to be maintained at 35mTorr and RF power at 60W. The etching process was monitored using Laser End Point software, and a 30 second over-etch was added to process time to ensure complete removal of Si_3N_4 in the window areas. After inspection of the window areas under an optical microscope, the photoresist was removed in warm acetone, resulting in a fabricated profile as shown Fig. 4-12 (c).

➢ Top Contact Deposition

The samples were then aligned, exposed and developed with the metal contact pattern in SPR 350 possitive photoresist, as shown in Fig. 4-13 (a). A thermal evaporator was used for the deposition of Au/Zn/Au top ohmic contact. In order to remove native surface oxide, the samples were dipped in 19:1 H_2O : Analar Ammonia solution for 45 seconds, then rinsed in DI water and blown dry, before loading in to the evaporator and pumping down to a pressure of 2×10^{-6}mbar.

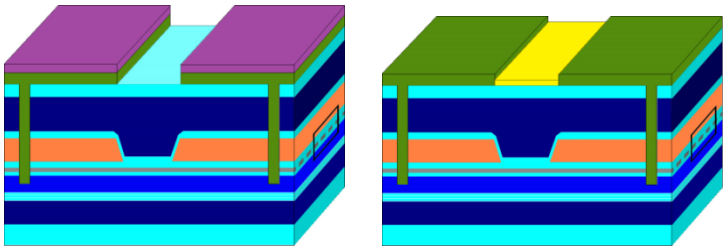

(a) (b)

Figure 4-13: Depostion of Au/Zn/Au Ohmic contact

The contact deposition included 5nm gold, then 10nm zinc and then 300nm gold. After lift-off and cleaning, a 2 minute oxygen plasma ash was performed to remove any residual resist. The cleanliness was inspected under an optical microscope. The samples were then annealed using the RTA at 360^{o}C with 30 seconds ramp and 3 seconds dwell the resultant structure is shown in Fig. 4-13 (b).

➢ Bond Pad Deposition

The deposition of bond pad was similar to that of contact, as illustrated in Fig. 4-14. Instead of being fixed at 6cm height as for zinc, a tungsten basket was fixed at 12cm height with ~10mg titanium due to a higher required deposition temperature. The deposition thicknesses were: 15nm titanium and 200nm gold.

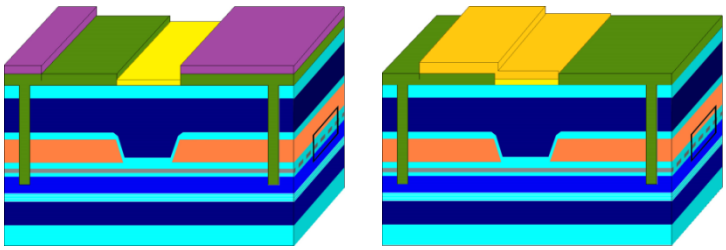

(a) (b)

Figure 4-14: Deposition of Ti/Au bond pad

➢ Substrate Thinning and Back Contact

The samples were thinned for better heat extraction, as well as to facilitate ease cleaving into short cavity length devices. A logitech LP50 lapper/polisher was employed for this process, and samples were thinned to ~150µm. After thinning and cleaning, In-Ge/Au back contact was deposited using a thermal evaporator. The deposition thicknesses were: 20nm In-Ge and 200 nm gold. This was followed by RTA annealing at 340^{o}C with 30 seconds ramp and 3 seconds dwell.

➢ Cleaving, AR Coating and Mounting

The fabricated samples were cleaved into 600µm long devices and anti-reflection coatings with reflectivity, R=0.1% at 1050nm with 25nm bandwidth, were applied to one facet by Helia Photonics. The central wavelength of 1050nm was a compromise made among many samples sent for coating together and while not optimum here, sufficiently low reflectivity for suppresion of feedback from the facets was anticipated. Lastly, devices were mounted epi-side-up on AlO_2 ceramic tiles with InAg paste and bonded using a K&S Ultrasonic Ball Bonder for characterisation.

4.3 Characterisation and Discussion

In practical operation of the DFB laser, a red-shift in the spectral position of the gain peak is unavoidable due to Joule-heating when pumping with high CW current or operating without adequate heat-sinking provision. In order to ensure that the gain is resonant with the DFB mode when pumped with CW current to achieve DFB single mode lasing, the grating period was designed to be on the long wavelength side of the gain peak in this material (~990nm) to ensure high injected current and high temperature operation. Based on the study and measurement in previous DFB ridge lasers, as described in Chapter 3, I designed 3 different grating periods (148nm, 149nm and 150nm) aiming at a DFB wavelength in the region of 990nm to 1010nm in order to coincide with the gain peak of this QW material.

4.3.1 4×QWs SAS-DFB

This section describes the measurement of three representative SAS-DFB lasers, for the three defined grating periods, incorporating 4×QWs. Representative devices were selected based a searching measurement over 10 devices for each grating period

➢ Grating Period 148nm

The following section describes the measurement of a representative 4×QWs SAS-DFB laser with a 148nm period grating. Fig. 4-15 plots the CW L-I-V characterisation of this device. The resistance of this device is calculated from the I-V curve to be ~4Ω. The L-I curve shows a CW lasing threshold at around 60mA with a slope efficiency of

~0.25W/A. This efficiency is maintained until ~100mA and reduces gradually until a clear kink is observed in the P-I characteristic at ~160mA. At 160mA onwards, the sample is operating with a higher efficiency (~0.4W/A). The appearance of this kink can be explained as follows:

The DFB wavelength associated with a 148nm grating period is ~996nm. This wavelength is resonant with the peak of the gain spectrum with ~I_{thresh} at room temperature. Therefore, the device starts lasing via the DFB mode upon reaching the threshold current. With an increase in the injected current, the gain peak experiences a red shift due to self-heating, detuning itself from the Bragg wavelength, which undergoes much less red-shift with increasing I. At ~150mA, the sample transfers from lasing via the DFB lasing mode to lasing via the Fabry-Pérot modes, as can be demonstrated in the following EL spectra.

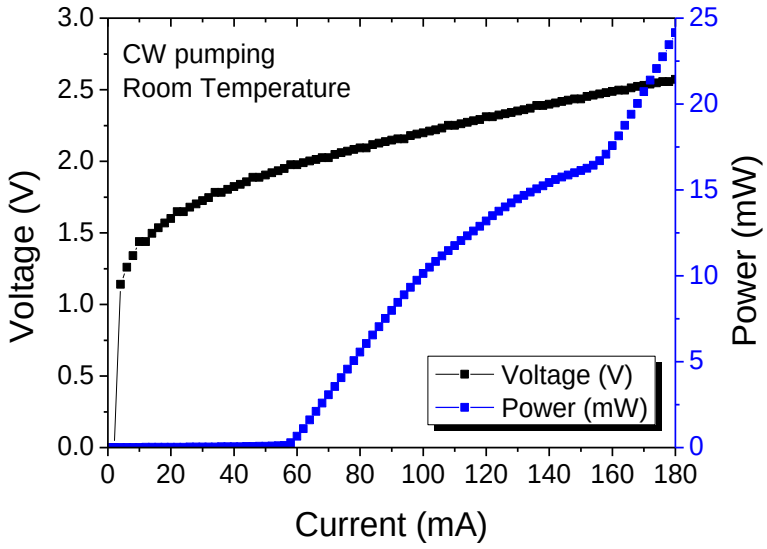

Figure 4-15: L-I-V curve measured at room temperature with CW pumping

Fig. 4-16 plots the electroluminescent spectra recorded from this device with increasing injection current (from 60mA to 180mA in 30mA increment) over a wavelength range of 992nm to 1008nm. As can be seen, the laser operates via a single lasing mode about the Bragg wavelength at 994nm to 994.5nm from 60mA (threshold)

until 120mA with a measured wavelength shif of 0.008nm/mA. Around 90mA-120mA, the laser maintains an SMSR of more than 30dB. Below 120mA, there is no obvious red shift of the gain peak from its centre at ~998nm because the self-heating is balanced by the heat extraction capability of the mounted device. From 150mA onwards, the red-shift of the gain peak becomes significant with the simple AlO_2 submount unable to efficiently heat-sink, thus increasing the detuning between the gain peak and the DFB mode, and the sample grudually undergoes a reduction in SMSR and eventually transfers from lasing via the DFB lasing mode to lasing via an ensemble of Fabry-Pérot modes at the shifted gain peak.

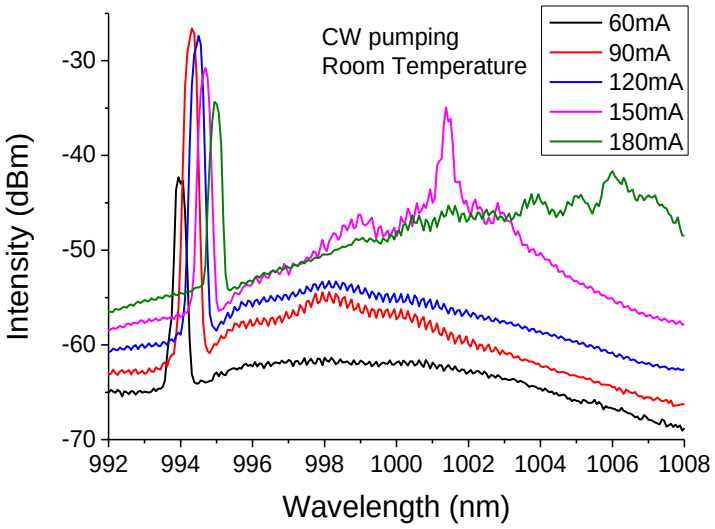

Figure 4-16: Spectrum taken at room temperature for CW pumping

Despite this, the spectra recorded at 150mA and 180mA current injection also demonstrate lasing via the DFB mode as well as the F-P modes, which suggests that better AR coating could result in continued DFB operation to higher currents. But one can expect that, when pumping the device harder to achieve a higher CW output power, the self-heating effect with higher current injection would significantly increase the detuning due to the red-shift of the gain peak, which results in continuous decrease in the L-I slope efficiency and eventually clamps the maximum output power of this device.

- **Discussion**

From the study of this representative device, it was found that, at ~I_{thresh}, the λ_{Bragg} of a 148nm grating period is positioned ~4nm on the short wavelength side of the gain peak, which would continue to increase as more current being injected, end up with significant detuning. Iit could be concluded that devices with this grating period fabricated from this sample are not suitable for high power CW operation due to the inevitable breakdown of DFB operation at higher current. Athough this issue could be tackled through improved heat extraction, which increasing the total cost of the device.

➢ Grating Period 149nm

The following section describes the measurement of a representative 4×QWs SAS-DFB laser with a 149nm period grating.

Fig. 4-17 plots the CW L-I-V characteristics. The resistance of this device is calculated from the I-V curve to be around 3Ω.

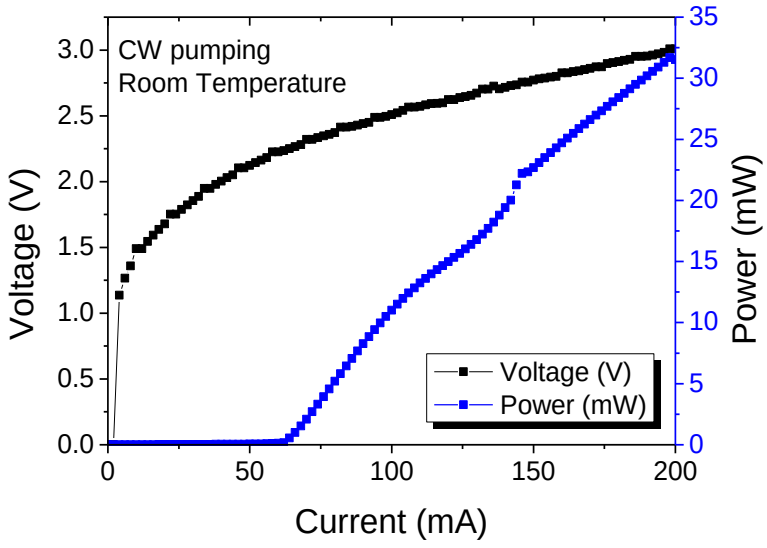

Figure 4-17: L-I-V curve measured at room temperature with CW pumping

The L-I curve shows a CW lasing threshold at around 65mA with an initial slope efficiency of ~0.29W/A. This efficiency is maintained until ~100mA and reduces slightly until ~125mA where a deflection to an improved efficiency at around 125mA-140mA, folloowing a kink in the L-I at around 150mA and becomes stable at ~0.22W/A until 200mA.

Fig. 4-18 plots the CW electroluminescent spectra recorded as a function of increasing injection current from 80mA to 200mA with 40mA increment over a wavelenght range of 990nm to 1020nm at room temperature. This figure can help explain the phenomenon observed in the L-I characteristic above. At low injection currents the EL peak is centred ~995nm and the DFB wavelengh is located slightly to the red side of the gain spectrum. The laser operates via a single DFB laser mode at 80mA at 999.6nm and reaches an SMSR of more than 45dB at around 120mA, with a small wavelength shift to 1000.0nm.

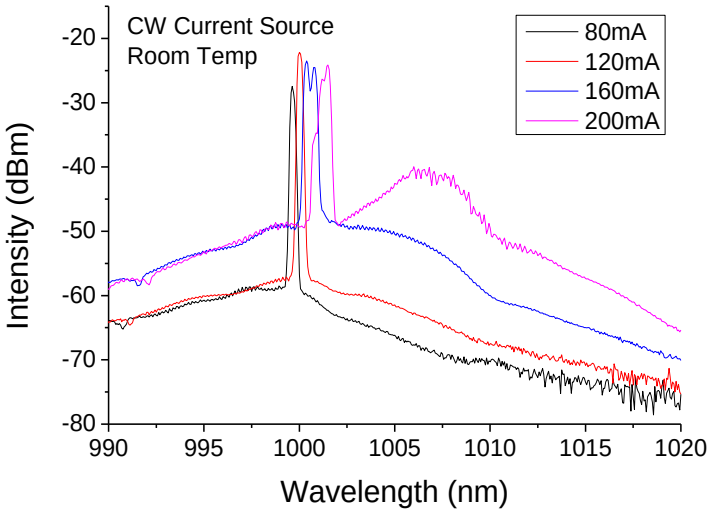

Figure 4-18: Spectrum recorded at room temperature with CW pumping

However, beyond 120mA mode hopping from the shorter DFB wavelength to the longer DFB mode takes place around 140-160mA. This is commensurate with the observed kink in the L-I characteristic in Fig. 4-17. Beyond this, the red shift of the gain peak becomes significant and increaes the detuning between the DFB mode and the gain

peak. At 200mA, the DFB lasing mode is accompanied by the F-P lasing modes at the gain peak at ~1007nm. It can be predicted that the lasing operation will be dominanted by Fabry-Pérot lasing mode with higher injected current.

- **Discussion**

Compared to the 148nm grating period devices, the 149nm grating devices exhibited improved performance to higher CW current injection with commensuratedly higher output power. This is a result of the transfer from DFB mode to Fabry-Pérot lasing occuring at higher currents, which is due to the wider range of curretns that the DFB mode remains resonant with the gain. Therefore, further study was conducted to investigate thermal tuning characteristics of these samples, in which pulsed current source was used to control the effect of self heating.

- **Thermal Tunability**

Fig. 4-19 plots the L-I characteristic of a 149nm grating period sample over a temperature range from 20°C to 80 °C.

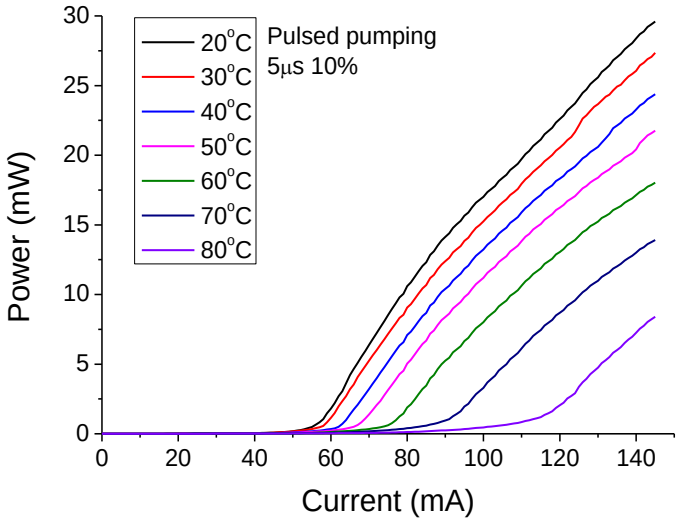

Figure 4-19: L-I curve measured at different temperature with pulsed pumping

The lasing threshold is observed to increase from 58mA at 20 °C, to 60mA at 30 °C, 63mA at 40°C, 68mA at 50 °C, 77mA at 60°C, 90mA at 70 °C and 120mA at 80°C. The

slope efficiency is correspondingly observed to decrease with rising temperature from from 0.42W/A at 20 ^{o}C, to 0.40W/A at 30 ^{o}C, 0.38W/A at 40^{o}C, 0.37W/A at 50 ^{o}C, 0.36W/A at 60^{o}C, 0.28W/A at 70 ^{o}C and 0.25W/A at 80^{o}C. The kinks at higher currents (~2×I_{th}) represent mode hopping from shorter DFB wavelengths to longer DFB wavelengths (occuring at 90mA at 20 ^{o}C, 120mA at 30 ^{o}C and 140mA at 40^{o}C respectively).

Fig. 4-20 plots the spectra recorded with 140mA pulsed (5μs, 10%) pumping for a range of temperatures from 20^{o}C to 60^{o}C using an Advantest Q8384 optical spectrum analyser with 0.01nm resolution.

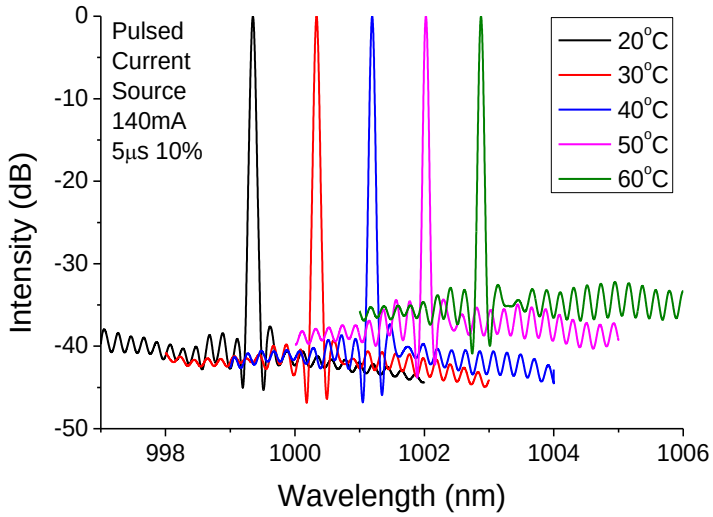

Figure 4-20: Spectrum recorded at different temperature with pulsed pumping at 140mA

The peaks of the spectra were normalised to 0dB for clarity of presentation. The laser operates via a single DFB mode over this range of temperatures and exhibits a temperature-dependent wavelength shift of 0.09nm/^{o}C, tuning from 999.3nm at 20^{o}C to 1002.9nm at 60^{o}C. Over this temperature range, an SMSR of about 35dB was maintained.

➢ Grating Period 150nm

The following section describes the measurement of a representative 4×QWs SAS-DFB laser with a 150nm period grating. Fig. 4-21 (a) plots the CW L-I characteristic of this device over a range of temperature from 20°C to 70°C. From a study of the threshold current as a function of temperature, a characteristic temperature, T_0, of 119 ℃ can be determined over this temperature range (i.e. 20 ℃-70 ℃). As shown, at 20 ℃ the device reaches lasing threshold at ~65mA with a kink exhibited in the power *versus* current (*P vs I*) characteristic at 110mA.

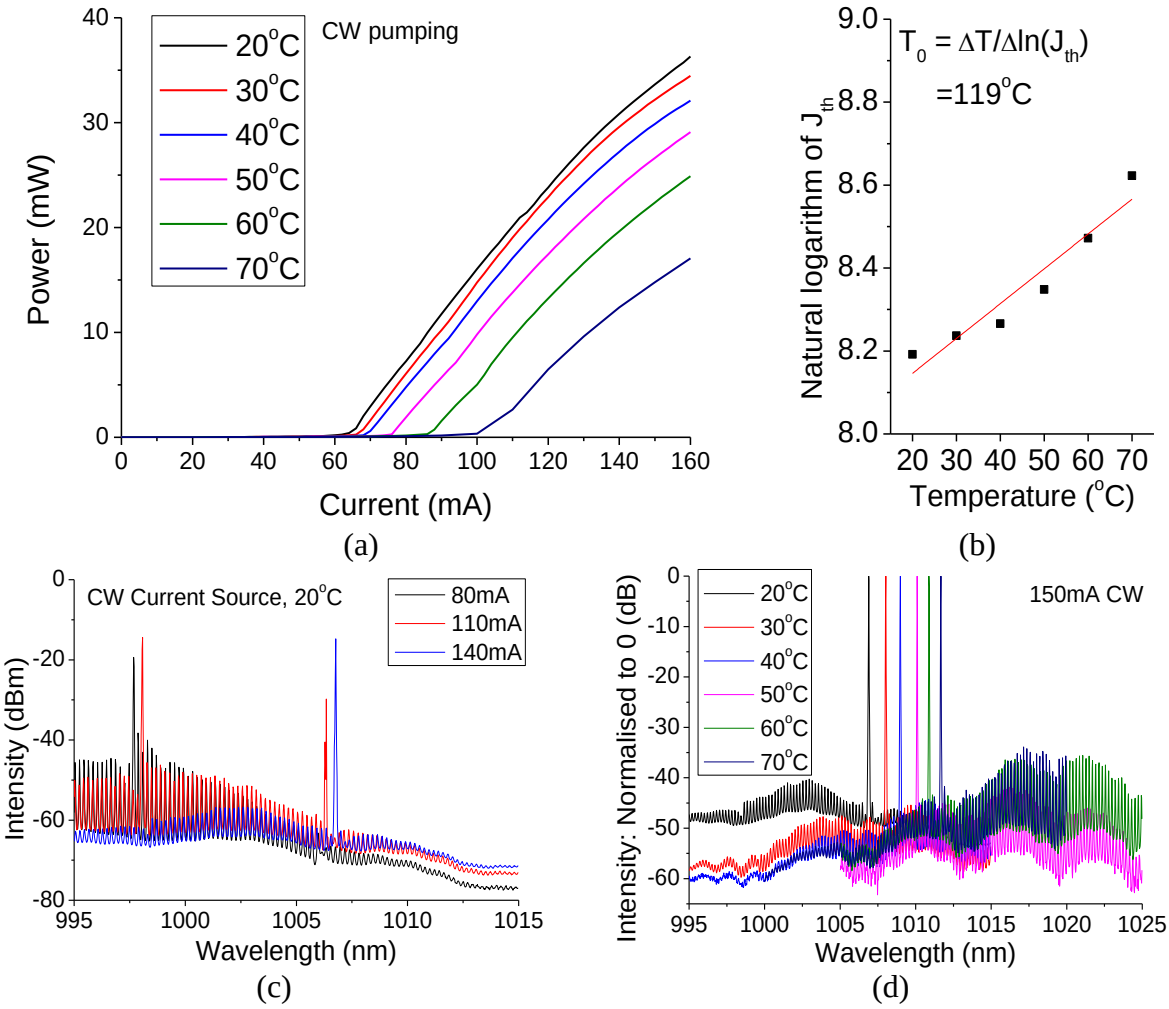

Figure 4-21: (a) Output power vs CW injected current under different temperature, (b) plotting natural logarithm of threshold current density as a function of temperature to calculate T_0, (c) spectra recorded with different injection current at 20°C and (d) spectra recorded with 140mA CW injection current at different temperatures

Fig. 4-21 (c) plots the recorded examination of the electroluminescence spectra using an Advantest Q8384 optical spectrum analyser with 0.01nm resolution, which revealed an expected transition from lasing on multiple Fabry-Pérot modes below 110mA to lasing via the single DFB mode above 130mA. At elevated substrate temperatures (30℃-70℃) lasing proceeded via the DFB mode from threshold. The device exhibits mode-hops from shorter to longer DFB wavelengths.

These mode hops are accompanied by kinks in each *P v's I* curve above threshold (occurring at 88mA at 30℃, 90mA at 40℃, 94mA at 50℃, 100mA at 60℃, and 110mA at 70℃). We attribute the mode-hops to random facet phase shifts at the cleaved facets. The device exhibits kink-free single mode operation with more than 35dB SMSR from 1.5× threshold current.

Fig. 4-21 (d) plots the spectra recorded at different temperatures when the device was operating with 150mA CW injection current, in which the intensity of the peaks was normalised to 0dB to assist analysis. Over this temperature range (20℃-70℃), the gain peak was observed to red-shift from the shorter wavelength side of the Bragg wavelength to its longer wavelength side, whilst this device maintained single mode lasing via the DFB mode over this temperature range.

- **Thermal Tunability**

The device was studied over a wide range of temperatures and currents. Fig. 4-22 plots the EL spectra for a range of CW currents at temperature of 30℃, 40℃, 50℃, 60℃ and 70℃. At each temperature, the spectra exhibit a single DFB mode over a range of currents. Here, for each temperature, the spectra were recorded at different currents higher than where the mode hoping occurs (as described above), i.e. when single-mode lasing via the longer DFB modes, as well as demonstrating an SMSR

larger than 35dB. The spectra shown in Fig. 4-22 can be summarised by plotting the lasing wavelength and SMSR over the range of currents applied at each temperature.

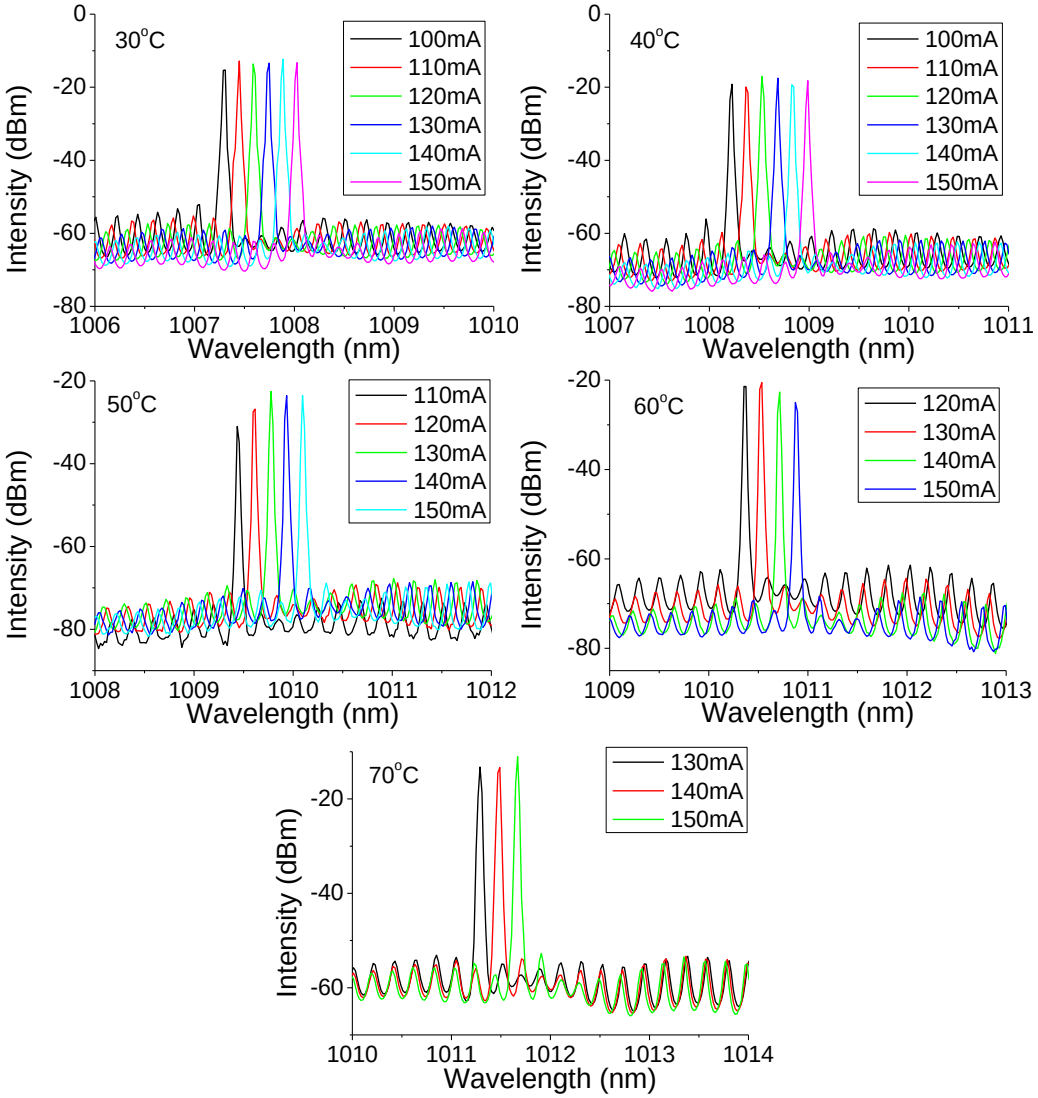

Figure 4-22: Spectrum recorded with different injected current under different temperature

Fig. 4-23 summaries the SMSR and the lasing wavelength between 100mA and 150mA, extracted from Fig. 4-22. The laser demonstrated operation on a single mode at 1007nm with an SMSR of ~37dB at 100mA (~1.5× threshold) at 30°C, rising up to ~45dB at 130mA (corresponding to >30mW output power at a wavelength of 1008nm), and similar behaviour was observed at 40°C and 50°C with 0.015nm/mA. At higher temperatures, single mode lasing was measured over a reduced range of currents (from 120mA at 60°C and 130mA at 70°C).

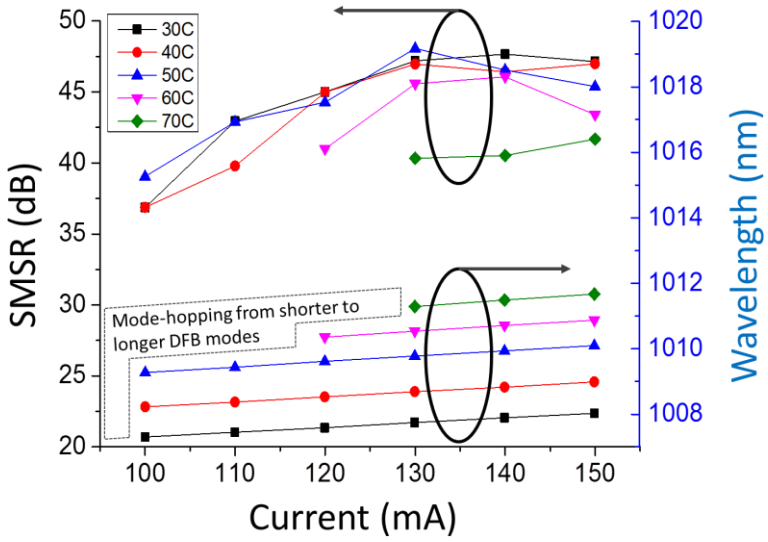

Figure 4-23: SMSR and wavelength shift under different temperature

- **Discussion**

In comparison, the representative device with a 150nm period grating demonstrated a much better performance at higher pumping current. Despite the observaation of transition from lasing on multiple Fabry-Pérot modes (immdieately above I_{thresh}) to lasing via the single DFB mode (above $2\times I_{thresh}$) at lower operating temperature (20^{o}C), the device demonstarted stable and kink-free DFB operation over a certain range of current at each elevated operating temperature (30/40/50/60/70^{o}C).

➢ Summary

Characterisation of these representative devices showed the effect of detuning (distance between λ_{Bragg} and material gain peak) upon DFB performance. Furthermore, the experimental observation of such effect was very significant for this batch of devices, because the exit facet AR coating was not optimal, as described in Section 4.2.2, resulting in inadequate suppression of facet reflection. In this premise, devices with a 150nm period grating are more suitable for high power DFB operation.

4.3.2 2×QWs SAS-DFB

Fig. 4-24 plots the L-I-V measurement of the best measured representative SAS DFB laser incorporating 2×QWs. This device demonstrates an output power of only ~11mW at 120mW (CW). Compared to the 4×QWs SAS-DFB in Fig. 4-21, this value was less than half of that measured. In addition, these 2×QWs devices demonstrate a nonlinear L-I slope above ~2.5×I_{thresh} and started rolling over above ~200mA. The I-V characteristic, which gives R~6Ω suggests the device is fine electrically. The problem was expected from the simulation of the waveguide, which showed a 2nd guided mode located around the grating, as shown in Fig. 4-3 (a). For an SAS structure, the in-plane (lateral and vertical) confinement of the optical mode is mainly realised through index-guiding.

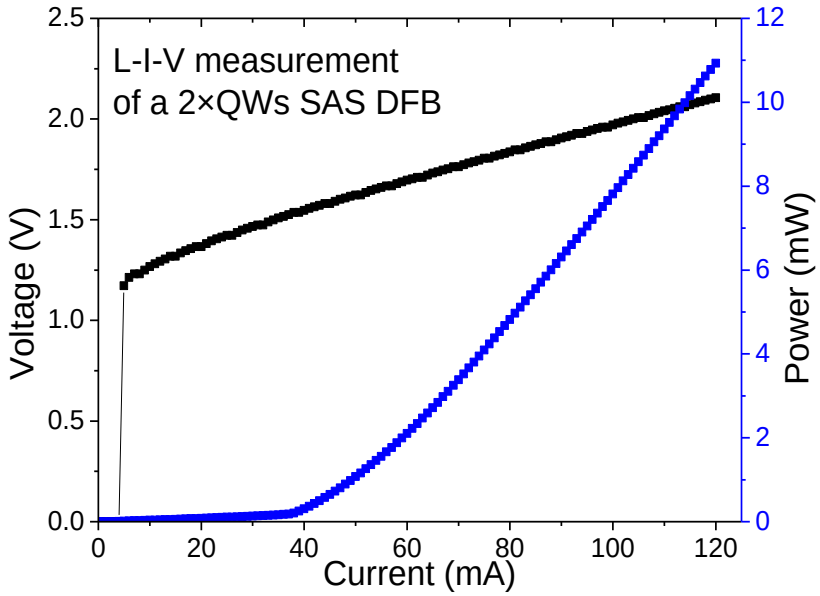

Figure 4-24: L-I-V measurement of a representative device of 2×QWs SAS-DFB

In Section 4.1.2, although some modification to the original SAS layer structure [16] had been made to improve the mode profile, the original design of the 2×QWs SAS-DFB still showed a problematic wave-guiding. Furthermore, the requirement of an

increase in thickness of the 1st layer of in-fill GaAs from 45nm, as designed, to 100nm to ensure the quality of overgrowth (Section 4.1.3) further affected the waveguide. Although some modification was made to reduce this effect in the 4×QWs SAS-DFB, it was not possible to do so separately for the 2×QWs SAS-DFB.

The spectra recorded from measurement found a different correspondence between the grating periods and DFB wavelengths to those recorded from 4×QWs SAS-DFBs. As described in Section 4.3.1, for the 4×QWs SAS-DFBs, the devices with grating periods of 148nm, 149nm and 150nm had a lasing wavelength with CW current injection just above the threshold at room temperature of ~994nm, ~1000nm and ~1006nm respectively. However, for the 2×QWs devices, as shown in Fig. 4-25, the 3 wavelengths reduce to ~977nm, ~983nm and ~989nm respectively.

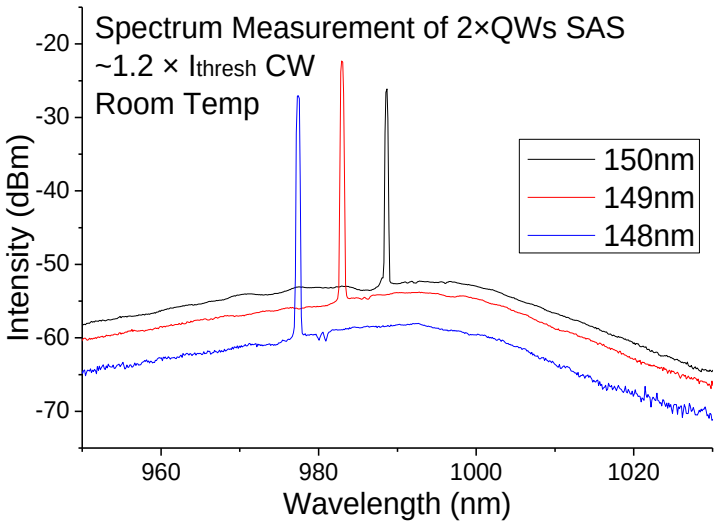

Figure 4-25: Spectrum measurement of 2×QWs SAS-DFBs

The Bragg wavelength of a 1st order grating period is determined by the equation:

$\lambda_B = 2\Lambda n_e$ (Λ: grating period; n_e: effective refractive index)

Therefore, the effective refractive index could be experimentally calculated from the wavelengths. A comparison of the calculated effective refractive index is shown in Table 4-3.

	Lasing Wavelength (nm)	Grating Period (nm)	Calculated n_{eff}
4×QWs SAS-DFBs	994	148	3.36
	1000	149	3.36
	1006	150	3.35
2×QWs SAS-DFBs	977	148	3.30
	983	149	3.30
	989	150	3.30

Table 4-3: Comparison of lasing wavelength of 2× and 4× QWs SAS-DFBs

The calculation shows an average difference in effective index of 0.057, which corresponded to a mismatch of ~1.7% between the two samples. The grating was designed to be formed by 50/50 InGaP/GaAs rectangular structures, and the refractive indices of GaAs and InGaP are 3.51 and 3.15 respectively. Therefore, a measured higher effective refractive index indicates a higher composition of GaAs in the actual grating structure. From the comparison, it can be speculated that, during the etch of the grating pattern, the InGaP layer was etched slightly deeper in the 4×QWs sample than in the 2×QWs sample, or that there was variation in the mark-to-space ratio from sample to sample. Both issues could result in a slightly different effective refractive index between samples.

4.3.3 Validation of Simulation

In order to validate the waveguide simulation of the device, as well as to feed back into the research cycle for future structural design, comparison has been made between the experimentally measured and the simulated optical far-field beam profile and coupling coefficient.

➢ Far-Field Beam Profile

The optical far-field profiles were measured for the 4×QWs lasers using a standard far-field goniometer with InGaAs detector. The measured horizontal (slow-axis) and vertical (fast-axis) profiles are plotted in Fig. 4-26. The experimental profiles correlated well with the simulated far-fields, which are shown by the dotted red lines superimposed upon the experimental data in the figure.

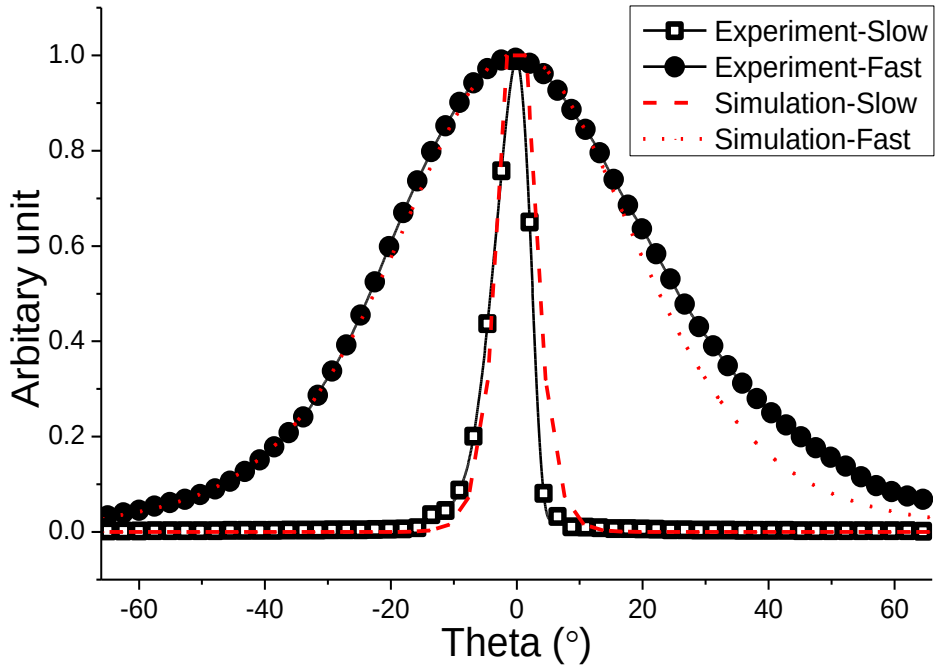

Figure 4-26: Comparison of simulated and experimental optical far-field beam profile

The experimental full-width-at-half-maximum (FWHM) divergence was measured as 49.4 ° in the fast axis and 6.6 ° in the slow axis, verifying both the simulation (46.1 ° and 6.9 °) and the origin of emitted light (i.e. via the fundamental lateral mode of the confined SAS). Small differences between the experimental and simulated far-fields were attributed to the effect of gain guiding in the structure and the approximation to a vertical profile of the SAS (i.e.: the shape of the etched stripe) in the simulation, rather than the angled planes provided by the etch process (described in earlier work [16]).

➢ Coupling Coefficient

Further correlation between the fabricated device and the simulated optical profile was provided by derivation of the grating coupling coefficient in the SAS-DFB and comparison with the simulated coupling coefficient. As described in Chapter 3, for a DFB laser of a given cavity length (L), by measuring the wavelength spacing (Δv) between the two adjacent sub-threshold DFB modes on either side of the Bragg wavelength and the longitudinal mode spacing (Δv_{long}), the coupling coefficient can be estimated from [19]:

$$K_{meas} = \frac{\pi \times \Delta v}{2 \times L \times \Delta v_{long}}$$

Care must be taken for non-zero facet reflectivity since this facet phase relative to the DFB grating distorts the subthreshold emission spectra [20]. However, a good approximation can be derived either by fitting the measured curve for a single laser, or by measuring many devices along the bar (which will have differing facet phase) and selecting the one with the ideal spectrum. The ideal spectrum is one without any residual peaks in the stop band, equal strength peaks either side of the stop band, and these two peaks are stronger than the higher order modes [20].

A range of $\Delta\lambda$ between 0.24 and 0.26 nm were measured across a laser bar. Fig. 4-27 plots the measurement of a representative device which demonstrated the most ideal spectral profile, in which (a) recorded the two sub-threshold DFB modes at ~1005.8nm and (b) recorded the F-P longitudinal modes. The Δv was measured from (a) as 2.37cm^{-1}, with Δv_{long} from (b) as 2.00cm^{-1}. The coupling coefficient, K, was therefore estimated as 29.51cm^{-1}, implying an optical confinement factor in the grating, $\Gamma_{grating}$, of 0.0041, which is higher than that obtained in our simulations (0.0031).

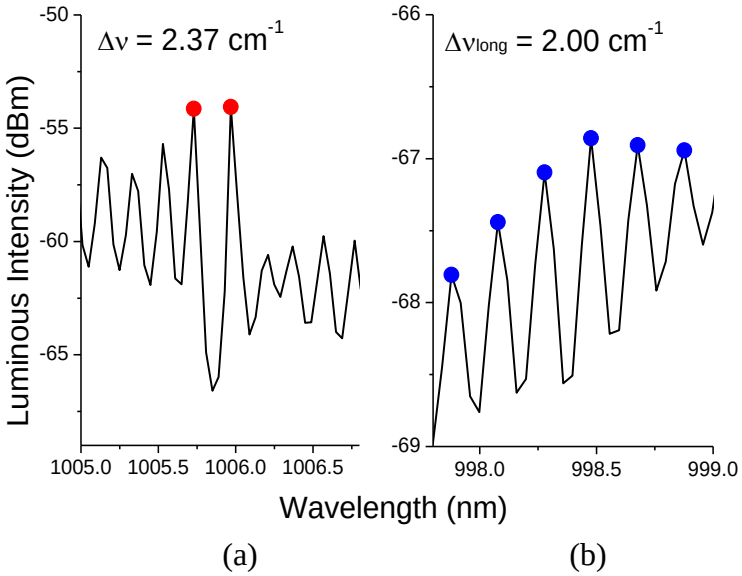

Figure 4-27: Recorded spectra showing (a) the two sub-threshold DFB modes, as annotated by the red dots, and (b) the F-P longitudinal modes, as annotated by blue dots, from which the DFB stop-band and longitudinal mode spacing were experimentally measured as 2.37cm^{-1} and 2.00cm^{-1} respectively

This mismatch was expected since the Fimmwave waveguide modelling was mainly based on its structural definition in terms of dimensions and refractive indices. The simulation did not take into account an additional lateral optical confinement provided by the stripe geometry. In the formation of the stripe geometry in this SAS structure, the n-doped InGaP electrical blocking layer on both sides of the etched stripe blocks the current though a p-n-p-n junction, electrically confining the current flow to the width of the etched stripe. This further determines the downwards distribution of the current passing through the stripe into the active region below, which results in a determination of the lateral dimension (width) of the gain area. This provides a certain amount of gain-guidance to the optical mode.

In the measurement, the optical mode was both index- and gain- guided. Receiving an additional lateral confinement compared with the simulation, the optical mode

narrowed slightly, resulting in a slight increase in the measurement of the confinement factor in the grating, and hence a stronger coupling coefficient.

A small deviation in the refractive indices used in the simulation could provide another possible cause for this small mismatch. Furthermore, the waveguide structure defined in the simulation was based on a simple rectangular profile for the etched InGaP layer for simplicity (3μm from top to bottom). However, in real device manufacture, as demonstrated in [16], the wet chemical etching proceeded with a 45^{o} angle, pinned laterally by the GaAs layer above, resulting in an actual stripe width of 2-2.5μm, which could also give rise to this mismatch.

4.3.4 Further Simulation for Future Work

The devices manufactured were realised through modification to the design of the upper cladding layers due to the emergence of a specific growth requirement for a thicker GaAs layer in the first overgrowth step for planarisation (Section 4.1.3). This was enabled through the high level of flexibility offered by this design, and my approach provided a demonstration of this important attribute. However, further simulation has been carried out for 4×QWs SAS DFB with the aim of designing a structure appropriate for use in future integrated designs, with a symmetric composition of Al_x in upper and lower cladding (i.e. growth of a new starting planar wafer).

Table 4-4 shows a modified design with x = 0.42. Instead of increasing the Al composition of the upper cladding, this structure is based on a 32 nm thick grating layer and an increased thickness of AlGaAs spacer layer between the grating and the active region of 540 nm.

Modified design (symmetric)	
$Al_xGa_{1-x}As$	x = 0.42
2nd GaAs in-fill	40 nm
1st GaAs in-fill	100 nm
Grating thickness	32 nm
Separation	540 nm
$\Gamma_{Grating}$	0.0033
Γ_{QWs}	0.0415

Table 4-4: Parameters used in the modified design together with the expected resultant optical properties

These modifications provide nearly identical confinement factor for the grating and QWs as before, but also with an improved optical mode profile, as shown in Fig. 4-28.

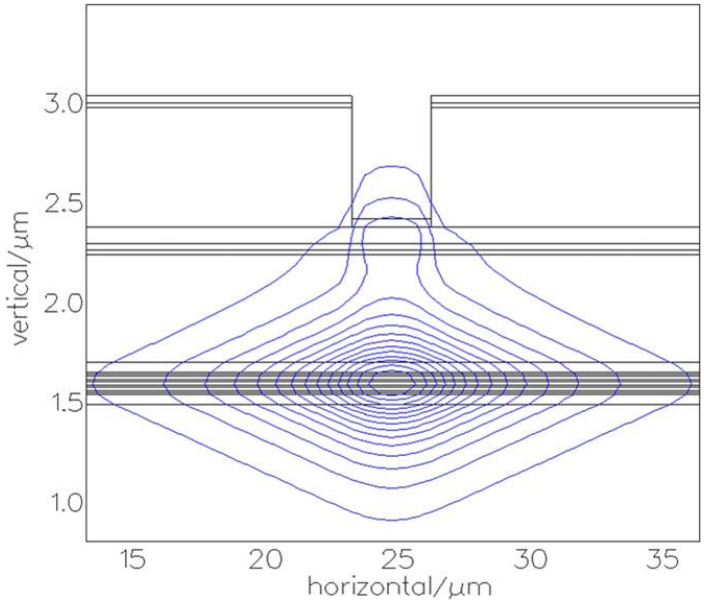

Figure 4-28: Simulation of optical mode profile

4.4 Conclusion

This chapter has demonstrated the 2× and 4× QWs GaAs-based DFB laser design incorporating a first order InGaP/GaAs index-coupled DFB grating built within a SAS buried waveguide structure. The preparation of the devices mainly consisted of six steps: planar growth, grating fabrication, 1st overgrowth, SAS etching, 2nd overgrowth and laser fabrication. In the process, it was found that a thickness of 100nm of the in-fill GaAs layer, instead of 45nm as designed, was required for the grating planarisation in the 1st overgrowth. Therefore, by making use of the tailor-ability of the waveguide provided by GaAs/AlGaAs system, the 2nd overgrowth was modified to maintain an expected confinement factor. This was achieved by reducing 2nd in-fill GaAs from 60nm to 40nm and modifying the composition of Al in the upper cladding from 0.42 to 0.7, as described in Section 4.1, which resulted in a weaker optical confinement (lower average refractive index) for the upper cladding to balance the increased confinement near grating layer provided by the additional 55nm in-fill GaAs. This modification ended up with SAS-DFB devices incorporating an asymmetric cladding scheme, which demonstrated the flexibility to tailor the optical profile afforded by the SAS approach.

For the 2×QWs design, problems with optical confinement were observed in the simulation stage. Due to the strong optical confinement near the grating layer by stacking GaAs layers in the manufacture process, the optical mode profile from simulation exhibited a secondary peak centred on the stacked GaAs layers. Although modifications were made to reduce the magnitude of the secondary peak, it could not be removed entirely. The requirement for a 100nm GaAs in-fill layer in the 1st overgrowth to fully planarise the grating pattern introduced even thicker stacking of GaAs.

Although modifications have been made to the 2nd overgrowth as described above, the wave-guiding in the 2×QWs design was not improved, which resulted in a less robust device performance compared to that of 4×QWs design.

For the 4×QWs design, devices with all three grating periods demonstrated single mode DFB lasing at a wavelength in the region of ~1μm. The representative devices with 148nm (~994nm) and 149nm (~1000nm) gratings both demonstrated lasing via the DFB mode upon reaching the threshold but is then dominated by the Fabry–Pérot mode with increased current injection. This was because the current-induced temperature increase inside the device caused a red-shift of the gain spectrum. With higher current injection, this red shift resulted in a significant detuning between the gain peak and the Bragg wavelength. As for the representative device with 150nm grating period, single mode emission was demonstrated at a wavelength of ~1006nm with a lasing output power of ~35mW (20 ℃, 160mA) and >40 dB SMSR over the temperature range 20 ℃–70 ℃.

Furthermore, comparison has been made between the experimentally measured far-field and grating coupling with that simulated for the sample. The results showed a high level of accordance in the far-field beam profile comparison, but with a +32% mismatch in coupling coefficient comparison. This mismatch could be due to the existence of gain guidance in the waveguide in real operation, which was not taken into account in the simulation. This introduced additional lateral confinement to the mode, resulting in a higher confinement factor in the grating layer.

Lastly, based on the requirement of 100nm in-fill GaAs for grating planarisation, a 4×QWs symmetric design with both upper and lower cladding of $Al_{0.42}Ga_{0.58}As$ has been simulated for future research.

4.5 Reference

[1] N. A. Morris, J. C. Connolly, R. U. Martinelli, J. H. Abeles and A. L. Cook, "Single-mode distributed-feedback 761-nm GaAs-AlGaAs quantum-well laser," *IEEE Photonics Technology Letters*, vol. 7, no. 5, pp. 455-457, May 1995.

[2] M. Nakamura, K. Aiki, J. Umeda, A. Katzir, A. Yariv and H. Yen, "GaAs GaAlAs double-heterostructure injection lasers with distributed feedback," *IEEE Journal of Quantum Electronics*, vol. 11, no. 7, pp. 436-439, July 1975.

[3] B. J. Stevens, K. M. Groom, J. S. Roberts, P. W. Fry, D. T. D. Childs and R. A. Hogg, "Distributed feedback laser employing buried GaAs/InGaP index-coupled grating," *Electronics Letters*, vol. 46, no. 15, pp. 1076-1077, July 22 2010.

[4] M. Fischer, D. Gollub, M. Reinhardt, M. Kamp and A. Forchel, "GaInNAs for GaAs based lasers for the 1.3 to 1.5μm range," *Journal of Crystal Growth*, vol. 251, no. 1-4, pp. 353–359, 2003.

[5] M. Muller, F. Klopf, M. Kamp, J. P. Reithmaier and A. Forchel, "Wide range tunable laterally coupled distributed-feedback lasers based on InGaAs-GaAs quantum dots," *IEEE Photonics Technology Letters*, vol. 14, no. 9, pp. 1246-1248, September 2002.

[6] R. Martin, S. Forouhar, S. Keo, R. Lang, R. Hunsperger, R. Tiberio and P. Chapman, "CW performance of an InGaAs-GaAs-AlGaAs laterally-coupled distributed feedback (LC-DFB) ridge laser diode," *IEEE Photonics Technology Letters*, vol. 7, no. 3, pp. 244–246, 1995.

[7] A. Yoshikawa, A. Yamamoto, M. Hirose, T. Sugino, G. Kano and I. Teramoto, "A self-aligned ridge substrate laser fabricated by single-step MOVPE," *Journal of Crystal Growth*, vol. 93, no. 1-4, pp. 843–849, 1988.

[8] K. Nakahara, Y. Wakayama, T. Kitatani, T. Taniguchi, T. Fukamachi, Y. Sakuma and S. Tanaka, "56-Gb/s Direct Modulation in InGaAlAs BH-DFB Lasers at 55°C," *Optical Fiber Communication Conference*, San Francisco, CA, 2014, pp. 1-3, 2014.

[9] J. Li, S. Tang, J. Wang, Y. Liu, H. Xu, Q. Tang, X. Chen and J. Cheng, "Monolithic Buried Heterostructure DFB Laser Array for Integrated Optical Interconnects and WDM systems," *Optical Fiber Communication Conference*, San Francisco, CA, 2014, pp. 1-3, 2014.

[10] C.-C. Chang, T. Kuech, C. Boyle, J. Kirch, T. Earles, D. Lindberg, L. Mawst, P. Buelow and D. Botez, "Buried-heterostructure mid-infrared quantum cascade lasers fabricated by non-selective regrowth and chemical polishing," *Electronics Letters*, vol. 51, no. 14, pp. 1098–1100, September 2015.

[11] T. Tsukada, "GaAs–$Ga_{1-x}Al_xAs$ buried-heterostructure injection lasers," *Journal of Applied Physics*, vol. 45, no. 11, pp. 4899–4906, 1974.

[12] R. D. Burnham, D. R. Scifres and W. Streifer, "Distributed Feedback Buried Heterostructure Diode Laser," *Applied Physics Letters*, vol. 29, no. 5, pp. 287–289, 1976.

[13] M. J. Adams, "The Cladded Parabolic-Index Profile Waveguide: Analysis and Application to Stripe-Geometry Lasers," *Optical and Quantum Electronics*, vol. 10, no. 1, pp. 17–29, 1978.

[14] M. Nido, I. Komazaki, K. Kobayashi, K. Endo, M. Ueno, T. Kamejima and T. Suzuki, "AlGaAs/GaAs self-aligned LD's fabricated by the process containing vapor phase etching and subsequent MOVPE regrowth," *IEEE Journal of Quantum Electronics*, vol. 23, no. 6, pp. 720–724, 1987.

[15] N.-T. Yeh, W.-S. Liu, S.-H. Chen, P.-C. Chiu and J.-I. Chyi, "InAs/GaAs quantum dot lasers with InGaP cladding layer grown by solid-source molecular-beam epitaxy," *Applied Physics Letters*, vol. 80, no. 4, pp. 535–537, 2002.

[16] K. M. Groom, B. J. Stevens, P. J. Assamoi, J. S. Roberts, M. Hugues, D. T. D. Childs, R. R. Alexander, M. Hopkinson, A. S. Helmy and R. A. Hogg, "Quantum Well and Dot Self-Aligned Stripe Lasers Utilizing an InGaP Optoelectronic Confinement Layer," *IEEE Journal of Selected Topics in Quantum Electronics*, vol. 15, no. 3, pp. 819–827, 2009.

[17] K. Shimoyama, Y. Inoue, M. Katoh, H. Gotoh, Y. Suzuki and H. Yajima, "Novel buried heterostructure laser triode for monolithic integration," *Electronics Letters*, vol. 25, no. 16, pp. 1096-1097, 3 August 1989.

[18] U. Koren, R. M. Jopson, B. I. Miller, M. Chien, M. G. Young, C. A. Burrus, C. R. Giles, H. M. Presby, G. Raybon, J. D. Evankow, B. Tell and K. Brown-Goebeler, "High power laser-amplifier photonic integrated circuit for 1.48 μm wavelength operation," *Applied Physics Letters*, vol. 59, no. 19, pp. 2351–2353, April 1991.

[19] K.-Y. Tu, T. Tamir and H. Lee, "Multiple-scattering theory of wave diffraction by superposed volume gratings," *Journal of the Optical Society of America A*, vol. 7, no. 8, p. 1421-1435, January 1990.

[20] T. Kjellberg, S. Nilsson, T. Klinga, B. Broberg and R. Schatz, "Investigation on the spectral characteristics of DFB lasers with different grating configurations made by electron-beam lithography," *Journal of Lightwave Technology*, vol. 11, no. 9, pp. 1405–1415, 1993.

Chapter 5. GaAs-Based Monolithically Integrated Self-Aligned Stripe Master Oscillator Power Amplifier

In recent decades, research interest in photonic systems has expanded from the optimisation of individual components to the methods and techniques for monolithic integration of discrete components. Real-life applications are usually based on functioning modules incorporating more than one optical component, and optical systems are composed discretely, where each integrated component is individually developed, manufactured and packaged. However, the nature of being assembled makes it very difficult to further optimise the system in terms of smaller sizes, lower costs and higher efficiency. A photonic integrated circuit (PIC) is the photonic equivalent of the electronic integrated circuit and refers to an optically functioning module that integrates a number of photonic components such as lasers, modulators, amplifiers on one chip. The result is a simplification of an optical system with increased functionality and the reductions in cost, space, power consumption as well as the improvement in reliability.

This chapter starts with an introduction of the concept of MOPA (Section 5.1), followed by a review of previous research conducted in the development of monolithically integrated MOPAs (Section 5.2). Then, the design of the waveguide and section geometry of two device types used in this research are described in Section 5.3, followed by a description of the process of growth and fabrication (Section 5.4). Section 5.5 presents the characterisation results of 6 representative MOPA devices, together with analysis, comparison and discussion.

5.1 Master Oscillator Power Amplifier

High-power, single-mode, diffraction-limited laser sources with output power of several Watts are required for many applications, for instance, free-space communications and frequency conversion for blue/green sources. Another application is in THz generation, where 2 high power DFBs (0.5-1W) are required to achieve usable THz radiation.

5.1.1 Discrete MOPA Designs

Conventional narrow ridge or narrow stripe semiconductor lasers cannot meet these requirements mainly due to wavelength stability and stand-alone DFB lasers have insufficient output power. MOPA systems, as illustrated in Fig. 5-1, provide promising potential for these applications, where the laser sections (MOs) operate independently for wavelength stability and the amplification of the light is facilitated by the semiconductor optical amplifier (SOA) sections (PAs), essentially de-coupling wavelength selection and power, within an integrated system.

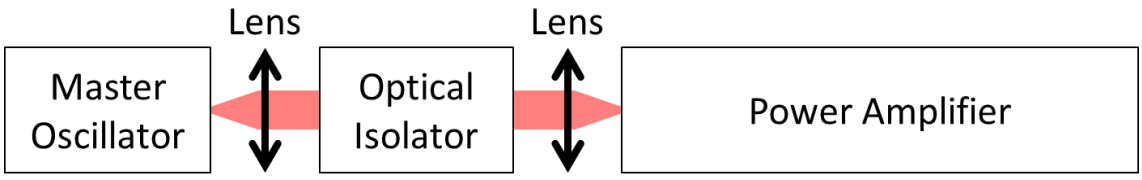

Figure 5-1: Schematic diagram of a basic MOPA system

In most of today's GaAs-based and InP-based MOPA structures, the systems are composed of a number of discrete components. For example, a study conducted by

Martin Maiwald from Ferdinand-Braun-Institut [1] reported their dual-wavelength MOPA system design operating at 785 nm for Raman spectroscopy. In this design, as shown in Fig. 5-2, the DBR master oscillators and the subsequent tilted SOA (angled to facet) were discrete system, and connected via an optical isolator to restrict the backward optical wave reflected from lenses and facets.

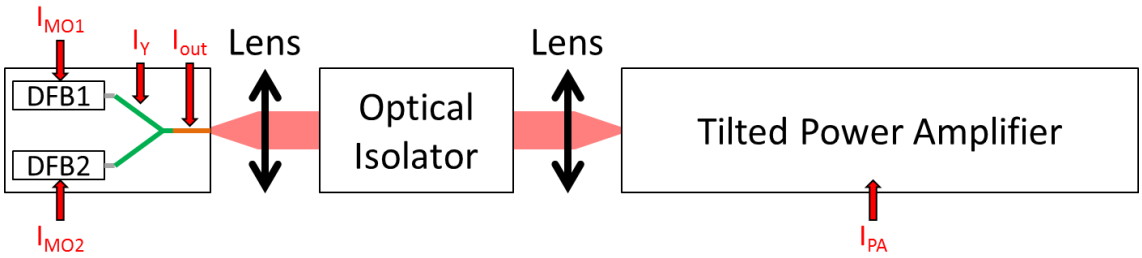

Figure 5-2: Schematic diagram of a discrete MOPA design reported in [1], where 2 DFBs were integrated as the MO

Another study of Ferdinand-Braun-Institut, conducted by Thi Nghiem Vu et al. [2], reported their discrete MOPA design for generating nanosecond optical pulses with stabilised wavelength, narrow spectral linewidth and high peak power, which aimed at applications like free-space communication and metrology. In this design, as shown in Fig. 5-3, the DFB master oscillator was also separated from the subsequent flared SOA. The two discrete components were connected by an optical isolator.

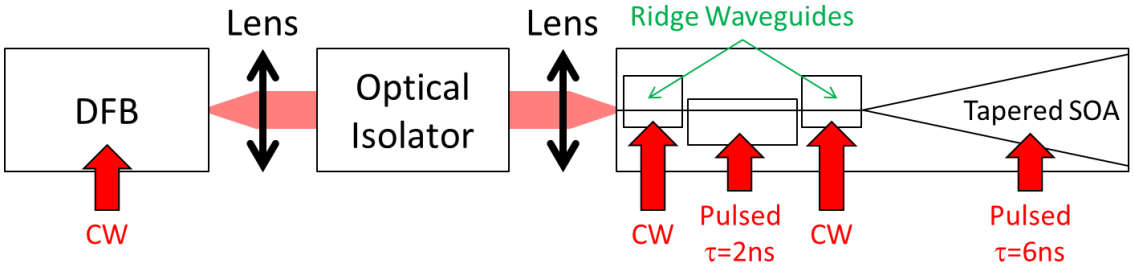

Figure 5-3: Schematic diagram of a discrete MOPA design reported in [2], where a tapered power amplifier with integrated pulse picker was incorporated for generation of nanosecond optical pulses

5.1.2 Monolithically Integrated MOPA Designs

Perhaps the simplest PIC is the MOPA device, which integrates 2 components (DFB and SOA), but arguably 3 building blocks of an integration platform (waveguide, amplifier and wavelength filter). For a monolithic MOPA design, the master oscillator (MO) is either a distributed Bragg reflector (DBR) [3] or a distributed feedback laser (DFB) [4]. Fig. 5-4 illustrates the fundamental design concept of two monolithically integrated ridge waveguide (RW) MOPA designs with DFB and DBR MOs respectively.

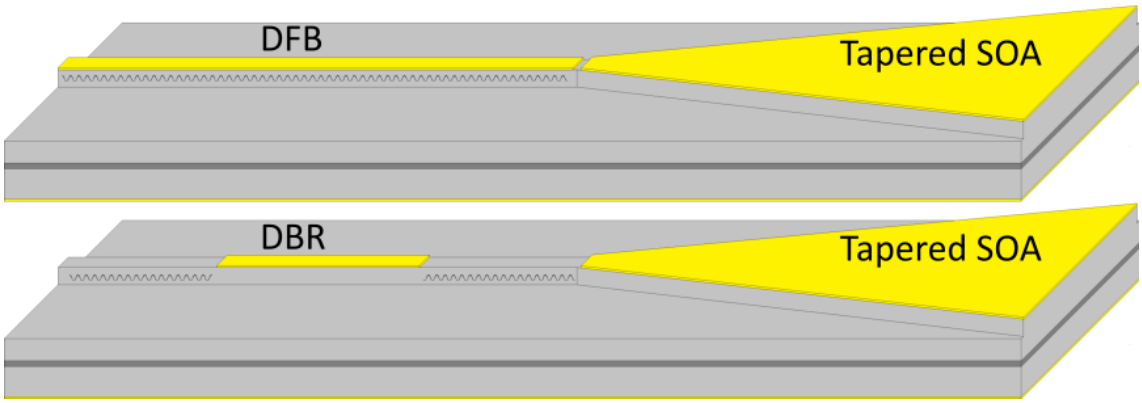

Figure 5-4: Schematic diagrams of typical monolithically integrated ridge waveguide (RW) DFB-MOPA and DBR-MOPA with flared SOA sections

In [3], Spectra Diode Labs reported their DBR design with a CW output power of 2.2W at 854nm, whilst in [4] the Ortel Corporation reported their DFB MOPA device with a CW output power of 1.5W at 980nm.

After, the Ferdinand-Braun-Institut has continued research into monolithically integrated MOPAs with both DFB [5] and DBR [6] master oscillators, with a reported output of 3.7W at 973nm and 10W at 977nm respectively. This chapter seeks to bring together the capability for DFBs demonstrated in Chapter 3 with the SAS in Chapter 4, and broader knowledge of amplifiers developed through simultaneous research on super-luminescent diodes by colleagues [7]. Compared to ridge waveguides, SAS

structures benefit from many advantages, including high reliability; small active widths, control of optoelectronic confinement and high stability of the guided mode profile. In addition, SAS structures are comparably thermally independent, which enables the possibility for on-chip tuning, e.g. by on-chip thin film heater, and hence potential for applications such as tunable THz generation and spectroscopy. The work in this chapter is therefore based on the preparatory study of ridge waveguide DFB lasers described in Chapter 3, and taken further to study the capability of simulating and manufacturing self-aligned stripe (SAS) DFB lasers in Chapter 4. In this chapter the SAS-DFB is monolithically integrated with a SAS-SOA structure to realise an integrated MOPA, whilst also looking to put together a platform for more complicated photonic integration.

For such discrete MOPA designs, although the functionality of each component could be optimised individually, they suffer from low coupling efficiency between the discrete components, as well as higher cost for manufacture and larger module sizes. First of all, the optical loss is unavoidable from the non-100% collection efficiency due to divergence from the facet. Also, the isolator and lenses inbetween also contribute further reduction of the collection efficiency. In real operation, the alignment between components requires frequent adjustment to maintain an already-low coupling efficiency for the system to operate properly. This would require even more precise alignment and maintenance for devices with narrow ridge (or stripe), e.g. single mode lasers. Furthermore, the system suffers from the high cost of assembling individually packaged chips, which also limits the system to relatively large sized modules or sub-assemblies.

5.2 Development of Monolithically Integrated MOPA

This section briefly reviews research being conducted into the development of integrated MOPAs reported by research groups over the world. Both DFB-MOPA and DBR-MOPA are considered in this section.

5.2.1 Realisations for Wide Tunability

SOAs have been monolithically integrated into more complex devices on InP, such as tunable lasers developed for telecommunication applications. Professor Larry Coldren, from the University of California Santa Barbara, developed prototype sampled-grating (SG) DBR lasers in the mid-1990s [8], which was already a monolithic multi-section device itself. In later designs, monolithic SOAs were also integrated into the design [9], as illustrated in Fig. 5-5.

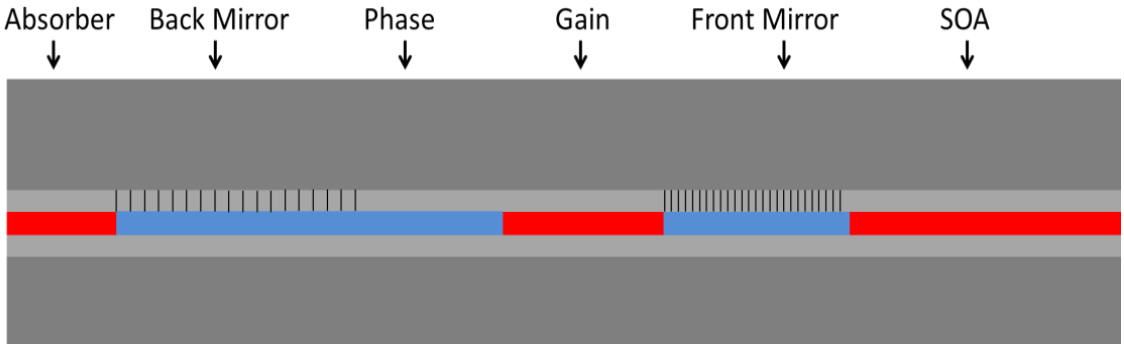

Figure 5-5: Schematic diagram of an SG-DBR with monolithically an integrated SOA section

Ward et al. (Bookham Inc.) reported a monolithically integrated design with digital super-mode (DS) DBR, which integrated a curved SOA (7^{o}-off) for applications requiring wide tunability (~45nm at ~1550nm) in 2005 [10] and now underpins a

successful telecoms product portfolio. Fig. 5-6 shows the plan view of their design, which consisted of a rear phase grating section to generate a comb of reflection peaks, a phase control section, a gain section, a front chirped grating section for coarse wavelength selection and a low gain SOA section for power levelling (output power boosting for 3-4 dB).

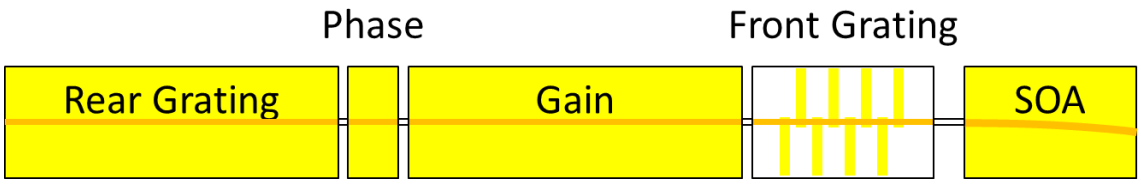

Figure 5-6: Schematic diagram of a monolithically integrated DS-DBR-SOA chip reported in [10]

In this design the wide tunability was realised by the control over the currents injected into the front and rear grating sections, and the SOA was used to level the output power across the tuning range to a similar amount. According to the report, the length of the SOA design (350μm) was a trade-off between SMSR and linewidth. The key was reported to be the minimisation of the optical feedback from the amplifier into the laser. Their techniques were to use a short amplifier in saturation (~150mA CW pumping only) and keep the facet reflection low (7^{o}-off tilting and <0.2% AR coating).

A research group in Harvard University reported a tunable MOPA design with DFB quantum cascade laser (QCL) array aiming at potential applications of spectroscopy in the mid-infrared wavelength range in 2012 [11]. In their design, pictured in Fig. 5-7, a QCL array was integrated with an array of tapered SOAs, which were electrically isolated by a 100μm wide gap in the gold metallisation. The front facet was AR coated to increase the SOA threshold for self-lasing, whilst a 360μm un-pumped absorber was incorporated between the back facet and the DFB section for each MOPA device to suppress the effect of the back facet mirror on mode selection.

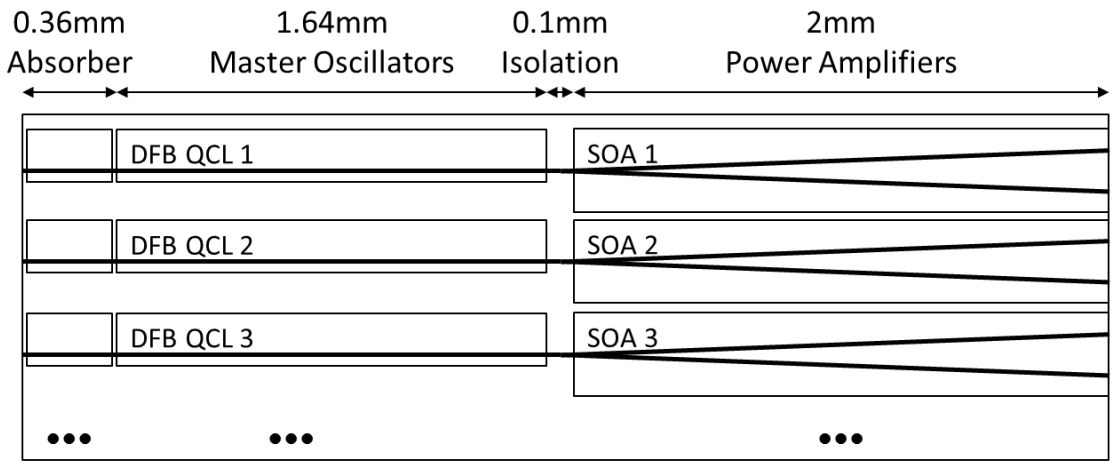

Figure 5-7: Schematic diagram of a DFB-QCL-MOPA reported in [11]

Researchers in Japan (Yokohama R&D Labs) realised wide tunability on photonic integrated circuits by integrating a twelve-channel DFB laser array [12]. As shown in Fig. 5-8, on the PIC, the array was connected through a twelve-channel S-bent waveguide into a multimode interferometer (MMI) coupler, then into a normal-to-facet SOA. They achieved ~40nm tuning range centred at 1550nm and maintained a relatively high output power of 90mW even at 70^{o}C operating temperature.

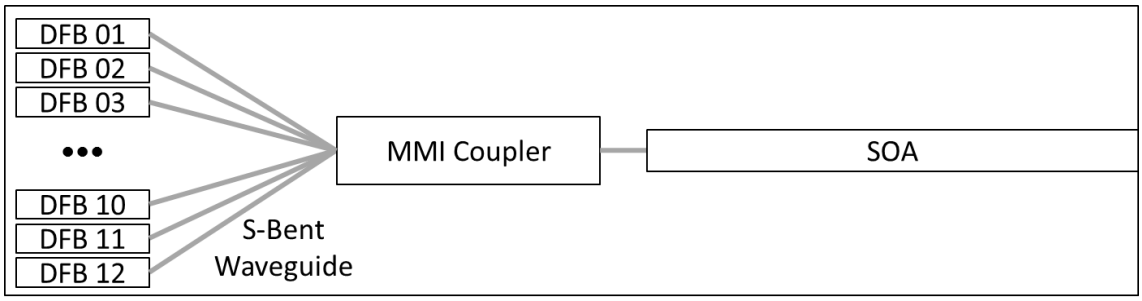

Figure 5-8: Schematic diagram of a widely tunable laser reported in [12]

5.2.2 Realisation for High Power

The group of Prof. Bernd Sumpf [13] (at the Ferdinand-Braun-Institut) have been highly active in GaAs-based DFB- and DBR- SOA research in recent years. Prof.

Sumpf suggests that in these kinds of MOPA systems, only a relatively small output power from a spatial fundamental mode laser with robust beam quality is needed to be injected into the SOA. For the tapered gain region of an SOA, a flared angle should be designed to match the divergence of the injected beam. Furthermore, both facets should have high-quality (<0.1%) antireflective coating.

Spectra Diode Labs has led extensive study into the monolithically integrated flared amplifier MOPA (MFA-MOPA) designs since the 1990s [14]-[16]. In their design, a DBR master oscillator was integrated with a flared SOA for an output power of several watts, as shown in Fig. 5-9.

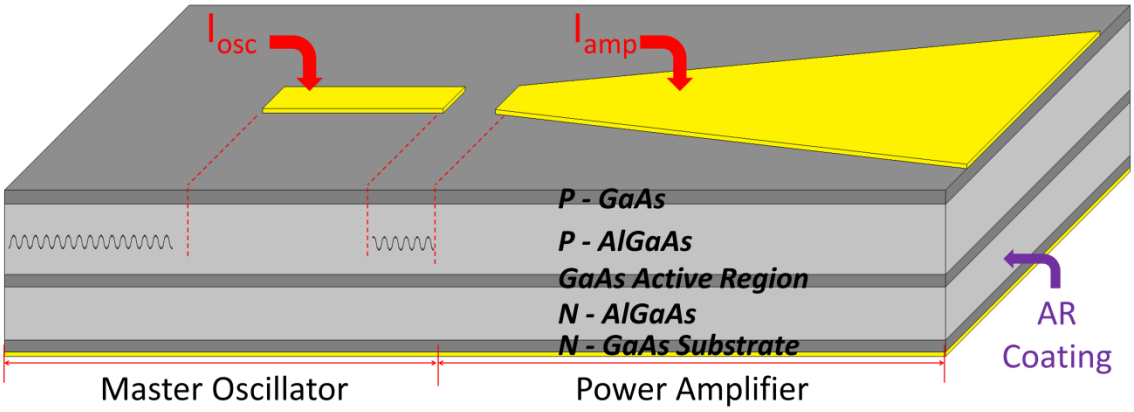

Figure 5-9: Schematic diagram of MFA-MOPA reported in [16]

For the device they developed in [16], it was reported to achieve 2.2W output power with a lasing wavelength of 854nm (I_{osc}=150mA, I_{amp}=5A, Temperature =5^{o}C).

Based on the above design concept, the Ferdinand-Braun-Institut has continued with the monolithic MOPA research with both DFB [5], 2009, and DBR [6], 2007, and a flared SOA. Fig. 5-10 illustrates the design of the MOPA in [5] and [6]. The DFB-MOPA achieved a CW output power of 3.7W at 973nm with current injection of DBR

and SOA to be 500mA and 5.4A respectively, whilst the DBR-MOPA achieved a CW output power of 10W at 977nm with current injection of DBR and SOA to be 200mA and 13A respectively.

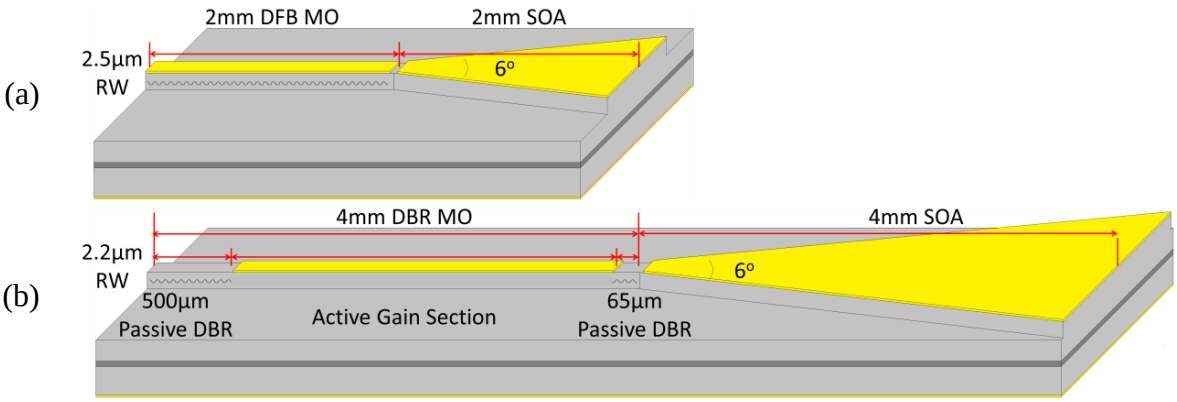

Figure 5-10: Schematic diagram of (a) a DFB-MOPA and (b) a DBR-MOPA as reported in [5] and [6] respectively

5.2.3 Realisations for Different Wavelength Generation

During the same period, Ferdinand-Braun-Institut also developed a 3-section 1060nm DFB-MOPA with a spacer section and a narrow ridge (un-tapered) tilted SOA section (5^{o}-off to facet) for potential application in green light generation [17] (2008). As illustrated in Fig. 5-11, a 1mm long spacer is integrated between a 1mm long DFB section and a 2mm long tilted SOA section. In the report, the spacer section was not electrically pumped and its role is mainly as a thermal isolator between the two sections.

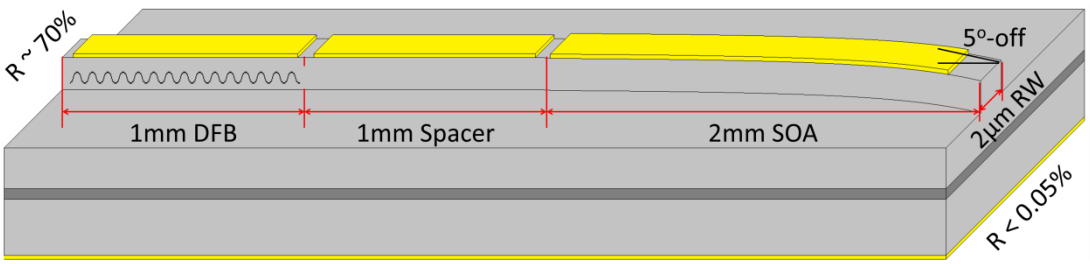

Figure 5-11: Schematic diagram of a DFB-spacer-SOA MOPA as reported in [17]

The suppression of reflections from the amplifier facet was achieved by both the 5^{o} tilting angle and the configuration of anti-reflection (AR) facet coating with an R less than 0.05%.

5.2.4 Disadvantages of Monolithic MOPA

Despite many benefits compared to discrete MOPA systems, monolithically integrated MOPAs are not without their disadvantages. The main issue is that each component of the module cannot be optimised independently, and the whole device is indeed optically and thermally coupled [13] and such a monolithically integrated device suffers from a dynamic nature among the integrated components which may interact in undesirable ways [18] [19]. Furthermore, in discrete MOPA systems, the SOAs can be easily selected to be positioned ~50nm shorter wavelength with respect to the desired operating wavelength to achieve very high saturation output powers [20]. However, it becomes complicated for a monolithic MOPA to achieve this. Although intermixing or selective area growth can facilitate this scheme, the cost of manufacture will increase for any additional treatment, as well introducing the potential for further problems associated with these methods, such as reduced gain.

5.3 SAS-MOPA Design

The main concept of the monolithically integrated MOPA design in this chapter is related to the MOPA concepts developed and realised by Spectra Diode Labs in 1990s [14]-[16] and that of the Ferdinand-Braun-Institut [5] [6]. However, advancements on these structures arise from application of the outcomes from my earlier studies on GaAs-based DFB lasers with GaAs/InGaP buried gratings in Chapter 3, and the SAS-DFB laser with n-doped InGaP optoelectronic confinement layers in Chapter 4.

This section describes the design of the two monolithically integrated MOPA structures studied in this chapter, starting with the SAS waveguide design based-on the 3-step growth process described in Chapter 4, followed by description of the two geometric designs along the waveguides.

5.3.1 Waveguide: Self-Aligned Stripe (SAS)

Following the study of SAS DFBs in Chapter 4, the waveguide of the monolithically integrated MOPA design in this chapter also adopted the SAS structure to form the laser and SOA waveguide. Fig. 5-12 shows the simulated (2D) optical mode profile in the SAS DFB waveguide. The blue contours represent the optical intensity, superimposed upon the structure input into the software, in the region about the SAS. A 3µm wide SAS is formed within a 600nm n-doped InGaP optoelectronic confinement layer, with a 7.5nm thick grating positioned 300nm (p-doped $Al_{0.42}Ga_{0.58}As$) above the 4× 7.6nm $In_{0.17}Ga_{0.83}As$ QWs active region. The simulation was aiming for a robust guided mode profile with a sufficiently high optical confinement factor in the QWs and a

confinement factor in the grating region to be ~0.0033, such that the resulting *KL* (coupling coefficient × cavity length ~ 1) for the designed length of laser section of 550~650nm in order to minimise the effect of spatial hole burning upon the performance of the device.

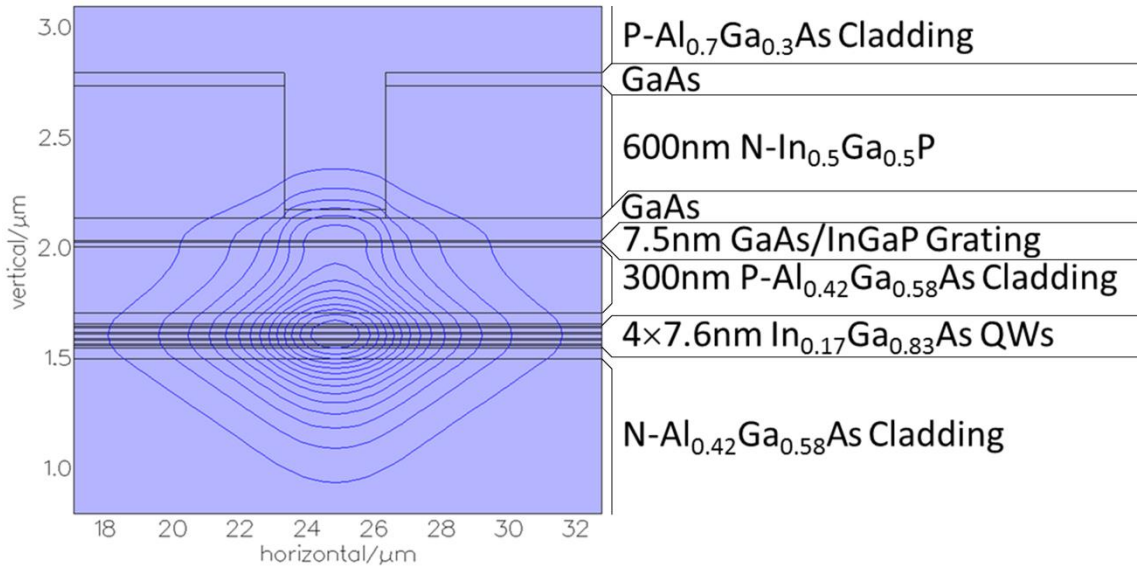

Figure 5-12: Simulation of 3μm SAS DFB laser section of the MOPA, showing a robust single-mode in the waveguide

Table 5-1 lists the detailed layer structure resulting from this design activity, with the indication of the 3-step growth process, as well as the thickness, material, doping requirement and description of each layer(s).

As highlighted, the structure used asymmetric upper- and lower- AlGaAs cladding compositions (upper cladding in 2nd overgrowth: Al-70%; upper cladding and lower cladding in planar growth: Al-42%), which was a result of the requirement of a thicker (100nm) in-fill GaAs layer in the 1st overgrowth for a higher growth quality. This was discussed in detail in Chapter 4, including the re-simulation of the structure and re-design of the 2nd overgrowth by utilising the ability to tailor the Al composition to optimise the waveguide formed in the GaAs-AlGaAs material system.

	Thickness(nm)	Material	Doping	Description
2nd Regrowth	300	GaAs	P	contact layer
	1500	$Al_{0.7}Ga_{0.3}As$	P	upper cladding
	40	GaAs	P	2nd in-fill GaAs
1st Regrowth	20	GaAs		
	600	$In_{0.5}Ga_{0.5}P$	N	blocking layer
	100	GaAs	P	1st in-fill GaAs
Planar Growth	10	GaAs	P	etch-capping GaAs
	7.5	$In_{0.5}Ga_{0.5}P$	P	grating layer
	15	GaAs	P	etch-stopping GaAs
	300	$Al_{0.42}Ga_{0.58}As$	P	upper cladding
	50	GaAs	-	active region 4× 7.6nm $In_{0.17}Ga_{0.83}As$ QWs spaced with GaAsP strain balancing layers sandwiched by GaAs barrier layers
	10	$GaAs_{0.885}P_{0.115}$	-	
	7.6	$In_{0.17}Ga_{0.83}As$	-	
	20	$GaAs_{0.885}P_{0.115}$	-	
	7.6	$In_{0.17}Ga_{0.83}As$	-	
	20	$GaAs_{0.885}P_{0.115}$	-	
	7.6	$In_{0.17}Ga_{0.83}As$	-	
	20	$GaAs_{0.885}P_{0.115}$	-	
	7.6	$In_{0.17}Ga_{0.83}As$	-	
	10	$GaAs_{0.885}P_{0.115}$	-	
	50	GaAs	-	
	1500	$Al_{0.42}Ga_{0.58}As$	N	lower cladding
	500	GaAs	N	buffer layer

Table 5-1: Layer information of the 3-step growth process of the wafer

Both MOPA designs were fabricated from the same wafer, i.e. having the same layer structures grown by this 3-step process. The difference between the MOPA types was only in the geometric design of the 2 sections.

5.3.2 Section Geometry: DFB and Flared SOAs

In this chapter, several MOPA structures were designed in order to investigate a number of design parameters. However, I concentrate on 2 specific designs due to subsequent problems in the manufacture of the MOPAs, which unfortunately limited the range of variables that could be studied. Fig. 5-13 illustrates the two MOPA designs

investigated. The upper MOPA was designed to have a 650µm long laser section to be monolithically integrated with a 2000µm long straight-flared semiconductor optical amplifier (SOA), i.e. normal to facet.

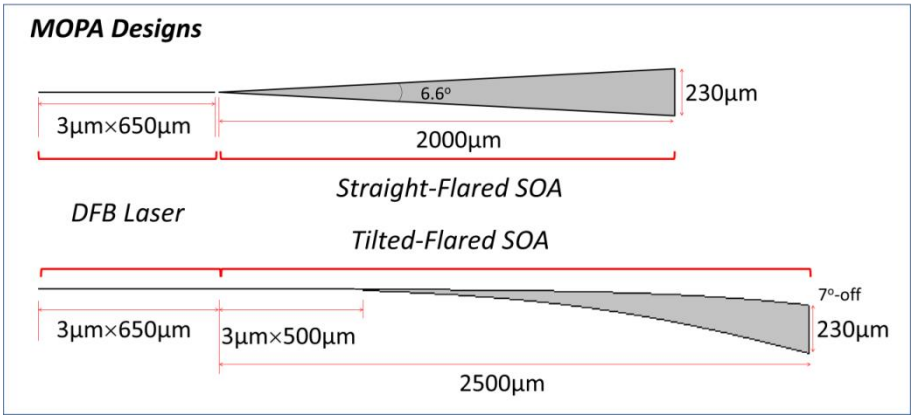

Figure 5-13: Two MOPA designs with straight and tilted SOAs

The lower MOPA was designed to also have a 650µm long laser section, but to be monolithically integrated with a 2500µm long tilted-flared SOA, i.e. 7°-off to the facet. Both SOAs have a 230µm wide output facet at the end of the SOA section. A flared SOA was used with the aim of generating high output power [5] [6] [11] [14]-[16], compared to more conventional narrow width SOAs [10] [12]. Aside from this obvious geometrical difference, the 2 MOPA structures also differed in the electrical isolation method used.

Fig. 5-14 illustrates how the 2 structures look after etching prior to the 2nd overgrowth. As illustrated in the figure, for the structure with a tilted SOA, the interface between the laser section and the SOA section contained a continuous SAS, formed by etching the InGaP layer continuously along the device. Electrical isolation was then provided solely by etching the GaAs contact layer between the 2 sections.

As for the structure with a straight SOA, a 15µm wide InGaP "window" was left un-etched between the two etched portions, forming the SAS in each section. This was used to create further discontinuity at the interface between the 2 sections. For this

monolithically integrated MOPA, the incorporation of an InGaP window in the interface would generate a small step of refractive index between the un-etched InGaP and the in-fill GaAs, which serves as a low reflectivity buried facet and therefore further results in optical reflectivity. The purpose of this particular design was for investigation of whether a buried facet fabricated in the interface can improve the stability performance of a MOPA PIC, for which optical back-reflections from SOA facet back into the DFB can be de-stabilising to DFB operation (hence the requirement for an isolator in discrete systems, e.g. Fig. 5-2)

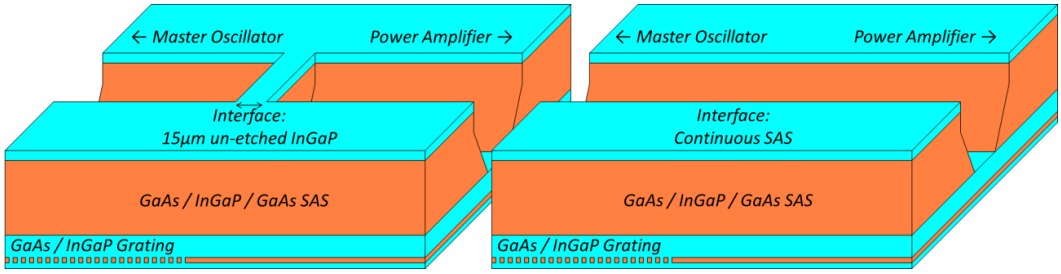

Figure 5-14: Schematic diagram of interfaces with/without InGaP window before 2nd overgrowth

Therefore, after the 2nd overgrowth, the MOPA with the tilted SOA is in-filled with a continuous SAS waveguide, whilst a 15µm InGaP window is formed at the interface between the DFB and SOA in the MOPA with a straight SOA. Fig. 5-15 shows the schematic cross-sectional view of the completed interface, whilst highlighting the introduced refractive index-step between the two components.

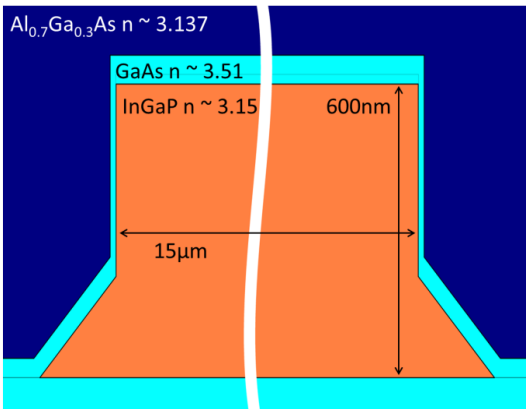

Figure 5-15: Schematic diagram of the cross-sectional view of the InGaP window showing the refractive-index-steps when optical wave propagating through the window from left to right

5.4 Device Manufacture

This section introduces the manufacture process of the MOPA structure. Fig. 5-16 shows a schematic diagram of the monolithically integrated SAS MOPA device with a straight-flared SOA. The cross sectional view of the DFB region illustrates the InGaP window and the formed GaAs/InGaP grating.

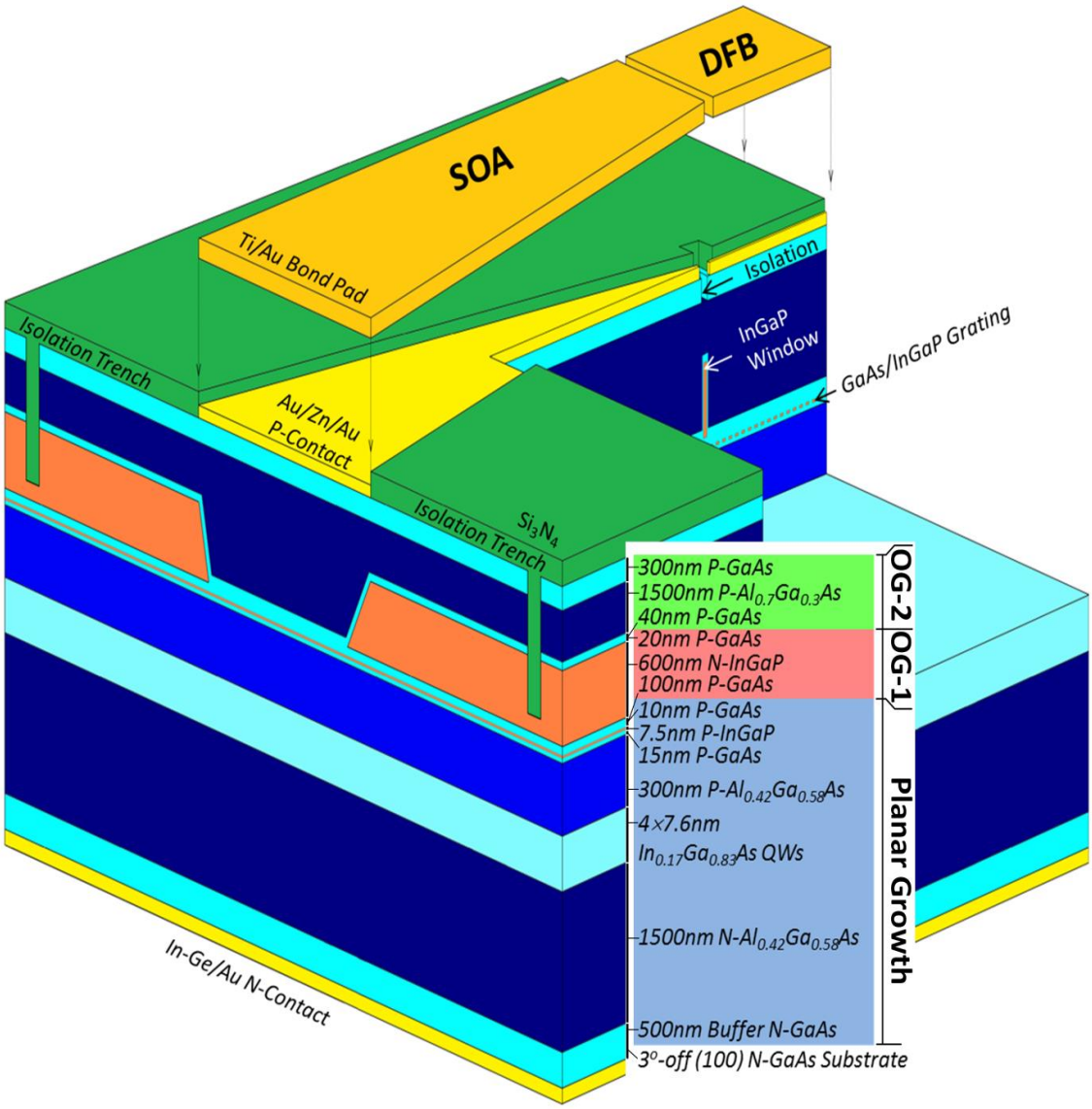

Figure 5-16: Schematic diagram of the SAS MOPA design with a straight SOA section and a 15μm wide InGaP "window" interface between the two sections

5.4.1 Epitaxial Growth

The epitaxial structure was grown using MOVPE (metal-organic vapour phase epitaxy). The manufacture process was similar to that described in detail for the SAS DFB laser in Chapter 4. The difference here concerns the monolithic integration of an SOA with the SAS-DFB, and investigation of the interface between the 2 components.

➢ Stage I: Planar Growth

The initial planar growth started with a 500nm GaAs buffer layer grown upon an n-doped GaAs substrate, which was mis-oriented by 3° to the (110) direction, above which 1500nm n-doped $Al_{0.42}Ga_{0.58}As$ lower cladding layer was grown, followed by partially strain-balanced quantum wells (QWs) in the active region. The core was stacked with 4× 7.6nm $In_{0.17}Ga_{0.83}As$ QWs (separated by 20nm $GaAs_{0.885}P_{0.115}$ strain balancing layers), with 50nm GaAs barrier layers grown on its upper and lower sides. 300nm p-doped $Al_{0.42}Ga_{0.58}As$ was grown above the core prior to growth of the grating layer. The first order DFB grating layer, as simulated, comprised a 7.5nm thick InGaP layer (lattice matched to GaAs) sandwiched between 15nm and 10nm thick GaAs layers.

➢ Stage II: Grating Formation – electron beam lithography / etch / 1st overgrowth

After EBL patterning of the grating pattern, inductively coupled plasma (ICP) Argon dry etching and HCl/H_3PO_4 selective wet etching of the InGaP matrix was performed in

predefined areas as used previously in Chapters 3 and 4. As for the design of the grating periods, again I applied the 1st order grating Bragg wavelength equation: $\lambda_B = 2\Lambda n_e$ (Λ: grating period; n_e: effective refractive index) with an experimentally estimated n_e as 3.35~3.36 (from Chapter 5). In order to make sure of overlap between the Bragg wavelength of gratings and the gain peak of the material, 3 periods of grating were designed: 148nm (~994nm), 149nm (~1000nm) and 150nm (~1006nm). Fig. 5-17 shows a schematic diagram of a repeating unit of the patterned sample surface. As illustrated, the surface size of the grating area was 50×650μm. The length corresponds to the designed laser cavity length as the master oscillator (MO), and the width of 50μm provided ample tolerance of alignment for the later fabrication of a 3μm wide SAS. The areas on the right-hand-side of each grating pattern were left un-patterned such that they could be used for definition of the integrated power amplifier (PA) during subsequent pattern/growth.

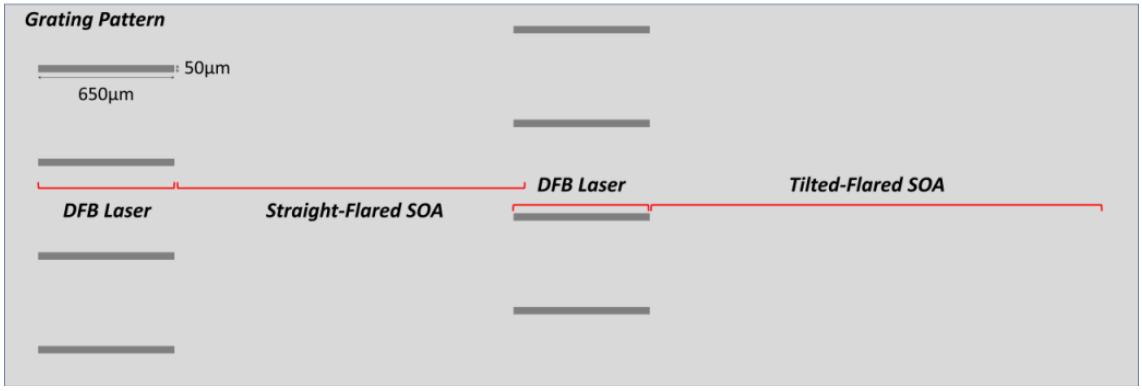

Figure 5-17: Schematic diagram of the patterned grating area of the sample surface, with a size of 50μm wide and 650μm long, and the spared space for the integrated SOA

The etched sample was washed in 1% diluted HF immediately prior to loading back into the MOVPE reactor for the 1st overgrowth. 100nm p-doped GaAs was overgrown to infill and planarise the index-coupled DFB grating, followed by a 600nm n-doped InGaP (lattice-matched to GaAs) optoelectronic confinement layer, and 20nm of GaAs to complete this step of the process.

➢ Stage III: Self-Aligned Stripe Formation – photolithography / etch / 2nd overgrowth

An SAS MOPA pattern was defined using standard UV optical lithography, aligned to the grating regions. The pattern was transferred to the sample surface by first dry etching through the top GaAs layer using a $SiCl_4$/Ar based ICP process and then HCl/H_3PO_4 wet etching the remaining InGaP down to the lower GaAs etch stop layer. Fig. 5-18 illustrates the SAS MOPA pattern where the n-doped InGaP current blocking layer was etched. Two SOA designs were produced. The MOPA structures on the left-hand-side are designed with straight-flared (i.e. normal facet) SOAs, those on the right-hand-side are designed with tilted-flared (i.e. based on a ~7^o-off the normal to facet termination) SOAs. For both structures, the laser sections are composed of 3µm×650µm stripes aligned to the centre of the 50µm×650µm grating region.

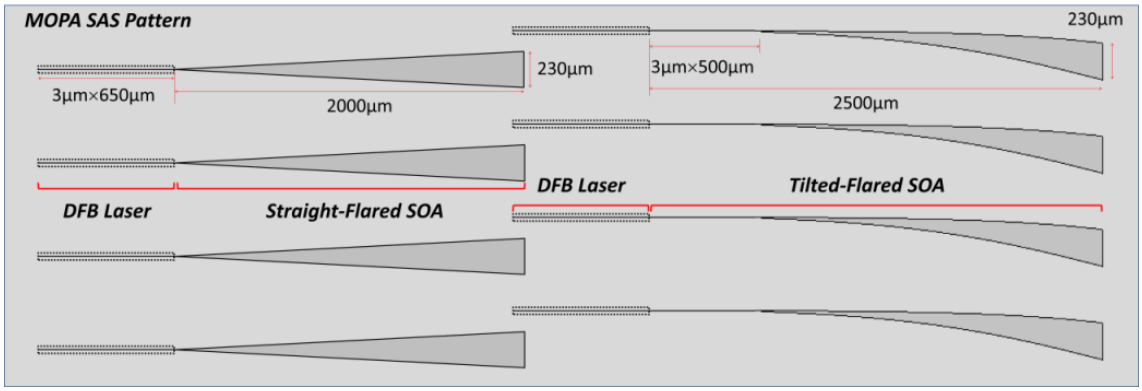

Figure 5-18: MOPA SAS pattern: straight-flared SOA design, left-hand-side, and tilted-flared SOA design, right-hand-side. The dotted stripes indicate the 50µm×650µm grating region formed (as in Fig. 5-17) underneath the 3µm×650µm SAS pattern

The sample was again washed in 1% diluted HF and loaded back to MOVPE reactor immediately for the 2nd overgrowth. 40nm p-doped GaAs was overgrown to form the buried hetero-structure, followed by 1500nm p-doped $Al_{0.7}Ga_{0.3}As$ and a 300nm GaAs contact layer to complete the structure.

5.4.2 Device Fabrication

The 2nd overgrowth did not proceed as planned. As shown in Fig. 5-19, the surface was highly defective, as a result of the growth temperature having not been optimised prior to the overgrowth. Despite the significant overall defectiveness of the regrown layers, the SAS of the DFB laser (MO) had a width of only 3μm, which allowed us to select MOPAs with non-defective MO sections, since the stripe could pass through higher quality material between defects. For example, in the image the 2nd and 3rd devices from the left-hand-side column did not contain obvious defects within the laser stripe. However, defects are evident in almost every SOA, contributing non-radiative recombination and scattering centres in the waveguide of fabricated devices, and affecting the electrical performance of devices.

In spite of this, considering the large surface size of the SOA, such that for SOAs with fewer defects, it might still be possible for the devices to work to some extent, I decided to proceed with the fabrication process.

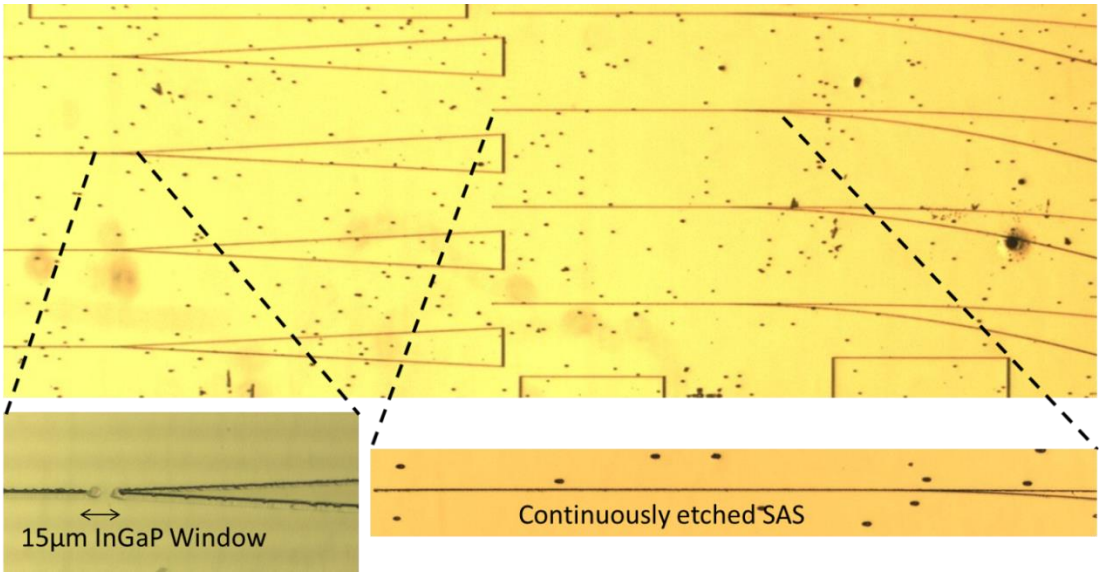

Figure 5-19: Microscope image of the sample after 2nd overgrowth, showing a defect density estimated as ~5700cm^{-1}, together with zoomed-in images taken at the DFB-SOA interfaces with/without InGaP window

The device fabrication process was similar to that of the SAS DFB, as described in Chapter 4. The fabrication process consisted of 6 steps, as annotated by arrows in Fig. 5-20 (a). Compared to the fabrication process described in Chapter 4, the only additional step was the incorporation of step 5, an isolation-etching between the MO/PA components. This step aimed to electrically isolate the DFB and SOA sections, such that they can be pumped independently, which was achieved by etching through the top GaAs contact layer to provide a resistance > 1kΩ between contacts, whilst terminating at the AlGaAs interface, so as not to influence the guided optical mode.

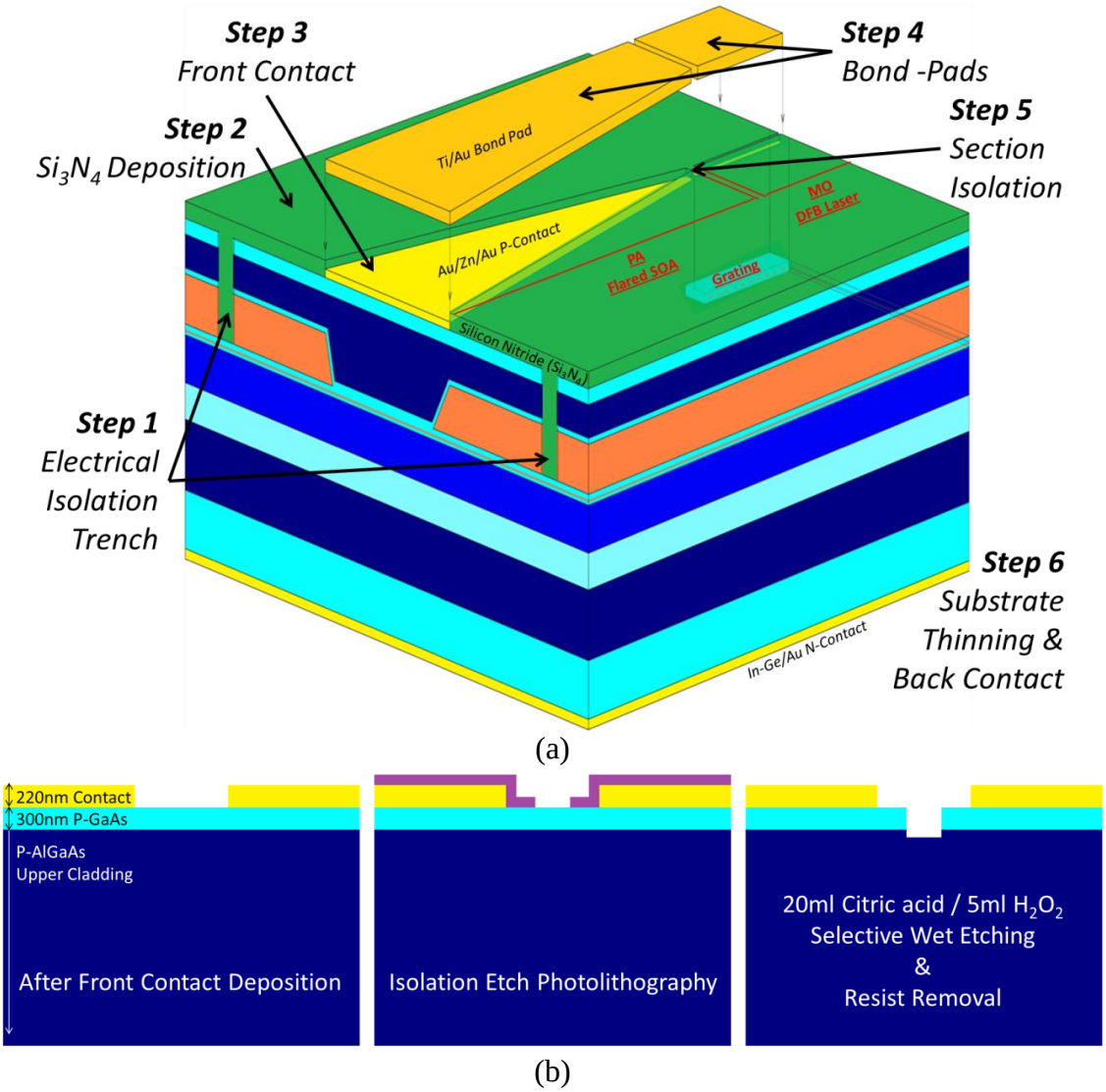

Figure 5-20: (a) Device fabrication process of SAS MOPA with straight-flared SOA and (b) electrical isolation etch between sections

As shown in Fig. 5-20 (b), this step started with photolithography to cover all but the interface areas. The wet etchant 4:1 Citric acid / H_2O_2, which selectively etches GaAs (~300nm/min) over AlGaAs (~3nm/min), was applied to the sample for 90sec to entirely etch the 300nm GaAs layer in the interface areas. This was verified by checking the resistance between adjacent sections.

After the 6th step, substrate thinning and n-type-ohmic back contact formation, devices were cleaved and sent to Helia Photonics for both facets to be coated with Ti_3O_5/SiO_2 anti-reflective (AR) coating (specification: reflectivity <0.1% at 1050nm, 25nm bandwidth). The central wavelength of 1050nm, rather than 1000nm, was a compromise made among this batch of devices and other devices that were sent together for coating. Therefore, whilst not optimised for <0.1% for these devices, one might expect a slightly higher reflectivity. Fig. 5-21 presents the images taken under an optical microscope of the fabricated SAS MOPA devices. The high defect density in the 2nd overgrown layer is clearly visible.

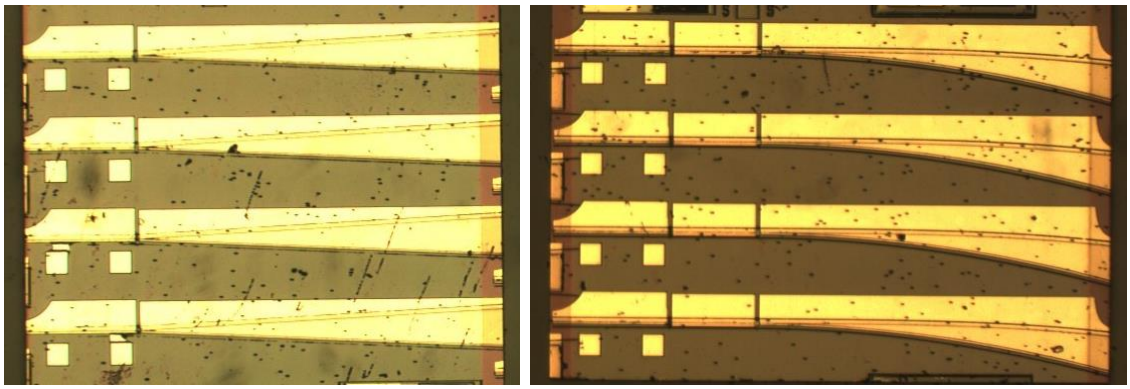

Figure 5-21: Images of fabricated devices taken under optical microscope

5.5 Device Characterisation

The measurement of MOPAs was conducted by pumping the DFB laser sections with a CW current source and pumping the SOA sections with a pulsed current source with 5μs pulse width and 10% duty cycle. SOA sections were unable to be driven continuously due to overheating resulting from the large current required to achieve gain. Samples were mounted epi-side up on AlO_2 ceramic tiles for characterisation, and therefore heat-sinking was far from ideal. In total, six representative devices were measured, as listed in Table 5-2, covering all the 3 different DFB grating periods for 2 different SOA geometries:

Device	1	2	3	4	5	6
SOA Geometry	Straight	Straight	Straight	Tilted	Tilted	Tilted
Grating Period (nm)	148	149	150	148	149	150

Table 5-2: Information of six representative devices

5.5.1 DFB Laser Sections Characterisation

First of all, the DFB laser sections of the MOPA devices were characterised by measuring L-I-V and spectral properties from the rear facets, i.e. the laser back facet, while leaving the SOA section un-pumped, where it would effectively behave as an absorber. Fig. 5-22 (a) and (b) plot the L-I-V measurements for the straight-SOA MOPA and tilted-SOA devices respectively, where both light output power and applied voltage are plotted as a function of injected current for all the 6 representative devices. For the straight MOPA devices, the laser sections with 148nm and 149nm period gratings demonstrated a threshold current of ~80mA, whilst ~105mA for that of the

laser section with a 150nm period grating. For the tilted SOA devices, the laser sections with 148nm and 149nm period gratings demonstrated a threshold current of ~85mA, whilst ~95mA for that of the laser section with a 150nm period grating. As can be seen, the plots showed a similar amount (~7mW) of light output power at 150mA pumping for both structures, commensurate with near-identical DFB-SAS laser sections of sufficiently high quality in each.

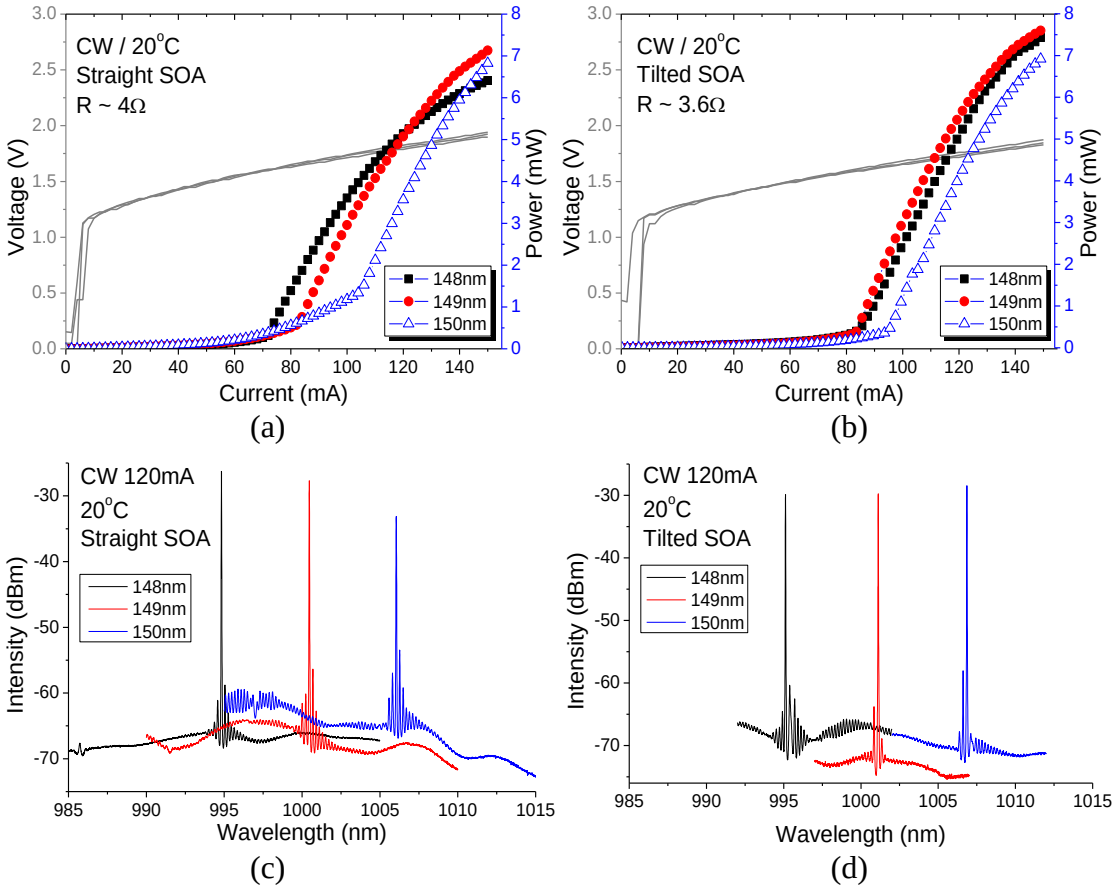

Figure 5-22: L-I-V measurement of laser sections of MOPA design with (a) straight SOA and (b) tilted SOA; Spectral measurement of laser sections of MOPA design with (c) straight SOA and (d) tilted SOA

Fig. 5-22 (c) and (d) plots the EL spectrum of devices with 148nm, 149nm and 150nm grating periods for the two MOPA structures. As can be seen, all the devices demonstrated lasing via a single mode at 120mA CW current at a heat-sink temperature of 20°C with reasonably large SMSR (>20dB). For both device types, the laser sections with 148nm, 149nm and 150nm grating periods demonstrated lasing wavelengths of

~995nm, ~1001nm and 1007nm respectively, which further demonstrates a strong correlation between the behaviour of the two laser sections. For both device types, a temperature tunability of ~0.09nm/^{o}C was measured.

- **Discussion**

For both structures, the laser with grating period of 150nm had a comparatively higher threshold current. The measured room-temperature lasing wavelength for the grating period of 150nm was ~1007nm and the centre of the spontaneous emission spectrum (approximately indicating the centre of the gain spectrum) for such material with the measurement condition was measured to be 995~1000nm, as shown in Fig. 5-22 (c), the red and blue spectra, and Fig. 5-22 (d), the black spectrum. Therefore, compared to devices with 148nm (lasing at ~995nm) and 149nm (lasing at ~1001nm) grating, the devices with a 150nm grating had the largest detuning between the gain peak and the Bragg wavelength, hence these devices required more current injection to reach the lasing condition. The longitudinal mode spacing of modes positioned away from the laser peak in the spectra was measured, i.e. at ~996nm on the blue spectrum in Fig. 5-22 (c) and at ~1000nm in the black spectrum in Fig. 5-22 (d). For both the straight SOA and the tilted SOA, MOPAs correspond to Fabry–Pérot modes from the laser cavity length of ~650μm. Whilst this could be expected from devices with a potentially reflective "window" section between DFB laser and SOA, its appearance in devices with no window was not expected. For the MOPAs with a straight SOA, the interfaces between lasers and SOAs were formed by leaving InGaP "windows", as described in Section 5.3.2, such that the light generated in the laser section would experience refractive-index-steps, as shown in Fig. 5-15, within the buried stripe geometry when propagating into the SOA section. This discontinuity in the SAS contributed to the formation of the Fabry–Pérot oscillation observed in the spectrum in

Fig. 5-22 (c). For the MOPAs with tilted SOA, the interfaces between lasers and SOAs were fabricated with a continuous SAS (i.e. without InGaP windows), as described in Section 5.3.2. Therefore the light would not experience such reflections within the buried stripe geometry when propagating from the laser sections into the SOA sections. However, this may result from reflection at the interface between pumped and un-pumped sections, for which the resulting refractive index change would result in a reflective interface.

5.5.2 SOA Sections Characterisation

➢ Four-Parameter Characterisation of SOA

The performance and quality of a stand-alone SOA is usually characterised by 4 parameters [21]: gain, bandwidth, saturation output power and noise figure. Fig. 5-23 illustrates the definition and measurement of these parameters by diagramming the corresponding input and the expected output for each parameter: (a) Gain is the most basic property of an SOA, which is calculated directly through dividing the output power by the input power and transferring into logarithmic unit (dB). This parameter numerically indicates how much the input light is amplified. (b) In an SOA, the transitions only take place between available energy levels in a given epitaxial active region, which results in a limited wavelength for operation and its gain varies across the spectral range. The second parameter, bandwidth, specifies an SOA's operating range. This is calculated as the wavelength range bound by the -3dB of the maximum gain. (c) At a given current injection level, as the input power increases, when the density of the free carriers becomes insufficient to maintain the spontaneous emission rate, the gain decreases.

After 3dB reduction from its maximum gain, the SOA reaches its saturation gain and the corresponding output power is its saturation power. (d) The fourth parameter describes the quality of an SOA with respect to its ability to maintain the signal to noise ratio (SNR) of the input light. The noise figure is defined as the ratio of the input SNR to the output SNR, calculated in dB.

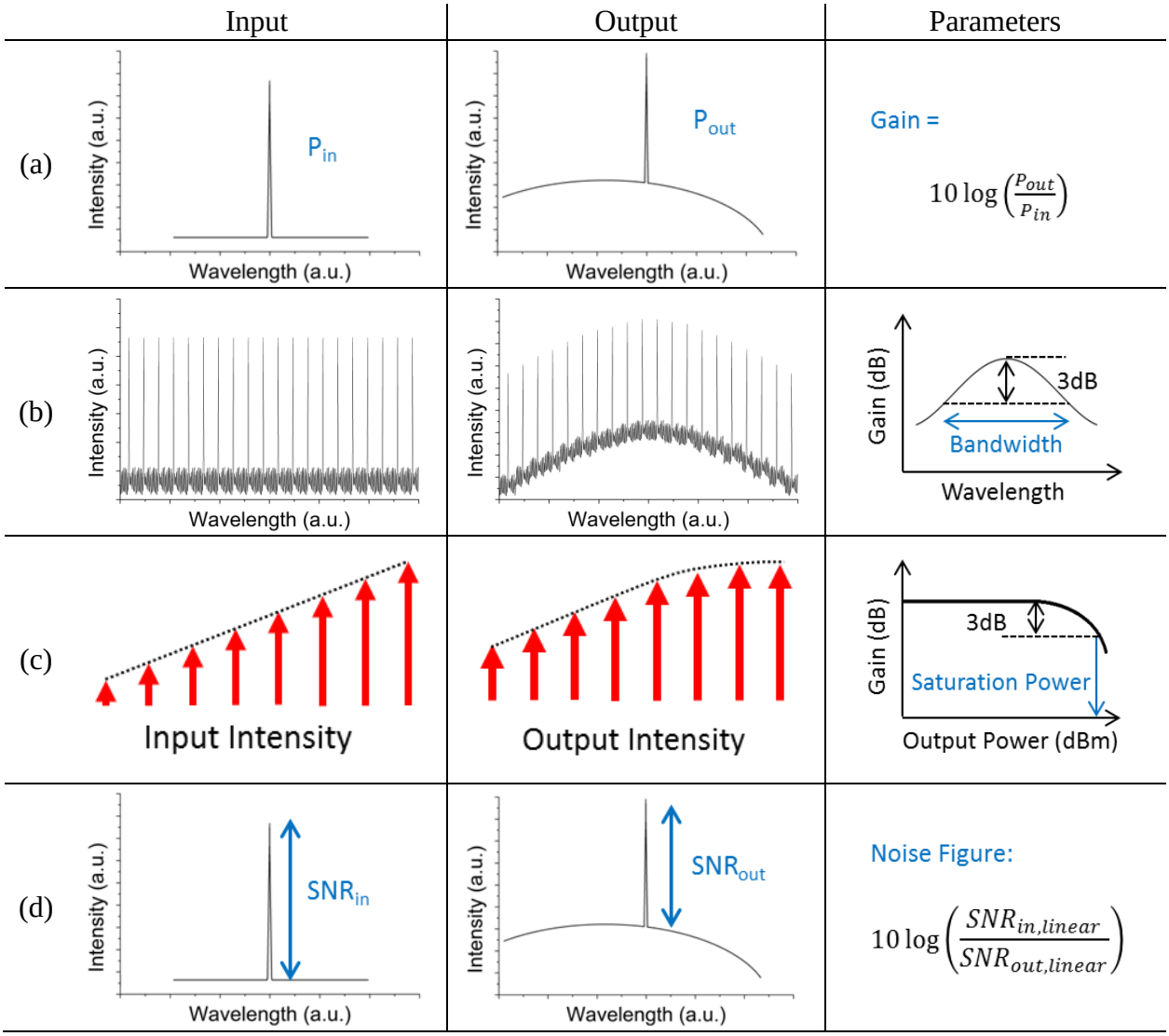

Figure 5-23: Evaluation of a stand-alone SOA using the four parameters suggested by Mukai and Yamamoto [21]: (a) gain, (b) bandwidth, (c) saturation power and (d) noise figure

However, this set of parameters is unable to be extracted from a monolithically integrated SOA as designed and fabricated in the MOPA structures in this chapter, where the spontaneous emission generated in the SOA section can propagate into the DFB laser section to interact with the grating structure. Therefore the output power is

not solely contributed by the amplification of the input power, but also by the portion from such interaction, which makes it impossible to determine the gain, saturation gain and saturation power. Furthermore, the integrated SOA section has the same epitaxial structure as the DFB section. Given that the Bragg wavelength of the DFB is designed to overlap with the gain spectrum of the laser section, which intrinsically ensures the overlap between the gain spectrum of the SOA and the input DFB mode. Therefore the study of the SOA bandwidth becomes unnecessary. As to the fourth parameter, the SNR_{in} can be calculated from the spectrum recorded from the DFB rear facet with the DFB switched on and the SOA un-pumped, whilst the SNR_{out} can then be calculated from the spectrum recorded from the SOA front facet after turning on the SOA. However, the performance of this batch of devices is influenced by the non-optimum AR coating, resulting in significant loss of spectral purity observed from the output spectra, making calculation of the noise figure redundant.

In this chapter, I employed a straightforward method to numerically analyse the performance of the amplification. With this method, the portion of amplified DFB output power is estimated using the product of the total measured output power and a ratio of the integral computation of the range of the peak to the whole range of the recorded spectrum. The resultant power is then compared to that measured from the DFB rear facet with the DFB section operating alone. The concept of this method regards the MOPA device as one integrated device rather than seeing the two sections individually, such that comparison is made between performance of the MOPA and performance of a stand-alone DFB laser under the same pumping conditions.

Therefore, this section investigates the L-I and emission spectrum of the fabricated SOA sections operating with laser sections un-pumped.

➢ Characterisation of SOA Sections of Representative Devices

As described in Section 5.4.2, the poor quality 2nd overgrowth is expected to significantly influence the quality of the SOA component. In order to test the feasibility of their use, a number of SOAs were screened for their behaviour with DFB sections un-pumped. The CW L-I-V measurement on several devices showed that the SOA output power begins to roll-over before super-luminescence is observed, which suggests it would not be possible to drive the SOA section for optical amplification using a CW current source. This may be due to severe self-heating in the imperfect waveguide while operating with a ~500mA CW current injection. Hence, in order to reduce the self-heating and drive the devices in amplification, a pulsed current source was used for all the following measurements.

Fig. 5-24 compared the L-I-V measurement of a representative tilted SOA. The results showed that, with CW pumping, the slope efficiency started to decrease (roll-over) from ~450mA, whilst with pulsed current pumping (pulse width: 5μs; duty cycle: 10%), the SOA demonstrated super-luminescent operation from ~400mA.

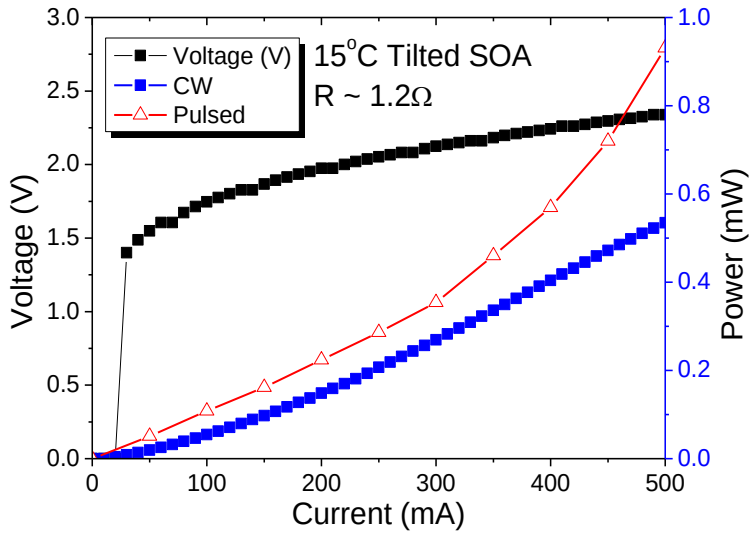

Figure 5-24: L-I-V measurement of SOA section using pulsed 5μs-10% (red triangle) and CW (blue square) current source

Effort was made to enhance the substrate heat-sinking by placing the device directly upon the copper heat-sink which was cooled to 10^{o}C using a thermoelectric cooler. The device still demonstrated roll-over at a current of ~600mA. The use of epi-side-down mounting could be expected to enable CW pumping, but this is not straightforward for integrated devices, with multiple contacts and has not been attempted here.

Fig. 5-25 summarises the LIV and spectral measurements recorded from SOA sections on both MOPA structures with different grating periods. The DFB sections were left un-pumped. In the figure, the left-hand-side column presents the measurements of the 3 MOPAs with straight SOAs and the right-hand-side presents the measurements of the 3 MOPA with tilted SOAs, in which Fig. 5-25 (a) and (b) are the L-I measurements under room temperature using a pulsed current source (5μs-10%), whilst (c) to (h) present the recorded emission spectra for each device with 500mA, 1000mA and 1500mA pumping.

The L-I measurements in Fig. 5-25 (a) and (b) showed that the SOA sections both operated in amplification with pulsed current pumping, as indicated by the super-linear increase in output power. The tilted SOAs operated with higher output power (normalised to CW) compared to the straight SOAs.

The reason for the lower power recorded from the straight SOAs is due to their shorter cavity length, as shown in Fig. 5-18, where for tilted SOAs the 0.5mm waveguide section between the laser component and the flared SOA section formed a longer amplifier, resulting in higher power according to the exponential relation between power, P, and gain, g, and length, l: $P \propto e^{gL}$.

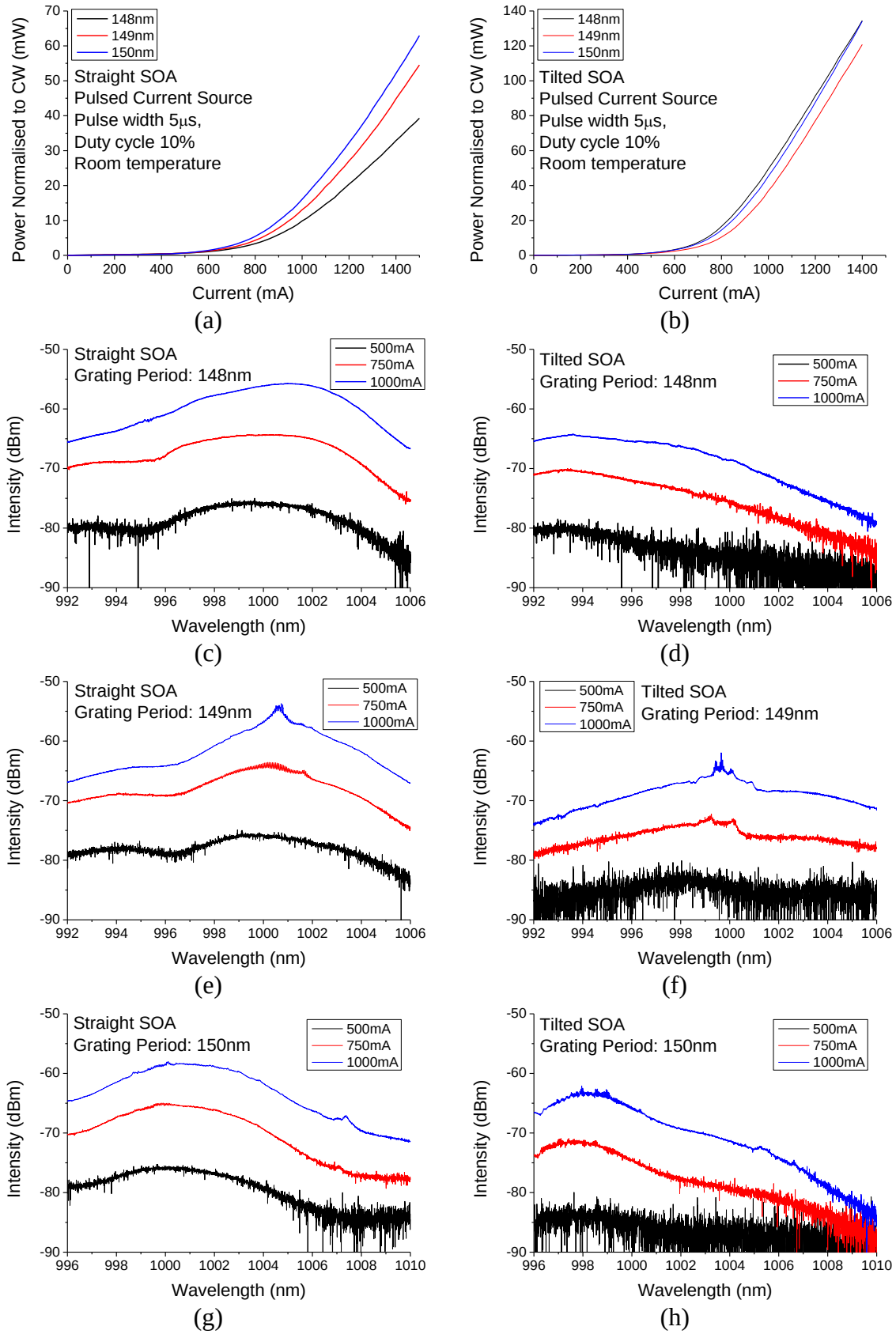

Figure 5-25: L-I and spectral measurements recorded from SOA sections on both MOPA structures with DFB sections left un-pumped

As shown in Fig. 5-25 (c) to (h), at 500-750mA pumping current, the amplified spontaneous emission (or super-luminescence) ASE started to establish in the SOA. Fig. 5-26 plots zoomed-in versions of the spectra shown in Fig. 5-25 (e) and (f) with 750mA pumping over a wavelength range of 2nm, centred about the peaks of the operating spontaneous emission, from which the mode spacing of both structures can be measured.

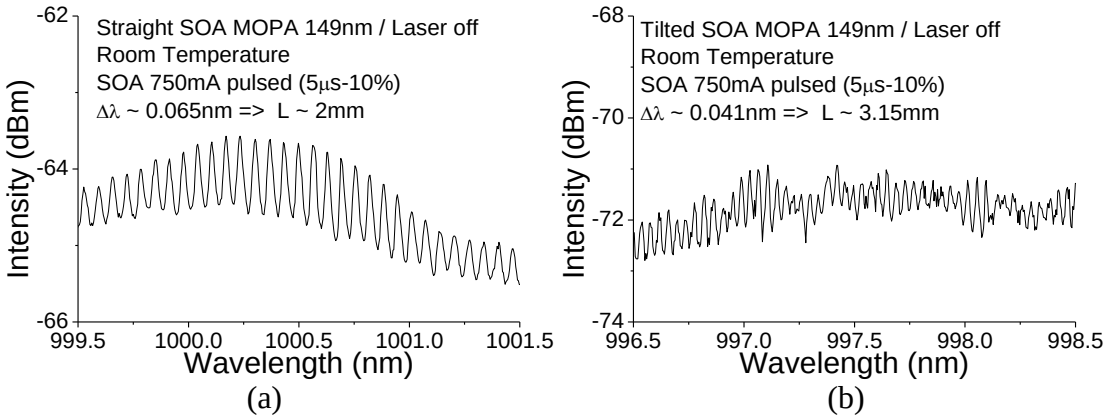

Figure 5-26: Zoomed-in spectrum of 750mA SOA pumping shown in Fig. 5-25 (e) and (f)

As highlighted in Fig. 5-25, the measurement reveals that in the straight SOA (with InGaP window), the resonance was established within the SOA only (~2mm), while in the tilted SOA (continuous SAS stripe), the resonance was mainly established though the whole device (~2.5mm SOA plus 0.65mm DFB), but subject also to the occurrence of beating between 2 back reflections. The beating observed in the spectrum could be a result of the superposition of two resonances of waves established from the SOA facet to the interface (2.5mm) and the DFB facet (3.15mm) respectively, with the latter one dominating the spectrum.

- **Discussion**

As described in Section 5.5.1, the reflection at the interface without an InGaP window (tilted SOA) was provided by the refractive index steps at the interface between pumped and un-pumped sections. With 1000mA pumping current, Fig. 5-25 (c) to (h)

exhibit additional peaks, situated at wavelengths corresponding to the Bragg wavelengths of the DFB gratings in the adjacent DFB laser sections. This suggests that, with only the SOA sections pumped, the spontaneous emission generated in the SOA sections could propagate into the adjacent DFB laser sections and interact with the grating structure to back-reflect at the Bragg wavelength (λ_B). This phenomenon was found to be even more significant when the λ_B of the buried grating more closely matches the ASE peak of the SOA, i.e. for 149nm grating period devices, where λ_B ~ 1000nm, the phenomenon becomes more apparent in the EL spectrum, as observed in Fig. 5-25 (e) and (f). This is suggestive of either optical pumping of the DFB component by the SOA section, or back-reflection from the grating at the Bragg wavelength.

5.5.3 Characterisation of MOPAs with Straight SOAs

In this section, MOPAs with straight SOAs are characterised as fully integrated devices, with electrical pumping of both the DFB laser and the SOA sections simultaneously.

Fig. 5-27 summarises the L-I and spectral measurement of the 3 representative straight SOA MOPA devices. In the figure, the left-hand-side column plots the L-I characteristics measured from 0mA to 1500mA with SOA section pulsed using 5μs pulse width and 10% duty cycle with the laser switched on at 120mA CW (red line) and off (black lines). The power plotted here is normalised to CW. The right-hand-side column plots the EL spectra recorded from the output facet of the SOA at different SOA pumping currents (0mA/500mA/1000mA) with the laser switched on (at 120mA CW).

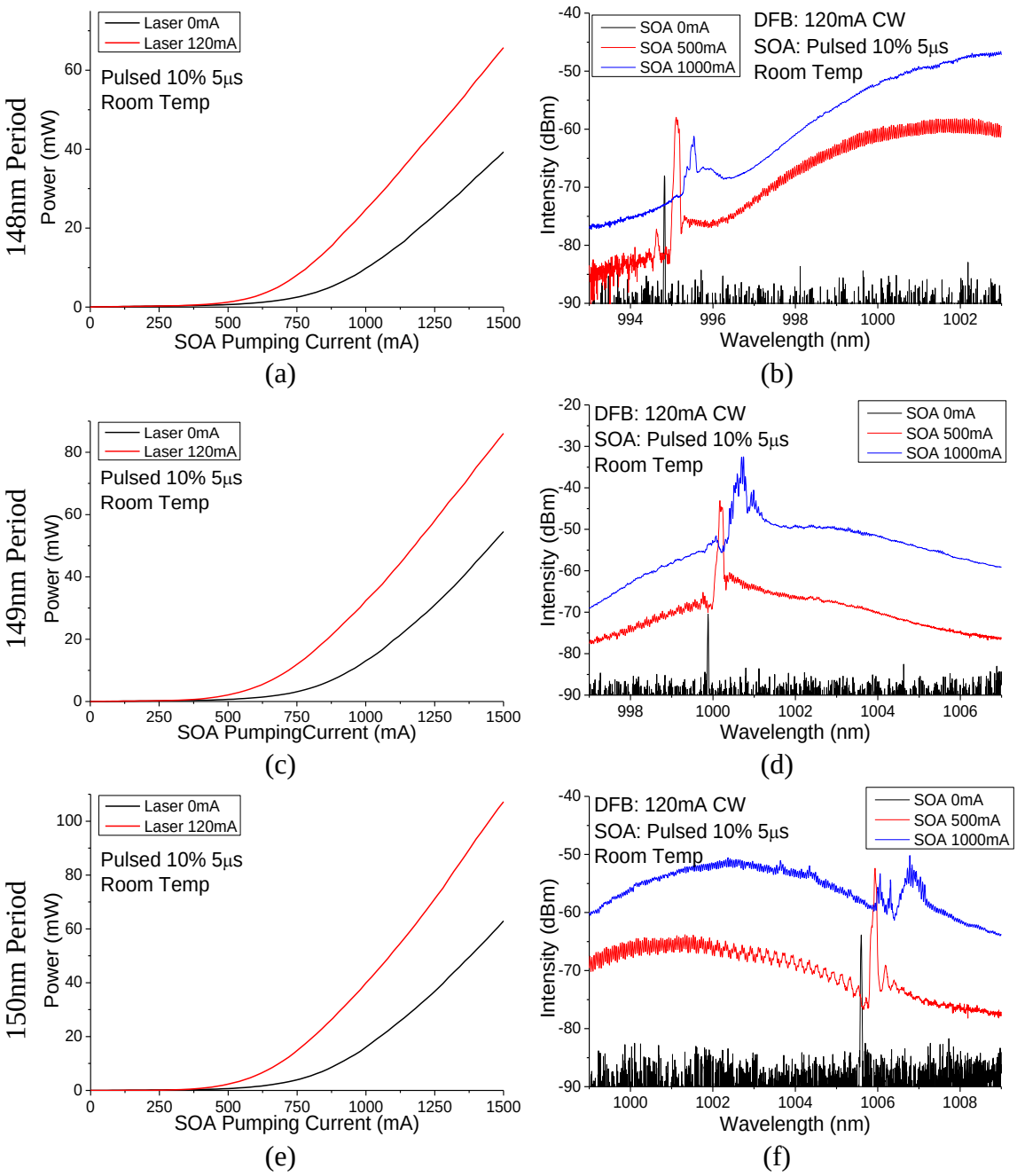

Figure 5-27: Light output power measurements from SOA facets as a function of pumping current (pulsed 5µs-10%) for SOA sections with lasers off and on (120mA CW pumping) and spectrum measurements from SOA facets with lasers on (120mA CW pumping) and SOA pulsed pumped (0/500/1000mA) for (a)/(b) Device-1, (c)/(d) Device-2 and (e)/(f) Device-3

The results of both L-I and spectral measurements demonstrate an amplification of the optical wave by turning on the SOA. With the SOA section un-pumped (0mA), the whole SOA section will act as an absorber. When light generated in the DFB section propagates through the cavity, a large portion of the power is absorbed. For an output power of 6.4~6.9mW measured from the laser back facet, only 0.09~0.14mW power

can be measured from the SOA facet when the SOA is left electrically un-pumped. This can be also seen from the black spectra in Fig. 5-27 (b), (d) and (f), where only very weak DFB peaks are recorded.

By turning on the SOA section with a pumping current of 500mA, the optical wave in all 3 devices experience amplification, as indicated by comparing the red and black spectra. Together with the increase in intensity, all 3 red spectra show an obvious red-shift compared to the black ones. However, an undesirable loss of spectral purity is also observed, which becomes even more severe when pumping the SOA sections with 1000mA current injection, as observed from the blue spectra. The decrease in intensity from red spectrum (SOA 500mA) to black spectrum (SOA 1000mA) for the device with 148nm period grating, (b), is due to a larger detuning between the ASE centre and the DFB wavelength. Furthermore, due to the non-optimal AR coating for this batch of samples, the suppression of ASE ripples in the SOA was not optimised, resulting in a large ASE ripple, which was measured as lager as ~2.4dBm from the red spectra from Fig. 5-27 (b) and (f) where the injected current of SOA sections are 500mA.

To assist with the analysis, Fig. 5-28 plots the measured DFB peak wavelength and intensity extracted from Fig. 5-27 (b), (d) and (f) as a function of current supplied to the SOA. As shown in Fig. 5-27 (b), (d) and (f) and Fig. 5-28 (a), a red shift of the lasing peak is observed for all 3 period devices with an increase of the SOA pumping current. Although the SOA was pumped with a pulsed current source, a duty cycle of 10% for hundreds of mAs is still a sufficient pumping current to induce self-heating in the SOA sections which due to its large size and proximity to the smaller DFB section, also heats up the DFB laser. A wavelength shift (from 0mA to 1000mA in the SOA) was measured for each of the 3 devices as 0.715nm, 0.855nm and 1.180nm respectively, corresponding to a temperature increase of approximately 7~11^{o}C in the DFB sections,

whilst the ASE peak shifts were estimated to be ~5nm in the same current range, corresponding to a temperature rise of ~10°C in the SOAs.

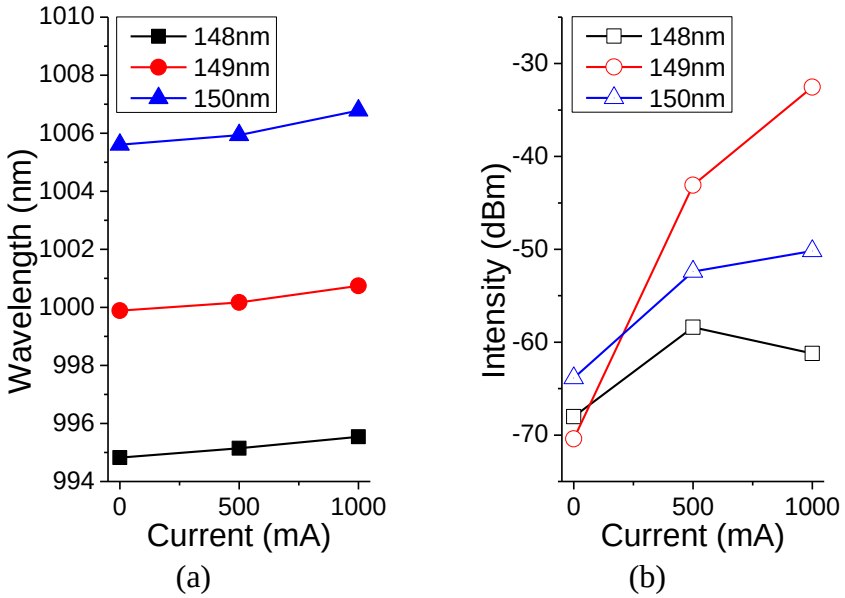

Figure 5-28: (a) Lasing peak wavelength shift and (b) peak intensity as function of SOA pumping current

Fig. 5-28 (b) shows that the optical waves in devices with 148nm and 150nm gratings increase by ~10dBm and the wave in the device with a 149nm grating increases by ~25dBm. This is because the grating period of 149nm corresponds to a DFB lasing wavelength of ~1000nm, which has the smallest amount of detuning from the centre of the gain spectrum of the SOA and can therefore be expected to undergo greater amplification compared to the detuned DFBs.

By increasing the SOA current from 500mA to 1000mA, the EL spectrum of all the 3 representative devices, as in Fig. 5-27 (b), (d) and (f), show a significant breakdown of the spectral purity of the highest intensity DFB peak. Also, for the representative device with 148nm grating (~994nm DFB lasing), shown in Fig. 5-27 (b), a significant increase in detuning is observed between the SOA gain peak and the DFB peak. This is a result of a red shift of the SOA gain peak with respect to the DFB peak. The result of this detuning is that the DFB lasing peak was not amplified as the available gain was

reduced by this increased detuning (observed in Fig. 5-28 (b) as the falling blue line at 1000mA). This behaviour could explain the lower output power and reduced efficiency observed in Fig. 5-27 (a) compared to Fig. 5-27 (c) and (e). Although the device was pumped using a pulsed current source with a duty cycle of 10%, the self-heating effect was still sufficiently severe to invoke a significant red-shift in the SOA section.

By studying the zoomed-in spectral window about the peak wavelength, we can investigate the origin of this single-mode-breakdown. Fig. 5-29 plots the spectrum shown in Fig. 5-27 (f) at a reduced range of 1nm around the peak.

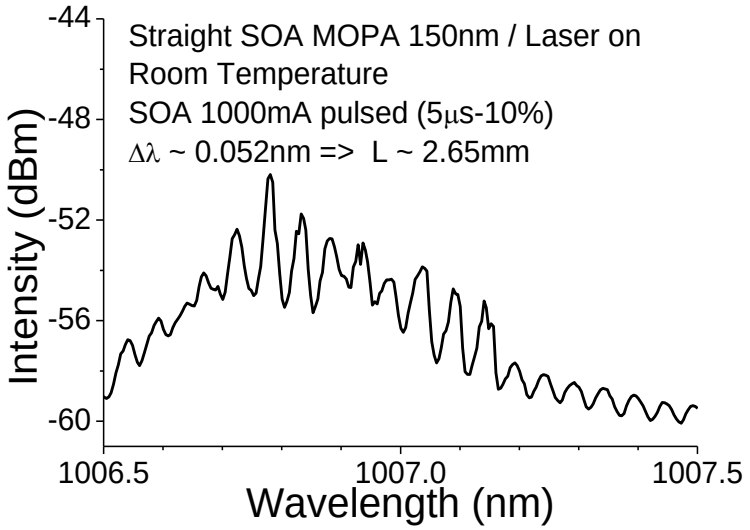

Figure 5-29: Zoomed-in spectrum of 1000mA SOA pumping shown in Fig. 5-27 (f)

In this figure, the DFB mode is no longer obvious as a single lasing mode, and is replaced by a highly modulated envelope of modes, with a mode spacing of ~0.51cm^{-1} (calculated from the measured $\Delta\lambda$~0.052nm at 1007nm) corresponding to a cavity length of ~2.65mm. This suggests that, despite the reflection provided by the 15μm InGaP window at the interface, the resonance is established over the whole cavity and overwhelms any resonance established within the SOA section alone, as shown in Fig. 5-26 (a) (Section 5.5.2). The spectrum in Fig. 5-29 appears to comprise the

superposition of two resonances; one from the SOA facet to interface (2mm) and the other from the SOA facet to the DFB facet (end-to-end, 2.65mm) respectively, with the latter dominating. These dominant end-to-end resonances may have been manifested as a result of the non-optimal AR coating and larger than desired facet reflectivity.

Since the role of the SOA component is to amplify the light generated by the DFB component, it is important to determine the percentage of the total measured output power from the SOA facet that is contributed by the amplified DFB mode. The measured output power from the SOA facet (normalised to CW from pulsed duty cycle of 10%) consists of both the DFB mode (generated in the DFB section and amplified in the SOA section) as well as the ASE generated in the SOA section. In order to estimate the ratio of the amplified DFB power to the total measured power, I employed a simple and straightforward method: the spectrum is firstly converted from dBm to Watt, by using the conversion equation blow:

$$P(\mathrm{mW}) = 1\mathrm{mW}\times 10^{(P(\mathrm{dBm})/10)}$$

Then, by running integral computations over the peak range (x,y) and the overall spectrum range (m,n) respectively, the ratio of the amplified DFB mode within the overall spectrum can be estimated:

$$Ratio(DFB) \cong \frac{\int_{\mathrm{x}}^{\mathrm{y}} P(\lambda)d\lambda}{\int_{\mathrm{m}}^{\mathrm{n}} P(\lambda)d\lambda}$$

As seen in Fig. 5-26 (b), the spectrum recorded for device-1 (148nm) exhibits a significant effect caused by detuning between the gain peak and the Bragg wavelength, resulting in a very similar peak power for the narrow DFB mode and the broad spectrum of the ASE. One can expect device-1 to be therefore exhibit an extremely low DFB to total output power ratio. Therefore, here I estimate the ratios for device-2 and device-3

with I_{SOA} of 500mA pulsed current injection. At this current, the device still operates via a single mode, with breakdown of this behaviour when I_{SOA} is increased to 1000mA). Fig. 5-30 plots the EL spectra converted into the unit of Watts, from which a ratio can be estimated:

$$Ratio(Device2; I_{DFB}: 120mA; I_{SOA}: 500mA) \cong \frac{\int_{999.96}^{1000.31} P(\lambda)d\lambda}{\int_{997}^{1007} P(\lambda)d\lambda} \cong 73\%$$

$$Ratio(Device3; I_{DFB}: 120mA; I_{SOA}: 500mA) \cong \frac{\int_{999.96}^{1000.31} P(\lambda)d\lambda}{\int_{997}^{1007} P(\lambda)d\lambda} \cong 18\%$$

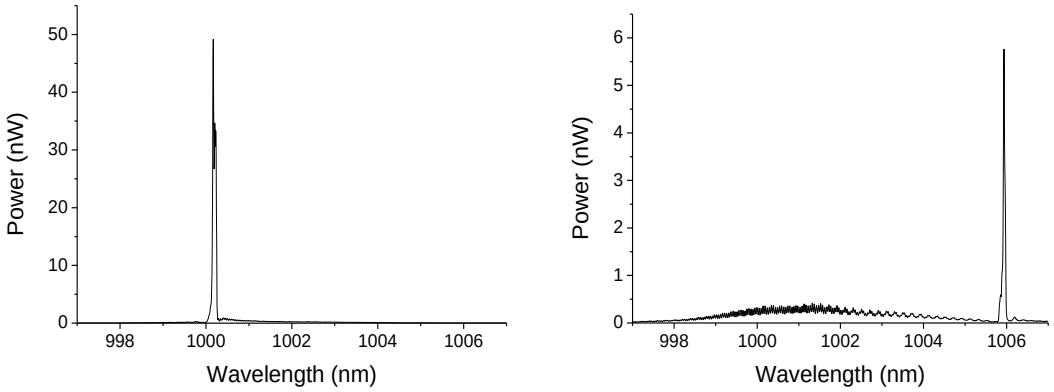

Figure 5-30: Conversion of the "SOA 500mA" (red curve) of (a) Fig. 5-26 (d) and (b) Fig. 5-26 (f) from dBm into nW

There is a significant difference between the ratios estimated from the 2 spectra. The reason lies in the larger detuning between the Bragg wavelength and the gain peak in device-3 compared to that in device-2, which results in less gain at the DFB lasing wavelength.

For the Device 2, by applying the ratio obtained (73%) to the power measured at 500mA (2.12mW) as plotted in Fig. 5-27 (c), an output DFB power of 1.55mW is estimated for this operating condition (I_{DFB} = 120mA, I_{SOA} = 500mA). Compared to the laser facet output power measured as 5.11mW, as plotted in Fig. 5-22 (a), it reveals that the power is not amplified while maintaining the single-mode spectral profile. When

applying the same calculation process above to the spectrum obtained with I_{SOA} =1000mA, as plotted in Fig. 5-27 (d), a ratio of 63% is obtained by performing integration over the range composed of multiple and broadened peaks from 1000.34nm to 1001.26nm as an envelope of the DFB power portion. An output DFB power of over 20.4mW was calculated, which is approximately 4 times that measured from DFB facet. One can expect that if perfectly AR coated, the effect of ASE ripples upon the DFB lasing mode could be significantly reduced and that the device can achieve a high output power with a much purer single-mode spectral profile.

5.5.4 Characterisation of MOPAs with Tilted SOAs

In this section, MOPAs with tilted SOAs are characterised as fully integrated devices, with electrical pumping of both the DFB laser and the SOA section simultaneously.

Fig. 5-31 summarises the L-I and spectral measurement of the 3 representative tilted SOA MOPA devices. In the figure, the left-hand-side column plots the L-I characteristics measured from 0mA to 1250mA with SOA sections pulsed using 5μs pulse width and 10% duty cycle with the laser switched either on or off. Again, the power plotted is normalised to CW. The right-hand-side column plots the EL spectrum recorded from the output facet at different SOA pumping currents (0mA/500mA/1000mA) with the lasers switched on.

The results of both L-I and spectral measurement of the SOA demonstrate an amplification of the optical wave by turning on the SOA.

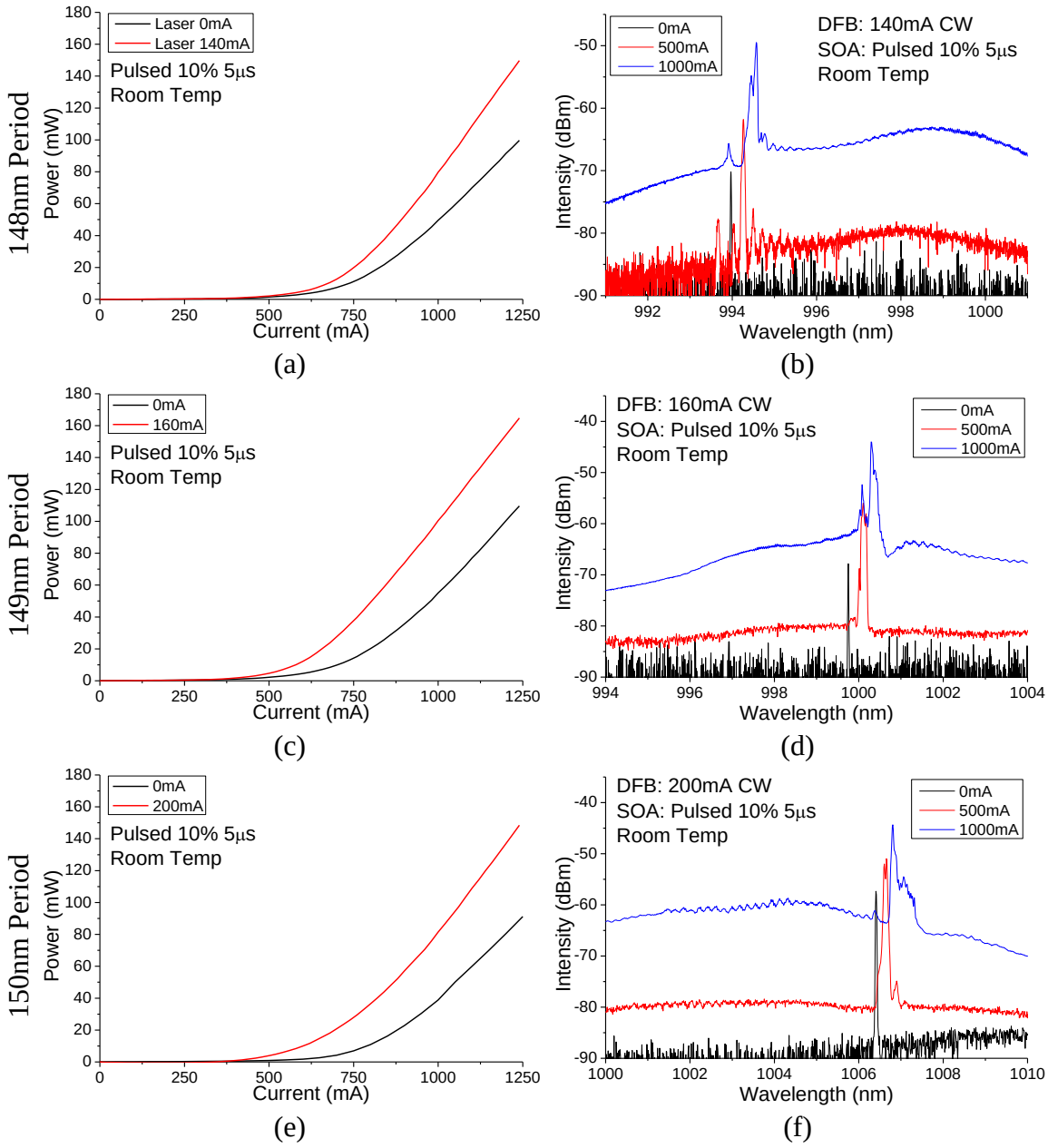

Figure 5-31: Light output power measurements from SOA facets as a function of pumping current (pulsed 5µs-10%) for SOA sections with lasers off and on (CW pumping) and spectrum measurements from SOA facets with lasers on (CW pumping) and SOA pulsed pumped (0/500 /1000mA) for (a)/(b) Device-4, (c)/(d) Device-5 and (e)/(f) Device-6

Again, to assist with the analysis, Fig. 5-32 plots the measured DFB peak wavelength and intensity extracted from Fig. 5-31 (b), (d) and (f). As shown in Fig. 5-31 (b), (d) and (f) and Fig. 5-32 (a), a red shift of the lasing peak was observed for Devices 4-6 with increasing SOA pumping current. This was also observed for Devices 1-3 in Section 5.5.3, where it was attributed to self-heating resulting from a large SOA section.

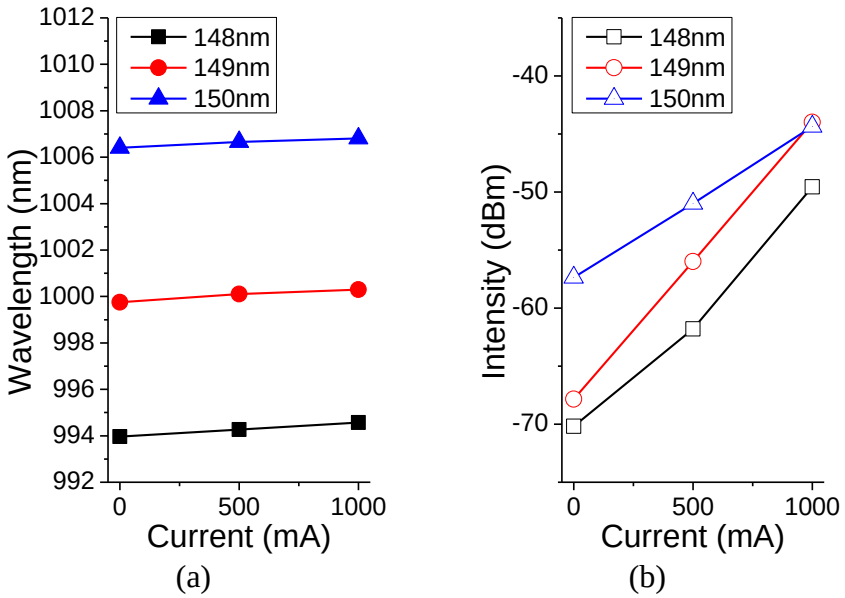

Figure 5-32: (a) Lasing peak wavelength shift and (b) peak intensity as function of SOA pumping current

A wavelength shift from 0mA to 1000mA was measured for each of the 3 devices as 0.600nm, 0.544nm and 0.400nm respectively, corresponding to a temperature increase of approximately 4~7^{o}C in the DFB sections. Compared to the estimated temperature increase of 8~13^{o}C in Devices 1-3, the reduced shift in these devices could be a result of the different geometry of the tilted SOA design, which incorporated a 0.5mm long narrow stripe before the tapered portion of the structure, which has the effect of better separating the laser section from the major source of self-heating in the tapered SOA. Fig. 5-32 (b) plots the intensity of the DFB peak as a function of SOA injected current. The device with a 149nm grating period has lasing wavelength ~1000nm and therefore exhibits the least detuning from ASE peak. This device exhibits the highest increase of ~24dBm over the I_{SOA} range from 0mA to 1000mA. This relationship among the 3 periods was similar to that demonstrated for Devices 1-3. Fig. 5-33 plots the spectrum shown in Fig. 5-31 (d) over a smaller range of 1nm about the DFB peak. The measured mode spacing (~0.04nm) indicates that the resonance of the wave is established in the entire cavity (3.15mm), which is in agreement with the measurement of tilted SOAs with the laser section turned off (section 5.5.2). In the figure, the modulation of ASE

peaks on the DFB peaks are much less pronounced compared to those observed in Fig. 3-29, which corresponds to a better performance of the SOAs with respect to maintaining the spectral profile of the input DFB lasing mode.

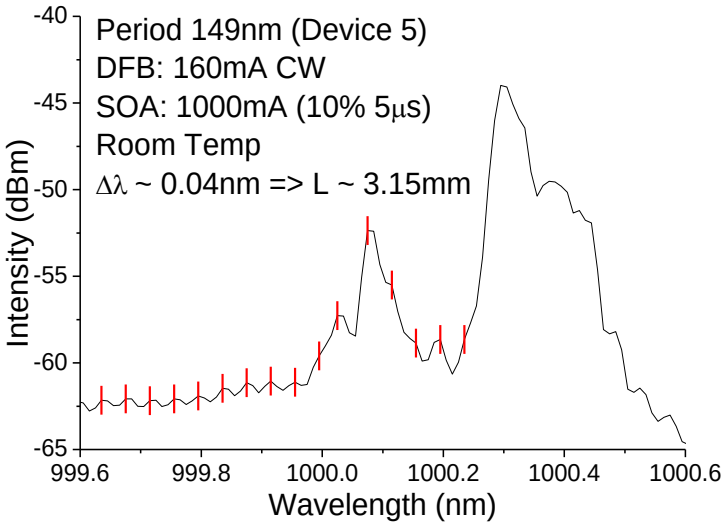

Figure 5-33: Zoomed-in spectrum of tilted facet MOPA output with 1000mA SOA pumping shown in Fig. 5-31 (d)

In order to further investigate the MOPA operation of the MOPA design, Device 5 was investigated further to study the characteristics of the integrated structure.

➢ Further Investigation of Device 5 (149nm Grating with Tilted SOA)

- **Power Amplification**

In order to characterise the effect of laser operating power upon the output power of the MOPA, Fig. 5-34 (a) plots the LI measurement from the SOA facet with different pumping currents applied to the laser section from 0 to 180mA. The figure shows an increase in the slope efficiency with increasing laser current injection. To assist in analysis, Fig. 5-34 (b) plots the output power obtained at I_{SOA} = 1240mA as a function of I_{DFB}, showing that the device output power tends to saturate when the I_{DFB} increases to ~160mA.

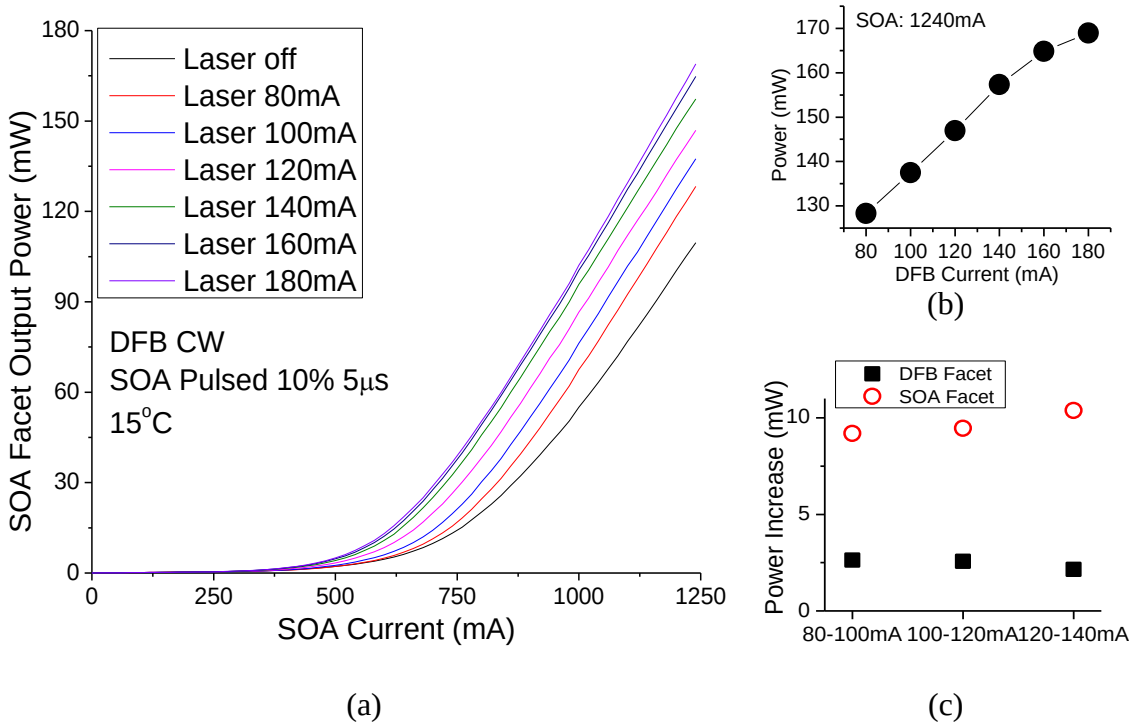

Figure 5-34: (a) Output power measured from SOA facet as a function of SOA pumping current (pulsed 5µs-10%) with different laser pumping current (CW); (b) the output power obtained at I_{SOA} = 1240mA as a function of I_{DFB}; and (c) the output power increase extracted at current step 80-100mA, 100-120mA and 120-140mA measured (■) from laser facet with SOA switched off and (○) from SOA facet with SOA 1000mA (pulsed 5µs-10%)

For the L-I measurement of the MOPA performance, one should keep in mind that the amplified DFB mode only comprises a portion of the total collected output power, as discussed in Section 5.5.3. However in this measurement the SOA is maintained at a fixed current injection whilst increasing the laser current injection, where we can assume an increase in the measured output power will represent an increase in the power of the amplified DFB peak.

Fig. 5-34 (c) compares the increase in power resulting from an increase of laser pumping current measured from the laser facet (■) when the laser is pumped only for laser characterisation and from the SOA facet (○) when the device is operated as a MOPA with the SOA pumped with 1240mA (pulsed 5µs-10%). For the laser section operating alone, a slope efficiency of ~0.1W/A was measured. After being amplified through the SOA operating with 1200mA, the slope efficiency increased to ~0.5W/A.

- **Portion of Amplified DFB Mode**

The ratio of the amplified DFB mode in the broad spectrum can be estimated using the method described in Section 5.5.3. Fig. 5-35 (a) shows the spectrum recorded when the laser section was operating with 200mA (CW) injection, whilst the SOA section was operating with 1000mA (pulsed: 5μs-10%) injection at a controlled substrate temperature of 15°C. Fig. 5-35 (b) plots the spectrum on a linear scale (i.e. dBm converted into Watt).

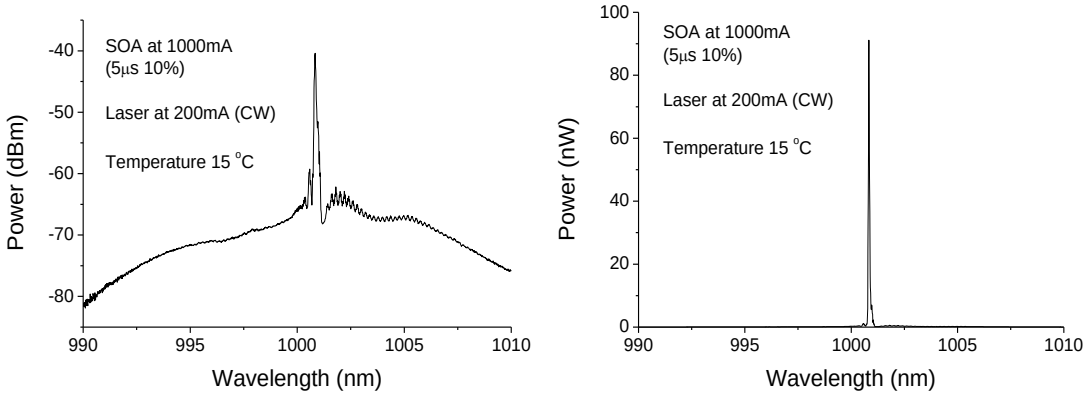

Figure 5-35: Conversion from dBm to Watt of ab example spectrum recorded with the laser section operating with 200mA (CW) injection and the SOA section operating with 1000mA (pulsed: 5μs-10%) at a controlled substrate temperature of 15°C

Then, by running integral computation over the peak range and the overall spectral range respectively, the ratio of the amplified DFB mode within the overall spectrum can be estimated for this device under this pumping condition:

$$Ratio(Device5; I_{DFB}: 200mA; I_{SOA}: 1000mA) \cong \frac{\int_{1000.76}^{1001.02} P(\lambda)d\lambda}{\int_{990}^{1010} P(\lambda)d\lambda} \cong 72\%$$

From Fig. 5-34 (a), it can be estimated that the DFB output power at this operating condition is approximately 70mW, which is roughly 7 times higher than can be approximated from the Fig. 5-22 (b).

- **Temperature Tunability**

In order to investigate whether an increased operating temperature could contribute to the modulation of the spectral profile of the amplified DFB peak, the MOPAs were measured as a function of temperature. The DFB laser spectrum was recorded at 20°C, 25°C and 30°C, as shown in Fig. 5-36 (a), and exhibits typical wavelength tuning of 0.9nm over this 10°C substrate temperature increase.

The spectrum recorded from the laser facet demonstrated DFB single-mode lasing operation over this temperature range. Therefore, for the observed wavelength shift of only 0.544nm that was measured for this device operating with SOA pumped from 0 at 1000mA, the increase in temperature of the laser cavity (due to SOA self-heating), equivalent to ~5°C, cannot explain the modulation observed.

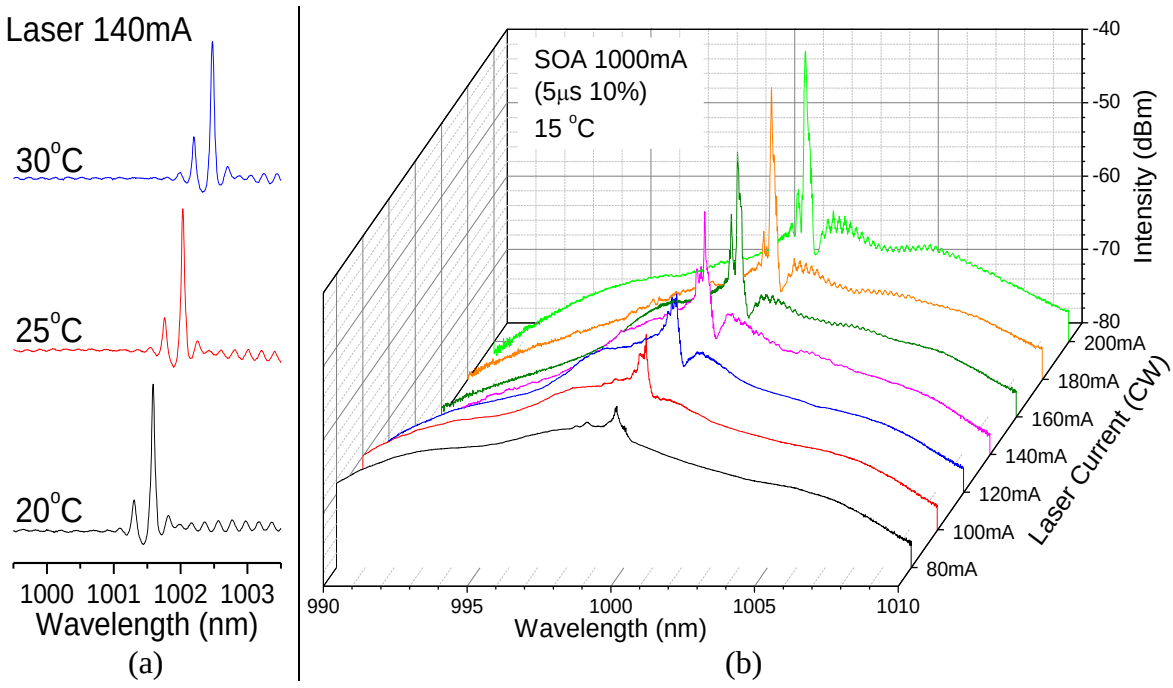

Figure 5-36: (a) Spectrum recorded from laser facet with SOA off and laser section on (140mA CW) under different substrate temperature; (b) Spectrum measured from SOA facet as a function of laser section pumping current (CW) with SOA 1000mA pulsed pumped (5μs-10%)

- **Spectral Profile with Increasing I_{DFB}**

The influence of the laser output power on the MOPA's amplified spectral profile was also investigated. Fig. 5-36 (b) plots the spectrum recorded from the SOA side of the MOPA as a function of the current injected into the laser with the SOA switched on (operated at 1000mA, pulsed 5μs-10% duty cycle) with increasing the laser pumping current. This shows that, with increasing the current injected into the laser, the SMSR and spectral form of the amplified DFB mode profile improves.

That is, the appearance of a well-defined, dominant single peak in the form of a typical DFB spectral profile, such as that exhibited in Fig. 5-36 (a). For the highest current plot (200mA) in Fig. 5-36 (b), the side-modes on the right-hand-side of the DFB lasing peak could already be identified, which was not the case at lower currents, although the SMSR remains strong.

Fig. 5-37 plots these spectral side-modes on a reduced scale for a range of laser injection currents from 100 to 200mA. The spectra demonstrate that when the DFB laser is operated at lower drive currents (100-140mA), the ASE ripples overwhelm the DFB spectral profile, such that the DFB side modes are not resolvable in the ASE spectrum. With more injected current (160-200mA), the spectrum appears to superpose DFB laser and SOA F-P modes, such that, the DFB spectral profile can be observed within the combined spectrum.

This is clearer in Fig. 5-38, which plots the emission spectrum of the MOPA, recorded from the SOA output facet at 200mA laser pumping current, 1000mA SOA (i.e. Fig. 5-37: 200mA) together with that recorded from the laser back facet with 200mA laser current (SOA off) on the same scale, but over an adjusted range.

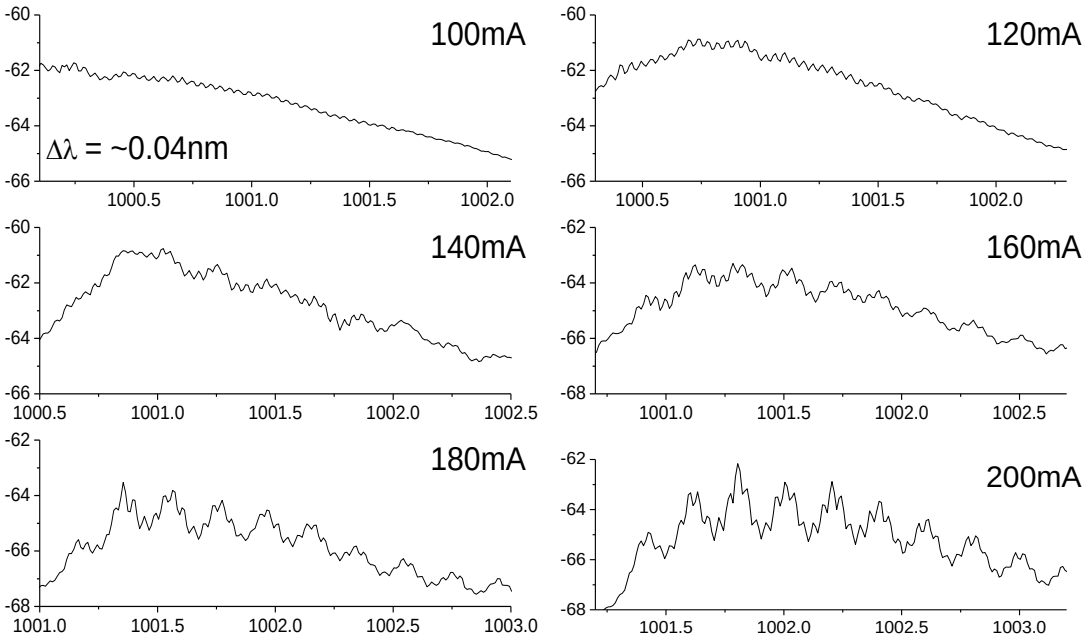

Figure 5-37: Zoomed-in spectrum of Fig. 5-36 (b) showing the DFB side modes on the right-hand-side of DFB lasing peak for 80-200mA laser pumping current

The laser spectrum in Fig. 5-38 (a) exhibits a consistent mode spacing of ~0.2nm (at ~1003nm). This is consistent with the dominant profile in the MOPA spectrum in Fig. 5-38 (b), also measured as ~0.2nm, but which also exhibits a further modulation with a smaller spacing of 0.04nm, which is the contribution made by the SOA ASE ripple.

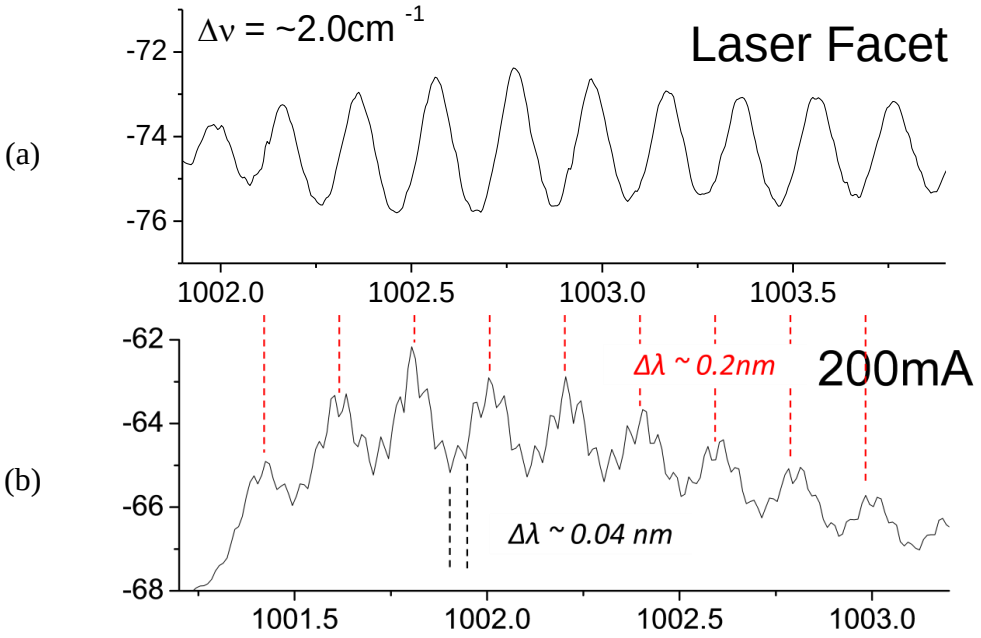

Figure 5-38: (a) Zoomed-in spectrum of DFB characterisation (SOA off) measured from laser facet showing the DFB side modes on the right-hand-side of DFB lasing peak; (b) Analysis of the modulation of spectrum of 200mA

5.5.5 Comparison and Discussion

For both MOPA types, light can propagate into the laser sections where it propagates through the laser section and a portion of it is reflected back from the DFB back facet to build front-to-end cavity resonance. Such resonance leads to modulation of the ASE spectrum, which affects the purity of the spectral profile of the amplified light. With higher operating current injections to the device, this could further result in self-lasing within a cavity length of the entire device. In order to suppress this, AR coatings were applied to both the DFB back facets and the SOA front facets to reduce the amount of reflected light. In addition, the InGaP window structures in the straight SOA MOPAs provide further suppression by reducing the amount of light propagating between sections. Furthermore, in the tilted SOA MOPAs, the 7^{o} incident angle at the output effectively reduces the reflected light from the SOA front facets back in to the waveguide.

➢ Comparison of Interfaces with/without InGaP Window

Based on the experimental observation of performance and behaviour of the devices: (1) With the laser section operating only, for both structures the longitudinal mode spacing measured in the spectra recorded from the DFB facets correspond to only the laser cavity length. This suggests that in the structure without a window, the interface between pumped and un-pumped regions provides a reflective interface resulting from the refractive index step. (2) With the SOA section operating only, the longitudinal mode spacing measured in the spectra recorded from the SOA facets for windowed and the non-windowed structures correspond to the SOA cavity length and the device (SOA

+ laser) cavity length, respectively. This suggests that the InGaP window achieves its designed functionality to provide suppression of light propagating from the SOA section into the DFB section. (3) While the MOPA is in operation with both the laser section and SOA section electrically pumped, for both structures the longitudinal mode spacing measured in the spectra recorded from the SOA facets correspond to the device (SOA + laser) cavity length. This suggests that the window loses its designed functionality when switching on the laser section.

The above experimentally observed behaviour of the InGaP window is expected and Fig. 5-39 schematically illustrates this phenomenon, where (a) shows the absorption of the light propagating through the window into an un-pumped laser section and (b) shows the amplification of the light when the laser section is switched on.

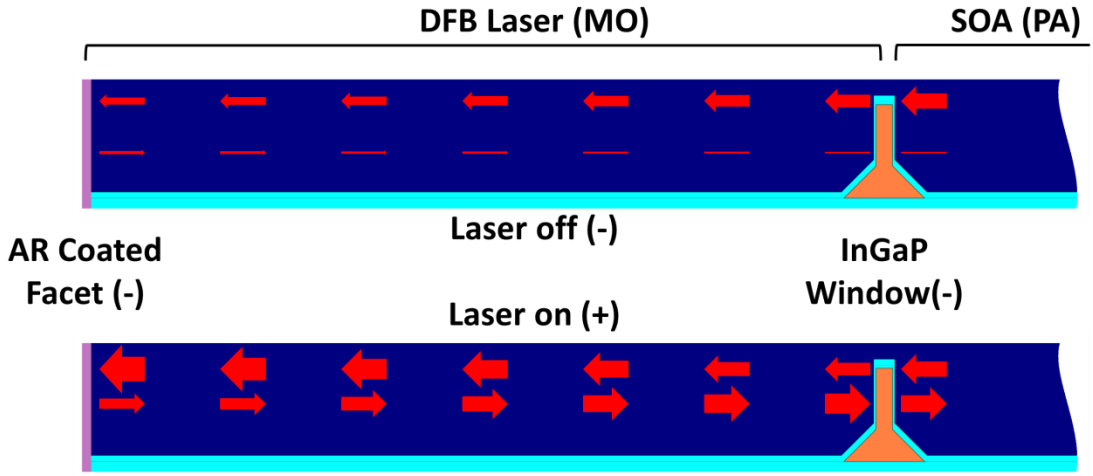

Figure 5-39: Schematic diagram of the propagation of slight from SOA section into the laser section with an InGaP window

When the laser section is un-pumped it behaves as an absorber, where any light propagating through this section is subjected to strong optical loss, providing suppression of the reflected light from the back facet. Despite the suppression, standing waves with a mode spacing corresponding to the total cavity length were still measured on the recorded spectra of non-windowed MOPAs, whilst that measured for windowed MOPAs corresponds to only the length of SOA sections. This difference is caused by a

further suppression of light propagating from SOA sections to DFB provided by the 15μm-wide InGaP window, which generates a small refractive index-step when the light penetrates all the layers as shown in Fig. 5-15, resulting in light reflection at the interface. Due to this mechanism, the wave reflected from the laser facet (the portion that contributes to device-length resonance) experiences further intensity loss as it penetrates the InGaP window twice. Hence the window demonstrates its functionality in suppression of back-reflection effects.

When the laser is pumped, the light experiences gain when propagating in the laser section. Therefore, the light generated in the SOA portion is no longer absorbed after penetrating the window, such that the resonance established between both end facets overwhelms that established between the InGaP window and SOA facet, where the window is no longer effective. Such undesired loss of functionality of the InGaP window allows the ASE ripples to establish over the resonant cavity of the entire device length. With higher SOA pumping current, the modulation between the DFB spectrum and ripples results in the breakdown of the single mode DFB peak in the amplified spectrum.

- **Discussion**

The effectiveness of the InGaP window is highly dependent on the overlap of the guided optical mode with the cross-sectional area of the window structure, i.e. the optical confinement factor of the area. As described in Section 5.3.2, the waveguide structure was modified due to the requirement of growing a 100nm thick in-fill GaAs layer, where $Al_{0.7}Ga_{0.3}As$ was used instead of $Al_{0.42}Ga_{0.58}As$, resulting in a lower refractive index (3.29 to 3.14), which not only reduces the index-step achieved by the

InGaP window, but reduces its optical overlap also. This can be seen in Fig. 5-40 (a) and Fig. 5-40 (b), which compare the simulated confinement factors of the cross-sectional area of the window structure of the original and the modified waveguide designs, showing an obvious decrease from 0.0283 to 0.0093 with a factor of ~3 after the structural modification. Fig. 5-40 (c) presents a demonstration of the possible improvements that could be made to the original waveguide for future optimised designs, where the separation between the grating and the active region in these new planar structures is reduced from 300nm to 200nm, and the height of the InGaP optoelectronic confinement layer is increased from 600nm to 700nm. The simulated confinement factor increases with a factor of ~1.8 from 0.0283 to 0.0518, which is more than 5.5 times higher than that in the modified designs in this chapter.

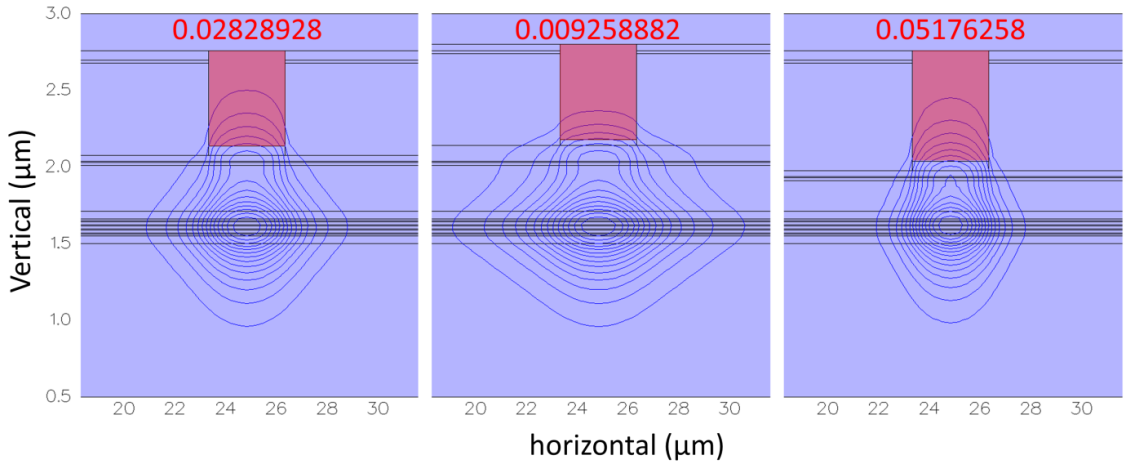

Figure 5-40: Simulated confinement factors of the cross-sectional area of the window structure in (a) the original waveguide, (b) the modified waveguide and (c) an example waveguide designed for higher overlap in the stripe region

➢ Comparison of Tilted and Straight SOA Geometries

Fig. 5-41 schematically compares the light propagation between the two different SOA geometries and the resultant parasitic facet reflections. The red arrows represent the amplified optical wave within and leaving the optical cavity. The black arrows represent the residual parasitic optical reflections from the AR coated SOA end cavity facets. In a tilted SOA, the light incident on the output facet is reflected and diverted away from waveguide due to the non-normal incident angle, As for a straight SOA, almost all of any reflected light is propagated straight back into the cavity. Therefore, less light can be reflected back from the tilted facet into the cavity, resulting in less intense ASE ripples, and a purer amplified DFB profile to higher injection currents.

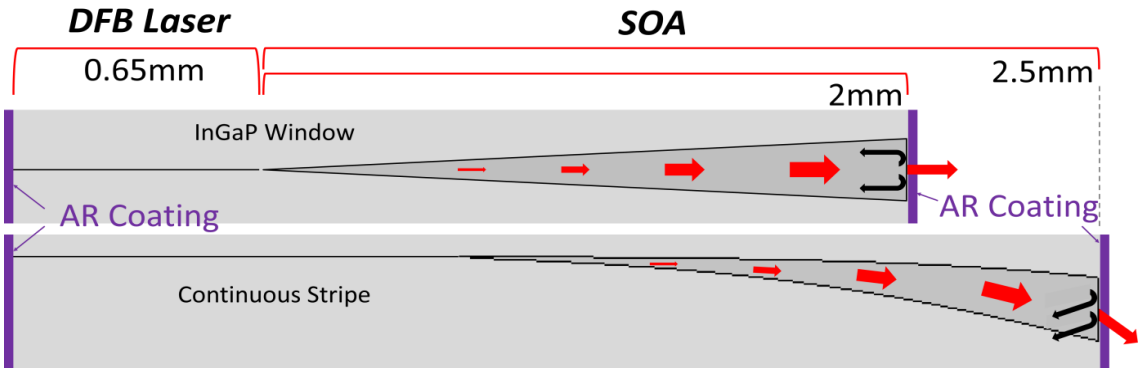

Figure 5-41: Comparison of two SOA geometries and facet reflection, where the red arrows represent optical wave being amplified in the cavity and the black arrows stand for reflected optical wave from facet

Comparison of the spectral profiles of the amplified DFB peak with a SOA injection current of 1000mA between the two MOPA types (Fig. 5-27 and Fig. 5-31) reveals that the breakdown of single mode lasing behaviour was much less severe in the tilted SOA MOPAs than the straight SOA MOPAs. Therefore, given that a further suppression of the end-to-end resonance is provided by an InGaP window in the straight SOA MOPAs, the MOPAs with tilted SOAs still demonstrate a better suppression of the ASE ripples due to their higher resistance to the disturbing back reflection from the SOA facets.

➢ Summary

In summary, because the un-optimal AR coating for these devices was specified to centre at 1050nm instead of 1000nm as a compromise made among other devices, the anti-reflective (AR) coating of the device facets was not optimal for the wavelength, the reflectivity at facets is expected to be higher than 0.1%, resulting in an undesired excessive amount of light to be reflected from both end facets. Under this configuration, the designed InGaP window structure in the interface between the sections is functional, but the suppression was not sufficient. One reason is that the refractive-index-step induced by the layers ($Al_{0.7}Ga_{0.3}As$-GaAs-InGaP-GaAs-$Al_{0.7}Ga_{0.3}As$) is rather small to generate a high reflectivity at the interface. Another reason for this is that the InGaP window is positioned to a distance above the active region, such that the overlap between the guided optical mode and the cross-sectional area of the window is small, which limits the effectiveness of the window. As to the geometry of the SOAs, the tilted SOAs demonstrate a higher suppression of the optical resonance established between the end-to-end facets by effectively reducing the reflected light at the SOA front facet back into the device, resulting in reduced influence of the single-mode lasing behaviour of the amplified DFB mode.

5.5.6 An Observed Issue of the Device Pumping Scheme

Another possible mechanism behind the appearance of the breakdown of single mode spectral profile could lie in the use of a pulsed current source for pumping the SOA, combined with a CW current source for the laser section. As discussed in Section 5.5.2, it was not possible to operate the SOA using a CW current source. A pulsed current source was adopted as an alternative option in order to reduce self-heating in the SOA and facilitate electrical pumping. During the experiment, it was noted that there was an observable difference in the output power collected from the DFB facet when the CW current source was connected (but switched off) compared to that collected with the CW source disconnected. This suggests an issue associated with the electrical circuit used in the measurements which may have subsequent implications for the spectral purity of the MOPA.

In order to investigate this phenomenon, the voltage applied to the impedance-matching resistor (connected in series, therefore the voltage profile reveals the current profile) was examined using an oscilloscope.

Fig. 5-42 shows photographs of the recorded voltage transients measured (a) when the SOA was pumped only with CW current source disconnected, and (b) with the CW current source connected to the laser section but switched off. The latter demonstrates a clear breakdown from the square-pulse signal recorded in the former, which was a result of simply connecting the CW current source into the circuit. Adjustment of the pulse width, duty cycle and the impedance-matching resistor could not resolve this issue due to the dependence of the square-pulse breakdown on set values of currents.

Furthermore, when operating the laser with the CW current source at a fixed current, e.g. 160mA, turning on the SOA section with a pulsed current, e.g. 1000mA, caused the CW current source to become unstable, with a fluctuation of ±0.5mA about its set value.

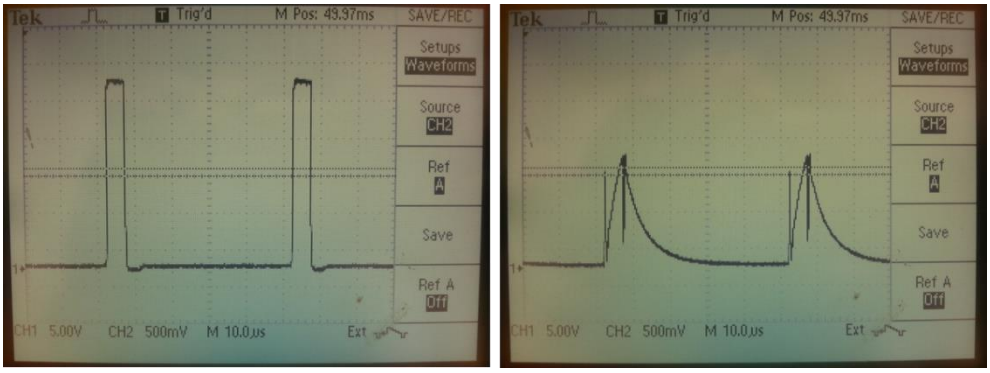

(a) (b)

Figure 5-42: Investigation of pulsed current applied to device using oscilloscope to measure the voltage applied in the impedance-matching resistor when (a) only pulsed current source operating and (b) CW and pulsed current source operating simultaneously

Fig. 5-43 illustrates the electrical connection of the device when both current sources were connected during the experiment.

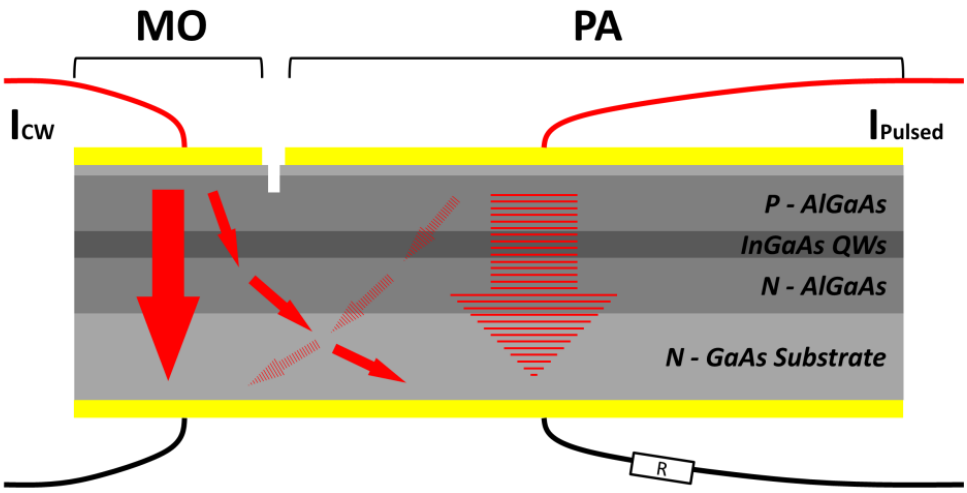

Figure 5-43: Schematic diagram of device pumping scheme, CW current applied to DFB and pulsed current to SOA

Although the top p-GaAs was etched for isolation between the two top contacts, the two current sources share the continuous back contact and are therefore mutually connected in each other's supply circuit, such that when two current sources were simultaneously turned on, the two active circuits were not operating independently and

current was allowed to flow into each other's circuit, resulting in impedance mismatch in the pulsed current source.

The application of another pulsed current source to supply the DFB section, clocked together with the SOA pulsed, and with both circuits having impedance-matching resistors could not resolve the problem fully either.

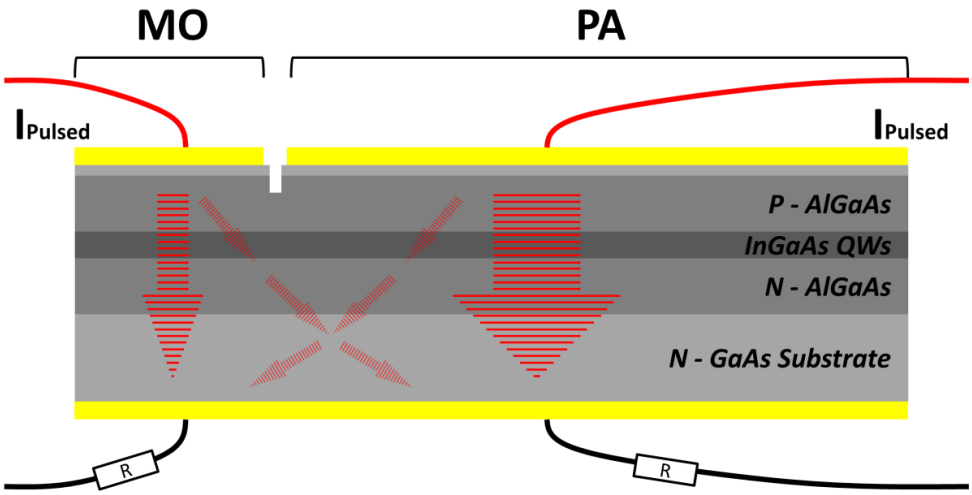

Figure 5-44: Schematic diagram of device pumping scheme, pulsed current applied to both DFB and SOA, where the pulsed current source were clocked together

Although better voltage transient profiles were achieved, the interaction between the inter-dependent active circuits made it impossible to stably pump the two sections when turning on the I_{SOA} to ~600mA.

Although the impact of this phenomenon upon output spectrum still remains unclear, the application of pulsed current to SOA sections in this chapter was only for experimental purposes for this batch of devices. In future optimised MOPA designs, as will be described in Chapter 6, the devices are expected to be driven with CW currents in both DFB and SOA sections, such that the phenomenon observed here will not pose a problem.

5.6 Conclusion

This chapter started with an introduction of the MOPA concept and a review of current state-of-the-art (Sections 5.1 and 5.2). The design and manufacture of the 2 MOPA structures in this chapter was described in Section 5.3 and 5.4. In Section 5.5, the 2 MOPA structures were characterised and their comparative performance was analysed and discussed. In Sections 5.5.1 and 5.5.2, the laser sections and SOA sections were first measured individually. The lasers demonstrated robust single mode DFB operation with CW injection. Although the SOAs were not able to operate under CW current injection, a pulsed current source was used as alternative to drive the SOAs into amplification. In Sections 5.5.3 and 5.5.4, the measurement of MOPA operation of both MOPA structures demonstrated amplification of the DFB mode by increasing the pulsed current applied to the SOAs whilst the laser sections were operated with a fixed CW current. Especially, more experiments were performed to investigate the origin of single-mode breakdown at higher SOA current injection. Section 5.5.6 described the observed issue with the pumping scheme in this chapter (DFB: CW; SOA: pulsed), where the two active circuits were not independent because of the continuous back contact.

For a monolithically integrated device, the transmission of light from the section where it is generated to other is inevitable. In addition, for real world devices, the facet AR coating cannot reach 0% reflectivity. Therefore, the transmitted light will establish ASE ripples in the resonant cavity, which can generate significant impact upon the device performance. In my MOPA designs, the type with straight SOAs has a 15μm

wide InGaP window designed in the interface to suppress the amount of spontaneous emission generated in SOA section from propagating into the laser section by introducing refractive index steps. For the MOPAs with tilted SOAs, the 7^{o}-off incident angle at the output facet reduces the amount of reflected light back into the waveguide.

As discussed throughout this chapter, there remains much room for improvement of this concept of MOPA PIC for future studies.

The problem of highly defective 2^{nd} overgrowth has limited the research accomplished in this chapter, not only that a large amount of fabricated devices were screened out due to SOA failure, but also that the SOA sections were not able to be driven with CW current injection due to significant self-heating to the point that amplification was not possible. In future research, the effect of growth temperature on the quality of both overgrowth steps has to be fully investigated and optimised before proceeding. Given this problem being solved, both DFB and SOA sections will be operated with CW currents, such that the electrical issue observed and described in Section 5.5.7 will no longer exist.

As discussed, one main issue that breaks down the functionality of the devices is the ASE ripples established in the whole device cavity. Methods to solve this problem are therefore to reduce the reflection of light from the facets, whilst lowering the portion that can propagate back into the waveguide.

Four possible methods to reduce the facet reflectivity are:

1. To apply AR coating designed for a reflectivity of <0.1% at the centre wavelength;
2. To continue with the tilted SOA design instead of straight SOA design to effectively reduce the amount of reflected light that propagates back into the waveguide;
3. Introduce an un-pumped window section at the SOA facet to reduce the amount of reflected light that propagates back into the waveguide, for both tilted and straight SOA designs;
4. If 1/4-λ-shifted (or double-1/8-λ-shifted DFB) is to be designed for the MO in future designs, there will be no necessity to make use of the random facet-grating phase to yield single mode operation. A rear absorber can be integrated between the DFB section and the rear facet to reduce the amount of reflected light that propagates back into the waveguide.

Another scheme for ASE suppression is to introduce discontinuities inside the device, such as the InGaP window method developed in this chapter, where alternative methods include asymmetric waveguide designs and etched facets. As discussed in Section 5.5.5, the examination of the InGaP window in operation (both sections are switched on simultaneously) reveals that the designed 15μm wide InGaP window and the isolation etch could not function sufficiently to suppress the ASE generated in the SOA section from propagating into the laser section. This can be improved by increasing the optical confinement factor in the area of the etched stripe geometry, which corresponds to portion of the guided optical mode that overlaps with the InGaP window.

5.7 Reference

[1] M. Maiwald, A. Klehr, B. Sumpf, G. Erbert and G. Tränkle, "Dual-Wavelength Master Oscillator Power Amplifier Diode-Laser System at 785 nm," *IEEE* Photonics Technology Letters, vol. 26, no. 11, pp. 1120-1123, June 2014.

[2] T. N. Vu, A. Klehr, B. Sumpf, H. Wenzel, G. Erbert and G. Tränkle, "Wavelength stabilized ns-MOPA diode laser system with 16 W peak power and a spectral line width below 10 pm," *Semiconductor Science and Technology*, vol. 29, no. 3, p. 035012, December 2014.

[3] S. O'Brien, R. Lang, R. Parke, J. Major, D. F. Welch and D. Mehuys, "2.2-W continuous-wave diffraction-limited monolithically integrated master oscillator power amplifier at 854 nm," *IEEE Photonics Technology Letters*, vol. 9, no. 4, pp. 440-442, April 1997.

[4] R. M. Lammert, J. E. Ungar, M. L. Osowski, H. Qi, M. A. Newkirk and N. Bar Chaim, "980-nm master oscillator power amplifiers with nonabsorbing mirrors," *IEEE Photonics Technology Letters*, vol. 11, no. 9, pp. 1099-1101, September 1999.

[5] M. Spreemann, M. Lichtner, M. Radziunas, U. Bandelow and H. Wenzel, "Measurement and Simulation of Distributed-Feedback Tapered Master-Oscillator Power Amplifiers," *IEEE* Journal of Quantum Electronics, vol. 45, no. 6, pp. 609-616, June 2009.

[6] H. Wenzel, K. Paschke, O. Brox, F. Bugge, J. Fricke, A. Ginolas, A. Knauer, P. Ressel and G. Erbert, "10 W continuous-wave monolithically integrated master-oscillator power-amplifier," *Electronics Letters*, vol. 43, no. 3, pp. 160-161, February 2007.

[7] O. M. S. Ghazal, D. T. Childs, B. J. Stevens, N. Babazadeh, R. A. Hogg and K. M. Groom, "GaAs-based superluminescent diodes with window-like facet structure for low spectral modulation at high output powers," *Semiconductor Science and Technology*, vol. 31, no. 4, January 2016.

[8] E. J. Skogen, J. S. Barton, S. P. DenBaars and L. A. Coldren, "Tunable sampled-grating DBR lasers using quantum-well intermixing," *IEEE Photonics Technology Letters*, vol. 14, no. 9, pp. 1243-1245, September 2002.

[9] Y. Akulova, G. Fish, P.-C. Koh, C. Schow, P. Kozodoy, A. Dahl, S. Nakagawa, M. Larson, M. Mack, T. Strand, C. Coldren, E. Hegblom, S. Penniman, T. Wipiejewski and L. Coldren, "Widely tunable electroabsorption-modulated sampled-grating DBR laser transmitter," *IEEE Journal of Selected Topics in Quantum Electronics*, vol. 8, no. 6, pp. 1349–1357, November - December 2002.

[10] A. Ward, D. Robbins, G. Busico, E. Barton, L. Ponnampalam, J. Duck, N. Whitbread, P. Williams, D. Reid, A. Carter and M. Wale, "Widely tunable DS-DBR laser with monolithically integrated SOA: design and performance," *IEEE Journal of Selected Topics in Quantum Electronics*, vol. 11, no. 1, pp. 149–156, January - February 2005.

[11] P. Rauter, S. Menzel, A. K. Goyal, B. Gökden, C. A. Wang, A. Sanchez, G. W. Turner and F. Capasso, "Master-oscillator power-amplifier quantum cascade laser array," *Applied Physics Letters*, vol. 101, no. 26, p. 261117, 2012.

[12] M. Wakaba, N. Iwai, K. Kiyota, H. Hasegawa, T. Kurobe, G. Kobayashi, E. Kaji, M. Kobayakawa, T. Kimoto, N. Yokouchi and A. Kasukawa, "High Power Operation at High Temperature of AlGaInAs/InP Widely Tunable BH Laser," *2013 18th OptoElectronics and Communications Conference held jointly with 2013 International Conference on Photonics in Switching (OECC/PS)*, Kyoto, Japan, pp. 1-2, 2013.

[13] B. Sumpf, K.-H. Hasler, P. Adamiec, F. Bugge, F. Dittmar, J. Fricke, H. Wenzel, M. Zorn, G. Erbert and G. Tränkle, "High-Brightness Quantum Well Tapered Lasers," *IEEE Journal of Selected Topics in Quantum Electronics*, vol. 15, no. 3, pp. 1009–1020, May-June 2009.

[14] D. Welch, R. Parke, D. Mehuys, A. Hardy, R. Lang, S. O'brien and S. Scifres, "1.1 W CW, diffraction-limited operation of a monolithically integrated flared-amplifier master oscillator power amplifier," *Electronics Letters*, vol. 28, no. 21, pp. 2011-2013, October 1992.

[15] S. O'Brien, R. Parke, D. F. Welch, D. Mehuys and D. Scifres, "High power singlemode edge-emitting master oscillator power amplifier," *Electronics Letters*, vol. 28, no. 15, pp. 1429-1431, July 1992.

[16] S. O'Brien, R. Lang, R. Parke, J. Major, D. F. Welch and D. Mehuys, "2.2-W continuous-wave diffraction-limited monolithically integrated master oscillator power amplifier at 854 nm," *IEEE Photonics Technology Letters*, vol. 9, no. 4, pp. 440-442, April 1997.

[17] O. Brox, J. Wiedmann, F. Scholz, F. Bugge, J. Fricke, A. Klehr, T. Laurent, P. Ressel, H. Wenzel, G. Erbert and G. Tränkle, "Integrated 1060nm MOPA pump source for high-power green light emitters in display technology," *Proc. SPIE 6909, Novel In-Plane Semiconductor Lasers VII*, vol. 6909, no. 1G, pp. 1-8, January 2008.

[18] A. Egan, C. Z. Ning, J. V. Moloney, R. A. Indik, M. W. Wright, D. J. Bossert and J. G. McInerney, "Dynamic instabilities in master oscillator power amplifier semiconductor lasers," *IEEE Journal of Quantum Electronics*, vol. 34, no. 1, pp. 166–170, January 1998.

[19] G. C. Dente and M. L. Tilton, "Modelling multiple-longitudinal-mode dynamics in semiconductor lasers," *IEEE Journal of Quantum Electronics*, vol. 34, no. 2, pp. 325–335, February 1998.

[20] Kamelian Ltd., *Semiconductor Optical Amplifiers (SOAs) as Power Boosters, Applications Note No. 0001*, 2003. [Online]. Available: http://www.ing.unitn.it/~fontana/GreenInternet/OpticalSwitching/DataSheets/opr02FH4.pdf, Accessed on: 16 December 2016.

[21] T. Mukai and Y. Yamamoto, "Gain, frequency bandwidth, and saturation output power of AlGaAs DH laser amplifiers," *IEEE Journal of Quantum Electronics*, vol. 17, no. 6, pp. 1028–1034, 1981.

This Page
Intentionally
Left Blank

Chapter 6. Future Work

The previous chapters described the development of GaAs-based self-aligned stripe distributed feedback laser (GaAs SAS-DFB) technologies. This chapter outlines the future work suggested to further the achievement of GaAs photonic integrated circuits. Based on the conceptualisation of the SAS-DFB-MOPA prototype in Chapter 5, in Section 6.1 an optimised four-section MOPA design is first presented. Section 6.2 and 6.3, present the preparatory works conducted for the development of (1) GaAs-based SAS sampled grating distributed Bragg reflector (SG-DBR) and (2) high power ~1180nm InAs/GaAs quantum dot SAS-DFB-MOPA.

6.1 Optimisation of SAS-DFB-MOPA

Based on the study of the prototype SAS-DFB-MOPA designs in Chapter 5, I conceptualised an optimised four-section tunable laser design. As illustrated in Fig. 6-1, this concept incorporates (1) a tilted rear absorber, (2) a DFB laser section, (3) a spacer and a (4) tilted-flared SOA section with an un-pumped area at output facet. As highlighted in the figure, all the interfaces between sections are fabricated with an un-etched InGaP “window”, together with the top isolation etch during fabrication. The front and rear facets are coated with optimal AR coating with a reflectively to be less than 1%. The two enlarged pictures of rear back and front facets illustrate the reduction of the facet reflection afforded by the newly introduced absorber and un-pumped

window area, where the red arrows represent the light exiting the device and the black arrows are the reflected light.

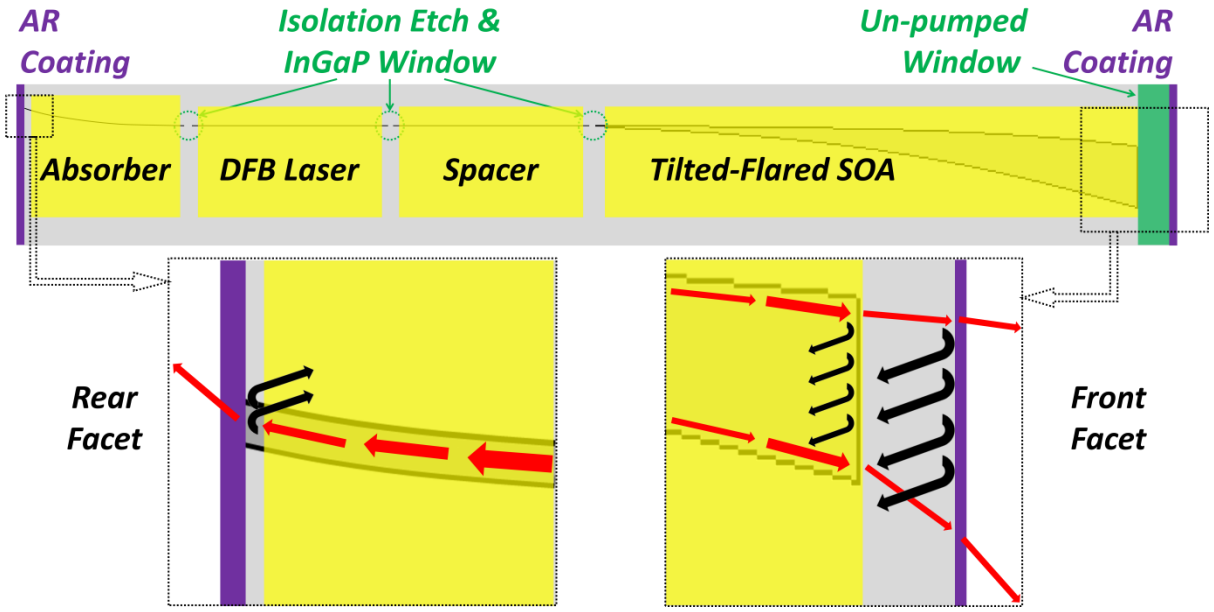

Figure 6-1: Schematic diagram of the optimised four-section SAS-DFB-MOPA design, together with the illustrations of reduction of reflected light from rear and front facets by introducing a tilted rear absorber and an un-pumped front window area respectively

The rear absorber is used to effectively reduce the rear facet reflection by absorbing the light propagating in the section and diverting a large portion of the reflected light away so that it cannot re-couple back into the waveguide. Compared to the current SOA design, the additional un-pumped area is designed to further reduce the amount of front facet reflection by broadening the divergence of the beam reaching the front facet, resulting in a broadened divergence of any reflected light, hence a much smaller portion of back-reflected light can re-couple back into the waveguide.

Furthermore, a spacer section is positioned inbetween the DFB section and the SOA section for better thermal separation, which is pumped into transparency while in operation.

In order to visually present the key features of this multi-section waveguide, Fig. 6-2 presents both lateral and longitudinal cross-sectional views of the epitaxial structure

centred at the DFB section. The definition of the SAS is shown in Fig. 6-2 (a) together with the specification of layer information; whilst (b) shows the key structural feature at the interfaces and the position of the buried grating.

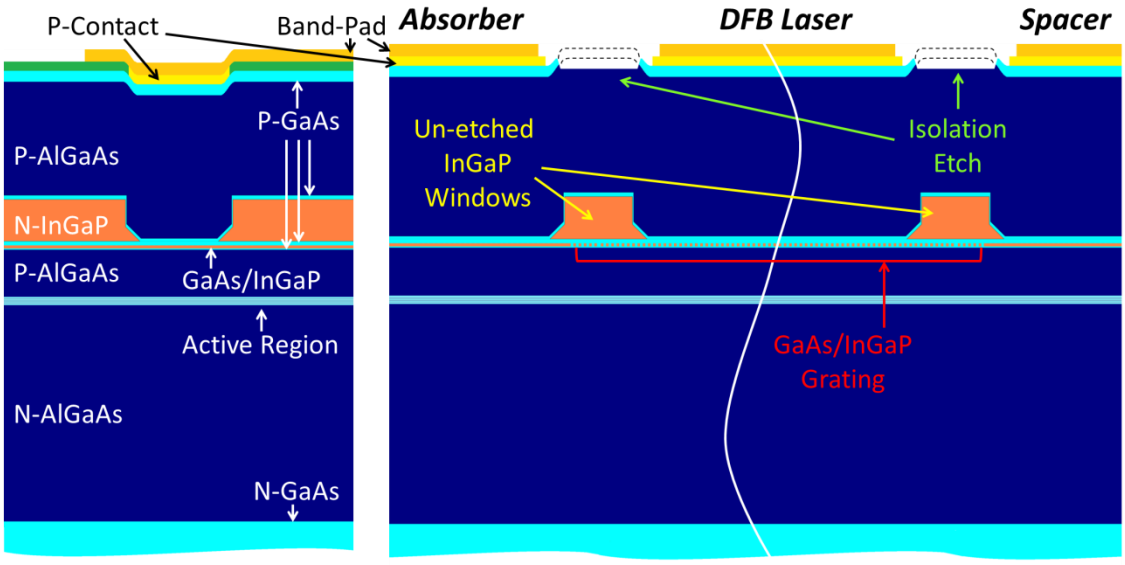

(a) Front View (b) Side View

Figure 6-2: Cross-sectional schematic diagrams of the DFB section from (a) epitaxial-lateral front view, where the layers of the SAS structure are specified, and (b) epitaxial-longitudinal side view, where the structural features are highlighted

In order to improve the waveguide design of the prototype design, as illustrated in Fig. 5-12, simulation activities will be conducted aiming at a certain coupling confinement factor of the grating layer corresponding to the designed length of the DFB section for a $KL \sim 1$, whilst optimising (1) the mode profile of the wave-guiding for stable single lateral mode, (2) the confinement factor in the active region for sufficient gain, and (3) the overlap of the guided mode to the cross-sectional area of etched InGaP stripe for better functionality of the InGaP windows. The available variables to be investigated include: the thickness of the grating, the separation between the grating and active region, the thickness of the 1st and 2nd overgrown in-fill GaAs layers. Additional variables such as the dimensions of the etched isolation notches and the InGaP window may also afford extended flexibility for structural design.

6.2 SAS-SGDBR

In a large number of PIC designs, it is necessary to integrate active and passive sections for certain functionalities relaying on passive waveguides (e.g. couplers, DBRs, etc.). Typical active sections include the gain section and SOA section, whilst typical passive sections include the phase section and grating section. Without any treatment to achieve multiple band edges, un-pumped sections would perform as absorbers for light generated in the active session(s) to propagate through, e.g. grating sections.

In the early 2000s, the research group led by Prof. Larry Coldren in UCSB developed their monolithic SG-DBR designs employing a QW intermixing method [1]-[3], which aimed at applications of wavelength-division-multiplexing (WDM) in fibre optic networks. This followed an initial realisation of the SG-DBR using a more complex butt-joint regrowth method.

Fig. 6-3 illustrates the structure reported in [2]. The key sections of an SG-DBR are the back and front mirrors (sampled grating), phase section, gain section and the rear absorber to reduce the reflected light from the back facet.

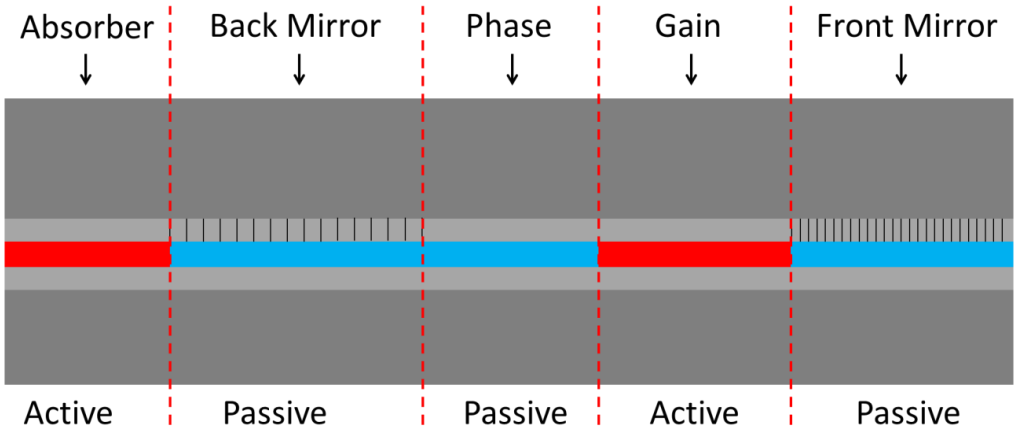

Figure 6-3: Schematic diagram of the main concept of an SG-DBR reported in [2]

As reported in [2], they achieved a blue-shift of ~100nm of the gain peak in the phase and grating sections, supporting a tuning range of 37nm centred at 1540nm. In [3], they demonstrated additional integration of an electro-absorption modulator between the front mirror section and the front facet.

The operating principle of an SG-DBR, as illustrated in Fig. 6-4, is to utilise the slightly mismatched reflectivity spectra of the front and back sampled gratings, where only one pair of the reflectivity spikes, i.e. the selected wavelength, can overlap at any relative position (tuned by current injection I_{Front_Mirror} and I_{Back_Mirror}) over the wavelength range of the gain.

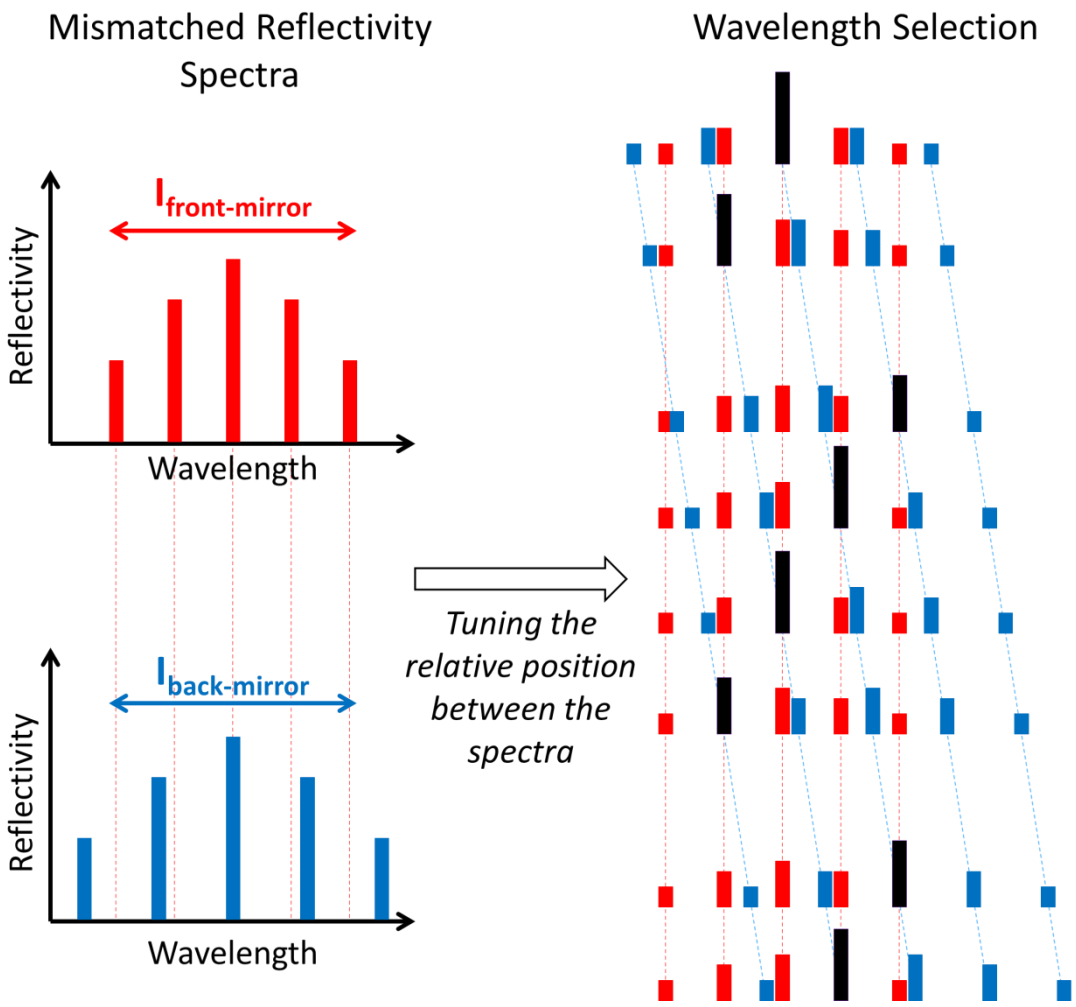

Figure 6-4: Schematic diagram of the wavelength section mechanism of an SG-DBR

In 2005, Skogen et al. discussed the advantages of photonic integration and provided an overview of the various integration techniques possible [4] and summarised 4 typical integration methods, i.e. butt-joint regrowth method [5], selective area growth (SAG) method [6], offset quantum-well active region method [7], and quantum well intermixing (QWI) method [8], among which QWI is more desirable due to its relative simplicity. Many techniques to achieve QWI have been studied, including impurity-induced disordering (IID) [9], implantation-enhanced interdiffusion [10] and impurity-free vacancy diffusion (IFVD) [11].

In order to develop GaAs-based SG-DBR to achieve wide tunability, some preparatory works has been conducted to examine the effectiveness of the IFVD intermixing method due to its effectiveness and ease of operation. At elevated temperatures, Gallium atoms are soluble in the SiO_2 with a high diffusion coefficient coating. During annealing, Gallium atoms dissolve into the cap leaving vacancies, which moves towards the remainder of the layers with a high diffusion coefficient and generate intermixing effect. As Gallium diffused out of the active region, Aluminium starts to move in along with the diffusion of vacancies resulting in a broadened band gap, corresponding to a blue-shift of the gain peak.

In order to examine the ability to perform such active-passive integration, a 1060nm InGaAs/GaAs quantum dot wafer was prepared. The samples were coated with SiO_2 and TiO_2 dielectric coatings and annealed for different time durations and temperatures.

Fig. 6-5 plots the shifts of the gain peak measured from SiO_2 and TiO_2 coated areas using an annealing temperature of 750^oC and 800^oC for difference time duration. A relative wavelength difference between SiO_2 and TiO_2 coated samples as large as 58nm was measured (5min at 800^oC). This is a sufficient value for a target tuning range of ~40nm.

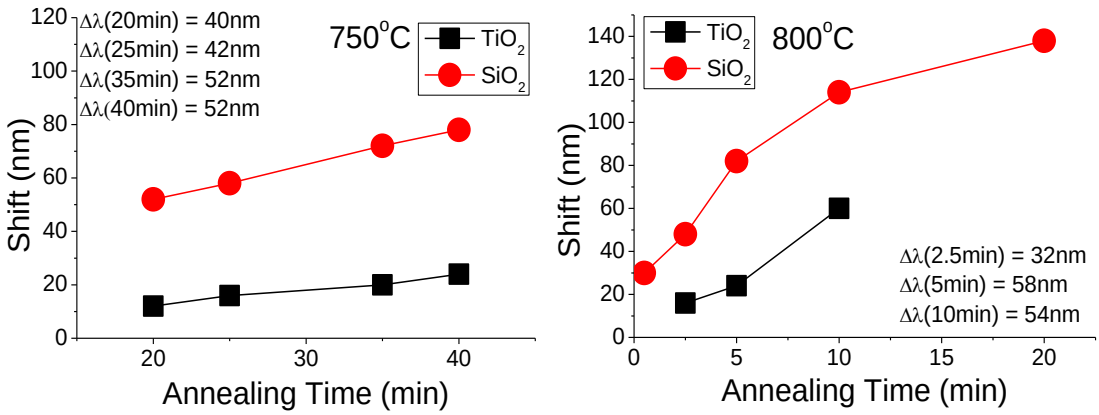

Figure 6-5: Comparison of wavelength shifts with SiO_2 and TiO_2 coating with different annealing temperature and time duration

Fig. 6-6 plots the PL scan performed on a sample annealed at 750°C for 40min, from the TiO_2 coated area across the interface to the SiO_2 coated area. As shown, the transition from the active region to the passive region was within a width of 50μm. The spectra were recorded with certain mechanical limitation of the resolution, which means that the actual width of the interface could be narrower.

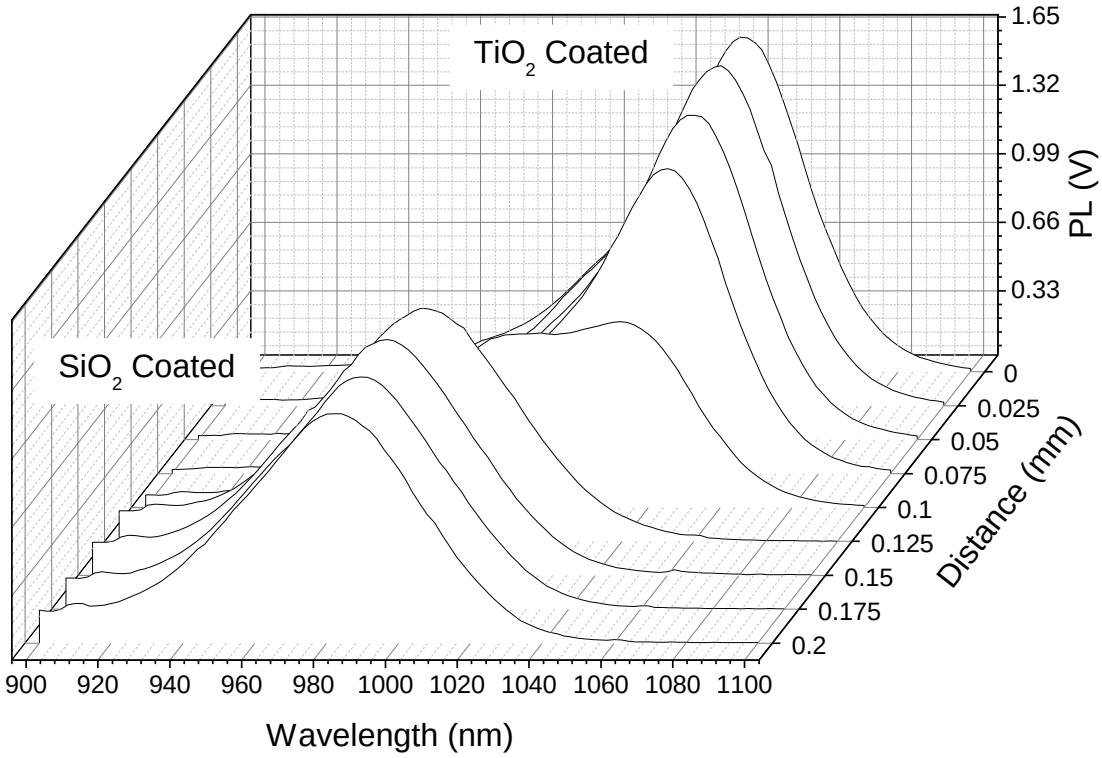

Figure 6-6: Cross-sectional PL scan after annealing at 750°C for 40min, from the active to passive areas, where the transition was observed to be within in a width of 50μm

6.3 1180nm In(Ga)As/GaAs DWELL SAS-DFB-MOPA

Currently, the research conducted on the development of SAS-DFB-based PIC has been limited in the use of InGaAs quantum well active regions with an emitting wavelength of ~1000nm. In order to broaden the scope of this technology, I have initiated the development of In(Ga)As/GaAs DWELL (dot-in-a-well) SAS-DFB-MOPA with an expected lasing wavelength of ~1180nm. This wavelength was chosen in order to target potential application in adaptive optics by sodium guide star excitation.

Two 5× In(Ga)As/GaAs DWELL materials were prepared. One wafer (Type-A) was designed to have a QD ground state transition at ~1180nm, whilst the other (Type-B) had a ~1300nm ground state and its excited state transition is at ~1180nm. The purpose of these 2 structures was to compare their ability for high power and high speed operation, since the greater degeneracy of the excited state should enable high power operation despite the relatively low ground state saturation of QD lasers, and high speed due to higher differential gain. Preparatory experimental activities have been conducted by fabricating and characterising broad area lasers from these materials.

Fig. 6-7 shows schematic representations of these two DWELL epitaxial layer structures with the origin of the different gain wavelength is highlighted. As illustrated, both wafers were grown on a 3 ºoff to (110) N-GaAs substrate with an active region incorporating 5 layers of InAs QDs in an InGaAs QW. The core was sandwiched by $Al_{0.4}Ga_{0.6}As$ upper and lower claddings with a graded region consisting of 25 repeats of 0.5nm/0.5nm GaAs/$Al_{0.4}Ga_{0.6}As$ on either side. The wafers were completed with a 300nm thick highly P-doped GaAs top contact layer.

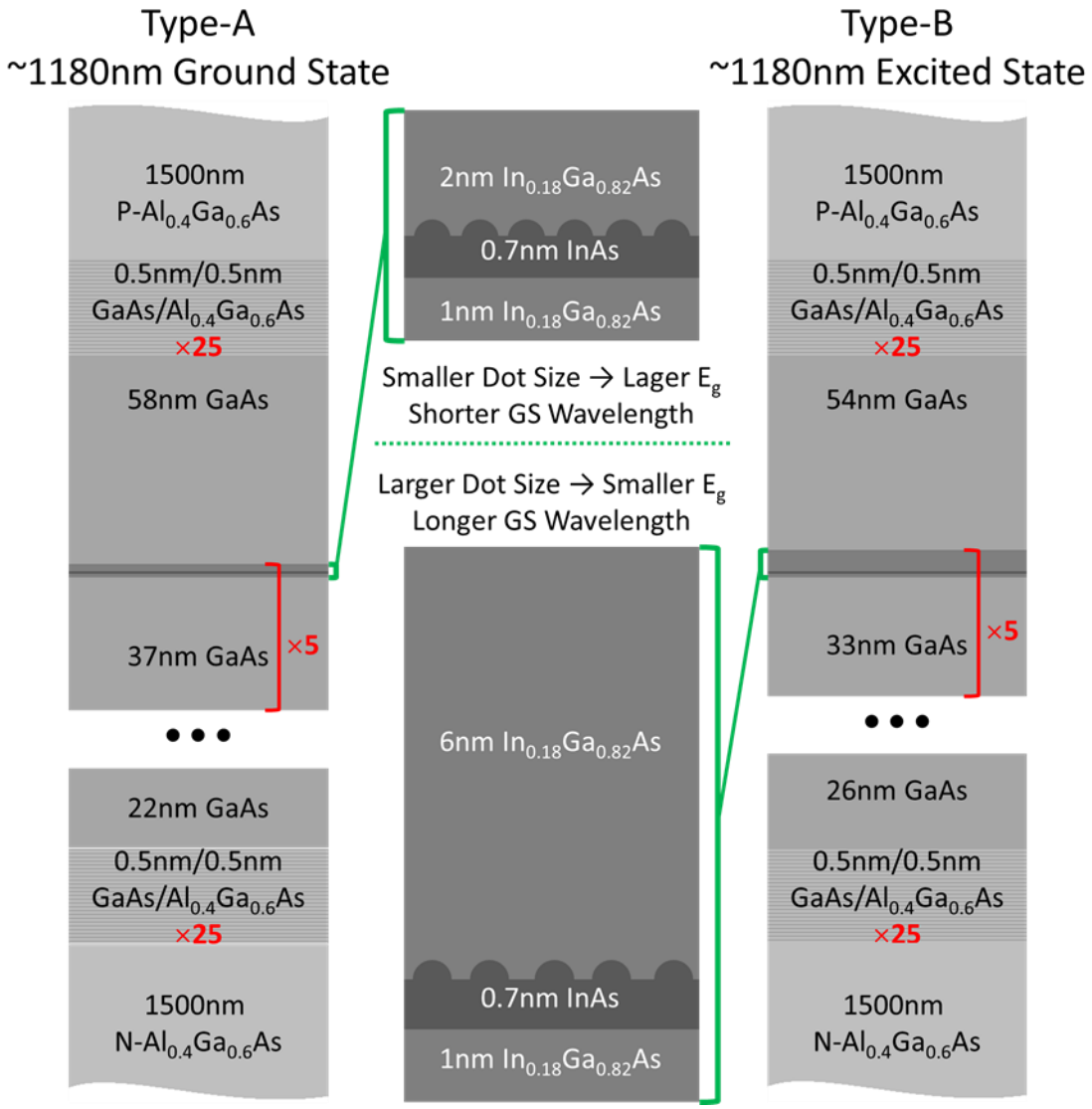

Figure 6-7: Comparison of the epitaxial layers of the two In(Ga)As/GaAs 5× DWELL wafers

The different ground state transition wavelengths between these two materials are achieved by adjusting the $In_{0.18}Ga_{0.82}As$ capping layers in their DWELL structures, resulting in a change in dot sizes. Based on the "a particle in a box" concept, the energy gap between different energy states is proportional to the reciprocal of the square of box width, which corresponds to the size of a dot. Therefore, an increase in the dot size results in a decrease in bandgap energy leading to a longer emission wavelength.

Two materials were fabricated and cleaved into broad area lasers with difference cavity lengths and characterised.

Fig. 6-8 plots the length dependent L-I characteristic and recorded EL spectra showing the devices lasing via the 1st excited state transition in a shorter cavity length and via the ground state transition in the next shortest length. The measurement was conducted at a heat-sink temperature of 15°C using a pulsed current source with a pulse width of 5μs and a duty cycle of 1%.

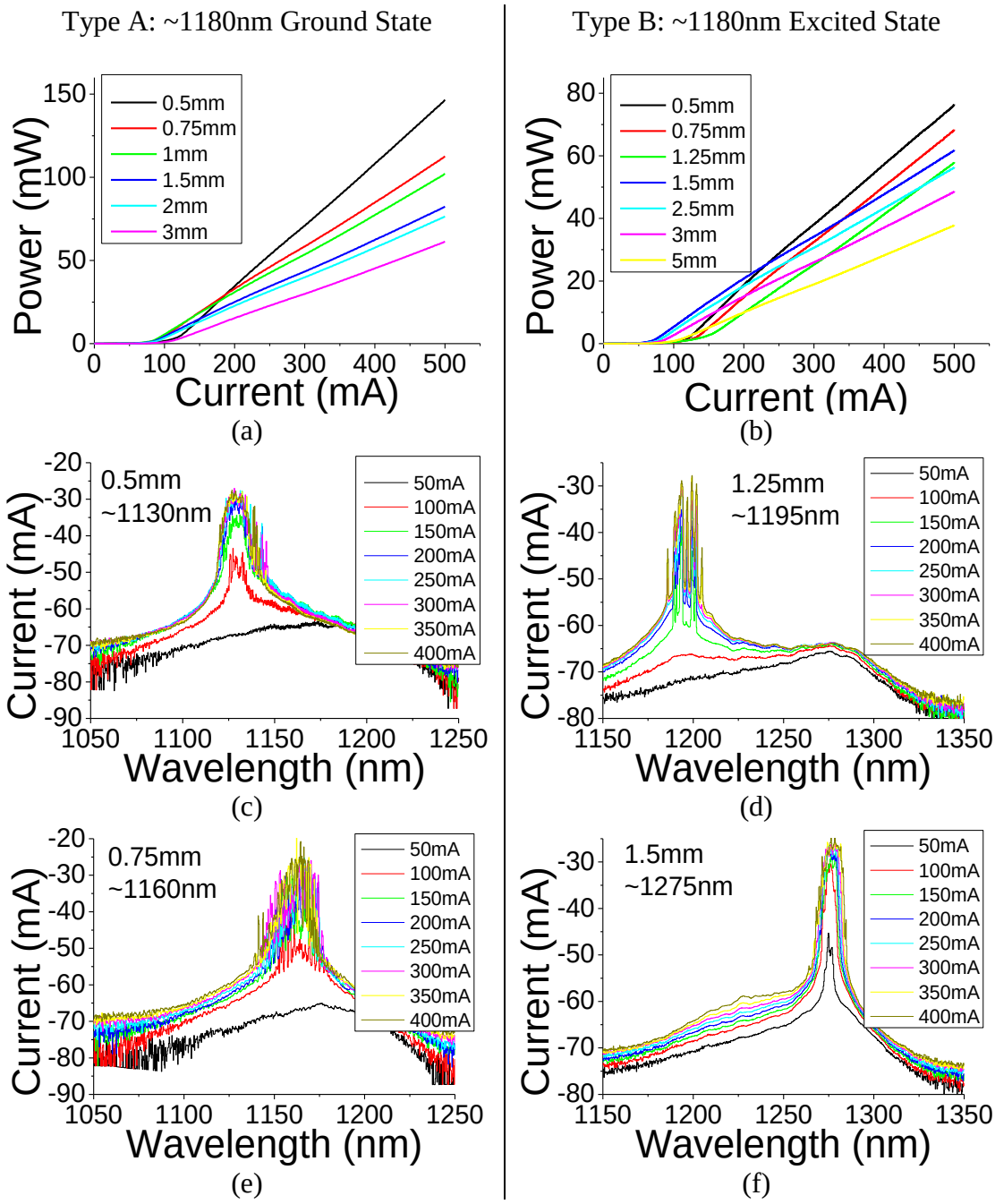

Figure 6-8: L-I measurement of Type-A and –B DWELL broad area lasers and recoded spectra showing the devices lasing via the 1st excited state and the ground state transitions in a shorter and the next shortest cavity length respectively

In the figure, the left-hand-side column presents the results of the Type-A wafer, and the right-hand-side presents those of the Type-B. Based on the length dependent measurement of these lasers, it was observed that for short cavities, the lasers lase via excited states, as the cavity length increases, the lasers start to lase via ground states. This phenomenon was expected. In short cavity devices, as injection current increases, the ground state gain saturates below the threshold gain, so that carries start to fill-up excited states. As more current is injected the excited state gain increases, and the device starts to lase upon reaching the threshold gain. In longer cavity devices, the ground state gain reaches the threshold gain before saturation, hence lasing via ground state upon reaching the threshold current.

➢ Estimation of Gain

The results show that the Type-A lasers start lasing via ground state with a shortest cavity length of 0.75mm, while the Type-B lasers start with a cavity length of 1.5m. This observation demonstrates that the ground state gain in Type A material is higher than that of Type B. Estimation of the gain for these materials can then be performed based on a typical internal loss, α_i, to be ~10cm^{-1} and a typical approximation of as-cleaved facet reflectivity for GaAs-based waveguides, R, to be ~0.31, using the equation:

$$g^{th} = \alpha_i + \frac{1}{2L}\ln\frac{1}{R^2}$$

For Type A material, the ground state saturation gain was estimated to be 25.62~33.42cm^{-1}, and that of Type B material was estimated to be 17.81~19.37cm^{-1}. As illustrated in Fig. 6-7, compared to those in Type-B material, the QDs in Type A

material have a smaller average dot size to achieve larger bandgap energy (E_g) for a shorter ground state wavelength. Since the volume of the grown InAs is kept constant (0.7nm thick), a smaller average dot size results in a higher dot density, resulting in a higher gain.

➢ Laser Characterisation

From the L-I properties presented in Fig. 6-8 (a) and (b), Fig. 6-9 plots the length dependent characterisation of the two structures.

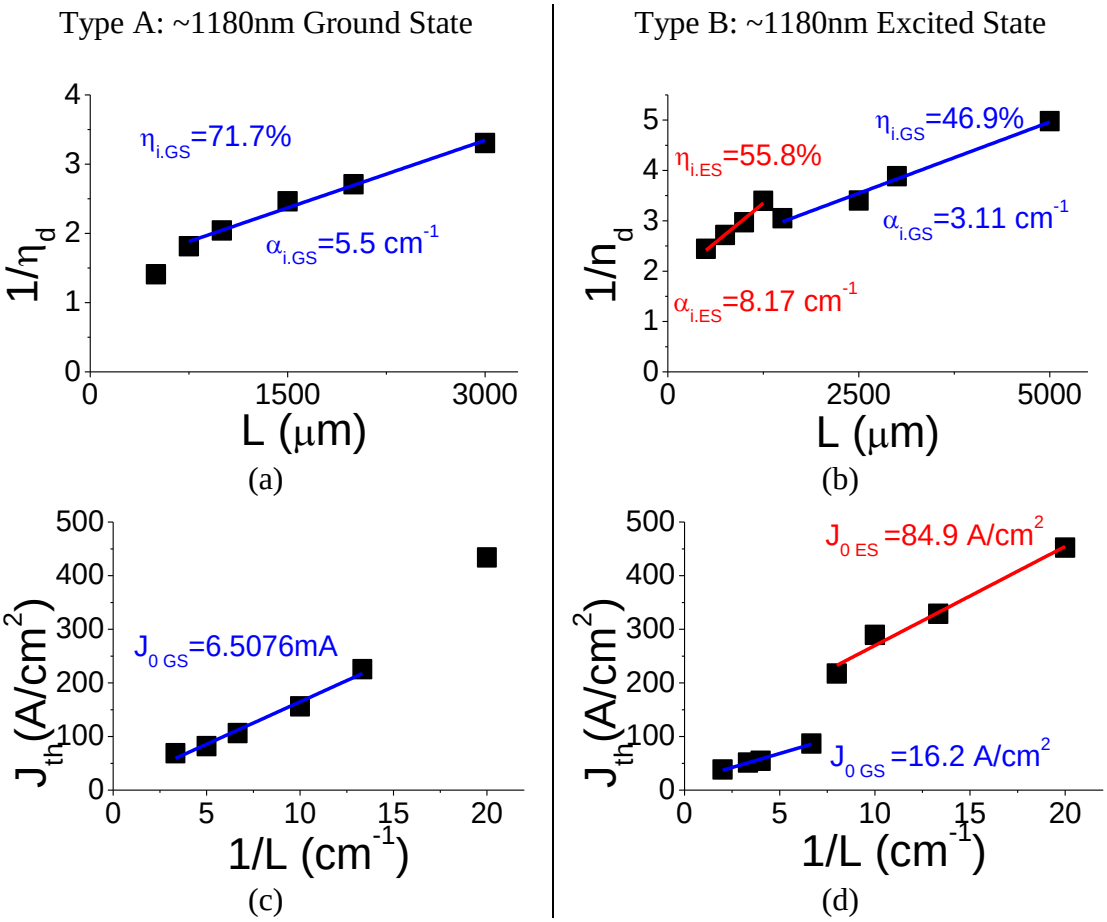

Figure 6-9: Length dependent characterisation of Type-A and –B DWELL broad area lasers

In (a) and (b), the internal quantum efficiency (η_i) and internal loss (α_i) are estimated by plotting the inverse external differential quantum efficiency ($1/\eta_d$) as a function of cavity length (L). In (c) and (d), the transparency threshold current density (J_0) is

estimated by plotting the current density (J) as a function of inversed cavity length ($1/L$). The estimated parameters demonstrate that the Type-A (ground state ~1180nm) structure operated with a better performance with respect to a higher η_i, a smaller α_i and a lower J_0. However, it is reported that excited state QD lasers perform better with high speed direct modulation [12]. Therefore, despite a comparatively poorer characterised performance, DWELL SAS-MOPAs with an MO of an excited state DFB may be better fit for such modulation applications.

➢ Effect of Using 3 Degree off Substrates

For the above 2 structures, the use of substrates 3^o-off to (110) was aimed at future development of SAS structures, where MOVPE overgrowth processes (in-fill and planarisation) necessitate the use of mis-oriented substrates involved, as described in Chapters 4 and 5. In order to investigate the effect of growing the In(Ga)As/GaAs DWELL structures on 3^o-off substrates, a standard ~1310nm wafer was also grown as a control. This structure has the same epitaxial layer structure as the Type-B material but was grown on a (100) $\pm 0.1^o$ substrate. This material was also fabricated into 50μm wide broad area lasers together with the previous materials and characterised consecutively under the same conditions.

Fig. 6-10 (a) to (d) plot the EL spectra recorded from these lasers with cavity lengths of 1, 1.25, 1.5 and 1.75mm respectively. For 1.75mm long lasers lasing proceeded via the ground state transition about a wavelength of 1310nm. For shorter cavities, dual state lasing was observed, with distinct groups of lasing modes centred at both 1240 and 1310nm for 1.5 and 1.25mm long cavities commensurate with lasing occurring via both

ground state and the 1st excited state transitions. For cavities shorter than 1.25mm (ie. 1mm), lasing proceeded via the 1st excited state alone.

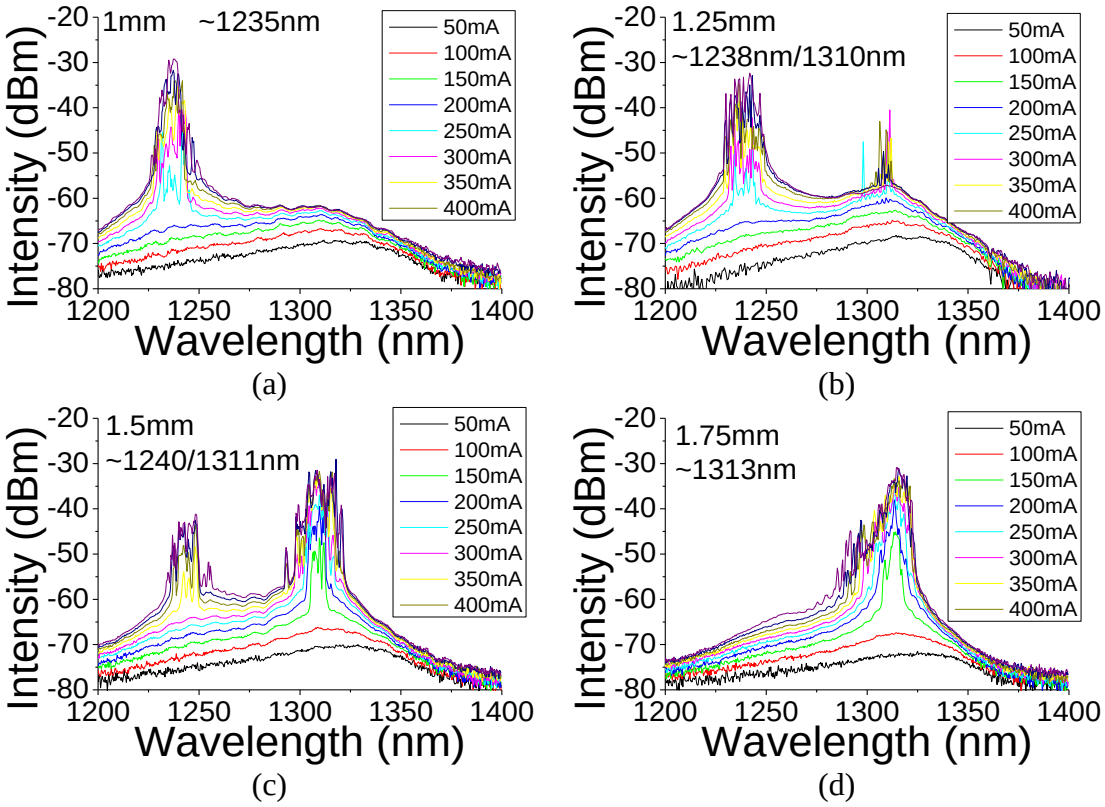

Figure 6-10: Spectra recoded from broad area lasers made from a standard ~1310nm DWELL structure with cavity lengths of 1, 1.25, 1.5 and 1.75mm

As shown in the figure, unlike the Type-A and -B materials, where the switch between lasing via the ground state and lasing via the first excited state occurs sharply as cavity length is reduced (within an increment of 0.25mm), dual lasing via both transitions is observed here over a range of cavity lengths >0.25mm. This phenomenon is a result of the regional variation of the dot density. In operation, the portion of the active region with relatively higher dot density enjoys a higher ground state saturation gain, which can reach the threshold gain at a shorter cavity length, while for the region with a comparably lower dot density, its ground state gain remains saturated below the threshold gain and lasing continues via the 1st excited state transition, as observed in Fig. 6-10 (b) and (c).

This suggests that the dot density in the Type-B material is more uniform than that in this standard material, resulting in the switch from excited state to ground state taking place immediately within a cavity length increase of 0.25mm, as was also observed for Type-A lasers.

Comparing the ground state saturation gain, the Type B material exhibits lasing via the ground state with a cavity length of 1.5mm. In this standard material, although a small portion of the active region can lase via the ground state transition with a cavity length of 1.25mm, when increasing to 1.5mm, there is still a certain portion of it maintains lasing via the 1^{st} excited state transition. This suggests that the Type B material potentially benefits from a higher average ground state saturation gain, thus a higher average dot density. Consequently, the Type B material should have a smaller average dot size hence shorter wavelength, which is in agreement with the measurement of the recorded EL spectra: the ground state and excited state lasing wavelengths of this standard material are measured to be ~1310nm and ~1240nm respectively, whilst those measured for Type B material are ~1275nm and ~1195nm respectively.

The above findings could result from the step-like crystal structures when growing epitaxial layers on a 3^{o}-off substrate, which affect the self-organisation process for the formation of quantum dots, resulting in a more uniform and higher dot density.

6.4 Reference

[1] E. J. Skogen, J. Barton, S. P. DenBaars and L. A. Coldren, "Tunable buried ridge stripe sampled grating distributed Bragg reflector lasers utilizing quantum well intermixing," *LEOS 2001. 14th Annual Meeting of the IEEE Lasers and Electro-Optics Society (Cat. No.01CH37242)*, San Diego, CA, vol. 1, pp. 169-170, 2001

[2] E. J. Skogen, J. S. Barton, S. P. Denbaars and L. A. Coldren, "A quantum-well-intermixing process for wavelength-agile photonic integrated circuits," *IEEE Journal of Selected Topics in Quantum Electronics*, vol. 8, no. 4, pp. 863-869, July - August 2002.

[3] E. J. Skogen, J. W. Raring, J. S. Barton, S. P. DenBaars and L. A. Coldren, "Postgrowth control of the quantum-well band edge for the monolithic integration of widely tunable lasers and electroabsorption modulators," *IEEE Journal of Selected Topics in Quantum Electronics*, vol. 9, no. 5, pp. 1183-1190, September - October 2003.

[4] E. Skogen, J. Raring, G. Morrison, C. Wang, V. Lal, M. Masanovic and L. Coldren, "Monolithically integrated active components: a quantum-well intermixing approach," *IEEE Journal of Selected Topics in Quantum Electronics*, vol. 11, no. 2, pp. 343-355, March - April 2005.

[5] B. Stoltz, M. Dasler and O. Sahlen, "Low threshold-current, wide tuning-range, butt-joint DBB laser grown with four MOVPE steps," *Electronics Letters*, vol. 29, no. 8, pp. 700-702, April 1993.

[6] M. Aoki, M. Suzuki, H. Sano, T. Kawano, T. Ido, T. Taniwatari, K. Uomi and A. Takai, "InGaAs/InGaAsP MQW electroabsorption modulator integrated with a DFB laser fabricated by band-gap energy control selective area MOCVD," *IEEE Journal of Quantum Electronics*, vol. 29, no. 6, pp. 2088–2096, June 1993.

[7] B. Mason, G. A. Fish, S. P. DenBaars and L. A. Coldren, "Ridge waveguide sampled grating DBR lasers with 22-nm quasi-continuous tuning range," *IEEE Photonics Technology Letters*, vol. 10, no. 9, pp. 1211-1213, September 1998.

[8] S. McDougall, O. Kowalski, C. Hamilton, F. Camacho, B. Qiu, M. Ke, R. De La Rue, A. Bryce and J. Marsh, "Monolithic integration via a universal damage enhanced quantum-well intermixing technique," *IEEE Journal of Selected Topics in Quantum Electronics*, vol. 4, no. 4, pp. 636-646, July - August 1998.

[9] D. G. Deppe and N. Holonyak, "Atom diffusion and impurity-induced layer disordering in quantum well III-V semiconductor heterostructures," *Journal of Applied Physics*, vol. 64, no. 12, pp. 93–113, 1988.

[10] S. Charbonneau, P. J. Poole, Y. Feng, G. C. Aers, M. Dion, M. Davies, R. D. Goldberg and I. V. Mitchell, "Band-gap tuning of InGaAs/InGaAsP/InP laser using high energy ion implantation," *Applied Physics Letters*, vol. 67, no. 20, pp. 2954–2956, 1995.

[11] S. K. Si, D. H. Yeo, H. H. Yoon and S. J. Kim, "Area selectivity of InGaAsP-InP multiquantum-well intermixing by impurity-free vacancy diffusion," *IEEE Journal*

of Selected Topics in Quantum Electronics, vol. 4, no. 4, pp. 619–623, July - August 1998.

[12] B. J. Stevens, D. T. D. Childs, H. Shahid and R. A. Hogg, "Direct modulation of excited state quantum dot lasers," *Applied Physics Letters*, vol. 95, no. 6, p. 061101, October 2009.

This Page
Intentionally
Left Blank

Chapter 7. Conclusion

This thesis has presented research activities conducted in the development of GaAs-based self-aligned stripe (SAS) distributed feedback lasers (DFB) based on GaAs-InGaP regrowth technology and its incorporation into the conceptualisation of monolithically integrated master oscillator power amplifier (MOPA) designs, into the scheme of photonic integration.

In Chapter 1, I briefly went through the development of DFB lasers in more than 4 decades since its birth in 1970s. Emphasis was put into the development of different methods of gratings fabrication, where the two main approaches used in nowadays (lateral gratings and overgrown gratings) were introduced and compared. Then, I described the gap between the current GaAs-based photonic integration technologies and its commercialisation, as comparing to the maturity in the InP-based photonic integrated circuits, where a certain technological barrier concerning the Al-containing layers in usual GaAs-based waveguides has to be overcome. After, I highlighted the motivation behind the research activities in this thesis.

In Chapter 2, I introduced the experimental methodology involved in the research in the rest of the chapters with respect to a typical 4-stage research process: (1) waveguide design, (2) wafer growth, (3) device fabrication and (4) device characterisation. Fimmwave, supplied by Photon Design, has been used for waveguide designing and simulating, then the epitaxial layer structures were grown in the EPSRC National Centre

for III-V Technologies based in Sheffield. The devices were mostly fabricated in the device fabrication clean room and characterised using the characterisation setups in the Nanoscience & Technology Building.

In Chapter 3, I presented the development process for a set of narrow ridge 2×, 4× and 6× QWs DFB lasers operating at ~1000nm. This study was primarily carried out as preparatory work to support the development of the SAS DFB lasers in Chapter 4. The research started with ridge waveguide modelling to simulate the confinement factors in QWs (Γ_{QWs}) and grating layers ($\Gamma_{grating}$), so as to design three 2×QWs structures with different $\Gamma_{grating}$, and 4× and 6× QWs structures with a constant $\Gamma_{grating}$. Broad area lasers were first made prior to the make of the DFBs to compare the properties of samples: (1) grown by MOVPE and MBE and (2) incorporating 2×, 4× and 6× QWs. In the fabrication of DFBs, A two-stage growth process was used, associated with a grating patterning-etching process between the planar growth and the overgrowth. 3μm wide ridge waveguide DFBs were fabricated and characterised. The main issue of this batch of designs was their in-stability for single lateral mode lasing, where the accidentally over-etched (through active region) ridge waveguide could support multi-lateral-mode operation. This unfortunately made it impossible for this batch of deigns to achieve high power single-mode lasers. However, compared to the previously reported DFB laser by my group, obvious improvement has been achieved with respect to threshold current, output power and SMSR. Also, the experimentally estimated coupling coefficients of each structure designed matched with those calculated from the simulated confinement factor, thereby validating the simulation of the structures in the waveguide design stage from the very beginning.

In Chapter 4, I described the conceptualisation and realisation of SAS DFB lasers. Based on the previous research of SAS lasers utilising an InGaP optoelectronic confinement layer and DFB lasers employing buried GaAs/InGaP index-coupled grating, this study incorporated the grating layer immediately below the SAS with a distance above the active region. A 3-stage growth process was used, associated with 2 patterning-etching processes to form the grating and the SAS respectively. 3μm SAS DFBs were fabricated and demonstrated single mode operation. Again, the experimental measurement was fed back to the simulation through comparison of experimentally measured and simulated coupling coefficient and simulated far-field beam profile.

In Chapter 5, the research conducted in Chapter 4 has been furthered into the development of GaAs-based SAS monolithically integrated master oscillator power amplifier (MOPA). After a brief review of the current state-of-the-art in the development of monolithic MOPAs, I described the two MOPA types designed and studied in the chapter. Both types incorporated an SAS-DFB section and a tapered SAS-SOA section, whilst one had normal-to-facet SOAs and the other was 7^{o}-off. Due to the poor quality of the 2^{nd} overgrowth, the SOA sections were highly defective which made it impossible to drive the SOAs with a CW current source. The devices were characterised with DFB sections CW pumped and the SOA sections pulsed pumped. The experimental results have been discussed and future improvement to this prototype design has also been presented.

In Chapter 6, an optimised version of SAS-DFB-MOPA was first presented. Based on the prototype 2-section designs studied in Chapter 5, this 4-section MOPA

incorporates a rear absorber, a DFB laser section, a spacer and an SOA with an un-pumped window area. Then, two other potential directions of future work for continuing this research have been described, together with brief discussions of some experimental results from preparatory work performed, including (1) the study of active-passive integration on a ~1060nm InGaAs QD material using impurity free vacancy disordering and (2) the comparison of ground state lasing and excited state lasing properties of two In(Ga)As/GaAs DWELL materials. These preparatory works were conducted to support the future development of (1) GaAs-based sampled-grating DBR (SG-DBR) tunable lasers and (2) high power ~1180nm monolithically integrated MOPA based on the techniques of SAS and GaAs/InGaP buried grating.

Appendix I: Fimmwave Simulation Example

This appendix describes the technical operation of the simulation tool, Fimmwave, used in this thesis.

Fig. 1 shows a screenshot of a ridge DFB waveguide design as an example, where the RWG interface, used for simulation of the ridge waveguides (RWG), was adopted to model the epitaxially grown structure. In the figure, the layer information for the ridge, i.e. the central segment in left-hand-side, is shown in a separate window on the right-hand-side for clarity. The red layer highlighted represents the grating layer, which has been selected as the section for optical confinement factor simulation (i.e. calculates overlap of optical mode with this layer), in order to help determine the grating coupling coefficient.

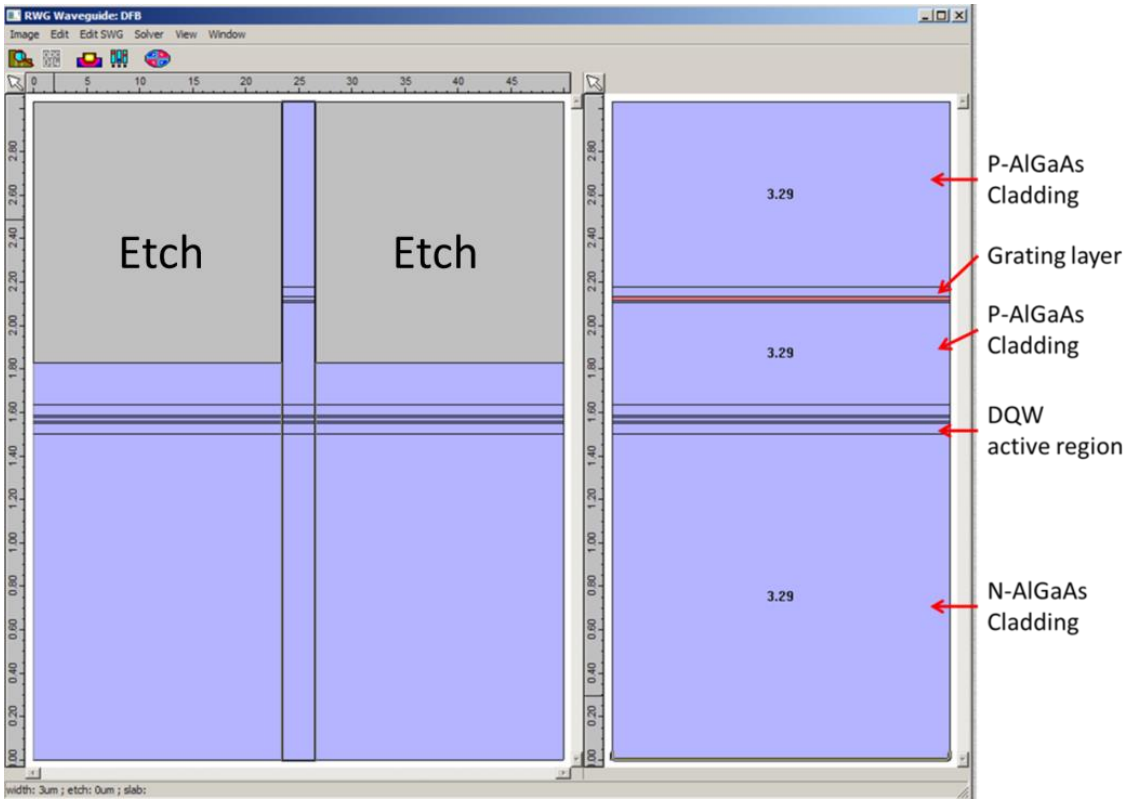

Figure 1: User interface of Fimmwave and an example of DFB ridge waveguide modelling

Fig. 2 presents the parameters associated with the modelled waveguide. The left-hand-side window illustrates a 3μm wide ridge defined by etching the material at either side of the 3μm central slice by 1.2μm (blue box).

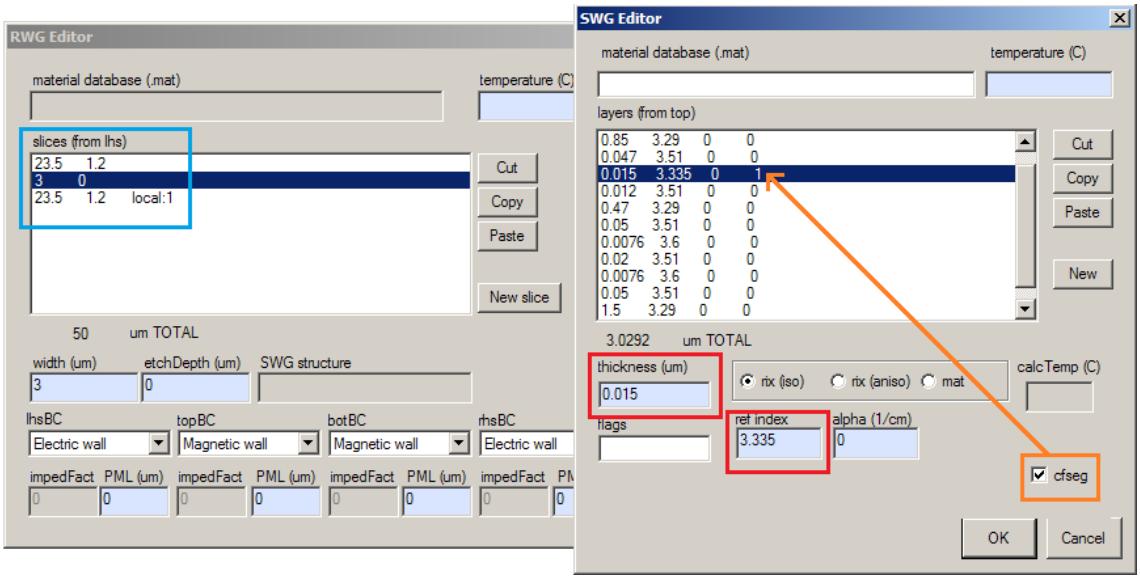

Figure 2: Waveguide editor for waveguide definition

The right-hand-side window shows the epitaxial layer structure, i.e. thickness and refractive index (red box), entered into the software. The "cfseg" (confinement factor segment) is selected for the grating layer for optical confinement factor analysis (orange box), such as to calculate optical overlaps with this segment of the ridge waveguide.

For structural modelling, Fimmwave provides several solvers to suit different requirements. In my work, the FMM solver was selected and "Semivec TE" (semi-vectorial transverse electric) type was chosen for simplicity, as shown in Fig. 3. The wavelength is set to 0.98μm to match the expected peak wavelength of the resultant material. By typing "10" into "max Nmodes" box, the solver is instructed to find a maximum of 10 modes when running the simulation.

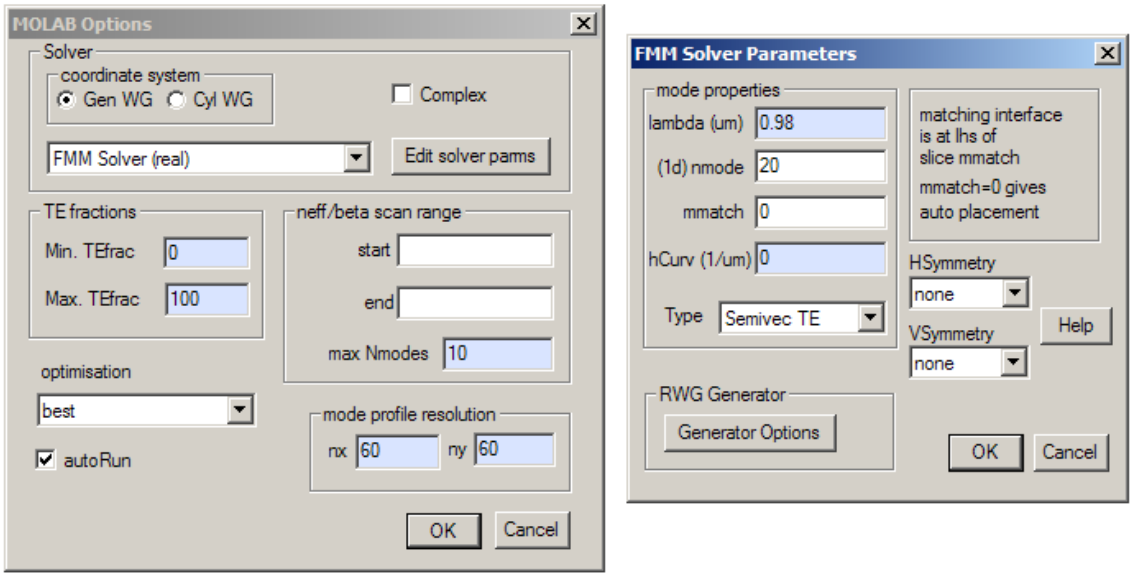

Figure 3: Solver settings for simulation

The simulation starts with a click on the "Build List" button in the left-hand-side window shown in Fig. 4. After, 10 modes (green box) are found and listed, which can each be inspected in detail, as in the right-hand-side window.

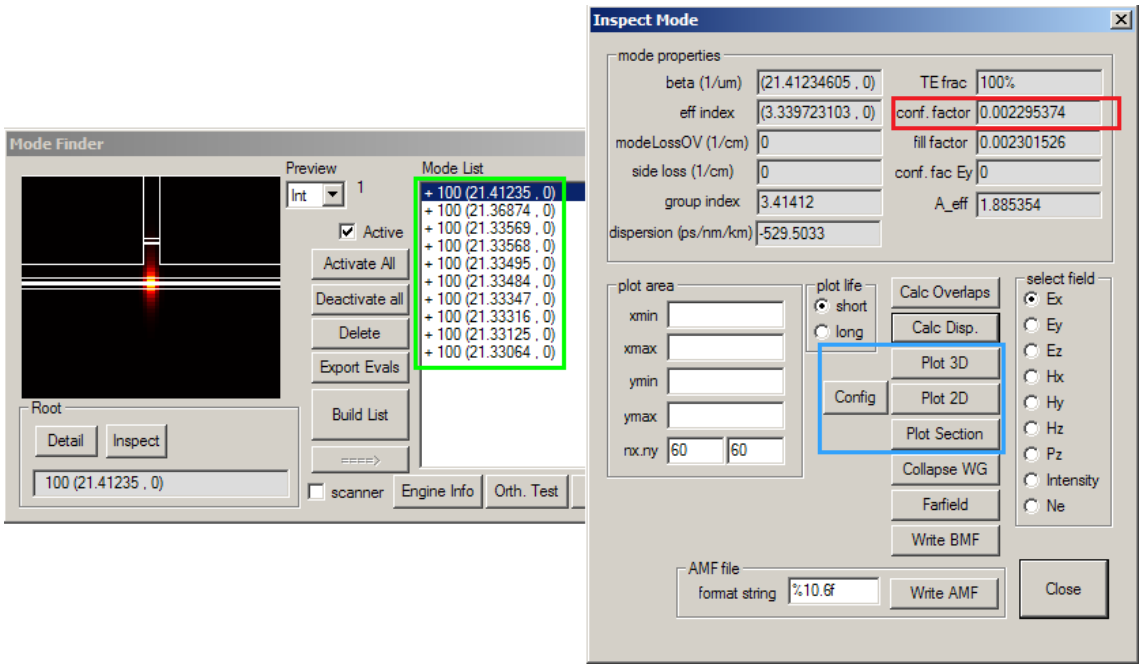

Figure 4: Waveguide simulation and mode inspection

The modes found by the solver are based on the analysis of the layer structure (defined by layer thicknesses and refractive indices) and the waveguide structure (defined by ridge width and etch depth), which does not take into account the electrical

properties such as the P/N doping and location of contact. This means that the solver finds any potentially supported index-guided optical mode regardless of the current flow in the junction, which determines where the light is generated. Therefore, an examination of the profile for each found mode (single peak is seen as it is; multiple-peak is seen as a group) is necessary to determine its validity. A found mode is only valid if the envelope of the mode is laterally centred at the defined ridge and vertically centred at the active region.

As shown in the blue box in Fig. 4, Fimmwave provides various methods for mode profile examination. By using the functions "Plot 2D" and "Plot 3D" and "Plot Section", the mode profile can be displayed in a variety of forms to assist in visualisation of the optical mode. By using these functions, the 1st mode is the only valid mode found in this example and the confinement factor in the grating is 0.002295, as highlighted in the red box. Fig. 5 shows the (a) 2-D view and (b) 3-D view of this mode by using "Plot 2D" and "Plot 3D" functions respectively.

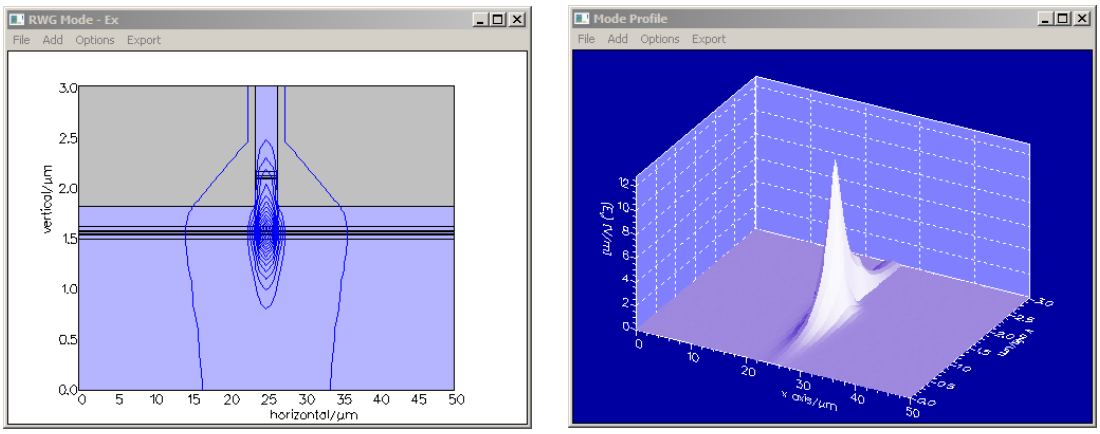

(a) (b)

Figure 5: Visulisation of optical mode profile: (a) 2-D plot and (b) 3-D plot

The result shows that a single mode is confined both vertically and laterally in the example ridge waveguide. Further, the fast/slow axis-sections can also be extracted by using "Plot Section" function.

In addition, Fimmwave supports simulation of the far-field beam profile of the waveguide. For the example waveguide, the far-field simulation (Fig. 6) shows a vertical FWHM (Full width at half maximum) of 38.51^{o} and a horizontal FWHM of 14.36^{o}, consistent with emission from the narrow (135.2 nm) active region and relatively broad (3μm-wide) ridge.

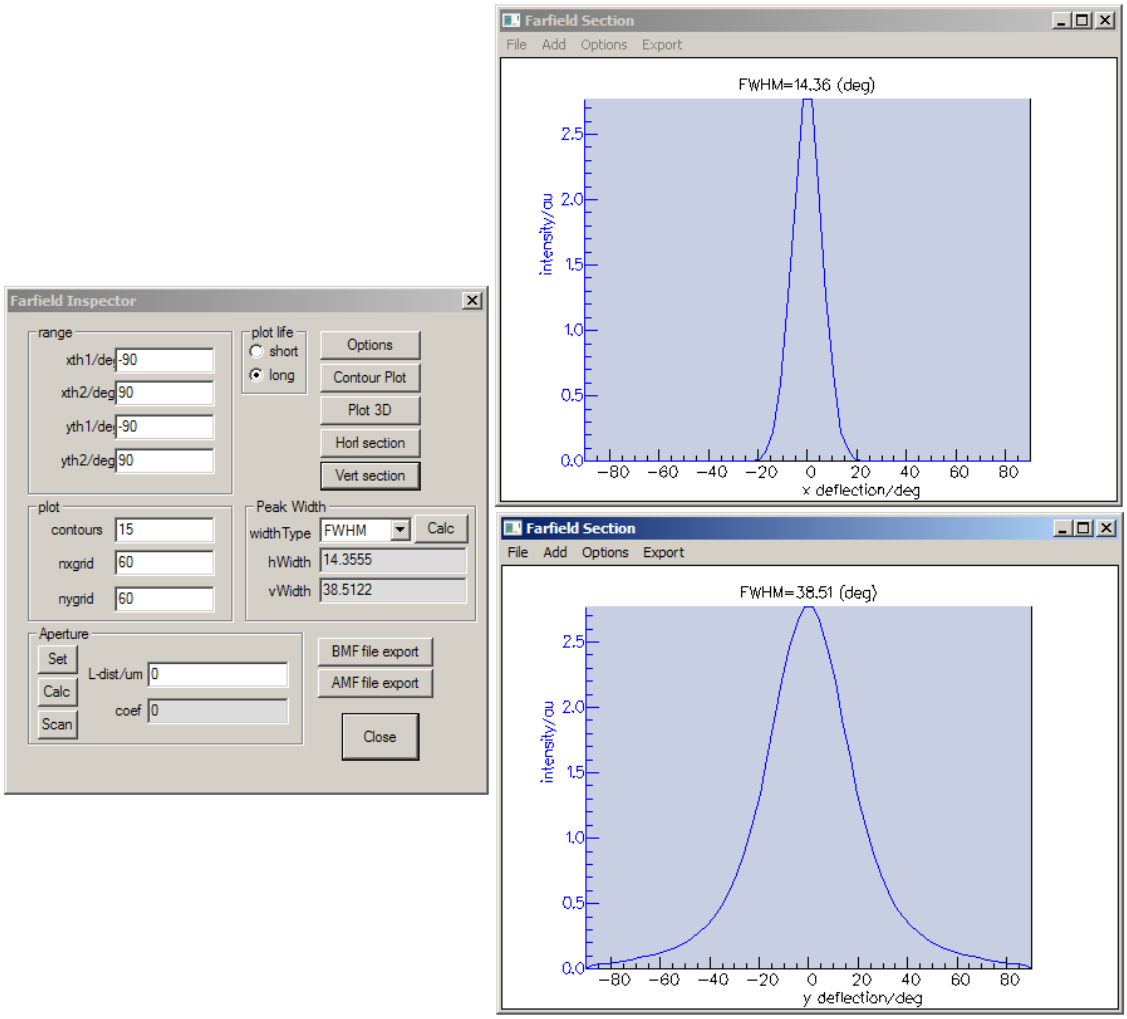

Figure 6: Far-field simulation: 2-D beam profile simulation